

ABSTRACT

GITTARD, SHAUN DAVIS. Light-based Rapid Prototyping of Micro- and Nanoscale Medical Devices for Drug Delivery and Regenerative Medicine. (Under the direction of Dr. Roger Jagdish Narayan).

Rapid prototyping technologies have developed significantly since their inception two decades ago. Techniques that utilize light for controlling structuring are particularly of interest for the medical device industry since they are able to produce devices with minimal effects that undesirable for medical devices, such as high temperatures and hazardous chemicals. The ability to guide and focus light has enabled micro- and even nanoscale device production with exceptional freedom in geometry. In these studies, the light-based rapid prototyping processes of two-photon polymerization, dynamic mask stereolithography, and UV soft lithography were used to produce medical devices for drug delivery and regenerative medicine applications. In the field of drug delivery, microneedles were the focal point. Discoveries made in microneedle production technique, design, functionalization, application, characterization, and materials are reported in this dissertation. Solid and hollow microneedles were produced by two-photon polymerization and dynamic mask lithography. The advantages and disadvantages of rapid replication by UV soft lithography of solid needles were investigated in detail. Delivery of quantum dots and antimicrobial agents by microneedles via injection with hollow microneedles and coating and encapsulation of solid microneedles are reported, respectively. Production of biofouling-resistant microneedles was achieved. Voltage-controlled drug delivery with nanoporous gold electrodes is also presented. In the field of regenerative medicine, advances in tissue engineering scaffold and also patient-specific prosthesis production are reported. Tissue engineering scaffolds of user defined geometries were produced by two-photon

polymerization. Patient-specific prostheses were produced by stereolithography. The medical devices and production techniques developed here have advanced the fields of drug delivery and regenerative medicine and are significant steps towards clinical devices.

© Copyright 2011 by Shaun Davis Gittard

All Rights Reserved

Light-based Rapid Prototyping of Micro- and Nanoscale Medical Devices for Drug Delivery
and Regenerative Medicine

by
Shaun Davis Gittard

A dissertation submitted to the Graduate Faculty of
North Carolina State University
in partial fulfillment of the
requirements for the degree of
Doctor of Philosophy

Biomedical Engineering

Raleigh, North Carolina

2011

APPROVED BY:

Dr. Roger J. Narayan
Committee Chair

Dr. Boris N. Chichkov

Dr. Nancy A. Monteiro Riviere

Dr. Jim E. Riviere

Dr. Harold C. Pillsbury

Dr. Oliver F. Adunka

DEDICATION

This dissertation is dedicated to my parents Norbert Gittard and Cynthia Holley and to my fiancée Ecaterina Panaiti. To my parents, thank you for instilling in me an unending thirst for knowledge and a drive to succeed. Norbert, merci pour tout ta sagesse et aide et pour m'enseigner comment de penser comme un ingénieur. Cindy, thank you for your help with everything, I wouldn't have been able to make it through venturing around the globe without you helping me take care of everything when I was gone. Also, thank you for all of your advice and wisdom. Și în cele din urmă, mulțumesc Catiusha mea. Fără tine aceasta realizare ar fi nimic. Ești inspirația mea. Ești tăria mea. Mulțumesc și te iubesc.

BIOGRAPHY

Shaun Davis Gittard was born on 4th of October 1984 in Madrid, Spain, to Cynthia Holley and Norbert Gittard. He attended Providence Day School in Charlotte and graduated in 2003. Shaun's career as a biomedical engineer began with an internship during the summer of 2003 performing cardiovascular biomedical research at Heineman Medical Research in Charlotte. He pursued his undergraduate studies at Washington University in Saint Louis and graduated in 2007 with his Bachelor of Science in Biomedical Engineering. Shaun began his graduate studies at the Joint Department of Biomedical Engineering at North Carolina State University and University of North Carolina Chapel Hill in 2007. During his graduate studies he conducted research at Duke University Medical Center, Laser Zentrum Hannover, Sandia National Laboratories, and North Carolina State University. In 2008 he was an author on the journal JOM's paper of the year. In 2009 he received the American Ceramics Society's Graduate Excellence in Materials Science (GEMS) Sapphire award and the Parenteral Drug Association's Student Award. As of March 2011, he has authored 24 peer-reviewed journal articles and one book chapter.

ACKNOWLEDGEMENTS

In my graduate studies I have had the unique opportunity of conducting research with outstanding scientists throughout the world. All of these people have been wonderful colleagues to me.

Firstly, I would like to thank Dr. Roger J Narayan, M.D., Ph.D. None of this would have been possible without you. Thank you for your guidance, advice, and all of the long nights proofing my papers. You provided me with numerous “once in a lifetime” experiences working all over the world; for these experiences I am particularly thankful. Our hours of discussions troubleshooting and coming up with new experiments were the most stimulating component of my researching.

Thank you to the members of our research group at NC State: Philip Miller, Ryan Boehm, Dr. Chunming Jin, Bonnie Pierson, Harry Scott, Alex Nguyen, Timothy Martin, Remya Srinivas, Bo Chen, Huadong Xu, Russell Meredith, Dr. Ravi Aggarwal, Dr. Wei Wei, and Dr. Anand Doraiswamy. Your training, assistance, and discussions were vital in completing my work.

Thank you to everyone at Laser Zentrum Hannover: Dr. Aleksandr Ovsianikov, Anastasia Koroleva, Andrea Deiwick, Dr. Arsenij Kuznetsov, Arune Gaidukeviciute, Dr. Boris Chichkov, Dr. Carsten Reinhardt, Claudia Unger, Elena Fadeeva, Fabrice Maiorana, Hasan

Akar, Jürgen Koch, Dr. Lothar Koch, Dr. Mangirdas Malinauskas, Martin Grüne, Dr. Kotaro Obata, Dr. Roman Kiyon, Dr. Sabrina Schlie, Wei Chen, and Xiao Shizhou. Anastasia, thank you for all of the help with cell studies and SEM, and especially for your assistance with living in Germany. Aleks, thank you for being such a good host and teaching me everything about two-photon polymerization. Boris, thank you for making my stays at LZH possible.

I would like to thank Dr. John Perfect and members of the Division of Infectious Diseases at Duke University Medical Center for allowing me to use their facilities and share with me their vast knowledge in microbiology. To Dr. Nancy Monteiro-Riviere, thank you for letting me work in your lab and for providing all of the skin samples. None of my microneedle research would have been possible without you. Al Inman, Leshuai Zhang, and Meghan Samberg, thank you for your help with the cytotoxicity and histology work. Thank you to Chung-An Max Wu, Cindy Ha, Marcus Ong, Ben Jacobs, Mary Langham, Stephen Fares, and especially Dave Robinson for making my visit to Sandia National Laboratories such a great experience. Thank you to Eva Johannes for your guidance and assistance with optical microscopy. Chuck Mooney deserves a special thank you for taking so many of the beautiful SEM images displayed throughout this dissertation. Thank you to my colleagues at North Dakota State University, Rutgers University, in Bucharest, and at Ceramatec for their contributions to this dissertation.

Thank you to Stephanie Gootnick, Rekha Balasubramanyam, Nancy McKinney, Linda Simerson, Sharon Womble, Harriet Brewer, and Steve Callendar for all of your patience with all of my unique administrative situations.

Lastly, I would like to thank my family for all of their help and support during my studies.

Thank you Cindy, Norbert, Patrick, Jake, Connie, Nancy, and especially Catia.

TABLE OF CONTENTS

LIST OF TABLES	xiii
LIST OF FIGURES	xiv
1. INTRODUCTION	1
A Brief History of Microscale Medicine	1
References	8
LITERATURE REVIEW	14
2.1 Rapid Prototyping of Medical Devices	14
Introduction	14
Stereolithography	18
Laser Machining/Ablation	24
Laser Bioprinting: MAPLE Direct Write and LIFT	33
Selective Laser Sintering/Melting	39
Two-Photon Polymerization	44
Conclusion	52
References	53
2.2 Microneedle-mediated Drug Delivery	86
2.2.1 Applications of Microneedle Technology to Transdermal Drug Delivery	86
Introduction	86
Aspects of Microneedle Design	91
Microneedle Materials	98
Fabrication of Microneedles	103
Methods of Drug Delivery with Microneedles	111
Conclusion	113

References	114
2.2.2 Recent Advances in Microneedle-mediated Parenteral Drug Delivery.....	126
Introduction	126
Advances in Microneedle Design and Production Techniques	126
Delivery Techniques.....	131
Recent Microneedle Drug Delivery Studies.....	133
Dyes.....	133
Insulin and other Pharmaceuticals.....	134
Vaccines	137
Assessment of Microneedle Properties	139
Conclusions	142
References	142
2.3 Micro- and Nanoscale Devices in Regenerative Medicine.....	153
2.3.1 Microscale Rapid Prototyping of Prosthetics	153
References	159
2.3.2 Micro- and Nanoscale Aspects of Tissue Engineering.....	165
Introduction	165
Effects of Scaffold Architecture on Tissue Engineering	165
Mass Transport in Tissue Engineering Scaffolds	169
Cell Seeding of Tissue Engineering Scaffolds	171
Conclusions	172
References	173
3 DRUG DELIVERY VIA MICRONEEDLES AND RELATED TECHNOLOGIES.....	180
3.1 Fabrication of Polymer Microneedles Using a Two-Photon Polymerization and Micromolding Process.....	180
Abstract	182

Introduction	183
Experimental Procedure	187
Results	192
Conclusions	197
References	199
3.2 The Effects of Geometry on Skin Penetration and Failure Mechanics of Polymer Microneedles	
Abstract	205
Introduction	206
Materials and Methods	211
Results	215
Discussion	224
Conclusions	228
References	229
3.3 Assessing the antimicrobial activity of zinc oxide thin films using disk diffusion and biofilm reactor	
Abstract	236
Introduction	238
Materials and methods.....	239
Results and discussion.....	247
Conclusions	251
References	256
3.4 Antifungal Textiles Formed Using Silver Deposition in Supercritical Carbon Dioxide ...	
Abstract	265
Introduction	266
Experimental Procedure	270

Results and Discussion.....	273
Summary	280
References	281
3.5 Pulsed laser deposition of antimicrobial silver coating on Ormocer® microneedles.....	289
Abstract	291
Body	292
References	303
3.6 Two Photon Polymerization-Micromolding of Polyethylene-Glycol Gentamicin Sulfate Microneedles	308
Abstract	309
Body	311
References	325
3.7 Pulsed Laser Deposition of Antimicrobial Metal Thin Film Coatings on Microneedles Produced by Visible Light Dynamic Mask Micro-stereolithography	329
Abstract	329
Introduction	330
Methods.....	338
Results	344
Discussion	356
Conclusion.....	361
References	362
3.8 Delivery of Radioactive Isotope Tracer in a Porcine Model via a Microneedle Patch System	375
Conclusions	398
Acknowledgements	399

3.9 Multiphoton microscopy of transdermal quantum dot delivery using two photon polymerization-fabricated polymer microneedles	400
Abstract	401
Introduction	402
Methods	411
Results and Discussion	419
Conclusions	431
References	432
3.10 Supercapacitive transport of pharmacologic agents using nanoporous gold electrodes ..	440
Abstract	441
Introduction	442
Experimental Procedure	448
Results and Discussion	453
Conclusions	460
References	461
4 RAPID PROTOTYPING OF MICRO- AND NANOSCALE DEVICES FOR REGENERATIVE MEDICINE	471
4.1 Rapid prototyping of scaphoid and lunate bones	471
Abstract	472
Body	473
References	485
4.2 Two-photon polymerization of Scaffolds for Tissue Engineering	491
Introduction	491
Materials and Methods	491
Results and Discussion	494
Conclusions	506

Acknowledgements	507
References	507
5 CONCLUSIONS	509

LIST OF TABLES

Section 2.1	
Table 1. Comparison of laser direct writing processes	18
Table 2. Properties of Ormocer®.....	49
Section 2.2	
Table 1. Strengths of Materials Used To Make Microneedles	100
Section 3.2	
Table 1. Dimensions of the microneedle geometries.....	212
Section 3.7	
Table 1. Microneedle Input and Actual Geometries.....	341
Table 2. Hole Resolution Results.....	346
Section 3.8	
Table 1. Day/time associated with time points for pharmacokinetic studies.....	386
Table 2. Summary of pharmacokinetics analysis	388
Table 3. Microneedle delivery test matrix	389
Table 4. Delivery results	398
Section 3.10	
Table 1. Theoretical storage capacity versus pore diameter for porous capacitor	448
Table 2. Experimental charge storage of nanoporous gold wires.....	458
Table 3. Release of benzylammonium salicylate measure via UV spectroscopy.....	458

Section 4.2

Table 1. Scaffold Dimensions.....	497
-----------------------------------	-----

LIST OF FIGURES

1. Introduction

Figure 1. Picture of Charles-Gabriel Pravaz and his 1852 depiction of the hypodermic syringe.....2

Figure 2. One of the first microscale medical devices, the stainless steel microelectrode by J. D. Green5

2. Literature Review

2.1 Light-based Rapid Prototyping

Figure 1. Stereolithography24

Figure 2. Jablonski diagrams of single-photon and two-photon fluorescence, polymerization, and photochemical ionization (ablation) 26

Figure 3. Laser machining30

Figure 4. Polylactic acid scaffold with controlled pore geometry produced by excimer laser ablation32

Figure 5. Laser bioprinting38

Figure 6. Selective laser sintering41

Figure 7. The two-photon polymerization process46

Figure 8. Ormocer® microneedles.....50

Figure 9. Tissue engineering scaffolds produced by two-photon polymerization.....52

2.2 Micro-mediated Drug Delivery

2.2.1 Applications of Microneedle Technology to Transdermal Drug Delivery

Figure 1. Deformation of the skin upon microneedle insertion91

Figure 2. Microneedle design types95

2.2.2 Recent Advances in Microneedle-mediated Parenteral Drug Delivery

Figure 1. Commercially available microneedle devices127

2.3 Micro- and Nanoscale Devices in Regenerative Medicine

2.3.1 Microscale Rapid Prototyping of Prosthetics

Figure 1. Screenshot of Mimics processing of CT data, final prosthesis CAD model design by 3-matic, and actual implant produced by electron beam melting156

2.3.2 Micro- and Nanoscale Aspects of Tissue Engineering

Figure 1. Effect of surface features on cells169

3 Drug Delivery Via Microneedles and Related Technologies

3.1 Fabrication of Polymer Microneedles Using a Two-Photon Polymerization and Micromolding Process

Figure 1. Scanning electron micrograph of an eShell 200 microneedle arrays (a) and individual microneedle (b) created using the 2PP microfabrication and subsequent PDMS micromolding process194

Figure 2. Characteristic plot of force versus displacement for eShell 200 microneedle array obtained during axial compression testing196

Figure 3. Optical micrograph of human stratum corneum and epidermis samples after eShell 200 microneedle array insertion and removal197

3.2 The Effects of Geometry on Skin Penetration and Failure Mechanics of Polymer Microneedles

Figure 1. Scanning electron microscopy image of a microneedle replica produced by indirect rapid prototyping using two-photon polymerization and UV soft lithography215

Figure 2. Microneedles after compression testing	216
Figure 3. Microneedle compression.....	217
Figure 4. Microneedle failure in force and displacement versus time	218
Figure 5. Microneedles after penetrating into skin with 1.0 N of compression.....	218
Figure 6. Skin Penetration: force versus displacement of microneedles penetrated into full-thickness porcine skin in displacement control mode.....	219
Figure 7. Characteristic example of penetration versus compression.....	220
Figure 8. Timeline of microneedle geometry B being compressed in displacement controlled mode	221
Figure 9. Timeline of microneedle geometry B penetrating skin in displacement controlled mode	222
Figure 10. Fluorescence microscopy of Lucifer Yellow delivery at surface of the skin and Confocal and DIC overlay of Lucifer yellow delivery at 120 um depth	223
Figure 11. Lucifer Yellow delivery into porcine skin assessed with multiphoton microscopy	223

3.3 Assessing the antimicrobial activity of zinc oxide thin films using disk diffusion and biofilm reactor

Figure 1. Atomic force micrograph of zinc oxide thin film grown on silicon wafer.....	251
Figure 2. X-ray photoelectron spectrum of zinc oxide-coated silicon wafer.....	252
Figure 3. Twenty-four hours MTT viability assays for zinc oxide-coated silicon wafers and uncoated silicon wafers	253
Figure 4. Light microscopy images of (A) disk diffusion studies of uncoated silicon wafer without light exposure, (B) zinc oxide-coated silicon wafer without light exposure, (C) uncoated silicon wafer with fluorescent light exposure, and (D) zinc oxide-coated silicon wafer with fluorescent light exposure.....	255

3.4 Antifungal Textiles Formed Using Silver Deposition in Supercritical Carbon Dioxide

Figure 1. Schematic of the scCO ₂ system.....	271
Figure 2. Procedure for fabrication of silver-coated cotton fabrics	272
Figure 3. Scanning electron micrographs of Ag(hepta)-modified fabric (top), Ag(cod)(hfac)-modified fabric (middle), and uncoated fabric (bottom)	274
Figure 4. Scanning electron micrographs of Ag(hepta)-modified fabric (top) and Ag(cod)(hfac)-modified fabric (bottom). The lighter-colored regions on the silver-modified fibers represent silver aggregates	276
Figure 5. Energy dispersive X-ray spectra overlay of Ag(hepta)-modified fabric (top) and Ag(cod)(hfac)-modified fabric (bottom). The spectra of the coated fabrics are in gray, and spectrum of the uncoated fabric is in black	277
Figure 6. Ag(hepta)-modified fabric (top), Ag(cod)(hfac)-modified fabric (center), and uncoated fabric (bottom).....	279
Figure 7. Optical micrographs showing zones of inhibition for Ag(hepta)-modified fabric (left) and Ag(cod)(hfac)-modified fabric (center) at 12 h. An optical micrograph of the uncoated fabric at 12 h (right) is provided for comparison purposes	279

3.5 Pulsed laser deposition of antimicrobial silver coating on Ormocer® microneedles

Figure 1. (a) Scanning electron micrograph of a SR 259 polyethylene glycol dimethacrylate microneedle array, which served as a master structure in the two-photon polymerization–micromolding process. (b) Scanning electron micrograph of a silver-coated Ormocer® microneedle array fabricated using two-photon polymerization–micromolding and pulsed laser deposition	297
Figure 2. (a) Scanning electron micrograph of an uncoated Ormocer® microneedle array. (b) Scanning electron micrograph of a silver-coated Ormocer® microneedle array. (c) Scanning electron micrograph of an individual uncoated Ormocer® microneedle. (d) Scanning electron micrograph of an individual silver-coated Ormocer® microneedle.....	300

Figure 3. (a) MTT viability of human epithelial keratinocytes on uncoated Ormocer and silver-coated Ormocer wafers. (b) Low magnification and (c) high magnification agar diffusion assay results for the uncoated Ormocer® microneedle array. (d) Low magnification and (e) high magnification agar diffusion assay results for the silver-coated Ormocer® microneedle array	302
---	-----

3.6 Two Photon Polymerization-Micromolding of Polyethylene Glycol-Gentamicin Sulfate Microneedles

Figure 1. Scanning electron micrographs of microneedle arrays	319
Figure 2. Fourier transform infrared spectrum of gentamicin-doped polyethylene glycol 600 diacrylate.....	320
Figure 3. Scanning electron micrographs of microneedle arrays after exposure to platelet rich plasma	321
Figure 4. Agar plating assay results	323

3.7 Pulsed Laser Deposition of Antimicrobial Metal Thin Film Coatings on Microneedles Produced by Visible Light Dynamic Mask Micro-stereolithography

Figure 1. a) layout of input STL files that are sent to the Perfactory® machine to produce, b) image of the resulting structures on the build platform, and c) STL drawing of the input STL file for making microneedles which consists of four microneedle arrays held onto a substrate by support structures.....	339
Figure 2. Drawings of input files for testing resolution of making circular holes (a), square holes (b), and line width (c) and the resulting structures that were produced by the Perfactory® system (d-f)	340
Figure 3. Input line width and average actual line width dimensions for the line width resolution test (a). Error bars are standard deviation. Image of diffusion driven polymerization on a line resolution test structure (b)	347
Figure 4. Scanning electron microscopy images of eShell 200 microneedles produced in varying geometries by stereolithography.....	349
Figure 5. SEM images of geometry D	350

Figure 6. a) SEM image of microneedles on a cross-shaped substrate produced by SLA; b) CAD drawing of the input file used to produce the device by SLA.....351

Figure 7. Trypan blue staining of pores in skin produced by application of SLA-produced microneedles352

Figure 8. Optical microscopy images (a-c) and high magnification SEM images (d-f) of uncoated (a,d), zinc oxide coated (b,e), and silver coated microneedle arrays (c, f)..... 353

Figure 9. AFM height data of ZnO (left) and Ag (right) PLD-deposited coatings on silicon over a 10 μm scan range.....354

Figure 10. Agar diffusion results of uncoated (left), Ag coated (center), and ZnO (right) coated D geometry microneedles against *E. coli* (top), *S. epidermidis* (center), and *S. aureus* (bottom). Microneedle arrays are 18 x 18 mm wide.....355

3.8 Delivery of Radioactive isotope in a Porcine Model via a Microneedle Patch System

Figure 1. Components of the microneedle patch376

Figure 2. Optical micrograph of a single microneedle from array 1378

Figure 3. Optical micrograph of a single microneedle from array 2379

Figure 4. Optical micrograph of a single microneedle from array 3379

Figure 5. Scanning electron micrographs of microneedles from array 1. (a) Image of a single microneedle obtained at 0° tilt. (b) Image of a single microneedle obtained at 45° tilt. (c) Image of microneedles obtained at 90° tilt.....380

Figure 6. Scanning electron micrographs of microneedles from array 2. (a) Image of a single microneedle obtained at 0° tilt. (b) Image of a single microneedle obtained at 45° tilt. (c) Image of microneedles obtained at 90° tilt.....381

Figure 7. Scanning electron micrographs of microneedles from array 3. (a) Image of a single microneedle obtained at 0° tilt. (b) Image of a single microneedle obtained at 45° tilt. (c) Image of microneedles obtained at 90° tilt.....381

Figure 8. Pharmacokinetic test #1 results385

Figure 9. Pharmacokinetic test #2 results	387
Figure 10. Microneedle patch test sites.....	390
Figure 11. Microneedle patch application	390
Figure 12. Image of test site during the removal of the microneedle patch.....	391
Figure 13. Test #1 counts with respect to time	392
Figure 14. Test #2 counts with respect to time	393
Figure 15. Test #3 counts with respect to time	394
Figure 16. Expected vs. actual counts for pig 67	396
Figure 17. Expected vs. actual counts for pig 69	397

3.9 Multiphoton microscopy of transdermal quantum dot delivery using two photon polymerization-fabricated polymer microneedles

Figure 1. (a) Schematic of the two-photon polymerization system. (b) Schematic of multiphoton microscopy system	408
Figure 2. (a) Input computer-aided design drawing of hollow microneedles processed via two-photon polymerization. (b) Diagram of hollow microneedle device fabrication by means of two-photon polymerization	414
Figure 3. Fourier transform infrared spectrum of e-shell 300 acrylate-based polymer ...	420
Figure 4. MTT viability of neonatal human epidermal keratinocytes and human dermal fibroblasts on e-shell 300 acrylate-based polymer, polystyrene well plate, and glass	422
Figure 5. Scanning electron microscopy image obtained at 45° tilt of solid e-shell 300 microneedles, which were created by means of two photon polymerization	423
Figure 6. Scanning electron microscopy images obtained at 45° tilt of e-shell 300 hollow microneedles on glass substrates, which were produced using two photon polymerization	425
Figure 7. Scanning electron microscopy images of e-shell 300 hollow microneedle array, which was produced using two photon polymerization.....	427

Figure 8. Multiphoton microscopy images of quantum dot injection via two photon polymerization- fabricated e-shell 300 microneedle array as well as via topical application.....429

3.10 Supercapacitive transport of pharmacologic agents using nanoporous gold electrodes

Figure 1. (a) Diagram showing electrochemical dealloying of Au–Ag alloy to produce nanoporous gold electrodes. (b) Chemical structure of sodium trifluoroacetate and benzylammonium salicylate. (c) Diagram of apparatus used for examining capacitive storage and delivery of benzylammonium salicylate.....450

Figure 2. (a) Scanning electron micrograph of nanoporous gold electrode produced by electrochemical etching. The average pore diameter is 9.86 ± 4.92 nm. (b) Energy dispersive X-ray spectrum of etched nanoporous wire after background subtraction.....454

Figure 3. Electrochemical characterization of nanoporous electrodes456

Figure 4. Net charge accumulated on electrodes during charging and discharging of 50 mM benzylammonium salicylate457

Figure 5. UV absorption spectrum of benzylammonium salicylate electrostatically stored in electrodes and delivered into 4 mL of 10 mM sodium trifluoroacetate..... 459

4 Rapid Prototyping of Micro- and Nanoscale Devices for Regenerative Medicine

4.1 Rapid prototyping of scaphoid and lunate bones

Figure 1. (a) CAD model of lunate (left) and scaphoid (right) bones based on patient computed tomography data. (b) Envisiontec eShell 200 prostheses of lunate (left) and scaphoid (right) bones481

Figure 2. Scanning electron micrograph of eShell 200 material polymerized using Perfactory® SXGA system.....482

Figure 3. Characteristic plot of force (black line) and displacement (gray line) *versus* time for an eShell 200 scaphoid prosthesis483

Figure 4. MTT viability of human epithelial keratinocytes on eShell 200 polymer and control substrates484

4.2 Two-Photon Polymerization of Scaffolds for Tissue Engineering

Figure 1. Stackable Lego®-like scaffolds concept	495
Figure 2. Scanning electron micrographs of Lego®-like scaffolds	496
Figure 3: scanning electron microscopy images of stackable scaffolds for tissue engineering vasculature	498
Figure 4. Hexagonal tissue engineering scaffold	498
Figure 5. CAD drawing of sideways hexagon scaffold design.....	500
Figure 6. Scanning electron micrographs of a perpendicular hexagonal scaffold	500
Figure 7. Six millimeter long sideways hexagon scaffold. Small lines equal 1 mm	501
Figure 8. High magnification fluorescence images of sideways hexagon populated by vascular smooth muscle cells.....	502
Figure 9: Entire 6 mm PEGda scaffold populated with murine vascular smooth muscle cells stained for viability with calcein AM	502
Figure 10. Fibroblast viability measured by CASY cell counting.....	504
Figure 11. UV-Vis absorption spectrum of riboflavin and triethanolamine in deionized water.....	505
Figure 12. Microstructures of polyethylene glycol diacrylate with 0.077 mg/mL riboflavin produced by 2PP	506

1. INTRODUCTION

A Brief History of Microscale Medicine

The first microscale medical device could be considered to be the needle. Acupuncture, which uses needles that have diameters on the order of several hundred microns, has been in practice in China since the Shang Dynasty (1600-1100 BCE) [1]. The Greek physician Galen used hollow needles to study the circulatory system [2]. However, it wasn't until the 1800s that the first use of a needle for drug delivery was reported. The medical use of hollow needles for drug delivery was first reported by Francis Rynd in 1844 [3, 4]. Subsequently the modern pressure-driven hypodermic syringe was independently invented in the 1850s by Alexander Wood and Charles Gabriel Pravaz (Figure 1) [5-7]. These needles were several millimeters in diameter and cannot truly be considered as microscale drug delivery devices, though the designs that they introduced were eventually reduced in size to be on the microscale. Hypodermic needles today are available in diameters ranging from 4.5 mm down to 0.18 mm. In 1859, Dr. H. D. Schmidt developed a "microscopic dissector" system using screws and needles to perform dissections of individual cells [8]. Not only did this device contain microscale elements, but it was capable of controlling positioning of the needle with sufficient precision to dissect cells.



Figure 1. Picture of Charles-Gabriel Pravaz and his 1852 depiction of the hypodermic syringe.

Source: <http://www.general-anaesthesia.com/people/charles-pravaz.html>

The field of medical devices underwent vast growth throughout the 20th century. Indwelling prosthetics, such as the artificial hip [9], and ex vivo organs, such as the dialysis machine [10], were developed. While microscale medical devices have been in existence for millennia, the field of studying microscale medical devices is very much still in its youth. Even though medical device research was expanding rapidly in the 20th century, it wasn't until the end of the 20th century that research of microscale medical devices took off. There are three exceptions that should be noted: the micropipette, the glass electrochemical electrode, and the solid metal microelectrode. In the early 1900s glass micropipettes were

developed by several researchers for injecting minute quantities of liquid into individual cells.

Glass micropipettes were first used for medical research in the early 1900s [11-14]. These devices consisted of hollow glass tubes that were drawn to form a fine point, several microns in diameter. The process of making these pipettes is well described in the 1918 review by Robert Chambers [14]. Micropipettes are used to withdraw material from and inject material into cells [14, 15]. In 1907 J.F. McClendon demonstrated using a glass micropipette to remove the nucleus from a cell.

Electrochemical microelectrodes have been in existence since the early 1900s. In 1921 I.H. Hyde proposed the first design of a microelectrode, using glass tubes that were drawn out to a tapering tip of a few microns diameter, which he proposed could apply electrical stimulation to individual cells [16]. Throughout the late 1920s, several electrochemical “microelectrode” devices were reported in the literature, which were used for performing electrochemical measurements of miniscule volumes of fluid [17-22]. These could be considered as the first “micro-fluidic” sensors. For example, Salle reported using a system composed of a drawn glass micropipette and a hydrogen electrode to measure the pH of blood [17]. While these two microscale devices were developed in the early 20th century, these devices were not a development in micro-technology. Both of these devices were made by drawing glass to a tapering point, a technique (with minimal control of microscale features) which had been performed for centuries, albeit not for medical applications.

Metal microelectrodes (also known as microneedle electrodes) were first reported in the 1950s. These electrodes were first produced by Grundfest *et al.* using “electrolytic etching”, where electrochemical etching was used to refine the tips of metal wires [23]. Metal wires or pins were immersed in and removed from a strong acid or oxidizing agent several times with alternating current applied [23-25]. Electrodes were first made from stainless steel [23, 25] and tungsten [24]. By etching stainless steel pins in hydrochloric acid, J. D. Green achieved tip thicknesses of approximately 0.5 μm (Figure 2b) [25]. Penetration of the microelectrode in tissue was confirmed by Prussian blue staining, a similar technique to what is used today to demonstrate skin penetration by microneedles (Figure 2a). These microelectrodes were able to measure the action potential of neural cells.

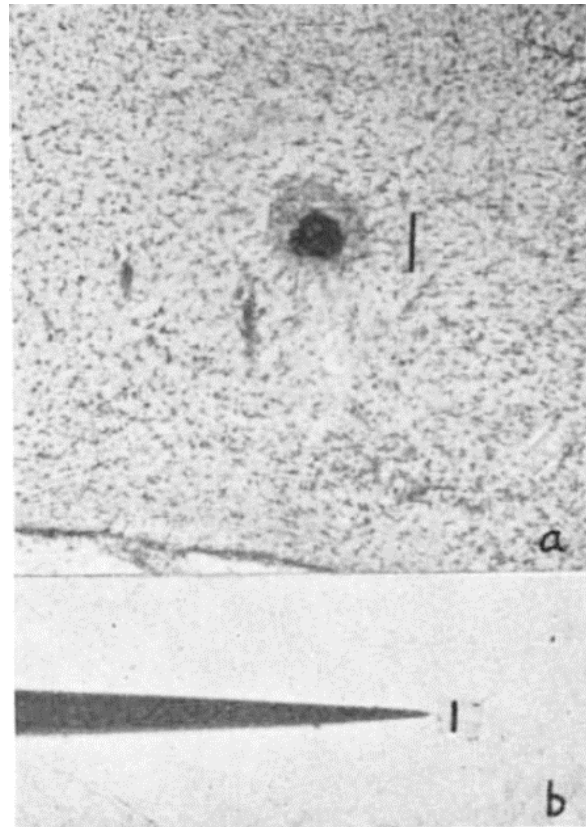


Figure 2. One of the first microscale medical devices, the stainless steel microelectrode by J. D. Green. A) Image of tissue penetration site stained with Prussian blue dye, a technique that is still used today to measure microneedle penetration into tissue. (Scale bar = 200 μm) B) Image of the stainless steel microelectrode. (Scale bar = 2 μm)

Source: Green JD. A Simple Microelectrode for recording from the Central Nervous System. *Nature* (1958) vol. 182, p. 962.

In the 1980s, the onset of rapid prototyping technology drastically changed the field of microscale medical device research. Rapid prototyping enabled researchers to easily manipulate the geometries of devices, including medical devices. The ability to rapidly and consistently produce structures opened a new area to medical device researchers, the field of

optimized device design. Scientists were then able to manipulate the structure of microscale devices to understand the effects of design and optimize performance. The 1980s was also the birth of tissue engineering as it is known today. Collaborations by Joseph P. Vacanti and Robert Langer led to the first results of tissues grown on synthetic scaffolds which were reported in 1988 at the meeting of the American College of Surgeons [26]. In his speech, Dr. Vacanti discussed his and Dr. Langer's findings related to growing parenchymal cells on synthetic polymer scaffolds.

In the 1990s, advances in computed tomography (CT), computer aided design (CAD) software, and image processing software opened the door to patient-specific prostheses [27]. Also in the 1990s, microfabrication technologies were perfected for production of semiconductor devices and the field of MEMS (microelectromechanical systems) was born. These techniques were used at the end of the 20th century to make the first microneedles for pain-free transdermal drug delivery [28]. In the 1990s tissue engineering grew from a field in its infancy to, at the end of the 20th century, Pubmed returning over 600 publications mentioning the term. The expansion of research into both microscale medical devices and tissue engineering led to the development of several journals tailored to these fields, such as Tissue Engineering, Biomedical Microdevices, and Journal of Micromechanics and Microengineering.

If development of tissue engineering in the 1990s was considered to be an expansion, then development in the 21st century could be considered an explosion. Whereas approximately

600 publications in the field of tissue engineering were produced in the 1990s, the first 10 years of the 21st century resulted in nearly 20,000 publications. Developments in understanding embryonic stem, adult stem, and progenitor cells and the ability to “reprogram” cells opened the door for engineering any tissue from just a few cells [29, 30]. Nonetheless, this rapid growth in research volume and knowledge did not necessarily correlate with great advances in actual regeneration of tissue. After 20 years and 20,000 publications, only 3 types of successful clinical *in vivo* autologous whole tissue replacements have been achieved: autologous bladder, urethra, and vasculature [31-35]. Major factors that are hampering the advance of tissue engineering are the ability to grow sufficient cells to produce an organ and to induce cells to behave as they do in their natural environment [36].

With applications in all areas of medicine, ranging from drug delivery to sensing to regenerative medicine, the field of micro- and nanoscale medical device design will continue to revolutionize medicine. Real-time response drug delivery, tissue regeneration, and patient-specific prostheses are just a hint of the future prospects of the fruits of this avenue of research. The focus of the henceforth presented research is expansion of the field of micro- and nanoscale medical devices. More specifically, my objective in this research is to advance the various techniques of light-based rapid prototyping for production of microscale and nanoscale medical devices. My efforts have been concentrated on the drug delivery and regenerative medicine applications of these devices. The research presented in this dissertation reports numerous advances in the field of micro- and nanoscale medical devices, including novel production techniques, materials, devices, applications, and characterization

techniques. Light-based rapid prototyping processes including two-photon polymerization, stereolithography, and UV soft lithography were used to create a range of micro- and nanoscale medical devices. Microneedles were produced for drug delivery and sensing applications. Additionally, tissue engineering scaffolds and prostheses were generated for regenerative medicine applications by these above mentioned techniques.

References

[1] Robson T. An Introduction to Complementary Medicine. Crows Nest, Australia: Allen & Unwin Academic; 2004.

[2] Kühn CG, editor. Claudii Galeni Opera Omnia. Leipzig: C Cnobloch, 1821-1833.

[3] Yaksh TL. Spinal Drug Delivery. Amsterdam: Elsevier Health Sciences; 1999.

[4] Rynd F. Neuralgia – Introduction of fluid to the nerve. Dublin Med Press 1844; 13:167-168.

[5] Rey R. The History of Pain [LE Wallace, JA Cadden, SW Cadden, trans]. Cambridge, MA: Harvard University Press; 1998.

[6] Pravaz CG. Sur un nouveau moyen d'opérer la coagulation du sang dans les artères, applicable à la guérison des aneurisms. Compt Rend Hebd Seances Acad Sci 1853.

[7] Wood A. Treatment of Neuralgic Pains by Narcotic Injections. *Brit Med J* 1858; 721-723.

[8] Chambers R. The microvivisection method. *Biol Bull* 1918; 34(2): 121-136.

[9] Charnley J. An artificial bearing in the hip joint: implications in biological lubrication. *Fed Proc* 1966; 25(3): 1079-1081.

[10] Kolff WJ, Berk J, Welle M, van der Ley AJW, van Dijk EC, and van Noordwijk J. The artificial kidney: a dialyser with a great area. *Acta Medica Scandinavica* 1944; 117(2): 121-134.

[11] Wilson. *J Morphol* 1899; 15 supplement: 1.

[12] Kite GL. Studies on the physical properties of protoplasm: I. The Physical Properties of the Protoplasm of Certain Animal and Plant Cells. *Am J Physiol* 1913; 32: 146-164.

[13] Kite GL. The relative permeability of the surface and interior portions of the cytoplasm of animal and plant cells. *Biol Bull* 1913; 25(1): 1-7.

[14] Chambers R. The microvivisection method. *Biol Bull* 1918; 34: 121-136.

- [15] Chamber R. Microdissection studies I. the visible structure of cell protoplasm and death changes. *Am J Physiol* 1917; 43(1): 1-12.
- [16] Hyde IH. A micro-electrode and unicellular stimulation. *Biol Bull* 1921; 40: 130-133.
- [17] Salle AJ. A micro electrode and vessel for the determination of the hydrogen ion concentration of blood media, whole blood, and other biological fluids. *J Biol Chem*; 83: 765-772.
- [18] Winterstein H. Mikroelektrode zur bestimmung der aktuellen cH. *Pflugers Archiv fur die Gesamte Physiologie des Menschen und der Tiere* 1927; 216: 267-270.
- [19] Wernicke R, Modern F. Hydrogen microelectrode. *Comptes Rendus des Seances de la Societe de Biologie et de ses Filiales* 1929; 100: 133-135.
- [20] Boez L. Microelectrode device with quinhydrone. *Comptes Rendus des Seances de la Societe de Biologie et de ses Filiales* 1929; 101: 524-526.
- [21] Delaville M, Tcherniakofsky P. Regarding the new microelectrode of quinhydrone. *Comptes Rendus des Seances de la Societe de Biologie et de ses Filiales* 1929; 101: 735-737.

- [22] Smolik L. The double electrode modification to a double microelectrode for the regulation of pH developed by Smolik. *Biochemische Zeitschrift* 1930; 217: 216-217.
- [23] Grundfest H, Sengstaken RW, Oettinger WH, Gurry RW. Stainless Steel Micro-Needle Electrodes Made by Electrolytic Pointing. *Rev Sci Instr* 1950; 21(4): 360-361.
- [24] Hubel DH. Microelectrode for Recording from Single Units. *Science* 1957; 125(3247): 549-550.
- [25] Green JD. A Simple Microelectrode for recording from the Central Nervous System. *Nature* 1958; 162: 962.
- [26] Vacanti JP. Beyond transplantation, the third annual Samuel Jason Mixter Lecture. *Arch Surg* 1988; 123: 545-549.
- [27] McGurk M, Potamianos P, Amis AA, Goodger NM. Rapid prototyping techniques for anatomical modeling in medicine. *Ann R Coll Surg Engl* 1997; 79: 169-174.
- [28] Henry S, McAllister DV, Allen MG, Prausnitz MR. Microfabricated Microneedles: A Novel Approach to Transdermal Drug Delivery. *J Pharm Sci* 1998; 87(8): 922-925.

[29] Takahashi K, Yamanaka S. Induction of Pluripotent Stem Cells from Mouse Embryonic and Adult Fibroblast Cultures by Defined Factors. *Cell* 2006; 126: 663-676.

[30] Takahashi K, Tanabe K, Ohnuki M, Narita M, Ichisaka T, Tomoda K, Yamanaka S. Induction of Pluripotent Stem Cells from Adult Human Fibroblasts by Defined Factors. *Cell* 2007; 131: 861-872.

[31] Atala A, Bauer SB, Soker S, Yoo JJ, Retik AB. Tissue-engineered autologous bladders for patients needing cystoplasty. *Lancet* 2006; 367: 1241-1246.

[32] Guan Y, Ou L, Hu G, Wang H, Xu Y, Chen J, Zhang J, Yu Y, Kong D. Tissue Engineering of Urethra Using Human Vascular Endothelial Growth Factor Gene-Modified Bladder Urothelial Cells. *Artificial Organs* 2008; 32(2): 91-99.

[33] Dorin RP, Pohl HG, De Filippo RE, Yoo JJ, Atala A. Tubularized urethral replacement with unseeded matrices: what is the maximum distance for normal tissue regeneration? *World J Urol* 2008; 26: 323-326.

[34] Shin'oka T, Imai Y, Ikada Y. Transplantation of a Tissue-Engineered Pulmonary Artery. *N Engl J Med* 2001; 344(7): 532-533.

[35] Shin'oka T, Matsumura G, Hibino N, Naito Y, Watanabe M, Konuma T, Sakamoto T, Masayoshi N, Kurosawa H. Midterm clinical result of tissue-engineered vascular autografts seeded with autologous bone marrow cells. *J Thorac Cardiovasc Surg* 2005; 129: 1330-1338.

[36] Atala A. Engineering Organs. *Curr Opin Biotechnol* 2009; 20: 575-592.

2. LITERATURE REVIEW

2.1 Light-based Rapid Prototyping

Introduction

Recently, medical devices with microscale and submicroscale features have been produced with laser-based fabrication techniques [1,2]. Several properties of lasers make them advantageous for medical device fabrication. When producing tissue engineering scaffolds, for example, it is often desirable to incorporate biological molecules (e.g., proteins) and cells [3,4]. Other microscale processes, such as fused deposition modeling and wet etching, are poorly suited for processing of biological materials. Biological molecules can be irreversibly damaged by high temperatures or extreme pH environments, conditions which occur in fused deposition modeling and wet etching, respectively. In contrast, laser direct write techniques do not require harsh chemicals and have minimal heat effects. Additionally, the exceptional resolution of laser-based production techniques may be used to control the attachment of biological molecules and cells on the micro- and even nanoscale. For example, nanostructured materials may be able to interact with proteins in a manner that does not alter their biological properties [5]. Numerous medical devices have been produced by laser-based processes, including stents, prostheses, sensors, drug delivery devices, and tissue engineering scaffolds.

Lasers provide spatially coherent (traveling in a single direction) energy, which can be focused with simple optics to process materials at the micro- and submicroscale [6]. Emission wavelengths vary greatly, depending on the mechanism used for photon generation. Excimer lasers (e.g., ArF, KrF and XeF lasers) and metal vapor lasers (e.g., HeCd lasers) generally operate in the ultraviolet range. The numerous solid-state lasers (e.g., Nd:YAG, etc) operate over a wide range from ultraviolet to infrared. CO₂ lasers operate at infrared wavelengths [6]. Lasers can either operate in continuous wave or pulsed modes. In continuous wave mode, the energy output is constant over time. Pulsed operation enables the energy to be compressed into short pulses, resulting in higher energies [6]. When pulses are extremely short, as is the case with ultra-short pulse lasers (e.g., Ti:sapphire lasers) that operate in the femtosecond range, nonlinear optical processes such as two-photon absorption can occur [7]. The phenomenon of two-photon absorption allows femtosecond lasers to perform processes at a resolution that is not possible with other lasers. The two-photon absorption phenomenon enables overcoming the diffraction limit and processing with submicro- and even nanoscale resolution. For additional information on various types of laser systems, the text *Introduction to Laser Technology* by Hitz, Ewing and Hecht is suggested [6].

In laser direct writing, 2-D and 3-D structures are prepared by directing a laser beam in a desired pattern over a region of a surface or in space. Writing can be controlled by translating the laser, translating the target and/or rotating the target. With three axes of translation and three axes of rotation, up to six degrees of freedom may be achieved. Medical device

production via direct write rapid prototyping processes has numerous advantages. One advantage of laser direct writing techniques over other manufacturing techniques, such as molding, is that devices with complex interior and nested (features inside of a hollow, solid body) geometries can be fabricated in order to precisely meet the needs of a given application, whereas molding can only produce structures with un-nested and at best, basic interior geometries. The geometry of a given structure may be determined by an input stereolithography (STL) file, which can be easily manipulated using standard computer-aided design (CAD) software [8]. Features may be incorporated into prostheses and scaffolds to promote various types of cell-prosthesis interaction, such as tissue ingrowth. Over the past two decades, technologies for producing CAD models based on computed tomography (CT), magnetic resonance imaging (MRI) and other medical imaging techniques have been developed [9–14]. Patient-specific medical devices and prostheses may be prepared using CAD models derived from patient data [15-22]. These patient-specific prostheses may perform superior to conventional prostheses due to better emulation of geometry, size, weight, and mechanical properties. In addition, surgeons can use rapid prototyping in order to fabricate an exact replica of a given patient's anatomical features to aid in surgical preparation and training.

Interaction between the near-surface region of a solid material and either a continuous wave or pulsed laser beam involves electronic excitation and de-excitation [23]. The most important parameter for understanding laser-material interaction is the laser wavelength, which determines the extent of absorption, penetration, and scattering of laser radiation in the

material [24]. Parameters of importance for pulsed lasers are the pulse duration (duration of laser emission), the repetition rate, the pulse energy (amount of energy in one laser pulse), the numerical aperture, the average power (total energy per unit time), the peak power (pulse energy divided by pulse duration) and the fluence (energy per unit area). The parameters of importance for continuous-wave lasers are the average power (total energy per unit time), the irradiance (power per unit area), the numerical aperture and the duration of laser exposure (time the laser is emitting radiation).

Absorption of photons can cause excitation of electrons in atoms and molecules of the target material. In ablation, energy transfer leads to nearly instantaneous release of the target material, either by thermal vaporization or by photochemical interactions [7]. At lower energies, the chemical bonds remain intact and energy is converted into heat [25]. In this case, localized heating of the target material results in either sintering or melting. Photopolymerization takes place when photoinitiator molecules absorb photons and form radicalized molecules, which can initiate polymerization reactions [26]. Numerous laser direct write techniques have been developed, which utilize these laser-target interactions. A summary of the laser-based direct write techniques is provided in Table 1. Commonly used laser-based direct write techniques include selective laser sintering/melting (SLS/M), laser ablation machining, matrix-assisted pulsed-laser evaporation direct write (MAPLE DW)/laser induced forward transfer (MAPLE DW/LIFT), stereolithography (SLA), and two-photon polymerization (2PP).

Table 1. Comparison of laser direct writing processes.					
Technique	Laser type	Resolution	Applications	Compatible materials	Limitations
Selective laser sintering/melting	CW, LP	50 μm	Prosthetics Tissue engineering	Ceramics Polymers Metals	Powder precursor High temperature Layered fabrication
Micro-laser sintering	LP	20 μm	Prosthetics	Ceramics Metals	Powder precursor High temperature Layered fabrication
Laser machining	CW, EX, LP, SP, USP	15 nm	Microfluidics Stents Tissue engineering	Ceramics Polymers Metals	Top-down
Matrix-assisted pulsed-laser evaporation direct write	EX	10 μm	Microelectronics Chemical sensors Tissue engineering	Polymers Metals Ceramics Biomolecules	Multiple processing parameters Layered fabrication
Stereolithography	CW	1 μm	Prosthetics Tissue engineering	Polymers Ceramic composites Biomolecule composites	Photopolymerization Layered fabrication
Two-photon polymerization	USP	<100 nm	Drug delivery prosthetics Tissue engineering	Polymers Ceramic composites	Photopolymerization

CW: Continuous wave (e.g., CO₂, Ar⁺); EX: Excimer (e.g., ArF, KrF); LP: Long pulse (ms – 100 ps); SP: Short pulse (<100 ps); USP: Ultra-short pulse (fs).

Source: Gittard SD and Narayan RJ. Laser direct writing of micro- and nano-scale medical devices. *Expert. Rev. Med. Devices* 2010; 7(3): 343-356.

Stereolithography

The process of stereolithography (SLA) utilizes the interaction of light with special photosensitive molecules called photoinitiators, which release free radicals upon interaction with light of a specific wavelength range (Figure 2, center). This reaction may be used to initiate polymerization of a resin composed of the photoinitiator and precursor molecules, generally molecules containing acrylate, epoxy, urethane acrylate, or vinyl ether functional groups [27]. Excitation of photoinitiator molecules, formation of reactive species, generation of free radical, and polymerization of the resin occurs at the site of laser-resin interaction. Thus, polymerization occurs in a localized volume, called a voxel. Since the resin absorbs

ultraviolet light, these interactions occur at the surface of the resin. Polymerization occurs in the range of a few to a hundred micrometers deep in the resin, depending on the resin material, wavelength, and light intensity [26, 28]. In order to produce structures via stereolithography, light (generally ultraviolet) is guided over the photosensitive resin in a lateral pattern to make the desired structure in a layer-by-layer fashion. The layer thickness is less than the penetration depth of light into the resin, so that the newly polymerized layer will fuse with the previous layer. To produce a structure in three dimensions, the structure is translated in the Z-direction with the focal plane remaining stationary, and the next layer is polymerized. After the structure has been built, unpolymerized resin is washed away by immersion in a developing solution. The developing solution should solvate the unpolymerized resin but not degrade the polymerized material. After developing, post-curing with a broad spectrum high-intensity lamp is generally performed in order to fully polymerize the structure. This post-curing process polymerizes residual monomers and oligomers in the resin which increases the hardness and reduces toxicity [29]. Post-curing may also be used to reduce production time; shells of a structure can be built with liquid resin trapped within the structure which is polymerized during post-curing [30]. This process decreases production time in scanning but not dynamic mask stereolithography, which will be discussed in the following paragraph.

There are several variations of stereolithography apparatus. There are two forms of controlling the Z-height of the structure. Conventionally, the stage is in a vat and is immersed deeper into the vat as each layer is created. Another design, for example on

Envisiontec stereolithography systems, is with an inverted stage. In these systems the stage is inverted in the bath and is moved away from the vat with each subsequent layer so that only a few millimeters of the build platform or structure is immersed in the resin. The inverted design requires less material since the resin vat is not required to contain the entire volume of the part. In both of these designs, the height of the optical focal point is maintained and the part is moved in the Z-direction to change Z-position of light-material interaction.

Additionally, there are two techniques for lateral patterning of resin. Traditionally, patterning was performed by rastering a laser in the desired pattern across the resin, a process called laser scanning stereolithography (Figure 1a) [22, 31-34]. Laser scanning stereolithography is generally performed with an ultraviolet laser [31-34]. Lateral resolutions down to 5 μm have been achieved with laser scanning stereolithography [44]. An example of a scaffold produced by laser scanning stereolithography is provided in Figure 1c. The second patterning technique is dynamic mask stereolithography (Figure 1b). In this process the light source is a less expensive lamp, generally ultraviolet, though use of visible wavelength lamps have also been reported [22]. The illumination pattern is controlled by a mask which selectively passes light. One of the greatest benefits of dynamic mask stereolithography is that an entire layer is polymerized at once, considerably reducing the production time. Dynamic mask stereolithography has generally been performed using high resolution mirror arrays. An everyday example of these mirror arrays are Texas Instruments's digital light projection (DLP) mirror arrays used in DLP high definition televisions. DLP chips are

composed of millions of tiny mirrors which control brightness by the angle at which they are reflecting light. Each mirror corresponds to a “pixel” in the exposure plane. One dynamic mask stereolithography system manufacturer, Envisiontec, offers systems with resolutions of 2800x2100 pixels (Envisiontec Mini Multi Lens). Pixel resolution is further increased by optics, which focuses the entire pixel array, decreasing the size of the pixels and the build area. An example of a microneedle array produced by dynamic mask stereolithography is provided in Figure 1d.

A wide range of biomedical devices have been produced by stereolithography. Gittard *et al.* created patient-specific prostheses of carpal bones using dynamic mask stereolithography [22]. Stereolithography (.STL) files of scaphoid and lunate bones were created using patient CT data via Mimics software (Materialise, Leuven, Belgium). A 1280x1024 pixel Perfactory system (Envisiontec GmbH, Gladbeck, Germany), operating in visible light mode, was used to produce these prostheses from a commercial acrylate-based polymer. These prostheses exhibited resolutions of approximately 50 μm , emulative replication of complex exterior and interior geometries, and fracture mechanics similar to healthy bones. In order to overcome restrictions in stereolithography-compatible materials, molding of stereolithography-produced master structures may be used to produce end structures from alternative materials. Several clinically implanted prostheses have been created via combination of SLA and molding, including auricular, maxillofacial, and cranial prostheses [19, 20, 35-40]. Wurm *et al.* produced cranial implants by using SLA to generate a mold and molding to produce the implant out of a carbon fiber-polymer composite [38]. Follow-up (mean time = 3.6 years

post-implantation) revealed that the implanted devices were successful overall, with only a few adverse effects such as infection, allergy and hematoma. It should be noted that using this combined process negates two of the advantages of SLA, particularly the reduced production time afforded by direct fabrication and the ability to produce complex interior geometries. To the author's knowledge, direct stereolithography of clinically used implants has not yet been documented. Recently, Liu *et al.* reported having performed clinical implantation of prosthetics using stereolithography, selective laser sintering, and laminated object manufacturing as tools [21]. While they indicate that the clinically implanted prosthetics (25 cases) were directly made by rapid prototyping, it is unclear which technique or techniques were used for production of the implanted devices.

In addition to prosthetics, stereolithography of tissue engineering scaffolds has been demonstrated with a number of materials, including ceramic-polymer composites, biodegradable polymers, and polymer-cell solutions [4, 41-43]. Structuring with polymer-ceramic composites may improve scaffold performance. Stereolithography-generated scaffolds of poly(propylene fumarate)/diethyl fumarate with hydroxyapatite exhibited superior cell proliferation to scaffolds of the same material without hydroxyapatite [42]. Lee *et al.* performed stereolithography of poly(lactic-co-glycolic acid) (PLGA) and bone morphogenetic protein 2 (BMP-2) to create tissue engineering scaffolds with well-defined pore architecture [4]. This study also highlights one of the benefits of stereolithography; this process does not involve high temperatures so biological materials such as proteins (e.g., BMP-2), antimicrobial agents, and viable cells may be incorporated within the device during

building. Arcaute *et al.* generated scaffolds with a resin of poly(ethylene glycol) dimethacrylate (PEGdma) with dermal fibroblasts; cell viability after structuring was greater than 87% [43]. It is important to note that ultraviolet light, photoinitiators, and monomers/oligomers may be cyto- and genotoxic [29, 44]. These issues need to be addressed before stereolithography of resins containing cells is introduced to clinical use.

Recently, the use of stereolithography for production of microscale drug delivery devices has been demonstrated. Choi *et al.* first demonstrated production of microneedle arrays by a custom-built dynamic mask stereolithography system [45]. These microneedle arrays had 30 μm to 80 μm tip radii. Insertion forces of 0.08 N to 3.04 N were reported, but the penetration depth of the needles was not. Gittard *et al.* created microneedle arrays with a commercial, visible light, dynamic mask stereolithography system [46]. These microneedle arrays had similar tip dimensions, with an average radius of curvature of 18 μm . Miller *et al.* reported the first case of hollow microneedles being produced by dynamic mask stereolithography [47]. Minimum channel diameters of 375 μm were achieved, and biochemical sensors were placed inside of these bores.

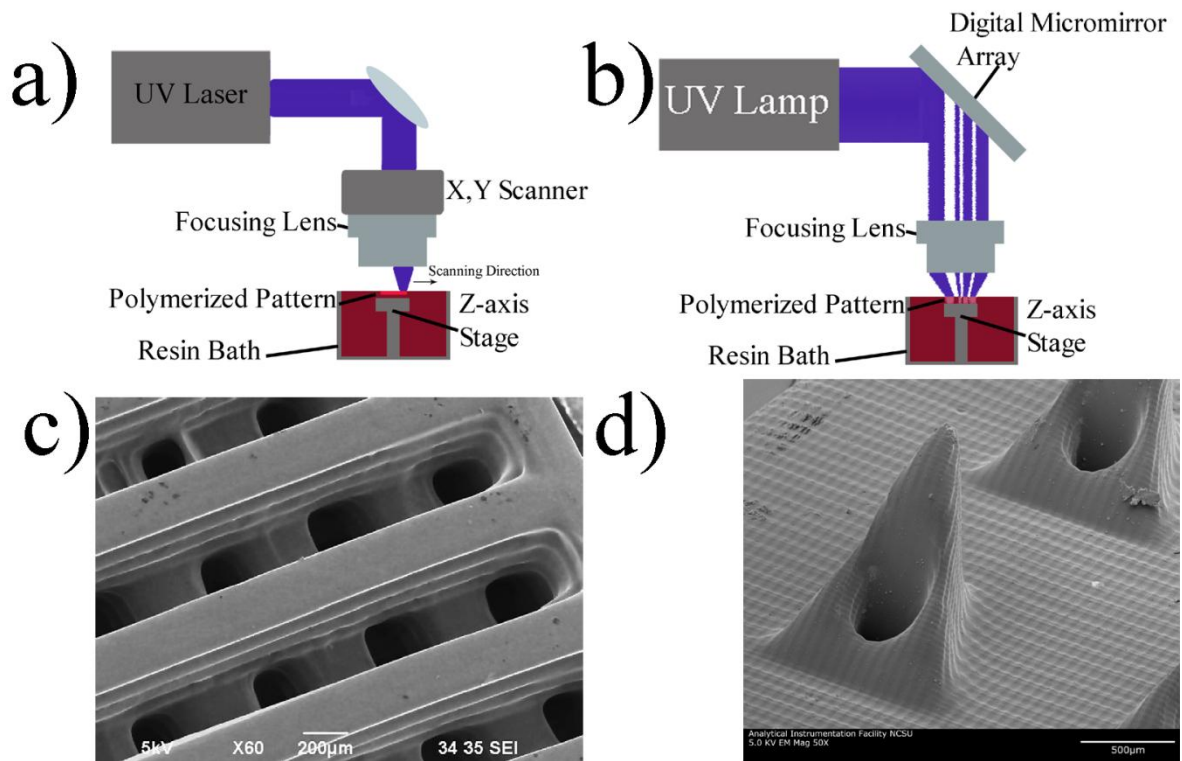


Figure 1. Stereolithography: a) Schematic of Laser Scanning Stereolithography; b) Schematic of Dynamic Mask Stereolithography; c) scaffold produced by laser scanning stereolithography*; d) hollow microneedles produced by dynamic mask stereolithography.

***Reprinted from *Microelectronic Engineering*, 84, Kim JY, Lee JW, Lee SJ, et al.**

Development of a bone scaffold using HA nanopowder and micro-stereolithography technology. 1762-1765, Copyright 2007, with permission from Elsevier.

Laser Machining/Ablation

In laser machining, a laser is used to remove small amounts of material from a bulk material, a process called ablation. Ablation occurs when the energy of photons absorbed by the

material is sufficiently great to break bonds in the material. Thus, the resolution of the process is related to the point spread function of the laser [48]. The laser may be focused by optics to decrease the spot size and increase the fluence, thus achieving sufficient energy for ablation to occur. Structuring is performed by selectively removing material by controlling the location of the laser-target interaction. Since laser machining is performed by incremental removal of material which occurs at the surface of a material, this process is generally limited to “line-of-sight” operations. Ablation cannot occur at a location where the laser path is obstructed. Therefore, structures with overhangs or interior geometries cannot be created.

Ablation can occur by either thermal or photochemical bond degradation [7]. During thermal ablation, energy absorbed from the laser results in rapid heating and vaporization of the target [7]. Thermal ablation is frequently observed with continuous wave lasers and may occur with pulsed lasers that have a long pulse duration [49]. Thermal ablation is generally avoided for production of medical devices since this process is associated with high temperatures and relatively large heat-affected zones. In contrast, the mechanism of photochemical ablation makes this process well suited for medical device fabrication. Absorption of the photons results in excitation of electrons in the target molecules. In photochemical ablation, the electrons are excited to a degree at which the chemical bonds in the material degrade (Figure 2, right). Thus, the target material vaporizes at the sight of absorption. At lower energies of light the excited electrons return to their resting state, resulting in emission of light at a higher wavelength than at which it was absorbed, a

phenomenon known as fluorescence (Figure 2, left). Fluorescence is utilized in a number of medical imaging techniques such as confocal fluorescence microscopy, multiphoton microscopy, and Förster resonance energy transfer microscopy [48, 50].

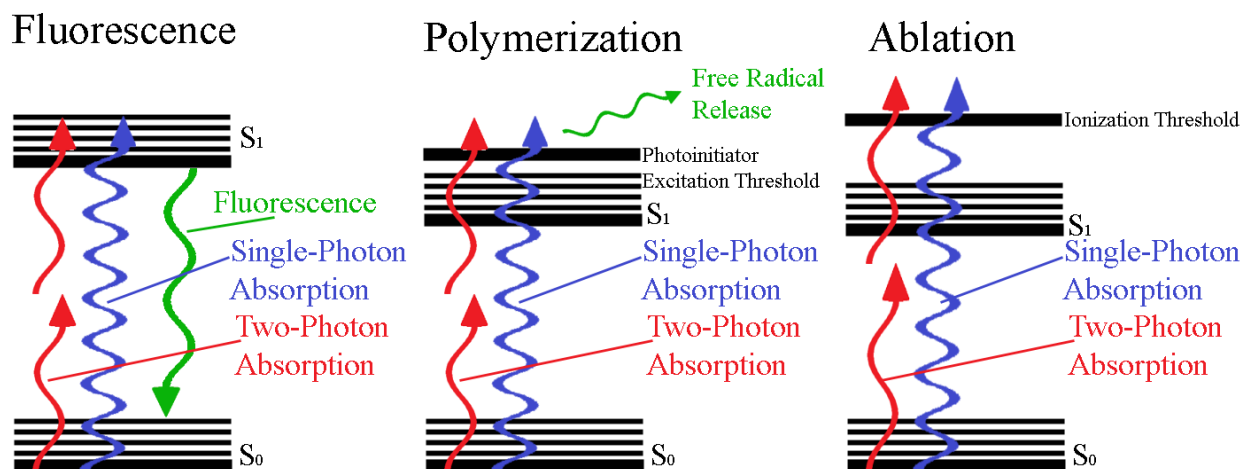


Figure 2. Jablonski diagrams of single-photon and two-photon fluorescence, polymerization, and photochemical ionization (ablation).

Since photochemical ablation is due to electron excitation, there are minimal thermal effects in photochemical ablation [51]. Materials with high photon absorption coefficients and low thermal conductivities are best suited for photochemical ablation since electrons are excited with greater efficiency [49]. Likewise, lasers with high energies and short pulses are preferable since they decrease the thermal effects. It is important to note that in order for ablation to occur, the target material must absorb energy at the given laser wavelength. Materials with strong photon absorption will ablate readily whereas materials with poor absorption require high energy levels for ablation to occur [48]. Since most materials have

strong absorption of ultraviolet light, ultraviolet lasers are frequently used for ablation. Pulsed lasers (e.g., excimer lasers) are commonly used due to their higher energy and smaller spot size. In cases where high throughput is a greater priority than precision, continuous wave lasers (minimum spot size of approximately 50 μm) are used [49, 52]. It should be noted that laser ablation with femtosecond lasers is not restricted to line-of-sight operations [1].

Ultra-short pulse lasers are capable of a phenomenon called two-photon or multi-photon absorption, a nonlinear process which involves simultaneous absorption of two or more photons by a material [51]. Simultaneous absorption of multiple photons results in higher energy states of the electrons. Single-photon processes are diffraction limited, meaning that they cannot achieve resolutions greater than the wavelength of the excitation light. Since the multi-photon absorption process involves the interaction of multiple photons and not the action of a single photon, multi-photon absorption is not limited by the diffraction limit and can achieve resolutions below the wavelength of excitation light. Sub-micron features have been achieved with ablation using femtosecond lasers [1, 53-55]. Multi-photon absorption generally occurs at twice the wavelength of single photon absorption, so materials with strong single photon absorption at 400 nm would have strong multiphoton absorption at 800 nm [56]. Multi-photon absorption is a function of photon density and not specifically interaction with the target material. Therefore, multi-photon processes can occur within a material and are not limited to the material surface, as long as the target material is optically transparent to the laser wavelength. Since multi-photon absorption uses longer wavelength

lasers (e.g., near-infrared), many materials are optically transparent and are conducive to multi-photon ablation within their interior [1]. Multi-photon absorption is dependent on a number of factors, including laser wavelength, pulse duration, exposure time, repetition rate, numerical aperture, and material properties (e.g., bandgap). Since multi-photon absorption results in higher energy states, materials that have poor photon absorption are capable of ablation with ultra-short pulse lasers. For example, fused quartz and various glasses have been ablated with femtosecond lasers [54]. Also, thermal effects are less pronounced in multi-photon ablation since interactions occur in a smaller volume [7].

Thermal effects can cause melting, cracking, spallation, and burr formation, and are thus a significant concern [49]. The ablated material, in either liquid or vapor states, is expelled away from the site of ablation in a mushroom cloud-like plume [57]. Redeposition, settling and recasting of the ablated material of the target, can occur during ablation [57]. This process is commonly observed during ablation of metals [58]. Redeposition is undesirable since it changes the surface morphology of the material. Performing ablation under vacuum is one technique that has been shown to reduce redeposition [59].

Vascular stents are one class of medical devices that are commonly produced by laser machining [60]. Metal stents have been fabricated by laser machining from a variety of materials, including stainless steel, tantalum, and platinum, niobium, and cobalt alloys [60]. Laser machining of stents has also been performed with shape memory materials, such as the nickel-titanium alloy, Nitinol [61]. Due to the minimal heat effects associated with laser

machining, this technique may be used to produce stents from polymeric materials, including resorbable polymers (e.g., polyesters) [53, 62, 63]. Pharmacologic agents encapsulated within the biodegradable stents can be released as the stent degrades [53, 62, 63]. Due to their temperature sensitivity, minimizing thermal effects is a significant concern in laser machining of polymers and other temperature-sensitive materials. With stents in particular, defects such as melted features, burrs, and cracks arising from laser micromachining may lead to failure of the device [49]. Figures 3a and 3b show polymer stents produced by two different laser micromachining processes. The poly(L-lactic acid) stent in Figure 3a was produced by micromachining with a continuous wave CO₂ laser, which are known for having stronger thermal effects. The stent exhibits indiscrete edges, melting, and other signs of large heat-affected zones. In contrast, the poly(L-lactic acid) stent in Figure 3b, which was prepared by femtosecond ablation, displays discrete, precise edges with no indications of thermal effects.

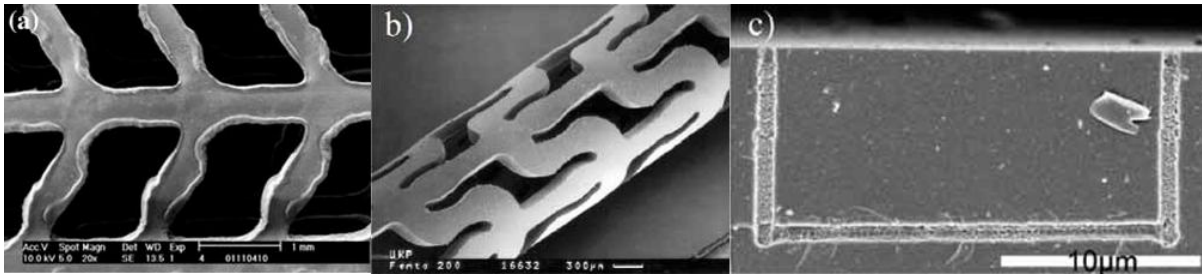


Figure 3. Laser machining: a) Poly(L-lactide) stent machined using a continuous wave CO₂ laser*; b) Poly(L-lactide) stent machined using a femtosecond laser; c) Glass microfluidic device containing a nano-scale channel machined on the interior of the structure using a femtosecond laser***.**

***Reprinted from Grabow N, Bunger CM, Schultze C, Schmohl K, Martin DP, Williams SF, Sternberg K, Schmitz KP. A Biodegradable Slotted Tube Stent Based on Poly(L-lactide) and Poly(4-hydroxybutyrate) for Rapid Balloon-Expansion. Annals of Biomedical Engineering 2007; 35(12): 2031-2038. © 2007 Springer**

****Reprinted with permission from Korte F, Nolte S, Chichkov BN, Bauer T, Kamlage G, Wagner T, Fallnich C, Welling H. Far-field and near-field material processing with femtosecond laser pulses. Appl Phys A-Mater Sci Process 1999 DEC;69:S7-S11. © 1999 Springer**

***** Reprinted with permission from Ke K, Hasselbrink EF, Hunt AJ. Rapidly prototyped three-dimensional nanofluidic channel networks in glass substrates. Anal Chem 2005 AUG 15;77(16):5083-5088. © 2005 American Chemical Society**

In the field of tissue engineering, laser micromachining of biomaterials has been used to create scaffolds. For example, electrospun scaffolds are one class of material being

investigated for tissue engineering applications; these materials are composed of nanoscale fibers which interact favorably with cell adhesion proteins. Laser machining of electrospun scaffolds has recently generated interest since ablation may be used to improve cell proliferation within the interior of the scaffold [64-66]. The polymer fibers in these scaffolds are extremely temperature sensitive due to their small size, therefore photochemical ablation is an appealing approach for processing these materials. For example, two studies by McCullen *et al.* utilized excimer laser micromachining to control pore size, location, and porosity in electrospun PLA (Figure 4a) [65, 67]. Ablation of the pores was performed with fibers displaying minimal signs of thermal effects [67]. Upon seeding and subsequently stacking sheets of machined PLA with human adipose-derived stem cells, the laser generated pores enabled distribution and growth of the cells throughout the interior of the scaffold (Figure 4b) [65]. Cell orientation and location may also be controlled by laser micromachining; for example creating channels into which cells are seeded or surface microtopographies that regulate cell orientation and adhesion [49, 64, 68-70]. For example, Duncan *et al.* machined channels in poly(ethylene terephthalate) of varying widths, spacings, and depths to study the effect of microscale surface features on endothelial cell orientation and adhesion [68]. Miller *et al.* controlled human aortic vascular smooth muscle cell orientation via laser-machined grooves in silicon [49]. Patz *et al.* performed micromachining with an ArF excimer laser to produce 60-400 μm wide channels in 2% agarose surfaces which were subsequently lined with basement membrane matrix solution [71]. C2C12 myoblast-like cells aligned parallel to the 60-150 μm channels. Further, some of the cells fused to form multinucleated myotube structures. In a similar study by Doraiswamy *et*

al., B35 neuroblast-like cells were shown to proliferate and form bundles after 72 hours of culturing on the channels [72]. Surface machining may also be used to select for cell type [70]. Schlie *et al.* produced titanium and silicon surfaces comprised of microscale spikes by femtosecond laser ablation. Neuroblasts and osteoblasts had increased proliferation on the surfaces while fibroblasts had decreased proliferation.

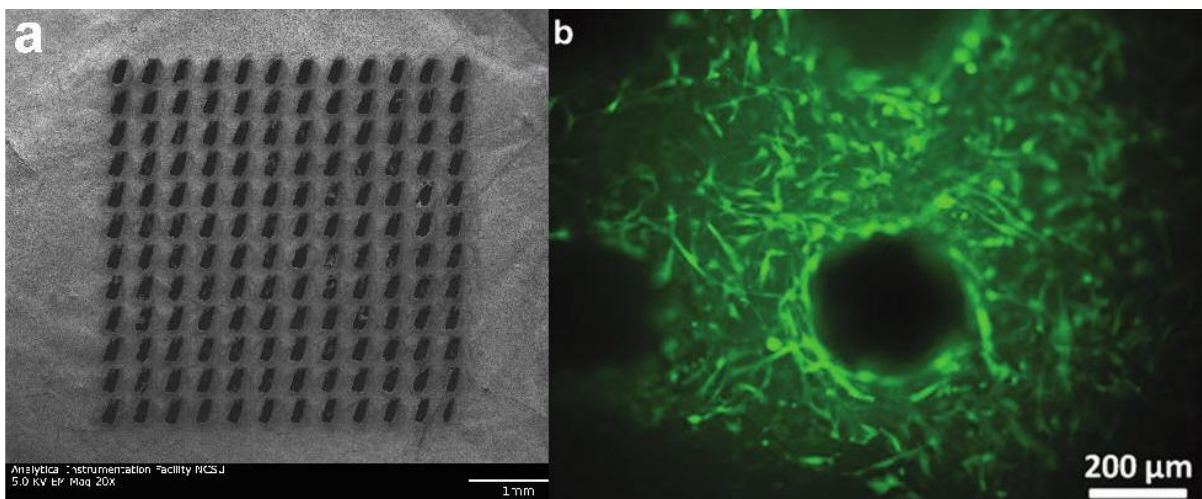


Figure 4. Polylactic acid scaffold with controlled pore geometry produced by excimer laser ablation: a) scanning electron microscopy of a 150 μm pore scaffold, b) live/dead stain of human adipose-derived stems cells on a scaffold of stacked, ablated, electrospun polylactic acid with 300 μm pores*.

*** Reproduced from Tissue Engineering C, Volume 16, McCullen SD, Miller PR, Gittard SD, Gorga RE, Pourdeyhimi B, Narayan RJ, and Lobo EG. *In situ* collagen polymerization of layered cell-seeded electrospun scaffolds for bone tissue engineering applications, © 2010 with permission of Mary Ann Liebert, Inc.**

Laser ablation may also be used to generate microfluidic devices. Ke *et al.* and Kim *et al.* demonstrated the ability to produce sub-micrometer channels with femtosecond lasers [1,2]. Further, femtosecond laser machining can produce microfluidic channels within the interior of materials [73, 74]. An example of a glass substrate with a femtosecond laser generated nanoscale channel in its interior is shown in Figure 3c. These microscale cell culture devices can be used to study small amounts or even single cells in an aqueous environment. Also, lab-on-chip devices with microfluidic optical sensors and optical waveguides for cell sorting have been generated using laser micromachining [75, 76].

In spite of the high cost, femtosecond laser machining of stents has undergone rapid commercialization. Nevertheless, recent research efforts have been directed to reducing the cost and improving the rate of laser micromachining. Ancona *et al.* demonstrates that short picosecond lasers are capable of faster machining speeds and lower costs than femtosecond lasers; a significantly less expensive 100-ps microchip fiber laser system was used to machine copper, carbon steel, and stainless steel [77, 78]. Some thermal effects were observed with picosecond ablation; a thin layer of melted material was present on the ablated structures [78].

Laser Bioprinting: MAPLE Direct Write and LIFT

Laser bioprinting is a category of rapid prototyping techniques in which a pulsed laser is used to transfer biological material from a donor substrate to a receptor substrate. The technique

of laser bioprinting is commonly referred to by several different names, as a result of the process developing from a combination of two different techniques. A laser bioprinting system, illustrated in Figure 5a, consists of a laser source, donor substrate, an optional release layer, biomaterial, receptor substrate, and positioning systems. Since transfer of the material is induced by a process similar to ablation, ultraviolet lasers (e.g., excimer, Nd:YAG). The donor substrate (sometimes referred to as a ribbon) is a solid, optically transparent material, such as borosilicate glass or quartz. A thin layer (or layers if a release layer and biomaterial are used) of the biomaterial of interest is deposited onto the surface of the donor substrate; spin coating [72, 79] and sputter coating [80-82] are two techniques that have been performed to deposit the release layer. Interaction of the laser pulse with the biomaterial layer results in a segment of the material that is approximately the spot size of the laser being propelled towards the receptor substrate.

The variations in laser bioprinting nomenclature and technique is a result of the technology being related to two processes, matrix assisted pulsed laser evaporation (MAPLE) and laser induced forward transfer (LIFT) [83]. In its conventional use, MAPLE is a process for generating thin film polymer coatings on a surface. In MAPLE, a matrix containing the material to be transferred and a binder material (e.g., polymer) is evaporated by a pulsed laser. Upon absorption of the laser, the matrix decomposes and the material of interest is transferred to the receptor substrate which is located parallel to the donor substrate [83], similarly to the physical deposition process pulsed laser deposition. Like pulsed laser deposition, MAPLE is performed under vacuum. Donor substrates are generally produced by

freezing a suspension of the desired coating material in a solvent [83, 84-86]. Interaction with the laser results in rapid vaporization of the solvent in the donor substrate. Conventional MAPLE has been used for deposition of thin films for biomedical applications. For example, numerous medically relevant organic molecules including carbohydrates [87], polysaccharides [88-90], collagen [91], other proteins [92-94], and antibiotics [95, 96] have been deposited using MAPLE. Also, antibacterial coatings composed of poly(methyl methacrylate) and silver nanoparticles have been produced [84]. LIFT is a process that is derived from the microelectronics industry. In LIFT, a focused pulsed laser is used to transfer a thin metal coating from a donor substrate to a receptor substrate in a specified pattern [83, 97]. The pattern of the deposited metal is controlled by moving the laser beam in the desired pattern over the donor substrate. This process was originally used to pattern microscale electrical circuits [97-99]. Bioprinting is a combination of the two techniques, where patterning of a laser is used to selectively transfer a biological material, either by degradation of a matrix or via a release layer. In this review, bioprinting without a release layer will be referred to as MAPLE DW and bioprinting with a release layer will be referred to as LIFT bioprinting.

The first cases of bioprinting were using a technique most similar to MAPLE and as such were referred to as MAPLE direct write (MAPLE DW). The MAPLE DW process was developed at the US Naval Research Laboratory at the turn of the 21st century. The MAPLE DW process consists of using a focused laser to selectively vaporize a thin coating on a target which results in transfer of the material to the receptor substrate. Initially, MAPLE DW was

not used for patterning of biological materials, but for microelectronics devices [83, 100-102]. The first reporting of MAPLE DW patterning of biological materials was in 2001. Wu *et al.* used MAPLE DW to pattern a number of biologicals including dextran, horseradish peroxidase, and even Chinese hamster ovaries [103]. In 2002, Ringeisen *et al.* demonstrated MAPLE DW patterning of living *Escherichia coli* cells [104].

In the MAPLE DW bioprinting approach, the matrix, which may include cells and/or other UV sensitive molecules are in direct contact with the UV laser pulse. As a result of concerns over damage from UV irradiation, in 2006 a two-layer (LIFT) approach was presented [72]. In the LIFT approach a release layer is placed in between the donor substrate and the material to be transferred. Doraiswamy *et al.* utilized a release layer of triazene to laser print patterns viable B35 neuroblasts (Figure 5c) [72]. In addition to avoiding interaction of the laser with the material of interest, their results suggest that use of release layers with high UV absorption may enable laser bioprinting at lower laser fluences. Release layers of extracellular matrix, Matrigel®, hydroxyapatite, and gold have since been utilized [3, 79-81].

While the MAPLE DW and LIFT approaches generally use nanosecond pulse lasers, Zergioti *et al.* demonstrated that laser bioprinting can be performed with femtosecond lasers [105]. They demonstrated that the wavelength, lower thermal effects and energy required for material transfer that is afforded by femtosecond lasers enables laser bioprinting to be performed with a matrix or release layer. DNA, bovine serum albumin, and glutathione S-Transferase were directly laser printed without a matrix or release layer. Hybridization

testing of DNA after printing confirmed that direct laser bioprinting did not cause damage to the material. Additionally, the higher repetition rate of femtosecond lasers may enable faster production times [106]. The resolution achieved in laser bioprinting is dependent on several parameters, including the matrix material, laser energy, and laser spot size. Figure 5b shows an example of spot size increasing with respect to increasing energy level [107]. If relatively large structures (e.g., cells) are being patterned, the feature size is limited by the dimensions of the transferred material. In the case where the dimension of the biological material being transferred is not the limiting factor (e.g., proteins), 10 μm features have been achieved [108, 109].

One of the greatest advantages of laser bioprinting is the wide range of compatible materials. Metals [83, 100-102], ceramics [3, 79], biological molecules [103, 105, 109, 110], viable cells [3, 71 72, 79, 80, 103, 104] and even viable tissues [81, 108] have been patterned with laser bioprinting. Laser-based bioprinting techniques have several advantages over solvent-based bioprinting techniques such as inkjet printing and Langmuir-Blodgett dip coating. Production of 3-D structures using these solvent-based techniques is problematic since deposition of a new layer may induce dissolution of the preceding layers [29]. Additionally, laser bioprinting is capable of printing higher cell densities than other printing techniques. In the solvent-based techniques the printed cells are in a solution and are therefore diluted. However, in laser bioprinting structures can be printed in high cell densities. For example, Gruene *et al.* performed laser bioprinting of 3-D constructs of porcine mesenchymal stem cells with an average cell density of 46,000 cells/ μl [80]. Further advantages are that laser

bioprinting occurs at ambient temperature and pressure, provides enhanced adhesion to the substrate, and multi-material patterns can be produced [79].

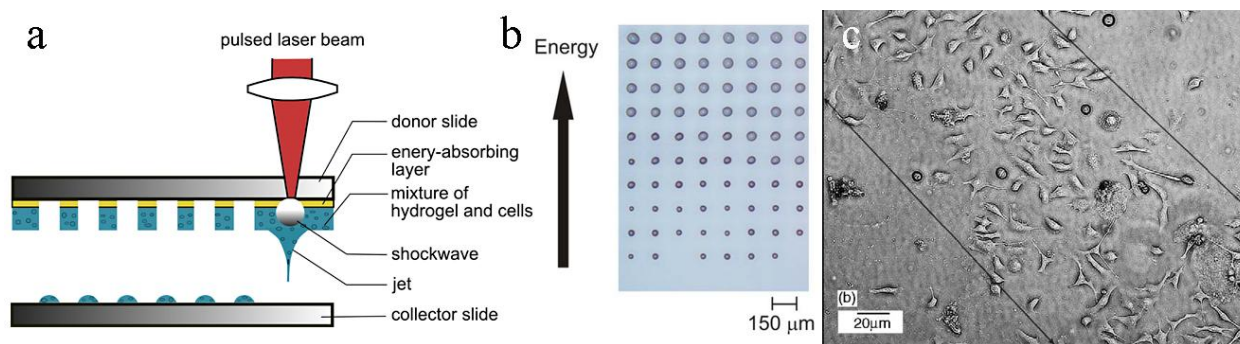


Figure 5. Laser bioprinting: a) Schematic of a laser bioprinting system*; b) optical microscopy image of laser-printed IgG solution with droplet size increasing with pulse energy; c) Line of laser-printed B35 neuroblasts***.**

***Reprinted with permission from: Unger C, Gruene M, Koch L, et al. Time-resolved imaging of hydrogel printing via laser-induced forward transfer. *Appl. Phys. A* (2010),**

DOI: 10.1007/s00339-010-6030-4. © 2010 Springer

*** Reprinted with permission from: Duocastella M, Fernandez-Pradas JM, Dominguez J, et al. Printing biological solutions through laser-induced forward transfer. *Appl.***

***Phys. A* (2008), 93: 941-945. © 2008 Springer**

*****Reprinted from Applied Surface Science, 252, Doraiswamy A, Narayan RJ, Lippert**

T, et al. Excimer laser forward transfer of mammalian cells using a novel triazene absorbing layer. 4743-4747, Copyright 2006, with permission from Elsevier.

Selective Laser Sintering/Melting

High power lasers may also be used to selectively melt or sinter a bed of powders or granules to form solid structures. In the processes selective laser sintering (SLS) and selective laser melting (SLM), a laser is used to heat a powder to a temperature at which the particles sinter or melt to fuse together, respectively [25]. Because a focused laser beam is used to heat the powder, sintering or melting is localized to the region immediately surrounding the point of laser-powder interaction. A common practice in these processes is to heat the powder bed prior to laser exposure, so that only a small increase in temperature is needed to sinter or melt the material. Selective laser sintering is also commonly performed in an inert gas environment to reduce oxidation of the powder. Unlike laser ablation, thermal effects are desirable in selective laser sintering and melting because heat is the mechanism for activating structuring. Therefore, lasers with greater thermal effects, such as continuous wave lasers (e.g., CO₂ lasers) [111] and long pulse lasers [112], are commonly used.

Sintering or melting only occurs along the trace of the laser since the source of heat is the point of laser-material interaction. Three-dimensional structures are produced in a layer by layer fashion using a powder bed that translates in the Z-direction. After a layer of the structure has been sintered, the height of the bed is translated and a new layer of powder is applied to the surface. The new layer is sintered and this process is repeated until building of the device is complete. A diagram of the SLS/SLM process is provided in Figure 6a. After structuring, the powder which was unsintered or unmelted is removed by breaking out

methods including manual removal, brushing, and powder blasting [113]. Since SLS and SLM are bottom up techniques and unsintered/unmelted powder provides support during building, structures with complex features such as overhangs and undercuts may be fabricated without using supports [30, 114].

Structures with 150-200 μm features are frequently generated with these selective heating techniques [115]. A process known as laser micro sintering has been described by researchers at Laserinstitut Mittelsachsen e.V. [116, 117]. This technique uses a q-switched solid-state laser with approximately 200-ns pulses. Sintering without oxidation was achieved in an air environment, which was attributed to vigorous plume expansion. Numerous metals and ceramics were processed with this technique including copper, molybdenum, silver, alumina, silicon carbide and silica. Layer thicknesses of 1 μm and lateral resolutions of 20 μm were achieved with laser micro sintering of sub-micron grain powders in an oxygen environment.

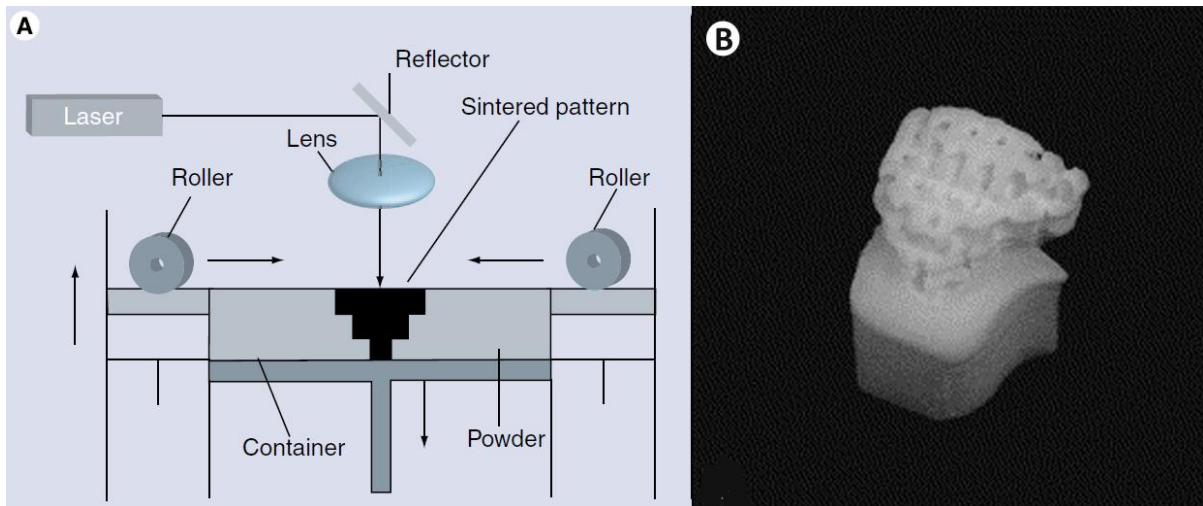


Figure 6. Selective laser sintering: a) Schematic of selective laser sintering*; b) SLS-produced poly(caprolactone) tissue engineering scaffold in the shape of a pig condyle.**

***Reprinted from Surface and Coatings Technology, Vol. 116, Kathuria YP.**

Microstructuring by selective laser sintering of metallic powder. 643-647, Copyright 1999, with permission from Elsevier.

***Reprinted from Biomaterials, Vol. 26, Williams JM, Adewunmi A, Schek RM,**

Flanagan CL, Krebsbach PH, Feinberg SE, Hollister SJ, Das S. Bone tissue engineering using polycaprolactone scaffolds fabricated via selective laser sintering,

Copyright 2005, with permission from Elsevier.

Several studies have been performed to determine whether the resolution of SLS is suitable for making prosthetics based on CT data. Ibrahim *et al.* found that the dimensional differences between master structures and SLS models fabricated from CT data of the master structures were 1.79% [118]. In a similar study, Kaim *et al.* compared patient craniofacial CT data, the resulting SLS replica and CT data of the SLS replica [119]. The differences between

these three data sets were shown to be statistically insignificant, indicating that the limiting factor in CT-based SLS is the resolution of CT and not the resolution of SLS. Further corroborating that CT-based SLS resolution is CT limited, dimensional errors in CT measurements have been reported as high as 2.16% [120]. With the ability to accurately fabricate structures based on CT data, patient-specific devices (e.g., prostheses) can be produced by SLS/SLM. Recently, nasal, dental, and maxillofacial prosthetics fabricated by SLS and SLM have been implanted into the human body [21, 121-124].

In addition to prosthetics, SLS-enabled tissue-engineering scaffold generation has been demonstrated [125-128]. For example, Williams *et al.* fabricated scaffolds in the anatomical shape of a pig mandibular condyle using micro-CT and SLS [127]. CT data of a pig condyle was modified to produce a porous STL model that replicated the geometry of the natural bone. This model was subsequently used to build the scaffold in the shape of the condyle by SLS (Figure 6b). *In vivo* studies of tissue-engineering scaffolds prepared using SLS have recently been reported. Kanczler *et al.* demonstrated that SLS-fabricated polylactic acid scaffolds support regrowth and bridging of bone gaps in mice [128].

Recently, research on performing SLS/SLM with nontoxic biocompatible materials that are used in artificial tissues and medical prostheses has gained interest. Bioactive ceramics, natural materials, thermoplastic polymers, metals, and polymer-coated metals are materials that have recently been processed by means of selective laser sintering [112, 115, 129-134]. Salmoria *et al.* fabricated biodegradable scaffolds from starch–cellulose and cellulose acetate

using selective laser sintering [135]. Several studies have shown that SLS/SLM is suitable for processing biocompatible ceramics, including alumina–zirconium, alumina–silica and PLGA–hydroxyapatite composites, hydroxyapatite-reinforced polyamide and polyethylene composites, and bioactive glasses [130-134, 136-139]. Zhang *et al.* demonstrated that SLS-produced hydroxyapatite-reinforced polyamide and polyethylene composites support healthy metabolism and growth of primary human osteoblasts [137]. Higher amounts of hydroxyapatite within the composites corresponded to increased rates of alkaline phosphatase activity, osteocalcin production and cell proliferation. A similar study by Hao *et al.* suggested that hydroxyapatite particles may impart bioactive properties, such as enhanced bone ingrowth and bone formation around the scaffold [139]. Von Wilmsky *et al.* utilized SLS to produce scaffolds that incorporated nanosized carbon black, b-tricalcium phosphate and bioactive glass within polyetheretherketone scaffolds [138]. Examinations of human osteoblast growth on the materials found that polyetheretherketone-bioactive glass composites exhibited the highest rates of cell proliferation. Shishkovsky *et al.* demonstrated building of porous titanium and nitinol structures using selective laser sintering/melting [130, 136]. Nitinol is a corrosion resistance, superelasticity and shape memory nickel-titanium alloy that has applications including stents, craniofacial implants and orthodontic devices [130, 140, 141]. In these studies, Shishkovsky *et al.* also synthesized implants from titanium-hydroxyapatite and nitinol-hydroxyapatite composites [130, 136]. Biocompatibility of these materials was confirmed by *in vitro* studies in a murine model. SLS of numerous biomedical polymers have also been demonstrated. Tan *et al.* performed SLS with polyetheretherketone,

poly(vinyl alcohol), polycaprolactone and poly(L-lactic acid) [129]. Further, Rimell and Marquis structured ultra-high molecular weight polyethylene using SLS [142].

Although SLS/SLM is compatible with a wide range of materials, the use of SLS/SLM in biomedical application is limited by several factors. When performing SLS/SLM, it is necessary that the precursor materials are in powder form [29]. Also, these processes involve high temperatures, eliminating the possibility of structuring with materials containing heat-sensitive components, such as proteins or cells. On the other hand, several studies have demonstrated that cells can be seeded onto materials after SLS/SLM processing is completed [136-138]. Materials processed by SLS generally exhibit high porosities and significant surface roughness, and, therefore, often have mechanical properties inferior to the bulk material [25, 112]. Since SLM involves complete melting of the feedstock material, materials processed using SLM exhibit lower porosities and exhibit mechanical properties that are more similar to those of the bulk material than structures produced by SLS [25]. It is important to note that SLS/SLM is currently the only laser direct write process that is capable of producing metallic medical devices.

Two-photon Polymerization

Two-photon polymerization (2PP) utilizes excitation of photoinitiator molecules to induce polymerization of a resin, similarly to stereolithography. Unlike conventional stereolithography, where the photoinitiator is excited by single-photon absorption, in 2PP

excitation occurs via multi-photon absorption, as is seen in femtosecond laser ablation and multi-photon microscopy (Figure 2, center). As mentioned in the description of femtosecond laser ablation, ultra-short-pulse lasers can induce nearly simultaneous absorption of photons. Upon absorption of multiple photons a virtual state is achieved, which creates an effect similar to single-photon absorption, but with significantly higher energies [143, 144]. Two-photon absorption results in a non-linear energy distribution that is radially dependent perpendicular to the axis of propagation and dependent on distance from the focal point along the axis of propagation; the energy distribution is quadratic in shape in both of these directions (Figure 7a) [29, 145]. This energy distribution results in a volume approximately in the shape of a bicone (two cones joined at their base) where the energy is above the photoinitiator threshold energy (Figure 7b). Polymerization occurs in this volume, known as a voxel, where the threshold excitation energy is achieved [56, 146]. Due to the nonlinear nature of two-photon absorption, the resolution of the polymerization voxel can be beyond the diffraction limit [56, 146]. Therefore, in contrast with other laser direct write techniques, 2PP can produce sub-micron features (e.g., on the same length scale as subcellular organelles). Resolutions of 30 nm have been reported [147]. While exceptionally high resolutions are capable with 2PP, the resolution is scalable, which facilitates tuning the resolution to one's needs and thus minimizing the fabrication time [50]. Since many medical devices do not require sub-100 nm or even sub-micron resolution, tailoring the resolution to the application minimizes production time and cost [29]. The resolution of 2PP is dependent on a wide range of factors. The laser spot size, wavelength, energy, pulse width, pulse duration, pulse frequency, and pulse peak intensity all affect the voxel size. From a

structuring perspective, scanning speed, rastering spacing, and layer spacing affect the resolution of a structure. Further, the optical properties of the resin, photoinitiator type and concentration, and additional of radical quenchers can influence the resolution.

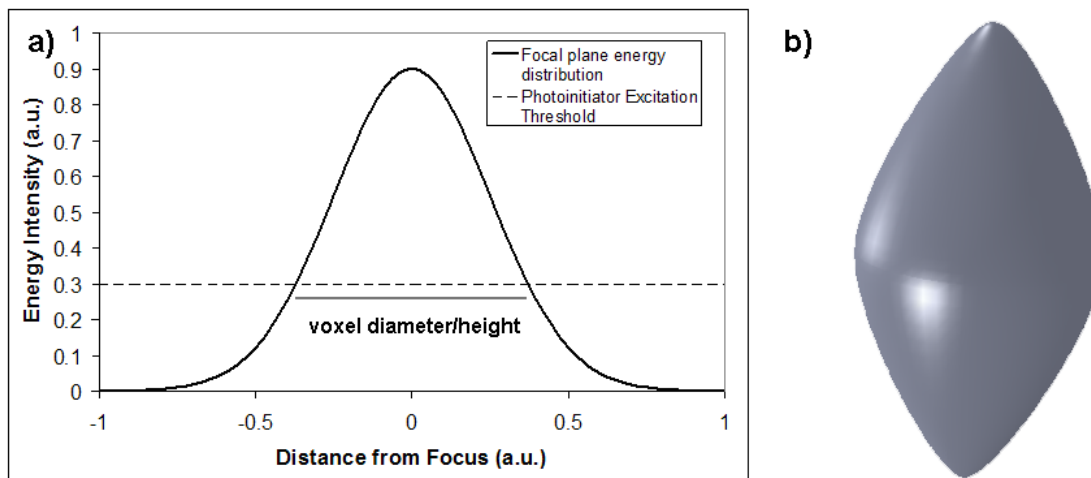


Figure 7. The two-photon polymerization process: a) Schematic of the two-photon polymerization process. The energy distribution of two-photon absorption is a Gaussian shape centered at the focal point of the laser. The radius of the polymerization voxel corresponds to the position at which the energy intensity exceeds the excitation threshold of the photoinitiator; b) representative model of a polymerization voxel.

The essential components of a 2PP setup are a femtosecond or short picosecond laser which is focused through a microscope objective and translational stages for moving the point of the laser within the resin on three dimensions. Most commonly, near-infrared femtosecond lasers are used; many materials are transparent to this wavelength range, enabling 3-D

writing with the laser within the material of interest. In contrast, conventional stereolithography which generally uses UV light is readily absorbed by many materials and therefore is limited to patterning at the surface of the resin [28]. With regards to the microscope objective, resolution is dependent on the numerical aperture [148]. Direct-writing of 3-D structures can be produced by any combination of two methods: moving the substrate and resin with respect to the laser or moving the laser focal point within the resin. A galvano-scanner, a system of two mirrors which controls the location of the laser transverse to the axis of propagation, may be used to dictate the X,Y location of the focal point. Two-photon polymerization is compatible with many of the materials used in conventional single-photon stereolithography. Since stereolithography is one of the oldest rapid prototyping techniques, a wide range of materials that are compatible with 2PP are available [29]. Two-photon polymerization does not require cleanroom facilities, greatly reducing the cost in comparison to standard microfabrication techniques such as deep reactive ion etching and LIGA which require a cleanroom [148, 149]. Not requiring a cleanroom is beneficial since a device for clinical use can be produced at or near an operating room or other clinical site. Recently, Obato *et al.* have demonstrated that 2PP with multiple focal points can be achieved which may enable even faster production of medical devices that are in arrays or other simple geometric patterns, such as microneedle arrays or tissue engineering scaffolds [150].

Two-photon polymerization has been used to process a wide range of materials, including Ormocer® [144, 148, 151-155], polyethylene glycol diacrylate [44, 156-158], biodegradable tri-block copolymers [159], Zr-based sol-gel composites [160, 161], Ti-based sol-gel

composites [162], metal ion-doped acrylates [163], commercial acrylates (e-Shell 300) [50], bovine serum albumin [164, 165], fibrinogen [164], and collagen [165]. Ormocer®s are one of the most widely used classes of materials for production of microscale medical devices. *OR*ganically *MO*dified *CER*amics (Ormocer®s) are organic-inorganic hybrids, meaning that they are materials containing both organic (polymer) functional groups and inorganic (ceramic) functional groups. Since these materials are comprised of organic polymer, silicone, and ceramic functional groups, they have properties that are a cross between these different materials. Their properties are also tunable depending on the components of the different functional groups. Some of the properties of Ormocer® in comparison to polymers and ceramics are presented in Table 2. Many types of Ormocer® are biocompatible [144, 151, 155, 166]. The biocompatibility and more importantly the nonfouling properties of polyethylene glycol diacrylate make this material appealing for medical devices, particularly devices where biofouling may lead to device failure [44, 158]. The ability to crosslink natural polymers with 2PP is interesting in that it may enable production of tissue engineering scaffolds from natural materials [164, 165].

Table 2. Properties ofOrmocer®

Property Type	Property	Ormocer®	Polymers	Ceramics
Mechanical	Young's Modulus	2100 MPa	20-2000 MPa	>50,000 MPa
	Hardness (Vickers)	13.33	<5	>5
Thermal	Coefficient of Thermal Expansion	$\sim 100 \times 10^{-6} \text{ K}^{-1} *$	$>40 \text{ K}^{-1}$	$<10 \text{ K}^{-1}$
Optical	Refractive Index	$\sim 1.5 *$		1.473 [Glass]
Surface	Contact Angle	83°	110° [PDMS]	51° [Glass]

* from www.microresist.de

Due to the many properties that are conducive to medical device production, a variety of 3-D micro-structured medical devices may be generated by 2PP. These devices have included microneedles [50, 144, 145, 151, 155-158], inner ear prosthetics [148], and tissue engineering scaffolds [44, 144, 152, 166-168]. Two-photon polymerization is an appealing technique for microneedle production in that it allows easy manipulation of the microscale geometry of these devices, which is an important factor in microneedle performance (Figure 8) [145, 151, 155, 169]. Numerous hard, yet flexible materials have been used for producing microneedles directly by 2PP, including Ormocer@s [144, 151, 155] and the commercial acrylate e-Shell 300 [50]. E-Shell 300 also has the advantage of autofluorescing, which enables non-invasive imaging of the needles within the skin [50]. Studies have shown that both of these materials are capable of penetrating the skin without damage to the needles [50, 144, 151, 155].

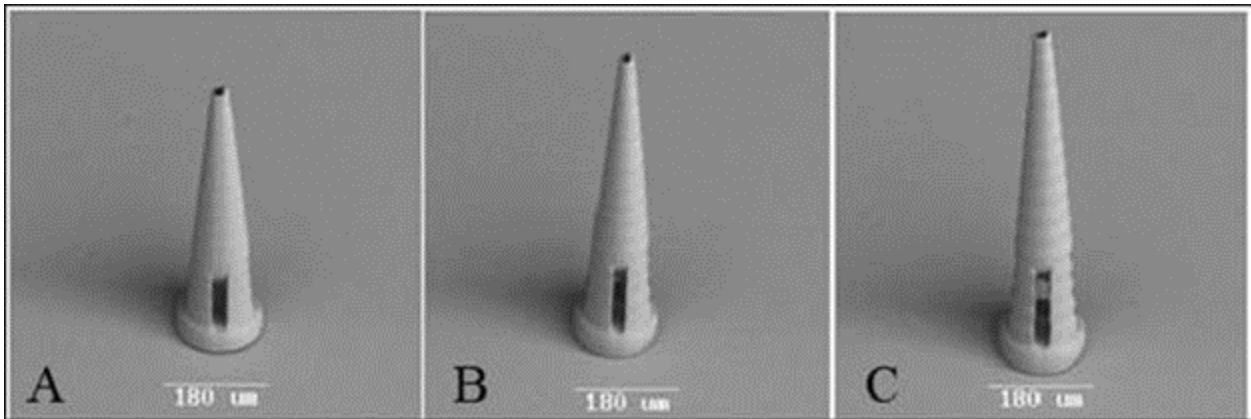


Figure 8: Ormocer® microneedles at a) 2:1 , b) 2.5:1, and c) 3:1 aspect ratios produced by two-photon polymerization.

Source: Doraiswamy A, Ovsianikov A, Gittard SD, Monteiro-Riviere NA, Crombez R, Montalvo E, Shen W, Chichkov BN, Narayan RJ. Fabrication of Microneedles Using Two Photon Polymerization For Transdermal Delivery of Nanomaterials. *J Nanosci Nanotechnol* 2010;10(10):6305-6312.

Small prostheses, such as ossicular prostheses, are another class of medical devices that may be produced by 2PP. Ovsianikov *et al.* produced TORPs (Total Ossicular Replacement Prostheses) out of Ormocer® by 2PP. Insertion and removal of the Ormocer® TORP from the intended site of use in a frozen cadaver head without fracture of the prosthesis was demonstrated [148]. The flexibility of 2PP may enable TORPs to be produced with dimensions that are specifically tuned to the patient. Recently, Schizas *et al.* have produced microscale valves via 2PP, indicating that 2PP may be used to produce prosthetic valves for vasculature.

Two-photon polymerization has been used to create tissue engineering scaffolds with complex geometries [44, 159, 167, 170-172]. Scaffolds containing pores of multiple sizes may allow preferential transport of cells versus smaller molecules (e.g., nutrient, waste, growth factors). For example, Tayalia *et al* produced scaffolds with pores ranging from 12 to 110 μm ; cells were able to penetrate the larger pores but not the smaller ones [171]. Stackable tissue engineering scaffolds have also been created by 2PP, which enable assembly of larger constructs after cell seeding (Figure 9a) [144, 170]. Ovsianikov *et al.* used 2PP to produce high porosity scaffolds in the shape of a hexagon with a hexagonal opening for vascular tissue engineering applications; the hexagonal “ring” is the wall of the blood vessel and the hexagonal opening in the center is the interior of the blood vessel [167]. Laser bioprinting was used to seed the scaffold, with endothelial cells being preferentially deposited along the interior of the wall and smooth muscle cells being preferentially deposited on the exterior of the wall (Figure 9b).

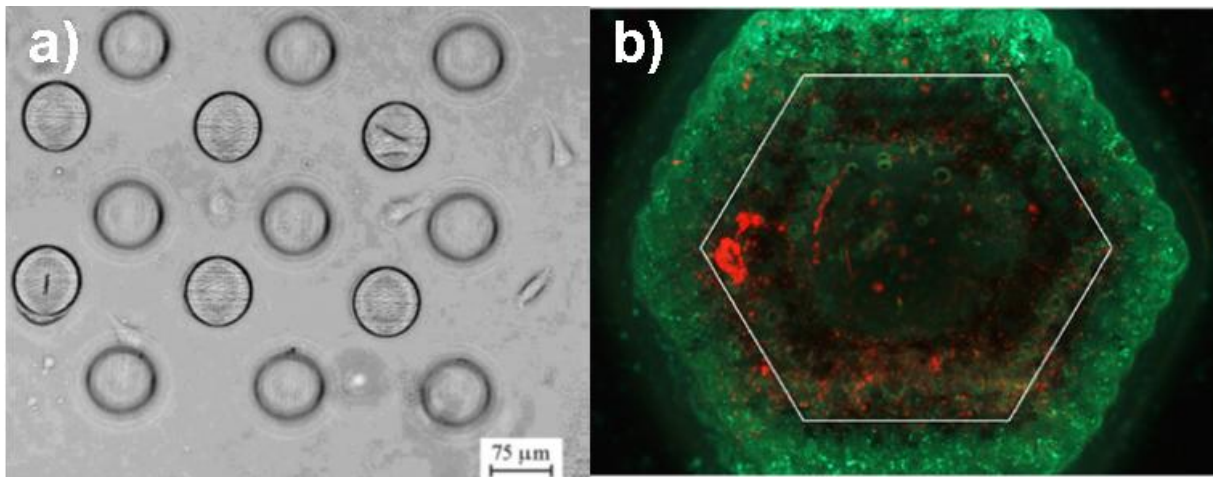


Figure 9. Tissue engineering scaffolds produced by two-photon polymerization: a) Stackable Ormocer® tissue engineering scaffold*; b) Polyethylene glycol diacrylate scaffold in the shape of a blood vessel with endothelial cells along the inner wall and smooth muscle cells along the outer wall, which were deposited by laser bioprinting.**

***Narayan RJ, Jin CM, Doraiswamy A, Mihailescu IN, Jelinek M, Ovsianikov A, Chichkov B, Chrisey DB. Laser processing of advanced bioceramics. *Advanced Engineering Materials* 2005 DEC;7(12):1083-1098. Copyright Wiley-VCH Verlag GmbH & Co. KGaA. Reproduced with permission.**

****Source: Ovsianikov A, Gruene M, Pflaum M, Koch L, Maiorana F, Wilhelmi M, Haverich A, Chichkov B. Laser printing of cells into 3D scaffolds. *Biofabrication* 2010 MAR;2(1):014104. doi: [10.1088/1758-5082/2/1/014104](https://doi.org/10.1088/1758-5082/2/1/014104)**

Conclusion

Rapid prototyping is a broad field; light-based rapid prototyping alone comprises the six main techniques that have just been discussed. While these techniques vary greatly in their materials compatibility, resolution, and numerous other properties, they are all powerful tools

for generating micro- and nanoscale medical devices. Continuing research into these production tools will be beneficial to the future of biomedical device development.

References

- [1] Ke K, Hasselbrink EF, Hunt AJ. Rapidly prototyped three-dimensional nanofluidic channel networks in glass substrates. *Anal Chem* 2005 AUG 15;77(16):5083-5088.

- [2] Kim TN, Campbell K, Groisman A, Kleinfeld D, Schaffer CB. Femtosecond laser-drilled capillary integrated into a microfluidic device. *Appl Phys Lett* 2005 MAY 16;86(20):201106.

- [3] Harris ML, Doraiswamy A, Narayan RJ, Patz TM, Chrisey DB. Recent progress in CAD/CAM laser direct-writing of biomaterials. *Mater Sci Eng C-Biomimetic Supramol Syst* 2008 APR 1;28(3):359-365.

- [4] Lee JW, Nguyen TA, Kang KS, Seol Y-, Cho D-. Development of a growth factor-embedded scaffold with controllable pore size and distribution using micro-stereolithography. *Tissue Eng Part A* 2008 MAY;14(5):835.

- [5] Lee KB, Solanki A, Kim JD, Jung J. Nanomedicine: dynamic integration of nanotechnology with biomaterials science. In: Zhang M, Xi N, editors. *Nanomedicine: A Systems Engineering Approach* Singapore: Pan Stanford; 2009. p. 1-38.

[6] Hitz CB, Ewing JJ, Hecht J, Hitz CB. Introduction to laser technology. 3rd ed. New York: IEEE Press; 2001.

[7] Liu X, Du D, Mourou G. Laser ablation and micromachining with ultrashort laser pulses. IEEE J Quant Electron 1997 OCT;33(10):1706-1716.

[8] Han J, Jia Y. CT Image Processing and Medical Rapid Prototyping. In: BMEI '08: Proceedings of the 2008 International Conference on BioMedical Engineering and Informatics Washington, DC, USA: IEEE Computer Society; 2008.

[9] Solar P, Ulm C, Lill W, Imhof H, Watzek G, Blahout R, Gruber H, Matejka M. Precision of three-dimensional CT-assisted model production in the maxillofacial area. Eur Radiol 1992;2(5):473-477.

[10] Ellis DS, Toth BA, Stewart WB. Temporoparietal fascial flap for orbital and eyelid reconstruction. Plast Reconstr Surg 1992 Apr;89(4):606-612.

[11] Klein HM, Schneider W, Alzen G, Voy ED, Gunther RW. Pediatric Craniofacial Surgery - Comparison of Milling and Stereolithography for 3D-Model Manufacturing. Pediatr Radiol 1992 OCT;22(6):458-460.

[12] Ono I, Gunji H, Kaneko F, Numazawa S, Kodama N, Yoza S. Treatment of Extensive Cranial Bone Defects using Computer-Designed Hydroxyapatite Ceramics and Periosteal Flaps. *Plast Reconstr Surg* 1993 OCT;92(5):819-830.

[13] Eufinger H, Wehmoller M, Machtens E, Heuser L, Harders A, Kruse D. Reconstruction of Craniofacial Bone Defects with Individual Alloplastic Implants Based on Cad/cam-Manipulated Ct-Data. *J Cranio-Maxillo-Fac Surg* 1995 JUN;23(3):175-181.

[14] McGurk M, Amis AA, Potamianos P, Goodger NM. Rapid prototyping techniques for anatomical modelling in medicine. *Ann R Coll Surg Engl* 1997 MAY;79(3):169-174.

[15] Nakai T, Marutani Y. Application of Uv Laser Fabrication to Organ Models Interpolated from Computed-Tomography and Magnetic-Resonance Images. *Appl Opt* 1992 SEP 1;31(25):5375-5379.

[16] Katsoulis J, Gisler V, Mericske-Stern R. Computer-Assisted Implant-Prosthetics for the Edentulous Maxilla in Special Care Patients - Case Series Introduction and Case 1 (Anxious Patient with Special Anatomy). *Implantologie* 2010 JUN;18(2):193-202.

[17] Chang CC, Lee MY, Wang SH. Digital denture manufacturing-An integrated technologies of abrasive computer tomography, CNC machining and rapid prototyping. *Int J Adv Manuf Technol* 2006 NOV;31(1-2):41-49.

[18] Dai K, Yan M, Zhu Z, Sun Y. Computer-aided custom-made hemipelvic prosthesis used in extensive pelvic lesions. *J Arthroplasty* 2007 OCT;22(7):981-986.

[19] Singare S, Dichen L, Bingheng L, Zhenyu G, Yaxiong L. Customized design and manufacturing of chin implant based on rapid prototyping. *Rapid Prototyping J* 2005;11(2):113-118.

[20] Subburaj K, Nair C, Rajesh S, Meshram SM, Ravi B. Rapid development of auricular prosthesis using CAD and rapid prototyping technologies. *Int J Oral Maxillofac Surg* 2007 OCT;36(10):938-943.

[21] Liu Y, Dong X, Zhu H, Peng W. Study on Application of Rapid Prototyping in Precise Oral and Maxillofacial Surgery. *Adv Mater Res* 2010;102-104:64-68.

[22] Gittard SD, Narayan RJ, Lusk J, Morel P, Stockmans F, Ramsey M, Laverde C, Phillips J, Monteiro-Riviere NA, Ovsianikov A, Chichkov BN. Rapid prototyping of scaphoid and lunate bones. *Biotechnol J* 2009 Jan;4(1):129-134.

[23] Majumdar JD, Manna I. Laser processing of materials. *Sadhana* 2003;28(3&4):495-562.

- [24] Jansen ED, Frenz M, Kadipasaoglu KA, Pfefer TJ, Altermatt HJ, Motamedi M, Welch AJ. Laser-tissue interaction during transmyocardial laser revascularization. *Ann Thorac Surg* 1997 MAR;63(3):640-647.
- [25] Kruth JP, Mercelis P, Van Vaerenbergh J, Froyen L, Rombouts M. Binding mechanisms in selective laser sintering and selective laser melting. *Rapid Prototyping J* 2005;11(1):26-36.
- [26] Zhang X, Jiang XN, Sun C. Micro-stereolithography of polymeric and ceramic microstructures. *Sens Actuator A-Phys* 1999 OCT 12;77(2):149-156.
- [27] Venuvinod PK, Ma W. *Rapid Prototyping: Laser-based and Other Technologies*. Dordrecht, The Netherlands: Kluwer Academic Publishers; 2004.
- [28] Ovsianikov A, Passinger S, Houbertz R, Chichkov BN. Three dimensional material processing with femtosecond lasers. In: Phipps C, editor. *Laser Ablation and its Applications* Berlin: Springer; 2007. p. 121-157.
- [29] Gittard SD, Narayan RJ. Laser direct writing of micro- and nano-scale medical devices. *Expert Rev Med Devices* 2010 2010 May;7(3):343-356.
- [30] Steen WM. *Rapid prototyping and low volume manufacture*. Laser Material Processing. 3rd ed. Berlin, Germany: Springer; 2003. p. 279-300.

[31] Lee IH, Cho DW. An investigation on photopolymer solidification considering laser irradiation energy in micro-stereolithography. *Microsyst Technol* 2004;10(8-9):592-598.

[32] Lee IH, Cho DW. Micro-stereolithography photopolymer solidification patterns for various laser beam exposure conditions. *Int J Adv Manuf Technol* 2003;22(5-6):410-416.

[33] Stampfl J, Baudis S, Heller C, Liska R, Neumeister A, Kling R, Ostendorf A, Spitzbart M. Photopolymers with tunable mechanical properties processed by laser-based high-resolution stereolithography. *J Micromech Microengineering* 2008;18(12):125014.

[34] Neumeister A, Himmelhuber R, Materlik C, Temme T, Pape F, Gatzel H, Ostendorf A. Properties of Three-Dimensional Precision Objects Fabricated by Using Laser Based Micro Stereo Lithography. *J Laser Micro Nanoeng* 2008;3(2):67-72.

[35] Singare S, Dichen L, Bingheng L, Yanpu L, Zhenyu G, Yaxiong L. Design and fabrication of custom mandible titanium tray based on rapid prototyping. *Med Eng Phys* 2004 OCT;26(8):671-676.

[36] Singare S, Lian Q, Wang WP, Wang J, Liu Y, Li D, Lu B. Rapid prototyping assisted surgery planning and custom implant design. *Rapid Prototyping J* 2009;15(1):19-23.

- [37] D'Urso PS, Earwaker WJ, Barker TM, Redmond MJ, Thompson RG, Effeney DJ, Tomlinson FH. Custom cranioplasty using stereolithography and acrylic. *Br J Plast Surg* 2000 APR;53(3):200-204.
- [38] Wurm G, Tomancok B, Holl K, Trenkler J. Prospective study on cranioplasty with individual carbon fiber reinforced polymere (CFRP) implants produced by means of stereolithography. *Surg Neurol* 2004 DEC;62(6):510-521.
- [39] Lee S, Wu C, Lee S, Chen P. Cranioplasty using polymethyl methacrylate prostheses. *J Clin Neurosci* 2009 JAN;16(1):56-63.
- [40] Staffa G, Nataloni A, Compagnone C, Servadei F. Custom made cranioplasty prostheses in porous hydroxy-apatite using 3D design techniques: 7 years experience in 25 patients. *Acta Neurochir* 2007 FEB;149(2):161-170.
- [41] Lee JW, Lan PX, Kim B, Lim G, Cho D. 3D scaffold fabrication with PPF/DEF using micro-stereolithography. *Microelectron Eng* 2007 MAY-AUG;84(5-8):1702-1705.
- [42] Lee JW, Ahn G, Kim DS, Cho D. Development of nano- and microscale composite 3D scaffolds using PPF/DEF-HA and micro-stereolithography. *Microelectron Eng* 2009 APR-JUN;86(4-6):1465-1467.

[43] Arcaute K, Mann BK, Wicker RB. Stereolithography of three-dimensional bioactive poly(ethylene glycol) constructs with encapsulated cells. *Ann Biomed Eng* 2006 SEP;34(9):1429-1441.

[44] Ovsianikov A, Malinauskas M, Schlie S, Chichkov B, Gittard S, Narayan R, Löbler M, Sternberg K, Schmitz K-, Haverich A. Three-dimensional laser micro- and nano-structuring of acrylated poly(ethylene glycol) materials and evaluation of their cytotoxicity for tissue engineering applications. *Acta Biomaterialia* 2011 3;7(3):967-974.

[45] Choi JW, Park IB, Ha YM, Jung MG, Lee SD, Lee SH. Insertion Force Estimation of Various Microneedle Array-type Structures Fabricated by a Microstereolithography Apparatus. *SICE-ICASE, 2006. International Joint Conference; 2006.*

[46] Gittard SD, Miller PR, Jin C, Martin TN, Boehm RD, Chisholm BJ, Stafslie SJ, Daniels JW, Cilz N, Narayan RJ. Pulsed Laser Deposition of Antimicrobial Metal Thin Film Coatings on Microneedles Produced by Visible Light Dynamic Mask Micro-stereolithography. *Biofabrication* 2011: under review.

[47] Miller PR, Gittard SD, Edwards TL, Lopez DM, Xiao X, Wheeler DR, Monteiro-Riviere NA, Polsky R, Narayan RJ. Integrated carbon fiber electrodes within polymer, hollow microneedles made via micro-stereolithography for transdermal electrochemical sensing applications. *Biomicrofluidics* 2011:under review.

- [48] Srinivasan R. Ablation of Polymers and Biological Tissue by Ultraviolet-Lasers. Science 1986 OCT 31;234(4776):559-565.
- [49] Miller PR, Aggarwal R, Doraiswamy A, Lin YJ, Lee YS, Narayan RJ. Laser micromachining for biomedical applications. JOM 2009;61(9):35-40.
- [50] Gittard SD, Miller PR, Boehm RD, Ovsianikov A, Chichkov BN, Heiser J, Gordon J, Monteiro-Riviere N, Narayan RJ. Multiphoton microscopy of transdermal quantum dot delivery using two photon polymerization-fabricated polymer microneedles. Faraday Discuss 2011;149:171-185.
- [51] Schmidt V, Kuna L, Satzinger V, Jakopic G, Leising G. Two-photon 3D lithography: A Versatile Fabrication Method for Complex 3D Shapes and Optical Interconnects within the Scope of Innovative Industrial Applications. Journal of Laser Micro Nanoengineering 2007 OCT;2(3):170-177.
- [52] Snakenborg D, Klank H, Kutter JP. Microstructure fabrication with a CO2 laser system. J Micromech Microengineering 2004 FEB;14(2):182-189.

[53] Korte F, Nolte S, Chichkov BN, Bauer T, Kamlage G, Wagner T, Fallnich C, Welling H. Far-field and near-field material processing with femtosecond laser pulses. *Appl Phys A-Mater Sci Process* 1999 DEC;69:S7-S11.

[54] Gattass RR, Mazur E. Femtosecond laser micromachining in transparent materials. *Nat Photonics* 2008 APR;2(4):219-225.

[55] Joglekar AP, Liu H, Spooner GJ, Meyhofer E, Mourou G, Hunt AJ. A study of the deterministic character of optical damage by femtosecond laser pulses and applications to nanomachining. *Appl Phys B-Lasers Opt* 2003 AUG;77(1):25-30.

[56] Lee K, Kim RH, Yang D, Park SH. Advances in 3D nano/microfabrication using two-photon initiated polymerization. *Progress in Polymer Science* 2008 JUN;33(6):631-681.

[57] Vogel A, Venugopalan V. Mechanisms of pulsed laser ablation of biological tissues. *Chem Rev* 2003 FEB;103(2):577-644.

[58] Chichkov BN, Momma C, Nolte S, vonAlvensleben F, Tunnermann A. Femtosecond, picosecond and nanosecond laser ablation of solids. *Appl Phys A-Mater Sci Process* 1996 AUG;63(2):109-115.

[59] Preuss S, Demchuk A, Stuke M. Subpicosecond Uv Laser-Ablation of Metals. Appl Phys A-Mater Sci Process 1995 JUL;61(1):33-37.

[60] Stoeckel D, Bonsignore C, Duda S. A survey of stent designs. Minim Invasive Ther Allied Technol 2002 JUL 01;11(4):137-147.

[61] Stoeckel D, Pelton A, Duerig T. Self-expanding nitinol stents: material and design considerations. Eur Radiol 2004 Feb;14(2):292-301.

[62] Momma C, Knop U, Nolte S. Laser Cutting of Slotted Tube Coronary Stents – State-of-the-Art and Future Developments. Prog Biomed Res 1999:39-44.

[63] Grabow N, Bungler CM, Schultze C, Schmohl K, Martin DP, Williams SF, Sternberg K, Schmitz KP. A Biodegradable Slotted Tube Stent Based on Poly(l-lactide) and Poly(4-hydroxybutyrate) for Rapid Balloon-Expansion. Annals of Biomedical Engineering 2007; 35(12): 2031-2038.

[64] Lannutti J, Reneker D, Ma T, Tomasko D, Farson DF. Electrospinning for tissue engineering scaffolds. Mater Sci Eng C-Biomimetic Supramol Syst 2007 APR;27(3):504-509.

[65] McCullen SD, Miller PR, Gittard SD, Gorga RE, Pourdeyhimi B, Narayan RJ, Lobo EG. In Situ Collagen Polymerization of Layered Cell-Seeded Electrospun Scaffolds for Bone Tissue Engineering Applications. *Tissue Engineering Part C-Methods* 2010 OCT;16(5):1095-1105.

[66] Choi HW, Johnson JK, Nam J, Farson DF, Lannutti J. Structuring electrospun polycaprolactone nanofiber tissue scaffolds by femtosecond laser ablation. *J Laser Appl* 2007 NOV;19(4):225-231.

[67] McCullen SD, Gittard SD, Miller PR, Gorga RE, Narayan RJ, Lobo EG. Laser ablation imparts controlled micro-scale pores in nanofibrous electrospun poly(l-lactic acid) scaffolds. *Ann Biomed Eng* 2011:under review.

[68] Duncan AC, Rouais F, Lazare S, Bordenave L, Baquey C. Effect of laser modified surface microtopochemistry on endothelial cell growth. *Colloid Surf B-Biointerfaces* 2007 FEB 15;54(2):150-159.

[69] Doraiswamy A, Narayan RJ. Vascular tissue engineering by computer-aided laser micromachining. *Philosophical Transactions of the Royal Society A: Mathematical, Physical and Engineering Sciences* 2010 04/28;368(1917):1891-1912.

[70] Schlie S, Fadeeva E, Koroleva A, Ovsianikov A, Koch J, Ngezahayo A, Chichkov BN. Laser-based nanoengineering of surface topographies for biomedical applications. *Photonics and Nanostructures - Fundamentals and Applications* ;In Press, Corrected Proof.

[71] Patz TM, Doraiswamy A, Narayan RJ, Modi R, Chrisey DB. Two-dimensional differential adherence and alignment of C2C12 myoblasts. *Mater Sci Eng B-Solid State Mater Adv Technol* 2005 NOV 25;123(3):242-247.

[72] Doraiswamy A, Narayan RJ, Lippert T, Urech L, Wokaun A, Nagel M, Hopp B, Dinescu M, Modi R, Auyeung RCY, Chrisey DB. Excimer laser forward transfer of mammalian cells using a novel triazene absorbing layer. *Appl Surf Sci* 2006 APR 30;252(13):4743-4747.

[73] Sugioka K, Hanada Y, Midorikawa K. 3D integration of microcomponents in a single glass chip by femtosecond laser direct writing for biochemical analysis. *Appl Surf Sci* 2007 MAY 30;253(15):6595-6598.

[74] Hanada Y, Sugioka K, Kawano H, Ishikawa IS, Miyawaki A, Midorikawa K. Nano-aquarium for dynamic observation of living cells fabricated by femtosecond laser direct writing of photostructurable glass. *Biomed Microdevices* 2008 JUN;10(3):403-410.

- [75] Applegate RW, Jr., Schafer DN, Amir W, Squier J, Vestad T, Oakey J, Marr DWM. Optically integrated microfluidic systems for cellular characterization and manipulation. *J Opt A-Pure Appl Opt* 2007 AUG;9(8):S122-S128.
- [76] Vazquez RM, Osellame R, Cretich M, Chiari M, Dongre C, Hoekstra HJWM, Pollnau M, van den Vlekkert H, Ramponi R, Cerullo G. Optical sensing in microfluidic lab-on-a-chip by femtosecond-laser-written waveguides. *Anal Bioanal Chem* 2009 FEB;393(4):1209-1216.
- [77] Ancona A, Roeser F, Rademaker K, Limpert J, Nolte S, Tuennermann A. High speed laser drilling of metals using a high repetition rate, high average power ultrafast fiber CPA system. *Opt Express* 2008 JUN 9;16(12):8958-8968.
- [78] Ancona A, Nodop D, Limpert J, Nolte S, Tuennermann A. Microdrilling of metals with an inexpensive and compact ultra-short-pulse fiber amplified microchip laser. *Appl Phys A-Mater Sci Process* 2009 JAN;94(1):19-24.
- [79] Doraiswamy A, Narayan RJ, Harris ML, Qadri SB, Modi R, Chrisey DB. Laser microfabrication of hydroxyapatite-osteoblast-like cell composites. *J Biomed Mater Res Part A* 2007 MAR 1;80A(3):635-643.

- [80] Gruene M, Deiwick A, Koch L, Schlie S, Unger C, Hofmann N, Bernemann I, Glasmacher B, Chichkov B. Laser Printing of Stem Cells for Biofabrication of Scaffold-Free Autologous Grafts. *Tissue Engineering Part C-Methods* 2011 JAN;17(1):79-87.
- [81] Koch L, Kuhn S, Sorg H, Gruene M, Schlie S, Gaebel R, Polchow B, Reimers K, Stoelting S, Ma N, Vogt PM, Steinhoff G, Chichkov B. Laser Printing of Skin Cells and Human Stem Cells. *Tissue Engineering Part C-Methods* 2010 OCT;16(5):847-854.
- [82] Unger C, Gruene M, Koch L, Koch J, Chichkov B. Time-resolved imaging of hydrogel printing via laser-induced forward transfer. *Appl Phys A* 2010:1-7.
- [83] Pique A, Chrisey DB, Auyeung RCY, Fitz-Gerald J, Wu HD, McGill RA, Lakeou S, Wu PK, Nguyen V, Duignan M. A novel laser transfer process for direct writing of electronic and sensor materials. *Appl Phys A-Mater Sci Process* 1999 DEC;69:S279-S284.
- [84] Khan M, Gittard SD, Narayan RJ. Antimicrobial testing, morphological characterization, and surface potential mapping of silver-poly-(methyl methacrylate) nanocomposite films made through matrix-assisted pulsed laser deposition against *S. aureus*. *Nano LIFE* 2010;1(1&2):145-152.
- [85] Chrisey DB, Pique A, McGill RA, Horwitz JS, Ringeisen BR, Bubb DM, Wu PK. Laser deposition of polymer and biomaterial films. *Chem Rev* 2003 FEB;103(2):553-576.

[86] Kokkinaki O, Georgiou S. Laser ablation of cryogenic films: Implications to Matrix-Assisted Pulsed Laser Deposition of biopolymers and dedicated applications in nanotechnology. *Digest Journal of Nanomaterials and Biostructures* 2007 JUN;2(2):221-241.

[87] Pique A, McGill RA, Chrisey DB, Leonhardt D, Mslina TE, Spargo BJ, Callahan JH, Vachet RW, Chung R, Bucaro MA. Growth of organic thin films by the matrix assisted pulsed laser evaporation (MAPLE) technique. *Thin Solid Films* 1999 NOV;355:536-541.

[88] Cristescu R, Dorcioman G, Ristoscu C, Axente E, Grigorescu S, Moldovan A, Mihailescu IN, Kocourek T, Jelinek M, Albulescu M, Buruiana T, Mihaiescu D, Stamatina I, Chrisey DB. Matrix assisted pulsed laser evaporation processing of triacetate-pullulan polysaccharide thin films for drug delivery systems. *Appl Surf Sci* 2006 APR 30;252(13):4647-4651.

[89] Cristescu R, Jelinek M, Kocourek T, Axente E, Grigorescu S, Moldovan A, Mihaiescu DE, Albulescu M, Buruiana T, Dybal J, Stamatina I, Mihailescu IN, Chrisey DB. Matrix assisted pulsed laser evaporation of pullulan tailor-made biomaterial thin films for controlled drug delivery systems. *Cola'05: 8th International Conference on Laser Ablation* 2007;59:144-149.

[90] Jelinek M, Cristescu R, Axente E, Kocourek T, Dybal J, Remsa J, Plestil J, Mihaiescu D, Albulescu M, Buruiana T, Stamatina I, Mihailescu IN, Chrisey DB. Matrix assisted pulsed laser evaporation of cinnamate-pullulan and tosylate-pullulan polysaccharide derivative thin films for pharmaceutical applications. *Appl Surf Sci* 2007 JUL 31;253(19):7755-7760.

[91] Cristescu R, Mihaiescu D, Socol G, Stamatina I, Mihailescu IN, Chrisey DB. Deposition of biopolymer thin films by matrix assisted pulsed laser evaporation. *Applied Physics A-Materials Science & Processing* 2004 SEP;79(4-6):1023-1026.

[92] Cristescu R, Kocourek T, Moldovan A, Stamatina L, Mihaiescu D, Jelinek M, Stamatina I, Mihailescu IN, Chrisey DB. Laser deposition of cryoglobulin blood proteins thin films by matrix assisted pulsed laser evaporation. *Appl Surf Sci* 2006 APR 30;252(13):4652-4655.

[93] Cristescu R, Patz T, Narayan RJ, Menegazzo N, Mizaikoff B, Mihaiescu DE, Messersmith PB, Stamatina I, Mihailescu IN, Chrisey DB. Processing of mussel adhesive protein analog thin films by matrix assisted pulsed laser evaporation. *Appl Surf Sci* 2005 JUL 15;247(1-4):217-224.

[94] Cristescu R, Mihailescu IN, Stamatina I, Doraiswamy A, Narayan RJ, Westwood G, Wilker JJ, Stafslin S, Chisholm B, Chrisey DB. Thin films of polymer mimics of cross-linking mussel adhesive proteins deposited by matrix assisted pulsed laser evaporation. *Appl Surf Sci* 2009 MAR 1;255(10):5496-5498.

[95] Cristescu R, Popescu C, Popescu A, Grigorescu S, Mihailescu IN, Mihaiescu D, Gittard SD, Narayan RJ, Buruiana T, Stamatina I, Chrisey DB. Functional polyethylene glycol derivatives nanostructured thin films synthesized by matrix-assisted pulsed laser evaporation. *Appl Surf Sci* 2009 SEP 30;255(24):9873-9876.

[96] Cristescu R, Popescu C, Socol G, Visan A, Mihailescu IN, Gittard SD, Miller PR, Martin TN, Narayan RJ, Andronie A, Stamatina I, Chrisey DB. Deposition of antibacterial of poly(1,3-bis-(p-carboxyphenoxy propane)-co-(sebacic anhydride)) 20:80/gentamicin sulfate composite coatings by MAPLE. *Appl Surf Sci* ;In Press, Corrected Proof.

[97] Adrian FJ, Bohandy J, Kim BF, Jette AN, Thompson P. A Study of the Mechanism of Metal-Deposition by the Laser-Induced Forward Transfer Process. *Journal of Vacuum Science & Technology B* 1987 SEP-OCT;5(5):1490-1494.

[98] Bohandy J, Kim BF, Adrian FJ. Metal-Deposition from a Supported Metal-Film using an Excimer Laser. *J Appl Phys* 1986 AUG 15;60(4):1538-1539.

[99] Bohandy J, Kim BF, Adrian FJ, Jette AN. Metal-Deposition at 532-Nm using a Laser Transfer Technique. *J Appl Phys* 1988 FEB 15;63(4):1158-1162.

[100] Chrisey DB, Pique A, Fitz-Gerald J, Auyeung RCY, McGill RA, Wu HD, Duignan M. New approach to laser direct writing active and passive mesoscopic circuit elements. *Appl Surf Sci* 2000 FEB;154:593-600.

[101] Chrisey DB, Pique A, Modi R, Wu HD, Auyeung RCY, Young HD. Direct writing of conformal mesoscopic electronic devices by MAPLE DW. *Appl Surf Sci* 2000 DEC 15;168(1-4):345-352.

[102] Fitz-Gerald JM, Pique A, Chrisey DB, Rack PD, Zeleznik M, Auyeung RCY, Lakeou S. Laser direct writing of phosphor screens for high-definition displays. *Appl Phys Lett* 2000 MAR 13;76(11):1386-1388.

[103] Wu PK, Ringeisen BR, Callahan J, Brooks M, Bubb DM, Wu HD, Pique A, Spargo B, McGill RA, Chrisey DB. The deposition, structure, pattern deposition, and activity of biomaterial thin-films by matrix-assisted pulsed-laser evaporation (MAPLE) and MAPLE direct write. *Thin Solid Films* 2001 NOV 1;398:607-614.

[104] Ringeisen BR, Chrisey DB, Pique A, Young HD, Modi R, Bucaro M, Jones-Meehan J, Spargo BJ. Generation of mesoscopic patterns of viable *Escherichia coli* by ambient laser transfer. *Biomaterials* 2002 JAN;23(1):161-166.

- [105] Zergioti I, Karaiskou A, Papazoglou DG, Fotakis C, Kapsetaki M, Kafetzopoulos D. Femtosecond laser microprinting of biomaterials. *Appl Phys Lett* 2005 APR 18;86(16):163902.
- [106] Banks DP, Grivas C, Mills JD, Eason RW, Zergioti I. Nanodroplets deposited in microarrays by femtosecond Ti : sapphire laser-induced forward transfer. *Appl Phys Lett* 2006 NOV 6;89(19):193107.
- [107] Duocastella M, Fernandez-Pradas JM, Dominguez J, Serra P, Morenza JL. Printing biological solutions through laser-induced forward transfer. *Applied Physics A-Materials Science & Processing* 2008 DEC;93(4):941-945.
- [108] Wu PK, Ringeisen BR, Krizman DB, Frondoza CG, Brooks M, Bubb DM, Auyeung RCY, Pique A, Spargo B, McGill RA, Chrisey DB. Laser transfer of biomaterials: Matrix-assisted pulsed laser evaporation (MAPLE) and MAPLE Direct Write. *Rev Sci Instrum* 2003 APR;74(4):2546-2557.
- [109] Dinu CZ, Dinca V, Howard J, Chrisey DB. Printing technologies for fabrication of bioactive and regular microarrays of streptavidin. *Appl Surf Sci* 2007 JUL 31;253(19):8119-8124.

[110] Dinca V, Farsari M, Kafetzopoulos D, Popescu A, Dinescu M, Fotakis C. Patterning parameters for biomolecules microarrays constructed with nanosecond and femtosecond UV lasers. *Thin Solid Films* 2008 JUL 31;516(18):6504-6511.

[111] Antonov EN, Bagratashvili VN, Whitaker MJ, Barry JJ, Shakesheff KM, Konovalov AN, Popov VK, Howdle SM. Three-Dimensional Bioactive and Biodegradable Scaffolds Fabricated by Surface-Selective Laser Sintering. *Adv Mater Deerfield* 2004 Dec 20;17(3):327-330.

[112] Kathuria YP. Microstructuring by selective laser sintering of metallic powder. *Surf Coat Technol* 1999 SEP;116:643-647.

[113] Berry E, Brown JM, Connell M, Craven CM, Efford ND, Radjenovic A, Smith MA. Preliminary experience with medical applications of rapid prototyping by selective laser sintering. *Med Eng Phys* 1997 JAN;19(1):90-96.

[114] Wendel B, Rietzel D, Kuehnlein F, Feulner R, Huelder G, Schmachtenberg E. Additive Processing of Polymers. *Macromol Mater Eng* 2008 OCT 10;293(10):799-809.

[115] Popov VK, Evseev AV, Antonov EN, Bagratashvili VN, Konovalov AN, Panchenko VY, Barry JJA, Whitaker MJ, Howdle SM. Laser technologies for fabricating individual

implants and matrices for tissue engineering. *Journal of Optical Technology* 2007

SEP;74(9):636-640.

[116] Exner H, Horn M, Streek A, Regenfuss P, Ullmann F, Ebert R. Laser micro sintering - a new method to generate metal and ceramic parts of high resolution with submicrometer powder. In: Bartolo PJ, Mateus AJ, Batista FDC, editors. *Virtual and Rapid Manufacturing - Advanced Research in Virtual and Rapid Prototyping* London, UK: Routledge; 2008. p. 491-499.

[117] Regenfuss P, Streek A, Hartwig L, Kloetzer S, Brabant T, Horn M, Ebert R, Exner H. Principles of laser micro sintering. *Rapid Prototyping Journal* 2007;13(4):204-212.

[118] Ibrahim D, Broilo TL, Heitz C, de Oliveira MG, de Oliveira HW, Wanderlei Nobre SM, Dos Santos Filho, Jose Henrique Gomes, Silva DN. Dimensional error of selective laser sintering, three-dimensional printing and PolyJet (TM) models in the reproduction of mandibular anatomy. *J Cranio-MaxilloFac Surg* 2009 APR;37(3):167-173.

[119] Kaim AH, Kirsch EC, Alder P, Bucher P, Hammer B. Preoperative Accuracy of Selective Laser Sintering (SLS) in Craniofacial 3D Modeling: Comparison with Patient CT Data. *Rofo-Fortschr Gebiet Rontgenstrahlen Bildgeb Verfahr* 2009 JUL;181(7):644-651.

[120] Asaumi J, Kawai N, Honda Y, Shigehara H, Wakasa T, Kishi K. Comparison of three-dimensional computed tomography with rapid prototype models in the management of coronoid hyperplasia. *Dentomaxillofac Radiol* 2001 NOV;30(6):330-335.

[121] Wu G, Zhou B, Bi Y, Zhao Y. Selective laser sintering technology for customized fabrication of facial prostheses. *J Prosthet Dent* 2008 JUL;100(1):56-60.

[122] Vandenbroucke B, Kruth JP. Direct Digital Manufacturing of Complex Dental Prostheses. In: Bartolo P, Bidanda B, editors. *Bio-materials and Prototyping Applications in Medicine*: Springer; 2008. p. 109-124.

[123] Vandenbroucke B, Kruth J. Selective laser melting of biocompatible metals for rapid manufacturing of medical parts. *Rapid Prototyping Journal* 2007;13(4):196-203.

[124] Bibb R, Eggbeer D, Evans P. Rapid prototyping technologies in soft tissue facial prosthetics: current state of the art. *Rapid Prototyping Journal* 2010;16(2):130-137.

[125] Lohfeld S, McHugh P, Serban D, Boyle D, O'Donnell G, Peckitt N. Engineering Assisted Surgery (TM) : A route for digital design and manufacturing of customised maxillofacial implants. *J Mater Process Technol* 2007 MAR 23;183(2-3):333-338.

[126] Partee B, Hollister SJ, Das S. Selective laser sintering process optimization for layered manufacturing of CAPA (R) 6501 polycaprolactone bone tissue engineering scaffolds. *J Manuf Sci Eng -Trans ASME* 2006 MAY;128(2):531-540.

[127] Williams JM, Adewunmi A, Schek RM, Flanagan CL, Krebsbach PH, Feinberg SE, Hollister SJ, Das S. Bone tissue engineering using polycaprolactone scaffolds fabricated via selective laser sintering. *Biomaterials* 2005 AUG;26(23):4817-4827.

[128] Kanczler JM, Mirmalek-Sani S, Hanley NA, Ivanov AL, Barry JJA, Upton C, Shakesheff KM, Howdle SM, Antonov EN, Bagratashvili VN, Popov VK, Oreffo ROC. Biocompatibility and osteogenic potential of human fetal femur-derived cells on surface selective laser sintered scaffolds. *Acta Biomater* 2009 JUL;5(6):2063-2071.

[129] Tan KH, Chua CK, Leong KF, Cheah CM, Gui WS, Tan WS, Wiria FE. Selective laser sintering of biocompatible polymers for applications in tissue engineering. *Biomed Mater Eng* 2005;15(1-2):113-124.

[130] Shishkovsky I, Yadroitsev I, Bertrand P, Smurov I. Alumina-zirconium ceramics synthesis by selective laser sintering/melting. *Appl Surf Sci* 2007 DEC 15;254(4):966-970.

[131] Gahler A, Heinrich JG, Guenster J. Direct laser sintering of Al₂O₃-SiO₂ dental ceramic components by layer-wise slurry deposition. *J Am Ceram Soc* 2006 OCT;89(10):3076-3080.

[132] Simpson RL, Wiria FE, Amis AA, Chua CK, Leong KF, Hansen UN, Chandrasekaran M, Lee MW. Development of a 95/5 poly(L-lactide-co-glycolide)/hydroxylapatite and beta-tricalcium phosphate scaffold as bone replacement material via selective laser sintering. *J Biomed Mater Res Part B* 2008 JAN;84B(1):17-25.

[133] Lorrison JC, Dalgarno KW, Wood DJ. Processing of an apatite-mullite glass-ceramic and an hydroxyapatite/phosphate glass composite by selective laser sintering. *J Mater Sci - Mater Med* 2005 AUG;16(8):775-781.

[134] Dyson JA, Genever PG, Dalgarno KW, Wood DJ. Development of custom-built bone scaffolds using mesenchymal stem cells and apatite-wollastonite glass-ceramics. *Tissue Eng* 2007 DEC;13(12):2891-2901.

[135] Salmoria GV, Klauss P, Paggi RA, Kanis LA, Lago A. Structure and mechanical properties of cellulose based scaffolds fabricated by selective laser sintering. *Polym Test* 2009 SEP;28(6):648-652.

- [136] Shishkovsky IV, Volova LT, Kuznetsov MV, Morozov YG, Parkin IP. Porous biocompatible implants and tissue scaffolds synthesized by selective laser sintering from Ti and NiTi. *Journal of Materials Chemistry* 2008;18(12):1309-1317.
- [137] Zhang Y, Hao L, Savalani MM, Harris RA, Di Silvio L, Tanner KE. In vitro biocompatibility of hydroxyapatite-reinforced polymeric composites manufactured by selective laser sintering. *Journal of Biomedical Materials Research Part a* 2009 DEC 15;91A(4):1018-1027.
- [138] von Wilmsky C, Vairaktaris E, Pohle D, Rechtenwald T, Lutz R, Muenstedt H, Koller G, Schmidt M, Neukam FW, Schlegel KA, Nkenke E. Effects of bioactive glass and beta-TCP containing three-dimensional laser sintered polyetheretherketone composites on osteoblasts in vitro. *Journal of Biomedical Materials Research Part a* 2008 DEC 15;87A(4):896-902.
- [139] Hao L, Savalani MM, Zhang Y, Tanner KE, Harris RA. Selective laser sintering of hydroxyapatite reinforced polyethylene composites for bioactive implants and tissue scaffold development. *Proceedings of the Institution of Mechanical Engineers Part H-Journal of Engineering in Medicine* 2006 MAY;220(H4):521-531.
- [140] Shabalovskaya SA. On the nature of the biocompatibility and on medical applications of NiTi shape memory and superelastic alloys. *Biomed Mater Eng* 1996;6(4):267-289.

- [141] Eliades T, Eliades G, Athanasiou AE, Bradley TG. Surface characterization of retrieved NiTi orthodontic archwires. *Eur J Orthod* 2000 JUN;22(3):317-326.
- [142] Rimell JT, Marquis PM. Selective laser sintering of ultra high molecular weight polyethylene for clinical applications. *J Biomed Mater Res* 2000 AUG;53(4):414-420.
- [143] (105) Narayan R. Two Photon Polymerization: An Emerging Method for Rapid Prototyping of Ceramic-Polymer Hybrid Materials for Medical Applications. *American Ceramic Society Bulletin* 2009 MAY;88(5):20-25.
- [144] Doraiswamy A, Jin C, Narayan RJ, Mageswaran P, Mente P, Modi R, Auyeung R, Chrisey DB, Ovsianikov A, Chichkov B. Two photon induced polymerization of organic-inorganic hybrid biomaterials for microstructured medical devices. *Acta Biomater* 2006 MAY;2(3):267-275.
- [145] Gittard SD, Ovsianikov A, Chichkov BN, Doraiswamy A, Narayan RJ. Two-photon polymerization of microneedles for transdermal drug delivery. *Expert Opin Drug Deliv* 2010 APR;7(4):513-533.
- [146] Serbin J, Egbert A, Ostendorf A, Chichkov BN, Houbertz R, Domann G, Schulz J, Cronauer C, Frohlich L, Popall M. Femtosecond laser-induced two-photon polymerization of

inorganic-organic hybrid materials for applications in photonics. *Opt Lett* 2003 MAR 1;28(5):301-303.

[147] Juodkazis S, Mizeikis V, Seet KK, Miwa M, Misawa H. Two-photon lithography of nanorods in SU-8 photoresist. *Nanotechnology* 2005 JUN;16(6):846-849.

[148] Ovsianikov A, Chichkov B, Adunka O, Pillsbury H, Doraiswamy A, Narayan RJ. Rapid prototyping of ossicular replacement prostheses. *Appl Surf Sci* 2007 MAY 30;253(15):6603-6607.

[149] Hemker KJ, Sharpe WN, Jr. Microscale characterization of mechanical properties. *Ann Rev Mater Res* 2007;37:93-126.

[150] Obata K, Koch J, Hinze U, Chichkov BN. Multi-focus two-photon polymerization technique based on individually controlled phase modulation. *Optics Express* 2010 AUG 2;18(16):17193-17200.

[151] Ovsianikov A, Chichkov B, Mente P, Monteiro-Riviere NA, Doraiswamy A, Narayan RJ. Two photon polymerization of polymer-ceramic hybrid materials for transdermal drug delivery. *Int J Appl Ceram Technol* 2007;4(1):22-29.

[152] Ovsianikov A, Ostendorf A, Chichkov BN. Three-dimensional photofabrication with femtosecond lasers for applications in photonics and biomedicine. *Appl Surf Sci* 2007 MAY 30;253(15):6599-6602.

[153] Hidai H, Jeon H, Hwang DJ, Grigoropoulos CP. Self-standing aligned fiber scaffold fabrication by two photon photopolymerization. *Biomed Microdevices* 2009 JUN;11(3):643-652.

[154] Jeon W, Kim S, Lim S, Ong JL, Oh DS. Histomorphometric evaluation of immediately loaded SSII implants of different surface treatments in a dog model. *Journal of Biomedical Materials Research Part a* 2009 AUG;90A(2):396-400.

[155] Doraiswamy A, Ovsianikov A, Gittard SD, Monteiro-Riviere NA, Crombez R, Montalvo E, Shen W, Chichkov BN, Narayan RJ. Fabrication of Microneedles Using Two Photon Polymerization For Transdermal Delivery of Nanomaterials. *J Nanosci Nanotechnol* 2010;10(10):6305-6312.

[156] Gittard SD, Ovsianikov A, Monteiro-Riviere NA, Lusk J, Morel P, Minghetti P, Lenardi C, Chichkov BN, Narayan RJ. Fabrication of Polymer Microneedles Using a Two-Photon Polymerization and Micromolding Process. *J Diabetes Sci Technol* 2009 March;3(2):304-311.

[157] Gittard SD, Narayan RJ, Jin C, Ovsianikov A, Chichkov BN, Monteiro-Riviere NA, Stafslie S, Chisholm B. Pulsed laser deposition of antimicrobial silver coating on Ormocer® microneedles. *Biofabrication* 2009;1(4):041001.

[158] Gittard SD, Ovsianikov A, Akar H, Chichkov B, Monteiro-Riviere NA, Stafslie S, Chisholm B, Shin C, Shih C, Lin S, Su Y, Narayan RJ. Two Photon Polymerization-Micromolding of Polyethylene Glycol-Gentamicin Sulfate Microneedles. *Advanced Engineering Materials* 2010;12(4):B77-B82.

[159] Claeysens F, Hasan EA, Gaidukeviciute A, Achilleos DS, Ranella A, Reinhardt C, Ovsianikov A, Xiao Shizhou, Fotakis C, Vamvakaki M, Chichkov BN, Farsari M. Three-Dimensional Biodegradable Structures Fabricated by Two-Photon Polymerization. *Langmuir* 2009 MAR 3;25(5):3219-3223.

[160] Ovsianikov A, Viertl J, Chichkov B, Oubaha M, MacCraith B, Sakellari L, Giakoumaki A, Gray D, Vamvakaki M, Farsari M, Fotakis C. Ultra-Low Shrinkage Hybrid Photosensitive Material for Two-Photon Polymerization Microfabrication. *Acs Nano* 2008 NOV;2(11):2257-2262.

[161] Ovsianikov A, Xiao Shizhou, Farsari M, Vamvakaki M, Fotakis C, Chichkov BN. Shrinkage of microstructures produced by two-photon polymerization of Zr-based hybrid photosensitive materials. *Optics Express* 2009 FEB 16;17(4):2143-2148.

- [162] Sakellari I, Gaidukeviciute A, Giakoumaki A, Gray D, Fotakis C, Farsari M, Vamvakaki M, Reinhardt C, Ovsianikov A, Chichkov BN. Two-photon polymerization of titanium-containing sol-gel composites for three-dimensional structure fabrication. *Applied Physics A-Materials Science & Processing* 2010 AUG;100(2):359-364.
- [163] Duan XM, Sun HB, Kaneko K, Kawata S. Two-photon polymerization of metal ions doped acrylate monomers and oligomers for three-dimensional structure fabrication. *Thin Solid Films* 2004 APR 1;453:518-521.
- [164] Pitts JD, Campagnola PJ, Epling GA, Goodman SL. Submicron multiphoton free-form fabrication of proteins and polymers: Studies of reaction efficiencies and applications in sustained release. *Macromolecules* 2000 MAR 7;33(5):1514-1523.
- [165] Pitts JD, Howell AR, Taboada R, Banerjee I, Wang J, Goodman SL, Campagnola PJ. New photoactivators for multiphoton excited three-dimensional submicron cross-linking of proteins: Bovine serum albumin and type 1 collagen. *Photochem Photobiol* 2002 AUG;76(2):135-144.
- [166] Ovsianikov A, Schlie S, Ngezahayo A, Haverich A, Chichkov BN. Two-photon polymerization technique for microfabrication of CAD-designed 3D scaffolds from

commercially available photosensitive materials. *Journal of Tissue Engineering and Regenerative Medicine* 2007 NOV-DEC;1(6):443-449.

[167] Ovsianikov A, Gruene M, Pflaum M, Koch L, Maiorana F, Wilhelmi M, Haverich A, Chichkov B. Laser printing of cells into 3D scaffolds. *Biofabrication* 2010 MAR;2(1):014104.

[168] Koroleva A, Schlie S, Fadeeva E, Gittard SD, Miller P, Ovsianikov A, Koch J, Narayan RJ. Microreplication of laser-fabricated surface and three-dimensional structures. *J Optics* 2010;12(12):124009.

[169] Gittard SD, Chen B, Xu H, Ovsianikov A, Chichkov BN, Monteiro-Riviere NA, Narayan RJ. The effects of geometry on skin penetration and failure mechanics of polymer microneedles. *Biomed Mater* 2011:under review.

[170] Narayan RJ, Jin CM, Doraiswamy A, Mihailescu IN, Jelinek M, Ovsianikov A, Chichkov B, Chrisey DB. Laser processing of advanced bioceramics. *Adv Eng Mater* 2005 DEC;7(12):1083-1098.

[171] Tayalia P, Mendonca CR, Baldacchini T, Mooney DJ, Mazur E. 3D Cell-Migration Studies using Two-Photon Engineered Polymer Scaffolds. *Adv Mater* 2008 DEC 2;20(23):4494-4498.

[172] Schlie S, Ngezahayo A, Ovsianikov A, Fabian T, Kolb H, Haferkamp H, Chichkov BN. Three-dimensional cell growth on structures fabricated from ORMOCER (R) by two-photon polymerization technique. *J Biomater Appl* 2007 NOV;22(3):275-287.

2.2 Microneedle-mediated Drug Delivery

*The following section is a complete chapter from the book: **Toxicology of the Skin**, edited by Dr. Nancy A. Monteiro Riviere © Informa Healthcare, 2010.*

*Source: Gittard SD and Narayan RJ. Chapter 20: Applications of Microneedle Technology to Transdermal Drug Delivery. In: **Toxicology of the Skin** Ed. Nancy A. Monteiro-Riviere. Informa Healthcare 2010; 301-316.*

Note: This article has been partially reformatted. In particular, the location of figures and spacing may have changed. The references are formatted as in the original manuscript.

2.2.1 Applications of Microneedle Technology to Transdermal Drug Delivery

Shaun D. Gittard and Roger J. Narayan

Department of Biomedical Engineering, North Carolina State University, Raleigh, North Carolina, U.S.A.

Introduction

Microneedles have recently entered the medical field as a promising innovation to drug delivery. These are small projections, less than a millimeter in length, that penetrate the stratum corneum and epidermis. By penetrating these skin layers they produce a conduit for drugs to bypass the defense mechanisms of the skin. This new technology has the capability

to both enhance the performance of transdermal patches and provide an alternative transdermal delivery method.

Presently, the oral route is the most common method of drug delivery. Oral administration is appealing for several reasons. The first reason is that it is easy for most patients to swallow pills, and second, there is virtually no risk of injury with oral delivery. Thus, most patients are capable of administering the drugs themselves without the presence of a medical professional. While oral delivery is convenient for patients and physicians, this method can be a challenge for the pharmaceutical field. The journey from the mouth to the bloodstream is a long and damaging route for drugs. Medications entering the body through this route are exposed to a variety of extreme environments meant to break down a wide array of nutrients into more useable forms. As a result of exposure to strong acids and enzymes in the digestive tract, the efficacy of many drugs is greatly reduced by the time they are absorbed into the bloodstream (1). Consequently, many drugs are either unable to enter the bloodstream or require significantly larger dosages when delivered via the oral route (2). Because of the difficulty in administering some drugs by this method, alternative means that are comparatively user-friendly and of low risk are being sought.

One of the most promising alternative methods of delivering medication is transdermal drug delivery, which is drug delivery through the skin. Transdermal drug delivery is appealing for a number of reasons. The skin is the largest organ of the body, which provides a substantial area in which drugs can be applied (2). In comparison, there are significantly fewer locations

that are compatible with intravenous injection. Transdermal drug delivery is virtually painless. Therefore, patient compliance is less of a concern, which is a problem with painful drug delivery techniques such as injections (1). While transdermal drug delivery is an appealing method for administering medication, there are also challenges associated with this technique. The most notable challenge to transdermal drug delivery is the diffusion properties of the stratum corneum.

The stratum corneum is the outermost layer of the skin. It is primarily composed of corneocytes held together by a lipid matrix. The thickness of the stratum corneum is 10 to 40 μm (3). This layer of lipids and dead cells greatly limits the diffusion of molecules through skin. The ability of the stratum corneum to prevent diffusion serves a number of purposes. It functions as a vital component of the immune system by preventing foreign objects from entering the body. Additionally the stratum corneum stops evaporative water loss, thus preventing dehydration (4). The stratum corneum is particularly effective at preventing the diffusion of molecules that are large (>500 Da), charged, or polar (5–7). Thus, only a handful of molecules are capable of entering the bloodstream by diffusion through the skin.

While the stratum corneum presents a great challenge to transdermal drug delivery, it also provides benefits. Since the stratum corneum is such an effective defense mechanism, upon crossing this layer, entry to the bloodstream is unimpeded. In comparison, during oral consumption, drugs are broken down by firstpass liver effects and gastrointestinal

metabolism, which reduce drug efficacy (5). Also, processing of orally delivered drugs can cause liver damage (5).

Microneedles provide a straightforward and effective means of enhancing diffusivity through the stratum corneum. When pressed against the skin, these projections pierce the stratum corneum and part of the epidermis, producing small holes in the diffusion barrier. These holes provide a passageway for drugs to travel through the stratum corneum and viable epidermis to reach the papillary dermis to the bloodstream. Microneedles should penetrate the stratum corneum and the epidermis, but they should not reach the dermis where nerve endings are located since interaction with these nerves may cause pain (1). The thickness of the stratum corneum and epidermis varies from 31 to 637 μm , depending on location (8).

Microneedles function similar to traditional hypodermic needles by physically creating a more direct conduit to the bloodstream. However, hypodermic needles are significantly larger and penetrate much deeper into the skin than microneedles. The invasiveness of this method of drug delivery results in trauma at the injection site (9). Consequently, repeated dosing requires injection at multiple sites. Additionally, there is often pain associated with drug delivery via hypodermic needles due to interaction with nerve endings in the skin and muscles (1). For patients requiring regular injections, such as diabetics, hypodermic needles can be a serious burden. In comparison, microneedles are virtually painless since they do not interact with sensory nerves. Also, trauma is less of a concern with microneedles since the stratum corneum is composed of dead cells. In vivo studies on human subjects have reported

occasional pressure sensations and relatively little pain associated with the application of microneedles to the skin (10–12). A study comparing microneedles of varying dimensions with hypodermic needles found that the pain associated with microneedles was 60% to 95% less than for hypodermic needles (13).

The two prevailing challenges with microneedles are stratum corneum penetration and mechanical failure of the microneedles. The force required for microneedle array penetration of the stratum corneum has been reported to be as high as 3.04 N (14). This penetration force varies greatly and can be reduced by optimizing microneedle geometry. Individual microneedles have been shown to fracture under less than 0.1 N of compressive force (15). Use of appropriate materials and geometries can help to increase the failure threshold.

Because of the viscoelastic properties of skin, it deforms upon application of compressive forces. Deformation is problematic for microneedle penetration since the needle simply bends the skin instead of piercing it. Upon a certain degree of deformation, the pressure of the needle tip on the skin is sufficient to result in penetration. Human skin has been reported to displace up to approximately 2 mm before microneedle penetration (16). In Figure 1, the skin deformation upon microneedle insertion can clearly be seen.

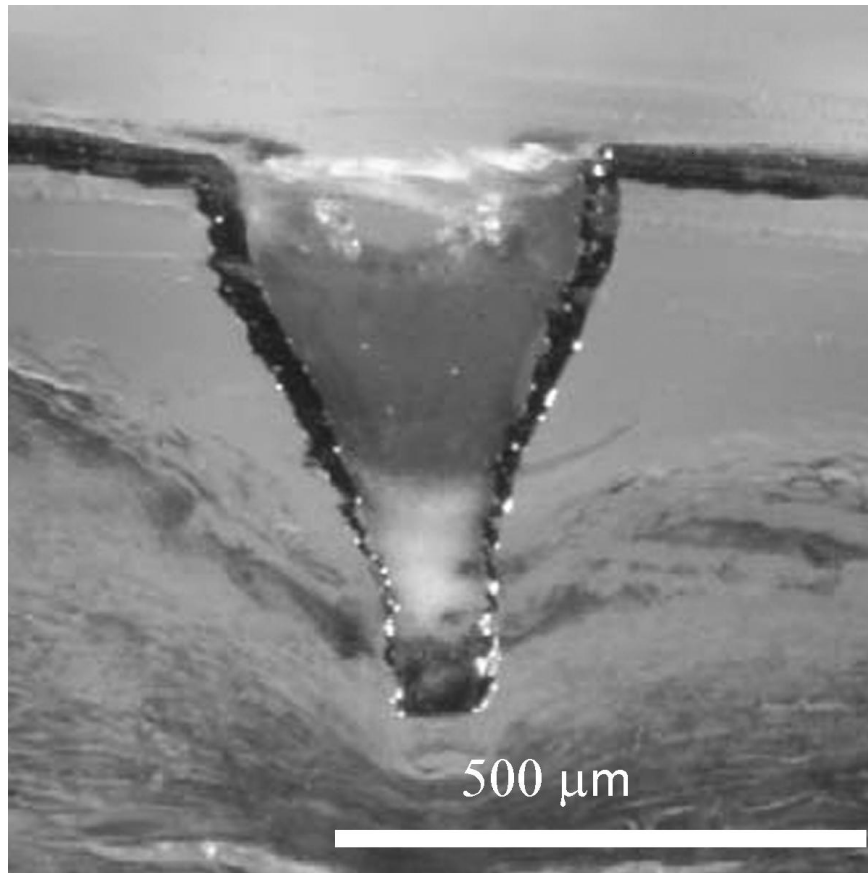


FIGURE 1. Deformation of the skin upon microneedle insertion.

Reprinted from *Journal of Biomechanics*, Vol. 37, Davis *et al*, Insertion of microneedles into skin: measurement and prediction of insertion force and needle fracture force, 1155-1163, Copyright 2004, with permission from Elsevier.

Aspects of Microneedle Design

Microneedles come in a variety of orientations, shapes, and sizes. Differing purposes and limitations in fabrication techniques are causes of the variations in the microneedle geometries. Microneedles for drug delivery need to penetrate through the stratum corneum

and into the epidermis. Thus, they should have greater than 20 μm of penetration to effectively deliver drugs (17). In comparison, needles for sampling interstitial fluid or blood should be longer (up to 1 mm) since they need to penetrate deeper into the epidermis where more capillaries are present (17).

As previously mentioned, skin deforms upon pressure on its surface. Therefore, microneedles should be longer than the desired penetration depth. A study by Teo et al. exhibits this principle. Hollow microneedles that were 150 μm in length were pressed against the skin of diabetic rats and insulin was injected through them. Upon injection, no change in blood glucose levels were observed, indicating that the needles did not penetrate the stratum corneum and thus insulin was not able to diffuse through the skin barrier (18).

In addition to length, the pitch angle of the tip is an important factor affecting microneedle piercing. Penetration of the stratum corneum with microneedles occurs by pressure forcing the microneedle tip through the extracellular matrix. Therefore, microneedles with smaller cross-sectional areas, which are achieved by having sharper tips, require lower forces to penetrate the stratum corneum. Penetration tests into skin found that penetration force increases approximately linearly with cross-sectional area (14). In agreement with this relationship between cross-sectional area and penetration force, minimizing the tip size also decreases penetration force and skin displacement.

Verbaan et al. performed an interesting investigation of another factor of microneedle penetration. This study examined the effect of insertion velocity on microneedle penetration (19). An applicator that regulated microneedle velocity was used to impact the skin with microneedles at 1 m/sec and 3 m/sec. Manually pressing the microneedle arrays against the skin was also tested. Diffusion of Cascade Blue dye was found to increase with increasing impact velocity, indicating that higher velocity microneedles have better penetration. Also, microneedles that were manually applied to the skin, but were too short to penetrate the stratum corneum, were able to penetrate at the elevated velocities (19,20).

As described in the preceding paragraphs, microneedle penetration is improved by maximizing the stresses at the point of contact between the microneedles and skin. However, increasing penetration by this technique results in elevated stress on microneedles, which increases the likelihood of microneedle fracture. Therefore, it is important that an appropriate balance is maintained between microneedle penetration and mechanical strength. Microneedles can be oriented in two directions: either in-plane, meaning they are in the same plane as the substrate, or out-of-plane, meaning that they project perpendicular to the substrate. Since in-plane microneedles are on the same plane as the substrate, they can only be fabricated into single rows. Out-of-plane microneedles can be fabricated into arrays, which increase the number of microneedles that can be made at once. Arrays of in-plane microneedles can be created by stacking rows on top of each other (21). However, this process is generally more labor intensive and time-consuming than fabricating out-of-plane microneedles.

Since in-plane microneedles are generally machined from flat pieces of material, they usually have a rectangular cross-sectional shape. A sample of a row of in-plane microneedles can be seen in Figure 2D. Although microneedles vary greatly in their size and shape, there are three general shapes that most out-of-plane microneedles fall into: conical, pyramidal, and sawtooth. Conical microneedles have a circular base with the centers of the circular cross-sections vertically aligned. Pyramidal microneedles have polygonal cross sections with their centers vertically aligned. Sawtooth microneedles also have either a square or triangular cross section. However, the centers of these cross sections are not vertically aligned. Instead at least one of the edges of the cross section is vertical and the microneedle tapers to a point at this edge. Examples of microneedles with these three different shapes can be seen in Figure 2A-C. These variations in the microneedle shape are artifacts of the method used to fabricate them, which is described later in this chapter.

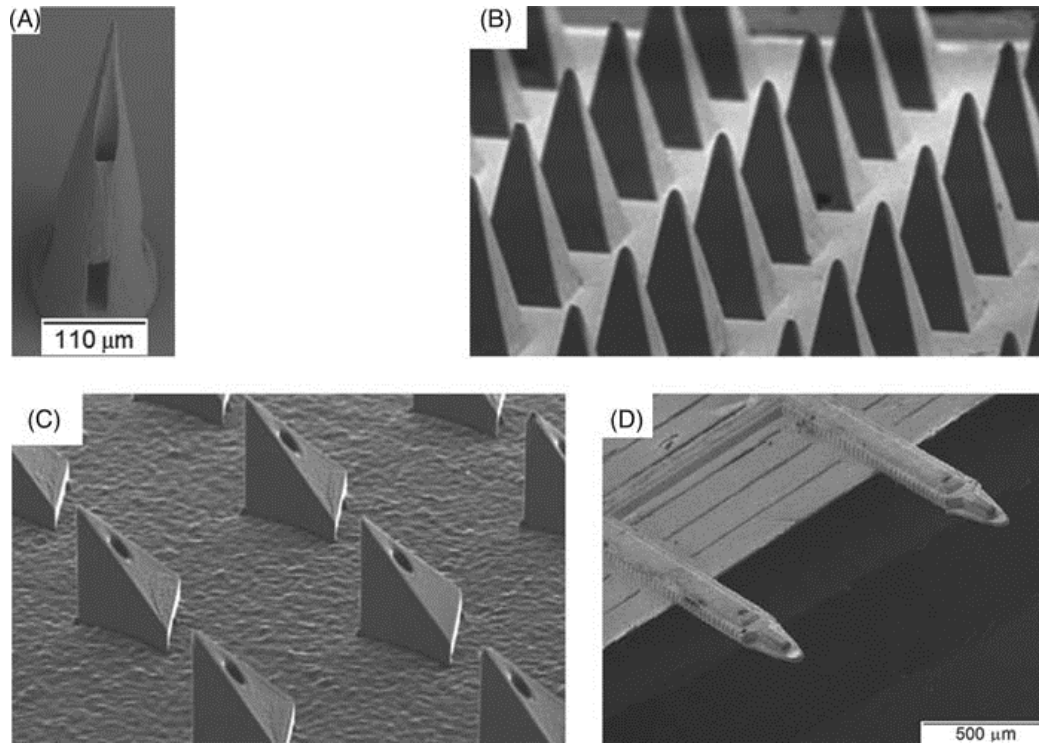


FIGURE 2 Microneedle design types: (A) out-of-plane conical*; (B) out-of-plane pyramid**; (C) out-of-plane sawtooth hollow***; and (D) in-plane shaped microneedles****.

*Reprinted from International Journal of Applied Ceramic Technology, Vol. 4, Ovsianikov *et al*, Two Photon Polymerization of Polymer–Ceramic Hybrid Materials for Transdermal Drug Delivery, 22-29,

Copyright 2007 John Wiley & Sons Inc.

**Reprinted from Biomaterials, Vol. 29, Lee *et al*, Dissolving microneedles for transdermal drug delivery, 2113-2124, Copyright 2008, with permission from Elsevier.

***Reprinted from Journal of Micromechanics and Microengineering, Vol. 16, Perennes *et al*, Sharp beveled tip hollow microneedle arrays fabricated by LIGA and 3D soft lithography with polyvinyl alcohol, 473-479, Copyright 2006 Institute of Physics Publishing. doi: [10.1088/0960-](https://doi.org/10.1088/0960-1317/16/3/001)

[1317/16/3/001](https://doi.org/10.1088/0960-1317/16/3/001)

****Reprinted from Journal of Microelectromechanical Systems, Vol. 12, Chandrasekaran *et al*, Surface micromachined metallic microneedles, 281-288, Copyright [2003] IEEE.

As previously described, microneedles can deliver drugs by two different methods: either by improving diffusion through the stratum corneum or by serving as a direct conduit through the stratum corneum. To discuss the microneedles corresponding to these different functions, we have separated microneedles into two classes: solid and hollow.

The function of solid microneedles is to make microscale holes in the stratum corneum that improve diffusion. These microneedles are simply solid projections that taper to a sharp point. Solid microneedles have been created over a wide range of geometries. An innovative addition to solid microneedles is the incorporation of pockets along the shaft of the microneedle. Gill et al. fabricated microneedles with pockets of various shapes in their shaft in which drugs were deposited (26). By depositing drugs in these pockets, the depth in the skin at which the drug is administered can be controlled (26).

Hollow microneedles serve a slightly different purpose than solid microneedles. While solid microneedles simply create holes to aid diffusion through the stratum corneum, in hollow microneedles the bore of the microneedle serves as a conduit to deliver a liquid formulation of drugs. Essentially, hollow microneedles are hypodermic needles but on a much smaller scale. The geometry of hollow microneedles is the same as solid microneedles with the exception of a channel along the vertical axis. This channel can either deliver drug solutions or take blood samples by providing a route of transport between the body and a reservoir on the microneedle apparatus.

Channel width and orientation are two factors that have an effect on hollow microneedle function. Wider channels allow fluid flow to occur at lower pressures. However, as channel width increases, either wall thickness decreases or cross-sectional area increases. Consequently, there is a trade-off between flow rate and mechanical strength as well as flow rate and penetration force in hollow microneedles.

Orientation of the channel has an effect on the force required for microneedles to penetrate the skin. If the channel is along the center of the vertical axis, then the minimum cross-sectional area of the microneedle is controlled by the channel width, which is always greater than if the microneedle had no channel. Therefore, the penetration force for a hollow needle with a centered channel is higher than for a solid needle of the same geometry. If the channel is offset from the center of the microneedle, the microneedle still tapers to a sharp point and a smaller cross-sectional area is achieved. Additionally, the channel can be shifted so that it intersects with the edge of the microneedle. In this case, the opening of the channel is not at the tip but instead along the side of the microneedle. This produces a groove, which runs along one of the edges of the microneedle (27).

In addition to the standard solid and hollow microneedle structures, microneedles with more complex architectures have been fabricated. One result of the ability to make more complex architectures has been the development of biomimetic microneedles. In particular, several groups have created microneedles that mimic the structure of the mosquito fascicle (28–30). One component of mosquito needles that has been replicated is the maxillae. The mosquito

fascicle is composed of two serrated maxillae that cut open the skin prior to insertion of the feeding tube (31). Finite element modeling determined that stress concentrations are increased in microneedles with this serrated shape (29). Higher stress concentrations reduce the force required for needle penetration into the skin. Observations of mosquitoes during feeding revealed that they vibrate their fascicles during insertion. Experiments have shown that vibrating microneedles during insertion reduces the penetration force (16,29). Skin deformation was also decreased by microneedle vibration (16).

Microneedle Materials

As previously explained, the material used to make microneedles has a significant impact on mechanical stability and preventing failure by fracture. A multitude of materials have been used to create microneedles. To discuss these materials, we have divided them into four classifications: ceramics, metals, polymers, and digestible organic molecules.

Many of the fabrication methods used to create microneedles are microfabrication techniques derived from the electronics industry. Because of the familiarity with its behavior in these fabrication methods, silicon is one of the most common materials used to make microneedles (4,6,7,13,18,32–34). Its biocompatibility and ease to work with makes silicon one of the preferred materials for microneedles. For more than 50 years, microneedles have been made from glass (35). Fabrication of glass microneedles is time-consuming since it is performed by hand (27). Because of the inefficiency of this technique, glass microneedles are still used

today, but only for experimental purposes and are not feasible for commercial use in drug delivery (36).

With regards to mechanical properties, ceramics such as silicon and glass are not preferential materials for microneedles. While the Young's modulus of these materials is higher than that of other materials used for microneedle fabrication, these materials are extremely brittle. Since ceramics do not have plastic deformation, they undergo catastrophic failure in the form of fracture or buckling when excessive forces are applied. Therefore, if sufficient forces are applied to ceramic microneedles, they will break in the stratum corneum. Also, stiffness does not directly correlate to the threshold failure force. Many metals and polymers actually have higher ultimate strengths (the materials science term for the stress where failure occurs) than ceramics. The mechanical properties of silicon, glass, and various other materials are discussed in the following paragraphs and in Table 1.

TABLE 1 Strengths of Materials Used To Make Microneedles

Material	Young's modulus	Ultimate tensile strength
Silicon	110 GPa (37)	7000 MPa (38)
Glass	85 GPa (39)	50 MPa (38)
Nickel	214 GPa (37)	586 MPa (40)
Palladium	117 GPa (37)	186 MPa (40)
Platinum	147 GPa (37)	117 MPa (40)
Titanium	110 GPa (37)	241 MPa (41)
Stainless Steel	200 GPa (37)	1000 MPa (37)
Ormocer [®]	17 GPa (42)	30 MPa (42)
PMMA	3 GPa (37)	170 MPa (37)
Maltose	31.1 GPa (43)	—
SU-8	3 GPa (44)	—

While metals generally have a lower elastic modulus than ceramics, their method of failure is better suited for microneedles. Metals are ductile, meaning that they bend when excessive force is applied to them. As a result, metal microneedles will simply bend rather than break if excessive forces are applied to them.

A wide range of metals has been used to make microneedles. Nickel (25,45,46), palladium (25,47), and platinum (48,49) have been used to make microneedles by electroplating. Titanium and stainless steel microneedles have been made by direct micromachining techniques (20,50–52). Titanium, platinum, and stainless steel are biocompatible and are regularly used for medical applications such as limb replacements, dental implants, and electrodes. On the other hand, caution should be used when employing nickel as a material

for fabricating microneedles. Nickel is carcinogenic and adverse allergic reactions have been problematic in the past with nickel biomaterials (53).

Polymers are long chains of molecules covalently bound together. The majority of polymers are organic molecules (plastics), with one notable exception being polydimethylsiloxane (PDMS). This material is commonly used for making negative molds for microneedle fabrication due to its low friction coefficient. Polymers are created by initiating the formation of covalent bonds between the precursor molecules, known as monomers. This polymerization process can be caused by a variety of methods, the most common being heat (thermoplastics), light (photosensitive polymers), and the addition of a catalyst (epoxies). In general, polymers have low melting points. Also, many of the monomers are available in liquid form and solidify when polymerization occurs. These two properties make polymers well suited for micromolding.

A multitude of polymers have been cast to make microneedles such as poly(methylmethacrylate) (PMMA) (24,54), poly(vinylpyrrolidone) (PVP) (55), copolymers of PVP and PMMA (55), polycarbonate (21), SU-8 photoresist (56), and aliphatic polyesters (27,28,57,58). All of these polymers are extremely biocompatible and are widely used in medical applications. PMMA is used as a bone cement and PVP is used as a component of many pharmaceuticals. In addition to being biocompatible, the aliphatic polyesters are biodegradable. This property makes them an appealing material to use for microneedles since they will degrade after piercing the skin (58). There are several benefits to having degrading

microneedles. Since the needles degrade during their application, there is a reduced risk of disease transfer via accidental puncture after treatment. Also, after the microneedles have degraded there is a larger space for drugs to pass through, which increases the efficiency of drug delivery. Lastly, drugs can be suspended in the microneedles and released as the needles degrade. The most commonly used aliphatic polyesters in microneedles are poly(glycolic acid) (PGA), poly(lactic acid) (PLA), and poly(lactic-co-glycolic acid) (PLGA) that is a mixture of the previous two polyesters. The degradation rates of these polyesters can be controlled by varying the ratio of PGA to PLA in the PLGA copolymer.

Ormocer[®]s are another promising class of polymers for microneedle manufacturing. They are amorphous organic-inorganic hybrid polymers, meaning that they are composed of organic polymers and inorganic ceramic precursors that are joined by covalent bonds. The chemical bonding of different material types allows Ormocer[®]s to have a mixture of their physical properties. For example, the Young's modulus and hardness values of Ormocer[®]s fall between the typical values of ceramics and organic polymers (59). Many Ormocer[®]s contain photoinitiators that allow them to be cured by light exposure. As photosensitive polymers, Ormocer[®]s are compatible with the extremely flexible two-photon polymerization fabrication process and have been used to make microneedles with complex geometries and high precision (22,30,42). Biocompatibility tests have shown that Ormocer[®]s are safe for use as medical materials (22,42,60). In fact, biocompatibility tests by Ovsianikov et al. have shown that Ormocer[®] materials do not adversely affect growth of human epidermal keratinocytes, a major cellular component of skin (22).

As an alternative to using biodegradable materials, some researchers have created microneedles out of digestible naturally occurring organic molecules. Maltose (61,62), carboxymethylcellulose (CMC) (23), and amylopectin (23) are biological materials that have been used to make microneedles by micromolding. All three of these materials are easily broken down by the body within minutes of piercing the skin (23,61,62). However, microneedles made of these materials should not be used for delivering insulin since these materials can be converted into glucose when digested.

Fabrication of Microneedles

A variety of techniques can be used for producing microneedles. Because of the small size of microneedles, the fabrication techniques must have microscale precision. A variety of fabrication techniques ranging from micromolding to laser processing to photolithography have been utilized to create microneedles. In this section, these different fabrication techniques are described.

Glass microneedles with extremely sharp tip diameters have been made by hand for more than 50 years (35). These microneedles are made by heating glass rods and manually stretching them to have tapered tips. After stretching the rods, they are placed in a chemical etchant, such as hydrogen fluoride, to refine the tips to a sharp point (35). This process is low

throughput and not viable for producing commercial drug delivery devices. However, manually making glass microneedles is still used today for conducting research (36).

A rather simple but direct way to make microneedles is to modify traditional hypodermic needles so that they are on the same size scale as microneedles (19,20). In this technique holes are drilled through a base substrate and hypodermic needles are inserted through these holes. The through holes in the substrate are of a size that allows just the tips to stick out the backside of the substrate to a desired length. This technique has been used to make microneedles in array of lengths varying from 300 to 900 μm (19,20). There are several drawbacks to this fabrication technique. These microneedles are simply the tips of hypodermic needles, so the only parameter that can be varied is the total length. Since hypodermic needles are designed with a different purpose than microneedles, their geometry and precision of geometry is not ideal for microneedles.

Direct cutting by high-powered lasers is another straightforward technique that has been used to make microneedles. Infrared lasers have been used to cut in-plane microneedles out of thin sheets of stainless steel (26,52). These needles can then be made into an out-of-plane array by bending them at their base. One drawback of this method is that the geometry of the needle can only be controlled in two dimensions. The third dimension is restricted to the thickness of the sheet that is being cut.

The most common technique to fabricate microneedles is photolithography. This technique was established by the semiconductor industry and is already well established in the microfabrication field. The unifying theme of photolithography is that a pattern is made into a mask on the surface of the material of interest. This mask protects the parts under it from whatever process is being performed from above. Photolithography can be broken into two types: etching, where the unprotected areas are removed, and inverse lithography, where the structure is in the unprotected areas. Several etching technologies exist including wet etching, dry etching, and deep X-ray lithography (DXRL).

Wet etching is a photolithographic microfabrication process where the surface of a structure is etched away by a solution of chemicals. In this process, a substrate is placed in a bath of a solution, called an etchant, which etches away exposed surfaces of the substrate. Wet etching is isotropic, meaning that the location of etching cannot be controlled. Masks that are resistant to etching can be patterned on the surface of the substrate to control the geometry of the structure that results from the etching process. Since the process is isotropic, etching will occur under the edges of the mask, but this takes longer to occur than at the uncovered sections. This delay in etching under the mask creates a tapered shape. The chemical etching behavior of various materials is well understood and software packages are available to model the etching of regularly used materials such as silicon (33,34,46). This process has been used to make out-of-plane solid microneedles in various geometries from silicon (33,34,46,50). It is not possible to make microneedles with channels by wet etching because

of the tapered etching direction. At the time of publication, microneedle fabrication by wet etching had only been performed with silicon wafers and KOH.

In dry etching, the substrate material is removed by ions in a gas instead of a liquid etchant. As in wet etching, masks on the surface of the substrate provide protection that prevents the areas underneath from etching. These ions usually travel in a unidirectional path, so unlike its wet counterpart, dry etching has almost no tapering. However, this process is not limited to vertical in-plane etching. By etching at an angle, etching can occur under the masks. Etching at multiple angles allows structures to be formed with tapered points. The angle of etching corresponds to the tip angle of the microneedle. Reactive ion etching (RIE) is a dry etching process where reactive ions in plasma remove material from the surface. Deep reactive ion etching (DRIE) is a type of RIE that is capable of nearly vertical etching and achieving much deeper etching depths. Thus, DRIE is well suited for making microneedles. Sulfur hexafluoride is one of the most commonly used gases in DRIE (17,63). A combination of isotropic wet etching and anisotropic dry etching can be used to make structures with both vertical and tapered parts (4,13,64). The equipment for DRIE is costly, so this process is not well suited for commercial production. It is suitable for making master structures that will serve as molds.

In DXRL, the mask is made of a material that prevents penetration of X rays such as gold. The sample is then exposed to X-rays, which remove material not protected by the mask (65). The X-ray beam etches anisotropically, so only straight lines are cut. As in dry etching,

etching at different angles can be used to remove substrate material underneath the mask. Performing X-ray exposure at multiple angles allows structures to be formed with tapered points. Inclined DXRL has been used to create sawtooth-shaped hollow needles (24,54,65). An example of a needle created by DXRL can be seen in Figure 2C. Since DXRL requires use of an X-ray synchrotron, it is an expensive fabrication process. Therefore, this technique is only viable for making a master structure, which is then replicated by less expensive methods.

In inverse lithography, the substrate is a photosensitive material that gets polymerized where it is exposed to light. The parts that are protected from the light exposure remain unpolymerized and are removed with a developing solution. Microneedles have been created out of SU-8 photoresist by utilizing inverse lithography (15,56). One drawback of inverse lithography is that it is difficult to create microneedles with sharp tip angles (56). Park et al. developed an interesting solution to improve the tip angle. Wet etching was used to create microscale lenses out of a glass substrate. When light passes through these lenses it is focused into a conical region, which is where polymerization of the SU-8 occurs (15).

Electroplating is an inexpensive and high-throughput micromachining technique. It is one of the components of LIGA, a microfabrication process involving lithography, electroplating, and molding that is used to make high aspect ratio microstructures. Photolithography, most commonly performed using either X-rays or UV light, is first used to make a master

structure. Electroplating is then performed to make a metal mold. This metal mold is then used to create microstructures of interest. This technique has also been used to make microneedles with DXRL (24). In electroplating, an electrical current is used to produce a metal coating on a surface. The surface to be coated and a second surface are submerged into a liquid solution of electrolytes. The two surfaces are then connected to a DC power source with the surface to be coated as the cathode and the other surface as the anode. Oxidizing of the anode and reduction of the cathode by the power supply causes the negative electrolytes to deposit on the anode and the positive (metal) ions to deposit on the target surface. Nickel, platinum, and copper are metals that have commonly been used in electroplating. Three different electroplating techniques have been used to make microneedles. One approach is to electroplate a wire and then chemically remove the wire (48,49). However, these microneedles have large tip diameters and shallow tip angles, which make them have poor penetration properties. The second approach is to electroplate a master microneedle array that has been made by some other method (25,45–47,57). This method allows the design aspects of the needle to be regulated by a more tightly controlled but lower-throughput method such as lithography. In the third approach, a polymer inverse mold is created by machining with an excimer laser, and this mold is electroplated (14,66). One drawback of electroplating is that the needles can be mechanically weak since they are shells and not solid throughout their interior architecture.

Two-photon polymerization is an extremely flexible direct writing process for making microneedles. In two-photon polymerization, a femtosecond laser is focused onto a liquid

photosensitive resin. At threshold intensity, temporal and spatial overlap of the photons in the laser beam breaks bonds in photoinitiator molecules causing the generation of radicals (67). These radicals then cause polymerization of the resin at the localized volume where the laser intensity was high enough to create radicals. The size of the polymerized volume can be controlled varying the beam size, beam energy, and write speed (22). Passing the laser through an optical microscope objective changes the beam size. By using high magnification objectives (100x), this fabrication process is capable of smaller than 100 nm precision. Passing the laser through an objective also makes the beam intensity depth-dependent. By making the intensity depth-dependent, it is possible to control polymerization location in three dimensions (68). After structuring, the remaining unpolymerized material is removed by submerging the structure in a developing solution. With the ability to completely control the point of polymerization, structures can be directly written by adjusting the location of the laser focus. Two-photon polymerization is capable of fabricating structures with any polymer that can be polymerized by a photoinitiator. However, since the laser must penetrate into the polymer, the materials must be transparent at the wavelength of the laser. Because of the flexibility of this technique, two-photon polymerization is capable of making microneedles with complex geometries (22,42). In addition to being able to control the design parameters such as base shape, tip angle, and channel location, this technique has been used to fabricate microneedles that mimic the geometry of mosquito fascicles (30). While all of these microneedles have been fabricated out of Ormocer[®] materials, other photosensitive polymers can be used. An example of a microneedle fabricated by two-photon polymerization can be seen in Figure 2A.

Many of the microneedle fabrication methods are expensive and not viable for commercial production. However, these costly methods can be used to make master structures that are replicated by faster and less expensive methods, such as electroplating. Micromolding is another inexpensive and rapid method for generating microneedle replicas. In micromolding, a negative mold of the microneedle is made by pouring a polymer such as poly(vinyl alcohol) (PVA) (24,54) and PDMS (27,57) and initiating polymerization of the mold. Also molds of silicon and polyethylene terephthalate have been directly made by machining with lasers (14,69). PVA is used as a sacrificial mold, meaning that the mold is destroyed when removing the structure. Since the mold is destroyed during replication, PVA molding is more costly and time-consuming than PDMS molding where the mold can be reused. Molding with PVA does have its benefits.

PVA is stiffer and stronger than PDMS, which allows it to be used for molding structures that would be too fragile for PDMS such as narrow channels (24,54). One challenge with molding is ensuring that the material used to create the structure completely fills the mold. To ensure that the mold is completely filled and no air voids are present, molding is performed under vacuum (27,29,57). Materials must be in a liquid state when molding occurs. This can be achieved either by melting a solid prior to molding or using an unpolymerized liquid and inducing polymerization once molding has occurred. The high precision, low cost, and high throughput of micromolding makes it a promising technique for commercial production.

Methods of Drug Delivery with Microneedles

There are several methods that can be used to deliver drugs with microneedles. These methods are coating, doping, and injection. In microneedle coating, a drug is applied to the surface of a part of the microneedle array. This coating can be applied in a variety of locations. One technique to coat the microneedles with drugs is to dip the microneedles into a drug solution. By controlling the depth of array submersion into the drug solution the degree of coating can be controlled so that only the tip, the entire needle, or the whole array is coated. Gill and Prausnitz tested the ability of coated microneedles to deliver a wide array of pharmacological agents including calcein, vitamin B, bovine serum albumin, plasmid DNA, and barium sulfate (52). Their study found that these coatings had dissolved into the surrounding tissue within seconds of application (52).

As an alternative to coating microneedles, if the microneedles are made by a molding technique, it is possible to suspend the drug in the microneedle itself. This technique, known as doping, is particularly useful when the drug is suspended in a microneedle made of biodegradable materials. When the microneedle degrades, the suspended drug is released. Microneedles made from maltose (61), CMC (23), amylopectin (23), and aliphatic polyesters (58) have been doped with drugs. Drugs that have been delivered by doping include calcein (58), bovine serum albumin (58), sulforhodamine (55), b-galactosidase (55), and ascorbate-2-glycoside (61). Drug release rate can be regulated by encapsulating the drugs in needles with

different degradation rates (58). Limitations of doping needles are that increasing drug concentration reduces mechanical strength, so there is a limit to the amount of drug that can be present. Thus, only drugs that are effective in low doses are applicable for this delivery technique.

The development of microfluidics technology has allowed hollow microneedles to be used for direct injection of drug solutions. A multitude of techniques exist for controlling the flow rate and volume dispensed via a microfluidics system (7,49,70). Incorporating these microfluidic systems with hollow microneedles has been used to transdermally deliver drug solutions by injection (7,49,70). Since the focus of this chapter is microneedles and not microfluidics, we will discuss the effects of microneedles on fluid injection into the epidermis and not the details of microfluidic dispensing systems. Delivery of insulin by microneedle injection was shown to decrease blood glucose levels by more than 60% (36). One reported difficulty with hollow microneedle injection is poor flow rates (36). When microneedles penetrate the stratum corneum, the skin gets compressed and may clog the channel. Having obstructed channels and densely packed cells surrounding the microneedles greatly reduces the diffusion rate into the surrounding tissue. Two techniques have been developed to alleviate these problems. By partially retracting the microneedle prior to delivery, the cells are less tightly compacted. Wang et al. found that by retracting microneedles 200 nm prior to insulin injection, blood glucose levels were more than 40% lower than when insulin was injected without retraction (36). Vibration of the microneedle, which was also shown to decrease insertion force, has also been shown to improve drug

delivery from hollow microneedles (36). There are several advantages to delivery of drugs via injection with microneedles. By using microfluidic devices the amount of drug delivered can be precisely regulated.

Sampling is a second function for hollow microneedles that are incorporated with microfluidics devices. By decreasing instead of increasing the pressure, hollow microneedles can be used to sample blood. Kobayashi et al. used a sampling microneedle/microfluidic system to determine blood glucose levels (7,48). The dual function of blood sampling and drug delivery shows promise for complex microneedle devices that can monitor and maintain blood glucose levels in real time.

Conclusion

Within the past 10 years, the technology of microneedles has undergone vast improvements. Presently, several techniques exist to fabricate high-precision microneedles that effectively penetrate the stratum corneum and improve diffusion rates through the skin. High-throughput and low-cost fabrication techniques have been developed that allow microneedle arrays to be produced at rates that are consistent with commercial demands. Macroflux[®] is a commercially available microneedle drug delivery system. This product utilizes coatings on titanium microneedles for drug delivery (50,71,72). The next stage in microneedle technology research will be to develop combinations of microneedle and microfluidics

technologies. These microneedle systems will be capable of both diagnosing and treating diseases such as diabetes in real time.

The ability to use microneedles to directly administer solutions to the bloodstream will enable the delivery of drugs such as insulin and vaccines that were previously incompatible with transdermal drug delivery.

References

1. Brown MB, Martin GP, Jone SA, et al. Dermal and transdermal drug delivery systems: current and future prospects. *Drug Deliv* 2006; 13(3):175–187.
2. Khafagy ES, Morishita M, Onuki Y, et al. Current challenges in noninvasive insulin delivery systems: a comparative review. *Adv Drug Deliv Rev* 2007; 59(15):1521–1546.
3. Elias PM. The stratum corneum as an organ of protection old and new concepts. In: Fritsch PG, Hintner H, eds. *Current Problems in Dermatology*. Vol 18. Basel, Switzerland: S. Karger Ag, 1989:10–21.
4. Griss P, Stemme G. Side-opened out-of-plane microneedles for microfluidic transdermal liquid transfer. *J Microelectromech Syst* 2003; 12(3):296–301.

5. Prausnitz MR, Mitragotri S, Langer R. Current status and future potential of transdermal drug delivery. *Nat Rev Drug Discov* 2004; 3(2):115–124.
6. Chabri F, Bouris K, Jones T, et al. Microfabricated silicon microneedles for nonviral cutaneous gene delivery. *Br J Dermatol* 2004; 150(5):869–877.
7. Mukerjee E, Collins SD, Isseroff RR, et al. Microneedle array for transdermal biological fluid extraction and in situ analysis. *Sens Actuators A Phys* 2004; 114(2–3): 267–275.
8. Lee Y, Hwang K. Skin thickness of Korean adults. *Surg Radiol Anat* 2002; 24(3–4): 183–189.
9. Nordquist L, Roxhed N, Griss P, et al. Novel microneedle patches for active insulin delivery are efficient in maintaining glycaemic control: an initial comparison with subcutaneous administration. *Pharm Res* 2007; 24(7):1381–1388.
10. Kaushik S, Hord AH, Denson DD, et al. Lack of pain associated with microfabricated microneedles. *Anesth Analg* 2001; 92(2):502–504.
11. Sivamani RK, Stoeber B, Wu GC, et al. Clinical microneedle injection of methyl nicotinate: stratum corneum penetration. *Skin Res Technol* 2005; 11(2):152–156.

12. Gill HS, Denson DD, Burris BA, et al. Effect of microneedle design on pain in human volunteers. *Clin J Pain* 2008; 24(7):585–594.
13. Roxhed N, Gasser TC, Griss P, et al. Penetration-enhanced ultrasharp microneedles and prediction on skin interaction for efficient transdermal drug delivery. *J Microelectromech Syst* 2007; 16(6):1429–1440.
14. Davis SP, Landis BJ, Adams ZH, et al. Insertion of microneedles into skin: measurement and prediction of insertion force and needle fracture force. *J Biomech* 2004; 37(8):1155–1163.
15. Park JH, Yoon YK, Choi SO, et al. Tapered conical polymer microneedles fabricated using an integrated lens technique for transdermal drug delivery. *IEEE Trans Biomed Eng* 2007; 54(5):903–913.
16. Yang M, Zahn JD. Microneedle insertion force reduction using vibratory actuation. *Biomed Microdevices* 2004; 6(3):177–182.
17. Gardeniers HJGE, Luttge R, Berenschot EJW, et al. Silicon micromachined hollow microneedles for transdermal liquid transport. *J Microelectromech Syst* 2003; 12(6): 855–862.

18. Teo MA, Shearwood C, Ng KC, et al. In vitro and in vivo characterization of MEMS microneedles. *Biomed Microdevices* 2005; 7(1):47–52.
19. Verbaan FJ, Bal SM, van den Berg DJ, et al. Improved piercing of microneedle arrays in dermatomed human skin by an impact insertion method. *J Control Release* 2008; 128(1):80–88.
20. Verbaan FJ, Bal SM, van den Berg DJ, et al. Assembled microneedle arrays enhance the transport of compounds varying over a large range of molecular weight across human dermatomed skin. *J Control Release* 2007; 117(2):238–245.
21. Han M, Hyun DH, Park HH, et al. A novel fabrication process for out-of-plane microneedle sheets of biocompatible polymer. *J Micromech Microeng* 2007; 17(6): 1184–1191.
22. Ovsianikov A, Chichkov B, Mente P, et al. Two photon polymerization of polymerceramic hybrid materials for transdermal drug delivery. *Int J Appl Ceram Technol* 2007; 4(1):22–29.
23. Lee JW, Park JH, Prausnitz MR. Dissolving microneedles for transdermal drug delivery. *Biomaterials* 2008; 29(13):2113–2124.

24. Perennes F, Marmiroli B, Matteucci M, et al. Sharp beveled tip hollow microneedle arrays fabricated by LIGA and 3D soft lithography with polyvinyl alcohol. *J Micromech Microeng* 2006; 16(3):473–479.
25. Chandrasekaran S, Brazzle JD, Frazier AB. Surface micromachined metallic microneedles. *J Microelectromech Syst* 2003; 12(3):281–288.
26. Gill HS, Prausnitz MR. Pocketed microneedles for drug delivery to the skin. *J Phys Chem Solids* 2008; 69(5–6):1537–1541.
27. McAllister DV, Wang PM, Davis SP, et al. Microfabricated needles for transdermal delivery of macromolecules and nanoparticles: fabrication methods and transport studies. *Proc Natl Acad Sci USA* 2003; 100(24):13755–13760.
28. Aoyagi S, Izumi H, Fukuda M. Biodegradable polymer needle with various tip angles and effect of vibration and surface tension on easy insertion. In: *Proceedings MEMS, Kobe, Japan, IEEE, Jan 21–25, 2007*:397–400.
29. Aoyagi S, Izumi H, Fukuda M. Biodegradable polymer needle with various tip angles and consideration on mechanism of mosquito's proboscis. *Sens Actuators A Phys* 2008; 143(1):20–28.

30. Biomedical Optics and Medical Imaging. Two-photon polymerization enhances Q6 rapid prototyping of medical devices. Available at: <http://spie.org/x13541.xml>. Accessed September, 2007.
31. Owen WB. Morphology of the head skeleton and muscles of the mosquito, *Culiseta inornata* (Williston) (Diptera: Culicidae). *J Morphol* 1985; 183(1):51–85.
32. Henry S, McAllister DV, Allen MP, et al. Microfabricated microneedles: a novel approach to transdermal drug delivery. *J Pharm Sci* 1998; 87(8):922–925.
33. Shikida M, Ando M, Ishihara Y, et al. Non-photolithographic pattern transfer for fabricating pen-shaped microneedle structures. *J Micromech Microeng* 2004; 14(11): 1462–1467.
34. Wilke N, Mulcahy A, Ye SR, et al. Process optimization and characterization of silicon microneedles fabricated by wet etch technology. *Microelectron J* 2005; 36:650–656.
35. Reaume SE. The use of hydrofluoric acid in making glass microneedles. *Science* 1952; 116(3023):641.
36. Wang PM, Cornwell M, Hill J, et al. Precise microinjection into skin using hollow microneedles. *J Invest Dermatol* 2006; 126(5):1080–1087.

37. Dorf RC, ed. CRC Handbook of Engineering Tables. Boca Raton: CRC Press, 2004.
38. Howatson AM, Lund PG, Todd JD. Engineering Tables and Data. 1st ed. Chapman and Hall, London, 1972.
39. Yoshida S, Tanaka H, Hayashi T, et al. Scratch resistance of sodium borosilicate glass. J Ceram Soc Japan 2001; 109(1270):511–515.
40. Brady GS, Clauser HR, Vaccari JA. Materials Handbook. 14th ed. New York: McGraw Hill, 1997.
41. Lynch CT. Table 1.5–1.7. In: Lynch CT, ed. CRC Handbook of Materials Science. 1st ed. Vol 2. Cleveland: CRC Press, 1974.
42. Doraiswamy A, Jin C, Narayan RJ, et al. Two photon induced polymerization of organic-inorganic hybrid biomaterials for microstructured medical devices. Acta Biomater 2006; 2(3):267–275.
43. Lourdin D, Colonna P, Ring SG. Volumetric behaviour of maltose-water, maltose-glycerol and starch-sorbitol-water systems mixtures in relation to structural relaxation. Carbohydr Res 2004; 338:2883–2887.

44. Hopcroft M, Kramer T, Kim G, et al. Micromechanical testing of SU-8 cantilevers. *Fatigue Fract Eng Mater Struct* 2005; 28(8):735–742.
45. Kim K, Lee JB. High aspect ratio tapered hollow metallic microneedle arrays with microfluidic interconnector. *Microsyst Technol* 2007; 13:3–4; 231–235.
46. Shikida M, Hasada T, Sato K. Fabrication of a hollow needle structure by dicing, wet etching, and metal deposition. *J Micromech Microeng* 2006; 16(10):2230–2239.
47. Brazzle J, Papautsky I, Frazier AB. Micromachined needle arrays for drug delivery or fluid extraction—design and fabrication aspects of fluid coupled arrays of hollow metallic microneedles. *IEEE Eng Med Biol Mag* 1999; 18(6):53–58.
48. Kobayashi K, Suzuki H. A sampling mechanism employing the phase transition of a gel and its application to a micro analysis system imitating a mosquito. *Sens Actuators B Chem* 2001; 80(1):1–8.
49. Suzuki H, Tokuda T, Kobayashi K. A disposable “intelligent mosquito” with a reversible sampling mechanism using the volume-phase transition of a gel. *Sens Actuators B Chem* 2002; 83(1–3):53–59.

50. Cormier M, Johnson B, Ameri M, et al. Transdermal delivery of desmopressin using a coated microneedle array patch system. *J Control Release* 2004; 97(3):503–511.
51. Parker ER, Rao MP, Turner KL, et al. Bulk micromachined titanium microneedles. *J Microelectromech Syst* 2007; 16(2):289–295.
52. Gill HS, Prausnitz MR. Coated microneedles for transdermal delivery. *J Control Release* 2007; 117(2):227–237.
53. Assad M, Lemieux N, Rivard CH, et al. Comparative in vitro biocompatibility of nickel-titanium, pure nickel, pure titanium, and stainless steel: genotoxicity and atomic absorption evaluation. *Biomed Mater Eng* 1999; 9(1):1–12.
54. Matteucci M, Casella M, Bedoni M, et al. A compact and disposable transdermal drug delivery system. *Microelectron Eng* 2008; 85(5–6):1066–1073.
55. Sullivan SP, Murthy N, Prausnitz MR. Minimally invasive protein delivery with rapidly dissolving polymer microneedles. *Adv Mater* 2008; 20:933–938.
56. Huang H, Fu C. Different fabrication methods of out-of-plane polymer hollow needle arrays and their variations. *J Micromech Microeng* 2007; 17(2):393–402.

57. Park JH, Allen MG, Prausnitz MR. Biodegradable polymer microneedles: fabrication, mechanics, and transdermal drug delivery. *J Control Release* 2005; 104(1):51–66.
58. Park JH, Allen MG, Prausnitz MR. Polymer microneedles for controlled-release drug delivery. *Pharm Res* 2006; 23(5):1008–1019.
59. Haas KH, Wolter H. Synthesis, properties, and applications of inorganic-organic copolymers (Ormocer1s). *Curr Opin Solid State Mater Sci* 1999; 4(6):571–580.
60. Schlie S, Ngezahayo A, Ovsianikov A, et al. Three-dimensional cell growth on structures fabricated from ORMOCER1 by two-photon polymerization technique. *J Biomater Appl* 2007; 22(3).
61. Miyano T, Tobinaga Y, Kanno T, et al. Sugar micro needles as transdermic drug delivery system. *Biomed Microdevices* 2005; 7(3):185–188.
62. Kolli CS, Banga AK. Characterization of solid maltose microneedles and their use for transdermal delivery. *Pharm Res* 2008; 25(1):104–113.
63. Ji J, Tay FEH, Miao JM, et al. Microfabricated microneedle with porous tip for drug delivery. *J Micromech Microeng* 2006; 16(5):958–964.

64. Stoeber B, Liepmann D. Arrays of hollow out-of-plane microneedles for drug delivery. *J Microelectromech Syst* 2005; 14(3):472–479.
65. Moon SJ, Lee SS, Lee HS, et al. Fabrication of microneedle array using LIGA and hot embossing process. *Microsyst Technol* 2005; 11(4–5):311–318.
66. Davis SP, Martano W, Allen MG, et al. Hollow metal microneedles for insulin delivery to diabetic rats. *IEEE Trans Biomed Eng* 2005; 52(5):909–915.
67. Serbin J, Egbert A, Ostendorf A, et al. Femtosecond laser-induced two-photon polymerization of inorganic-organic hybrid materials for applications in photonics. *Opt Lett* 2003; 28(5):301–303.
68. Maruo S, Nakamura O, Kawata S. Three-dimensional microfabrication with two-photon-absorbed photopolymerization. *Opt Lett* 1997; 22(2):132–134.
69. Aoyagi S, Izumi H, Isono Y, et al. Laser fabrication of high aspect ratio thin holes on biodegradable polymer and its application to a microneedle. *Sens Actuators A Phys* 2007; 139(1–2):293–302.

70. Zahn JD, Deshmukh A, Pisano AP, et al. Continuous on-chip micropumping for microneedle enhanced drug delivery. *Biomed Microdevices* 2004; 6(3):183–190.
71. Lin WQ, Cormier M, Samiee A, et al. Transdermal delivery of antisense oligonucleotides with microprojection patch (Macroflux1) technology. *Pharm Res* 2001; 18(12):1789–1793.
72. Matriano JA, Cormier M, Johnson J, et al. Macroflux1 microprojection array patch technology: a new and efficient approach for intracutaneous immunization. *Pharm Res* 2002; 19(1):63–70.

2.2.2 Recent Advances in Microneedle-mediated Parenteral Drug Delivery

Introduction

Microneedle technology for parenteral drug delivery has seen significant progress in recent years. Since 2008, advances have been made in microneedle design, production methods, materials, and performance assessment techniques. However, the most significant recent advances in microneedle technology have been in the development of novel drug delivery techniques and performance assessment techniques, namely *ex vivo* and *in vivo* studies of drug delivery with these devices, which is an important step in bringing this technology to clinical use.

Advances in Microneedle Design and Production Techniques

Patterning and bending metal foils has developed into one of the most widely used techniques for producing microneedles [1-4]. This technique, developed by the Prausnitz group at Georgia Institute of Technology [5-7], has seen numerous variations by other groups. Apogee Technology is producing a commercial device by hydrofluoric acid etching of titanium foil. AdminMed has produced commercially available microneedle devices by etching sheets of stainless steel foil and bending the needles out of plane [8, 9]. These microneedles have cutouts along the shaft to enable fluid flow through the substrate and potentially along the opening into the skin (Figure 1a). However, fluid generally follows the

path of least resistance, so there is a high likelihood that the majority of the pharmaceutical agent travels along the surface of the array and rests on the surface of the skin as opposed to traveling along the cutout and penetrating into the skin.

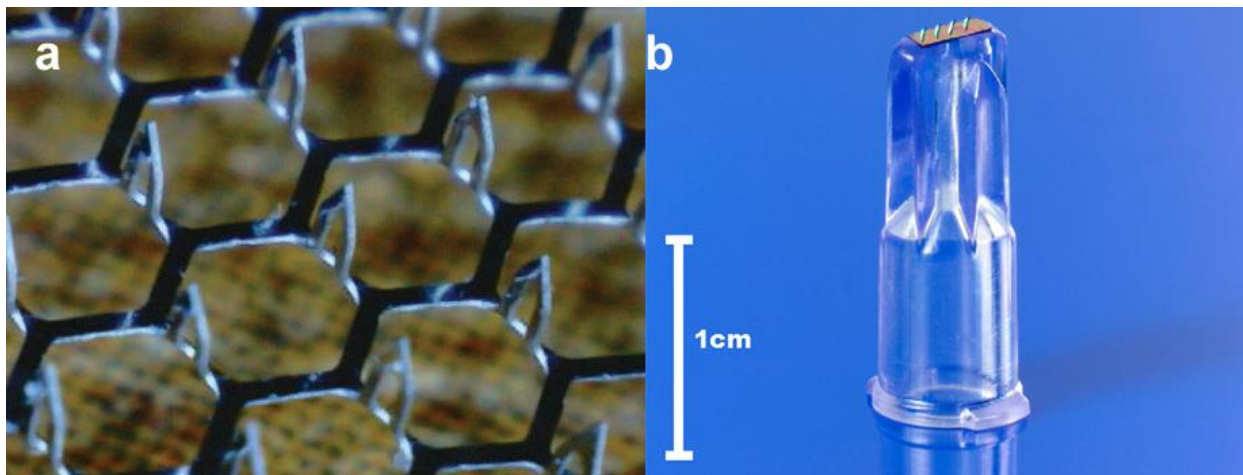


Figure 1. Commercially available microneedle devices: a) AdminPatch® microneedle array*,
b) the MicronJet device**.

*Source: Yuzhakov VV. The AdminPen™ Microneedle Device for Painless & Convenient Drug Delivery. *Drug Delivery Technology* 2010, 10: 32-36.

**Reprinted from: *Vaccine*, Vol 27, Van Damme P, Oosterhuis-Kafeja F, Van der Wielen M, et al. Safety and efficacy of a novel microneedles device for dose sparing intradermal influenza vaccination in healthy adults. 454-459, Copyright 2009, Elsevier.

A new microneedle production technique, drawing lithography, was recently reported by Lee *et al.* [10]. Ultra-high aspect ratio, hollow microneedles were generated by this technique, where a 2-D pattern of a thermosetting polymer is drawn out to produce a 3-D structure and

subsequently solidified by thermal curing. SU-8 2050 was spin-coated onto a glass substrate, drawn to produce a spear-shaped array, electroless coated on the tip, Ni electroplated, and then removed to produce high-aspect ratio hollow metal microneedles. These microneedles has a 300 μm diameter base, a 20 μm diameter tip opening, tunable wall thicknesses ranging from 20-30 μm , and tunable lengths of 600, 1200, 1800, and 2000 μm . Drug delivery capability was confirmed by injection of insulin into hyperglycemic rats, which resulted in changes in blood glucose levels similar to injection with 33-gauge needles. While production of hollow microneedles by electroplating has been previous demonstrated (Davis 2004, others), Lee *et al.* present a novel method for producing a mold for electroplating. In their technique length and wall thickness can be controlled; nevertheless, other significant geometrical features, such as tip geometry cannot be controlled with this technique.

A 2010 study by Choi *et al.* reported several novelties in production technique [11]. One area of innovation was in fabrication technique. An array of conducting microneedles was produced by micromolding, where PMMA microneedle arrays were produced via solvent casting at 50 $^{\circ}\text{C}$ in a PDMS mold. A metal seed layer of Ti/Cu was deposited by DC sputtering and subsequently patterned by excimer laser ablation. Electroplating was then used to coat the patterned seed layer with nickel. Interestingly, while uncoated PMMA needles bent without penetrating the skin, electroplating with Ni increased their mechanical strength to where skin penetration was achievable. Thickness of the Ni coating was also important, with 10 μm thick coatings showing signs of fatigue while 20 μm thick coatings were mechanically stable.

A novel microneedle design consisting of SU8 drug reservoir tubes with conical caps consisting of a dissolving polymer (a mixture of polyvinyl alcohol and polyvinylpyrrolidone) was presented by Paik *et al.* [12]. The tubes were produced by masked photolithography, using a patterned Cr mask, and the caps were produced by UV soft lithography. Delivery was modeled by inserting the needles, containing a red dye, into agarose gel and into chicken muscle tissue. Further studies will need to be conducted to see if these needles are capable of piercing skin, since the thin polymer walls are likely weaker than solid microneedles and other groups have found that some polymer microneedles have insufficient mechanical properties for piercing skin [11].

DeMuth *et al.* also used laser ablation to assist in microneedle production [13]. A laser was used to directly machine a microneedle mold from PDMS, which was subsequently used to mold PLGA microneedles. As with Choi *et al.*, these polymer microneedles were weak and showed signs of buckling during application to the skin. In this study the microneedles were applied to ear skin of mice, which is exceptionally thin in comparison to human skin [14, 15]. Consequently, microneedle penetration in this study may be significantly different than in humans.

At this point I would like to note that, while it has been used as a model in numerous studies [13, 16, 17], mouse skin, in particular skin of the ear, is a poor model for microneedle-mediated drug delivery in humans. The entire mouse ear is less than 300 μm thick,

containing 100 μm of cartilage and 2 approximately 100 μm thick layers of skin [18]. The stratum corneum of mouse skin is 9 μm thick, and the epidermis is 29 μm thick [14]. In contrast, the skin of the human forearm has a stratum corneum approximately 29 μm thick and an epidermis of 47-89 μm thick [18]. The upper dermis in the human forearm is located 136 μm deep [18], which is more than 30% deeper than total thickness of mouse ear skin. Further, ear skin is less compressible than skin with subdermal tissue, such as the forearm or shoulder. Both of which may improve microneedle penetration in mouse ear skin in comparison to human skin. Interestingly, Häfeli *et al.* reported poor delivery of drugs into mouse skin by hollow microneedle injection, with the majority of the injected fluid residing on the surface of the skin (36% delivery into the epidermis) [17]. Further, there was negligible delivery of the injected drug into the bloodstream. They attributed this difficulty to high tissue flexibility and poor absorption by the epidermis. In contrast, numerous studies have indicated that pig skin is the best model for human skin [14, 20]. The stratum corneum of pig skin is 9.88 μm (ear) to 15.17 μm (humeroscapular joint) and the epidermis is 46.76 μm (ventral abdomen) to 56.68 μm (buttocks) [20]. Studies with full thickness skin have reported significant compression of the skin and higher insertion forces than observed with studies of thin skin, even with sharp needles [17, 21]. Likewise, several groups have reported differences in *in vivo* versus *ex vivo* microneedle penetration [22, 23]. Due to the significant impact of tissue compressibility on microneedle penetration, it is important that studies with excised skin use sufficiently thick skin samples (preferably full thickness skin) to achieve results that are relevant to clinical use.

Delivery Techniques

Coating is still the dominant technique for intradermal delivery with microneedles [1-4, 13], most likely due to difficulties in producing hollow microneedles. Several advances in coating approaches have been reported [1, 13]. Demuth *et al.* coated PLGA microneedles using polyelectrolyte multilayer (PEM) engineering [13]. Thin film coatings of DNA-carrying self-assembled PEMs on microneedles were used for *in vivo* transfection of cells in the ears of mice. Confocal microscopy confirmed delivery of DNA into the epidermis. Kim *et al.* performed a study to optimize the formulation for solid-state influenza vaccine for coating solid, stainless steel microneedles [1]. Dip coating with standard vaccine formulations resulted in coatings with 2% influenza vaccine stability. Trehalose was found to be the stabilizer that best protected the antigen by minimizing particle aggregation. Carboxymethylcellulose, which was added to increase viscosity, was found to contribute to loss in vaccine activity. Application of the coated microneedles to mice resulted in effective antibody production, with antibody levels equal to vaccinations by intramuscular injection.

Some hollow microneedle devices are beginning to be available, such as the MicronJet device by NanoPass Technologies and the Microstructured Transdermal System by 3M. The NanoJet device consisted of a silicon wafer containing hollow microneedles (0.45 mm long) that was bonded to a plastic fitting for connecting to a conventional syringe (Figure 1b) [24]. Daugimont *et al.* produced hollow and solid polymer microneedles by conventional micromachining (e.g., drilling and milling) [25], which were 1200 μm long, 250 μm diameter

at the base, and had a 70 μm diameter channel. The needles were then coated with titanium and gold layers to make them electrically conducting. *Ex vivo* and *in vivo* studies were performed with porcine ear skin and with NMRI mice. Luciferase and ovalbumin delivery was similar for microneedles and 30 gauge hypodermic needles. However, electrotransfer of DNA proved to be difficult due to several factors including reservoir size, DNA viscosity, and the shape of the electrical field generated by the microneedle array. The electrical field generated by the microneedle arrays resulted in irreversible electroporation of cells located near the microneedle tips.

In a similar study, Choi *et al.* used micromolding, ablation, and electroplating to produce solid, electrically conducting microneedle arrays, which are capable of delivering DNA into cells by electroporation *in vitro* [11]. Electroporation of a cell suspension containing calcein resulted in an increase in cell uptake. At 50 V, cell viability was 91% with 40% of the cells having calcein uptake. This technique may improve delivery of DNA-based vaccines by improving vaccine uptake into cells in the bloodstream. However, further studies are necessary to determine if microneedle electroporation improves systemic DNA delivery under *in vivo* conditions. During *in vivo* conditions a significantly lower portion of the microneedle is in direct contact with the bloodstream, so the effect on the cells could be greatly reduced. Further, delivery throughout the bloodstream in quantities necessary to have a significant effect may be challenging since it is a significantly larger volume than what was tested in this *in vitro* study. Lastly, similar problems as those reported by Daugimont *et al.* may occur since cells will be immobilized instead of in suspension [25].

Recent Microneedle Drug Delivery Studies

Dyes

Numerous developments have been achieved with using dyes to assess drug delivery with microneedles. In addition to their extensive *in vivo* mouse study, Sullivan *et al.* also performed an *ex vivo* examination of microneedle delivery into pig skin by fluorescence and histology of sectioned skin after insertion of microneedles encapsulating sulforhodamine [26]. Jiang *et al.* used individual hand-drawn glass microneedles to inject sulforhodamine, Nile Red-encapsulated PLA nanospheres, and fluorescein-labeled latex microspheres into human cadaver sclera [27]. This study was the first demonstration of minimally-invasive drug delivery into the eye with microneedles. Bal *et al.* used confocal laser scanning microscopy (CLSM) to image *in vivo* delivery of sodium fluorescein dye into humans by a commercial microneedle device (DermaStamp®, Dermanroller Deutschland S.a.r.l., Wolfenbuettel, Germany) [28].

Wu *et al.* performed several experiments using dyes [29]. *In vitro* assessment was performed by applying needles that were coated with rhodamine B to dermatomed human skin and subsequently imaging the stratum corneum and dermal side of the skin with CLSM. *In vivo* assessment was also performed by applying microneedles to rats for 10 sec and then a cotton patch soaked in FITC-BSA for 1 hr. The skin was then excised and imaged by fluorescence microscopy. Also, a Franz-type diffusion cell was used to assess calcein delivery through dermatomed human skin. A similar study was performed by Coulman *et al.* [30]. They used a diffusion cell and fluorescent nanoparticles to quantify the effect of microneedles on skin

permeability. After applying and removing microneedles, the excised skin was mounted on a Franz-type diffusion cell with a fluorescent nanoparticle solution on the stratum corneum side of the membrane to assess nanoparticle perfusion. Perfusion of nanoparticles through the skin was determined by fluorescently measuring the nanoparticle concentration on the receiving end of the diffusion cell. The Narayan research group has performed several studies investigating delivery of quantum dots via hollow, polymer microneedles produced by two-photon polymerization [31, 32]. Histology and confocal laser scanning microscopy [31] as well as multiphoton microscopy [32] were used to image distribution of these model drugs throughout the skin. Quantum dots can be used for theranostics applications, where they are conjugated with a drug to allow imaging of the distribution of the drug within the body. This technique is particularly relevant to treatment of cancer [33].

Insulin and other Pharmaceuticals

To date, vaccines are the pharmaceutical class that has been most widely delivered with microneedles. Other drugs that have been delivered with microneedles include insulin [34-38], Naltrexone [39], hexyl nicotinate [40], methyl nicotinate [41], methotrexate [23], and antimicrobial agents [42-44]. The first clinical study of systemic delivery of a medication to human by microneedles was reported by Wermeling *et al.* in 2009. Stainless steel microneedles that were made by machining and bending were used to deliver Naltrexone, a mu-opioid receptor inhibitor that is used for treating opiate and alcohol dependence, to human subjects. Delivery was performed by applying and removing the microneedle array and subsequently placing a transdermal patch on the same skin location. The delivery system

was pain free and the microneedle arrays were not damaged by skin penetration. Naltrexone delivery via transdermal patches was achieved with the microneedle treated subjects but not with untreated subjects.

Sivamani *et al.* used hollow silicon microneedles to inject hexyl nicotinate, a drug that induces capillary vasodilation, into human volunteers. The advantage of this novel transdermal drug delivery indicator is that it has slow partition from the stratum corneum to the epidermis. As such, this pharmaceutical is an effective marker for determining whether microneedles deliver drug past versus into the stratum corneum. Their comparison of the effects of topical treatment, microneedle injection, and microneedle injection after tape stripping indicated that the tested microneedles indeed do deliver drug into the epidermis.

An *in vivo* study of microneedle delivery using hairless rats was reported by the Banga research group at Mercer University. A comparative study of delivery of methotrexate with solely iontophoresis, with solely microneedles, and with both iontophoresis and solid microneedles was conducted. The microneedles were solid tetrahedrons produced via micromolding of maltose. The maltose microneedles dissolved after insertion into the skin. *In vivo* delivery with solely microneedles was more effective than passive delivery but less effective than solely iontophoresis. The combination of iontophoresis plus microneedles was the most effective delivery technique.

The Narayan research group has performed several studies demonstrating the delivery of antimicrobial agents via microneedles [42-44]. Pulsed laser deposition was used to produce

thin film coatings of silver and zinc oxide on solid polymer microneedles [43-44]. In another study, solid microneedles were made from polyethylene glycol diacrylate hydrogel containing the antibiotic gentamicin sulfate [42]. Donnelly *et al.* have demonstrated that disease causing microbes are capable of penetrating pores produced by microneedles [45].

In 2009, Gupta *et al.* performed a clinical trial of insulin delivery with microneedles to subjects with type I diabetes [38]. Diabetes management with microneedle versus catheter infusion delivery of insulin was compared during a 3.5 hour time period. Hand-drawn glass microneedles and a 9-mm infusion catheter were used for insulin delivery. Microneedles were found to be as effective at delivering insulin as the catheter infusion set, while being significantly less invasive. Additionally, microneedles were displaced various depths into the skin from 1 mm to 5 mm. Displacements of 5 mm and 3.5 mm were significantly more effective than 1-mm displacement. It is important to note that this displacement does not correspond to the skin penetration depth since during microneedle displacement the skin is also compressing. Microneedle injection resulted in no erythema but swelling of the skin, which subsided within two hours, whereas the catheter injection resulted in mild erythema, which remained after two hours, and swelling of the skin. The results of this study confirms the general belief that insulin injections via microneedles are a promising, less painful, and less invasive alternative to conventional insulin delivery methods.

Vaccines

Vaccine delivery has been the primary focus of microneedle-mediated drug delivery from 2008 to 2011. Several groups have performed *ex vivo* vaccine delivery studies. In 2009, the research group of Dr. Banga at Mercer University reported microneedle delivery of monoclonal antibodies into excised full thickness skin of hairless rats [21]. This study used commercially available (Texmac Inc.) maltose microneedles with sharp tips (3 μm), which penetrated the skin with approximately 250 g of force. Longer microneedles (500 μm versus 200 μm) resulted in higher IgG uptake. Ng *et al.* developed an *ex vivo* system for modeling vaccination with microneedles [46]. This system consisted of excised human split-thickness or full-thickness skin sitting on a supporting metal grid in tissue culture medium, with the dermal side immersed in the tissue culture medium and the stratum corneum side exposed to air. Histology and gene expression were used to assess the immune response resulting from vaccine delivery. The vaccine was delivered by topical application to the skin and subsequent piercing of the skin with the microneedle array.

Due to the desire to measure the effects of the microneedle-delivered vaccines, numerous *in vivo* animal studies and clinical studies have been performed [1-4, 13]. With the recent outbreak of the H1N1 influenza epidemic, influenza vaccine delivery has seen the most widespread investigation [1, 3, 4, 24]. In particular, numerous studies were performed where coated solid microneedles were used to deliver influenza vaccine to mice [1, 3, 4, 26]. A detailed report of vaccination via dissolving microneedles was presented by Sullivan *et al.* in Nature Medicine [26]. This study consisted of producing polyvinylpyrrolidone microneedles

encapsulating lyophilized vaccine by molding. Influenza vaccination by the dissolving microneedles was compared to vaccination by intramuscular injections into mice. Vaccination by microneedles elicited robust immune responses that were as effective as the intramuscular injections.

Van Damme *et al.* published a report on influenza vaccine delivery via Nanopass Technologies' MicronJet device [24]. This report was one of the largest clinical studies of microneedle drug delivery to date, with 180 human subjects receiving vaccinations. While previous studies have investigated the pain of microneedles penetrating the skin, this was the first study comparing the *in vivo* effects of injection of a drug with hypodermic needles. Intradermal (microneedle) vaccination resulted in significantly less "prick-pain" though slightly higher "Administration-pain"; intradermal vaccination had less pain post-vaccination than intramuscular injections. Interestingly, intradermal injections resulted in greater incidence of redness, swelling, and induration, though these local reactions were mild. There was no significant difference in immunogenic effect between the delivery techniques. The higher delivery pain and local reactions may be a result of accumulation of vaccine in the epidermis. Using a lower delivery rate and longer microneedles are two factors that should be investigated for reducing the local effects of microneedle vaccination. Lower delivery rates may reduce local effects by allowing the vaccine more time to diffuse through the epidermis. Longer microneedles may have better access to capillary beds and faster distribution of the injected drug.

DNA-based vaccine delivery has been investigated in numerous studies. Choi *et al.* conducted an *in vitro* study with cells in culture to examine using electroporation by microneedles to improve DNA transfection rates [11]. Demuth *et al.* delivered plasmid DNA to mouse skin using coated microneedles [13]. Gill *et al.* demonstrated that DNA plasmid vaccine delivered by microneedles to mice induced a sufficient immune response in delivered DNA plasmid hepatitis C vaccine via microneedles to mice, with microneedle delivery being equally as effective as hypodermic needles and gene guns [2].

Assessment of Microneedle Properties

A particularly interesting study was performed by Donnelly *et al* [45]. They performed an in depth study of the ability of microbial organisms to penetrate pores created by microneedles in comparison to pores created by hypodermic needles. Silicon microneedles and hypodermic needles were used to penetrate Silescol® membranes, a synthetic model for mimicking drug diffusion through the stratum corneum, and excised porcine skin dermatomed to a thickness of 400 µm. Microbial suspensions (*C. albicans*, *P. aeruginosa*, and *S. epidermidis*) were perfused through the skin and membranes in a Franz cell to measure the effect of microneedles and hypodermic needles on the ability of these organisms to penetrate the skin. Hypodermic needles allowed significantly greater penetration of microorganisms through the synthetic membrane and excised skin than microneedles. *C. albicans* exhibited the greatest potential to penetrate the generated pores. This study indicates that a risk of infection from microneedle use does occur, most significantly with *C.*

albicans, though it is significantly less than the risk of infection associated with hypodermic needle use.

A study of the skin penetration mechanics of microneedles was performed by Takano *et al.* [47]. High molecular weight (6000 mw) polyethylene glycol microneedles, which dissolve by hydrolysis in the skin, were used in this penetration study. Microneedles were applied to commercial cultured human skin, 15-18 mm thick. They measured the thickness of the stratum corneum and epidermis to be approximately 0.1 mm. Biaxial tension was applied to the skin and a punch with an open center was pressed against the back side of the skin to achieve controlled tension and a more uniform skin surface. Loose skin resulted in tenting of the entire skin surface, whereas taut skin resulted in tenting only at the tips of the needles and also better penetration. The needles in this study are uncharacteristically large (1 mm base and 2 mm length, less sharp than a hypodermic needle), so further studies need to be done with other microneedle geometries to see how pronounced the tenting effect is with smaller needles. Regardless of the length of the needles, this study shows that the tension and curvature of the skin are important factors that must closely resemble the actual *in vivo* conditions in order to get skin penetration data that are relevant to actual clinical use. Testing microneedle penetration with *ex vivo* skin without tension will make penetration appear more difficult than in *in vivo* conditions whereas apply exceptionally high tension can make microneedle devices have falsely superior penetration properties. Another microneedle penetration mechanics study was performed by Verbaan *et al.* in 2008 [48]. In this study the effects of insertion speed and skin thickness were examined. Microneedles were applied to

the skin by either manual pressing or impacting at 1 m/s and 3 m/s. Both microneedles assembled from the tips of conventional needles and silicon microneedles were examined. Microneedles were applied to both full thickness skin and skin dermatomed to 300-400 μm . Microneedle penetration with impacting was superior to manual application and 3 m/s impacting had better penetration than impacting at 1 m/s. Dermatomed skin and full thickness skin were reported to have similar penetration, though no quantitative data were given.

Recently, an in depth clinical study of the pain associated with microneedle use was conducted by a research group at Cardiff University [49]. The pain associated with applying 25-gauge hypodermic needles, 280 μm long silicon microneedles, and 180 μm long silicon microneedles was investigated. At subjects found the hypodermic needle to be the most painful. Interestingly, the relative discomfort between the two microneedle lengths varied, with some subjects finding the shorter microneedles more painful and some finding the longer microneedles more painful. Both microneedle geometries were effective at piercing the skin, as determined by trans-epidermal water loss (TEWL) and methylene blue staining.

A report published by Birchall *et al.* discusses the public and healthcare professional opinions of microneedles [50]. This report provides an interesting view of the perception of microneedles outside of the research environment. Several focus groups of laypersons and healthcare professional were questioned on their thoughts about microneedles. One some points, the opinions was remarkably uniform, all focus groups were of the opinion that microneedles would be advantageous for their reduction in pain, their potential for self-

administration, and would be good for children, needlephobes, and diabetics. Likewise, there were some widely expressed concerns: lack of efficacy, delayed onset of action, inability to confirm delivery of dose, cost, potential for abuse, risk of cross contamination, variation in skin thickness, and difficulty in injecting small volumes. These concerns are all areas that will need to be addressed by microneedle researchers in future studies. Overall, the opinion of microneedles was positive, with microneedles being more preferred than traditional needles and tablets by the majority of study participants.

Conclusions

These recent studies have shown that microneedle technology is indeed progressing towards clinical use, with numerous *in vivo* and clinical studies already having been performed. Several commercial microneedle devices are now available. However, while microneedle technology is rapidly approaching widespread clinical capabilities, much still needs to be done to appease the public concerns with these devices.

References

[1] Kim Y, Quan F, Compans RW, Kang S, Prausnitz MR. Formulation and coating of microneedles with inactivated influenza virus to improve vaccine stability and immunogenicity. *J Controlled Release* 2010 MAR 3;142(2):187-195.

- [2] Gill HS, Soderholm J, Prausnitz MR, Sallberg M. Cutaneous vaccination using microneedles coated with hepatitis C DNA vaccine. *Gene Ther* 2010 JUN;17(6):811-814.
- [3] Quan F, Kim Y, Yoo D, Compans RW, Prausnitz MR, Kang S. Stabilization of Influenza Vaccine Enhances Protection by Microneedle Delivery in the Mouse Skin. *Plos One* 2009 SEP 25;4(9):e7152.
- [4] Zhu Q, Zarnitsyn VG, Ye L, Wen Z, Gao Y, Pan L, Skountzou I, Gill HS, Prausnitz MR, Yang C, Compans RW. Immunization by vaccine-coated microneedle arrays protects against lethal influenza virus challenge. *Proc Natl Acad Sci U S A* 2009 MAY 12;106(19):7968-7973.
- [5] Gill HS, Prausnitz MR. Coating formulations for microneedles. *Pharm Res* 2007 JUL;24(7):1369-1380.
- [6] Gill HS, Prausnitz MR. Coated microneedles for transdermal delivery. *J Controlled Release* 2007 FEB 12;117(2):227-237.
- [7] Gill HS, Denson DD, Burris BA, Prausnitz MR. Effect of microneedle design on pain in human volunteers. *Clin J Pain* 2008 SEP;24(7):585-594.

[8] Yuzhakov VV. The AdminPen™ Microneedle Device for Painless & Convenient Drug Delivery. *Adv Deliv Dev* 2010;10(4):32-36.

[9] Yuzhakov VV, inventor. Microneedle array, patch, and applicator for transdermal drug delivery. FL, United States Patent US7658728B2. 2007 Feb 9, 2010.

[10] Lee K, Lee HC, Lee D, Jung H. Drawing Lithography: Three-Dimensional Fabrication of an Ultrahigh-Aspect-Ratio Microneedle. *Adv Mater* 2010 JAN 26;22(4):483-486.

- [11] Choi S, Kim Y, Park J, Hutcheson J, Gill H, Yoon Y, Prausnitz M, Allen M. An electrically active microneedle array for electroporation. *Biomed Microdevices* 2010 04/01;12(2):263-273.
- [12] Paik SJ, Kim SH, Wang PC, Wester BA, Allen MG. Dissolvable-tipped, drug-reservoir integrated microneedle array for transdermal drug delivery. *Micro Electro Mechanical Systems (MEMS), 2010 IEEE 23rd International Conference on*; 2010.
- [13] DeMuth PC, Su X, Samuel RE, Hammond PT, Irvine DJ. Nano-Layered Microneedles for Transcutaneous Delivery of Polymer Nanoparticles and Plasmid DNA. *Adv Mater* 2010 NOV 16;22(43):4851-4856.
- [14] Godin B, Touitou E. Transdermal skin delivery: Predictions for humans from in vivo, ex vivo and animal models. *Adv Drug Deliv Rev* 2007 SEP 30;59(11):1152-1161.
- [15] Zheng Y, Danilenko DM, Valdez P, Kasman I, Eastham-Anderson J, Wu J, Ouyang W. Interleukin-22, a T(H)17 cytokine, mediates IL-23-induced dermal inflammation and acanthosis. *Nature* 2007 FEB 8;445(7128):648-651.
- [16] Ding Z, Verbaan FJ, Bivas-Benita M, Bungener L, Huckriede A, van den Berg DJ, Kersten G, Bouwstra JA. Microneedle arrays for the transcutaneous immunization of diphtheria and influenza in BALB/c mice. *J Controlled Release* 2009 MAY 21;136(1):71-78.

- [17] Hafeli UO, Mokhtari A, Liepmann D, Stoeber B. In vivo evaluation of a microneedle-based miniature syringe for intradermal drug delivery. *Biomed Microdevices* 2009 OCT;11(5):943-950.
- [18] Eriksson E, Boykin JV, Pittman RN. Method for Invivo Microscopy of the Cutaneous Micro-Circulation of the Hairless Mouse Ear. *Microvasc Res* 1980;19(3):374-379.
- [19] Neerken S, Lucassen GW, Bisschop MA, Lenderink E, Nuijs TAM. Characterization of age-related effects in human skin: A comparative study that applies confocal laser scanning microscopy and optical coherence tomography. *J Biomed Opt* 2004 MAR-APR;9(2):274-281.
- [20] Monteiro-Riviere N, Bristol DG, Manning TO, Rogers RA, Riviere JE. Interspecies and Interregional Analysis of the Comparative Histologic Thickness and Laser Doppler Blood Flow Measurements at Five Cutaneous Sites in Nine Species. *J Investig Dermatol* 1990 print;95(5):582-586.
- [21] Li G, Badkar A, Nema S, Kolli CS, Banga AK. In vitro transdermal delivery of therapeutic antibodies using maltose microneedles. *Int J Pharm* 2009 2/23;368(1-2):109-115.

- [22] Teo MAL, Shearwood C, Ng KC, Lu J, Moochhala S. In vitro and in vivo characterization of MEMS microneedles. *Biomed Microdevices* 2005 MAR;7(1):47-52.
- [23] Vemulapalli V, Yang Y, Friden PM, Banga AK. Synergistic effect of iontophoresis and soluble microneedles for transdermal delivery of methotrexate. *J Pharm Pharmacol* 2008;60(1):27-33.
- [24] Van Damme P, Oosterhuis-Kafeja F, Van der Wielen M, Almagor Y, Sharon O, Levin Y. Safety and efficacy of a novel microneedle device for dose sparing intradermal influenza vaccination in healthy adults. *Vaccine* 2009 Jan 14;27(3):454-459.
- [25] Daugimont L, Baron N, Vandermeulen G, Pavselj N, Miklavcic D, Jullien M, Cabodevila G, Mir LM, Preat V. Hollow Microneedle Arrays for Intradermal Drug Delivery and DNA Electroporation. *J Membr Biol* 2010 JUL;236(1):117-125.
- [26] Sullivan SP, Koutsonanos DG, Martin MdP, Lee JW, Zarnitsyn V, Choi S, Murthy N, Compans RW, Skountzou I, Prausnitz MR. Dissolving polymer microneedle patches for influenza vaccination. *Nat Med* 2010 AUG;16(8):915-U116.
- [27] Jiang J, Moore JS, Edelhauser HF, Prausnitz MR. Intrasceral Drug Delivery to the Eye Using Hollow Microneedles. *Pharm Res* 2009 FEB;26(2):395-403.

[28] Bal S, Kruithof AC, Liebl H, Tomerius M, Bouwstra J, Lademann J, Meinke M. In vivo visualization of microneedle conduits in human skin using laser scanning microscopy. *Laser Physics Letters* 2010;7(3):242-246.

[29] Wu Y, Qiu Y, Zhang S, Qin G, Gao Y. Microneedle-based drug delivery: studies on delivery parameters and biocompatibility. *Biomed Microdevices* 2008 OCT;10(5):601-610.

[30] Coulman SA, Anstey A, Gateley C, Morrissey A, McLoughlin P, Allender C, Birchall JC. Microneedle mediated delivery of nanoparticles into human skin. *Int J Pharm* 2009 JAN 21;366(1-2):190-200.

[31] Doraiswamy A, Ovsianikov A, Gittard SD, Monteiro-Riviere NA, Crombez R, Montalvo E, Shen W, Chichkov BN, Narayan RJ. Fabrication of Microneedles Using Two Photon Polymerization For Transdermal Delivery of Nanomaterials. *J Nanosci Nanotechnol* 2010;10(10):6305-6312.

[32] Gittard SD, Miller PR, Boehm RD, Ovsianikov A, Chichkov BN, Heiser J, Gordon J, Monteiro-Riviere N, Narayan RJ. Multiphoton microscopy of transdermal quantum dot delivery using two photon polymerization-fabricated polymer microneedles. *Faraday Discuss* 2011;149:171-185.

[33] Bagalkot V, Zhang L, Levy-Nissenbaum E, Jon S, Kantoff PW, Langer R, Farokhzad OC. Quantum dot - Aptamer conjugates for synchronous cancer imaging, therapy, and sensing of drug delivery based on Bi-fluorescence resonance energy transfer. *Nano Letters* 2007 OCT;7(10):3065-3070.

[34] Martanto W, Davis SP, Holiday NR, Wang J, Gill HS, Prausnitz MR. Transdermal delivery of insulin using microneedles in vivo. *Pharm Res* 2004 JUN;21(6):947-952.

[35] Davis SP, Martanto W, Allen MG, Prausnitz MR. Hollow metal microneedles for insulin delivery to diabetic rats. *Ieee Transactions on Biomedical Engineering* 2005 MAY;52(5):909-915.

[36] Ito Y, Hagiwara E, Saeki A, Sugioka N, Takada K. Feasibility of microneedles for percutaneous absorption of insulin. *European Journal of Pharmaceutical Sciences* 2006 SEP;29(1):82-88.

[37] Nordquist L, Roxhed N, Griss P, Stemme G. Novel microneedle patches for active insulin delivery are efficient in maintaining glycaemic control: An initial comparison with subcutaneous administration. *Pharm Res* 2007 JUL;24(7):1381-1388.

[38] Gupta J, Felner EI, Prausnitz MR. Minimally Invasive Insulin Delivery in Subjects with Type 1 Diabetes Using Hollow Microneedles. *Diabetes Technology & Therapeutics* 2009 JUN;11(6):329-337.

[39] Wermeling DP, Banks SL, Huclson DA, Gill HS, Gupta J, Prausnitz MR, Stinchcom AL. Microneedles permit transdermal delivery of a skin-impermeant medication to humans. *Proc Natl Acad Sci U S A* 2008 FEB 12;105(6):2058-2063.

[40] Sivamani RK, Stoeber B, Liepmann D, Maibach HI. Microneedle penetration and injection past the stratum corneum in humans. *J Dermatol Treat* 2009 01/01; 2011/02;20(3):156-159.

[41] Sivamani RK, Stoeber B, Wu GC, Zhai H, Liepmann D, Maibach H. Clinical microneedle injection of methyl nicotinate: stratum corneum penetration. *Skin Res Technol* 2005 May;11(2):152-156.

[42] Gittard SD, Ovsianikov A, Akar H, Chichkov B, Monteiro-Riviere NA, Stafslin S, Chisholm B, Shin C, Shih C, Lin S, Su Y, Narayan RJ. Two Photon Polymerization-Micromolding of Polyethylene Glycol-Gentamicin Sulfate Microneedles. *Advanced Engineering Materials* 2010;12(4):B77-B82.

[43] Gittard SD, Narayan RJ, Jin C, Ovsianikov A, Chichkov BN, Monteiro-Riviere NA, Stafslie S, Chisholm B. Pulsed laser deposition of antimicrobial silver coating on Ormocer® microneedles. *Biofabrication* 2009;1(4):041001.

[44] Gittard SD, Miller PR, Jin C, Martin TN, Boehm RD, Chisholm BJ, Stafslie SJ, Daniels JW, Cilz N, Narayan RJ. Pulsed Laser Deposition of Antimicrobial Metal Thin Film Coatings on Microneedles Produced by Visible Light Dynamic Mask Micro-stereolithography. *Biofabrication* 2011: under review.

[45] Donnelly RF, Singh TR, Tunney MM, Morrow DI, McCarron PA, O'Mahony C, Woolfson AD. Microneedle arrays allow lower microbial penetration than hypodermic needles in vitro. *Pharm Res* 2009 Nov;26(11):2513-2522.

[46] Ng KW, Pearton M, Coulman S, Anstey A, Gateley C, Morrissey A, Allender C, Birchall J. Development of an ex vivo human skin model for intradermal vaccination: Tissue viability and Langerhans cell behaviour. *Vaccine* 2009 OCT 9;27(43):5948-5955.

[47] Takano N, Tachikawa H, Miyano T, Nishiyabu K. Insertion testing of polyethylene glycol microneedle array into cultured human skin with biaxial tension. *J Solid Mech Mater Eng* 2009;3(3):604-612.

[48] Verbaan FJ, Bal SM, van den Berg DJ, Dijkman JA, van Hecke M, Verpoorten H, van den Berg A, Luttge R, Bouwstra JA. Improved piercing of microneedle arrays in dermatomed human skin by an impact insertion method. *J Controlled Release* 2008 5/22;128(1):80-88.

[49] Haq MI, Smith E, John DN, Kalavala M, Edwards C, Anstey A, Morrissey A, Birchall JC. Clinical administration of microneedles: skin puncture, pain and sensation. *Biomed Microdevices* 2009 Feb;11(1):35-47.

[50] Birchall JC, Clemo R, Anstey A, John DN. Microneedles in Clinical Practice-An Exploratory Study Into the Opinions of Healthcare Professionals and the Public. *Pharm Res* 2011 JAN;28(1):95-106.

2.3 Micro- and Nanoscale Devices in Regenerative Medicine

2.3.1 Microscale Rapid Prototyping of Prosthetics

For as long as the field of medicine has existed, human beings have been creating prostheses to treat lost or dysfunctional skeletal organs. Prosthetics have improved greatly since the crude “peg legs” of old. Nowadays, many prosthetics, such as the artificial hip, are nearly indistinguishable from the limbs they are replacing. However, there is still much room for improvement in this field.

While modern prostheses restore the patient to a nearly normal lifestyle, several problems still exist with these devices. One of the predominant sources of prosthesis complications is poor fitting. The current prosthetic gold standards, such as the Charnley hip, have a “one size fits all” approach, or at best a choice between several sizes [1]. As a result of this “close fit” approach, prosthesis complications arise, such as stress shielding [1], prosthesis migration [2], wear [3], poor lifetime [4], and development of secondary pathologies such as back pain and osteoarthritis [5]. Additionally, improving the prosthesis “fit”, meaning making implants that more closely meet their natural properties, has been shown to alleviate these problems since the forces in the prosthesis more closely match the natural forces [5].

Small bone prosthetics are especially susceptible to poor fit complications. Prostheses of intricate or articulating bones, such as the carpals in the wrist (under review), maxillofacial structures [6], the hip [7], and the knee [4], have relatively high rates of complications. Since these bones have fine details on their articulating surfaces, the prostheses need to mimic these intricate surfaces to achieve “normal” function. Additionally, small amounts of wear have more pronounced effects in these prostheses.

One promising approach to correct these problems is the development of patient-specific prostheses. The ultimate goal of patient-specific prostheses is to perfectly imitate both the structure and mechanical properties of the original healthy tissue. Computed Tomography-based modeling and rapid prototyping is a developing technology that shows promise to produce patient-specific prostheses. This review will discuss the past, current state, and future potentials for Computed Tomography (CT) assisted patient-specific prosthesis design and fabrication.

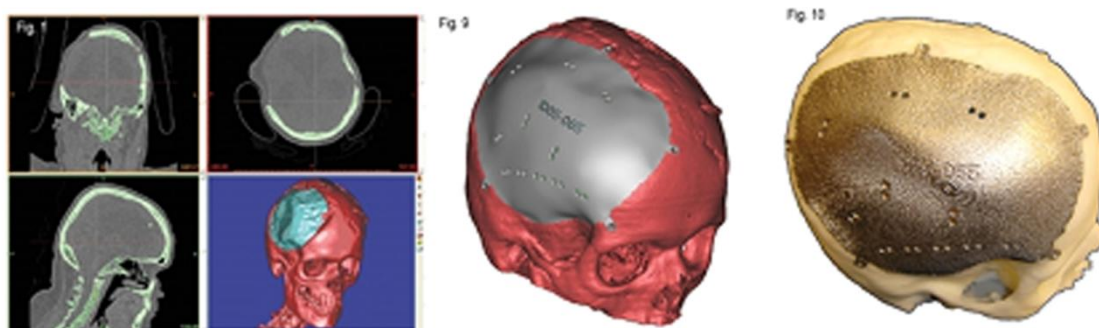
The development of 3-D computed tomography began with Radon in 1917 [8]. Radon provided a mathematical basis for describing how a series of 2-D images could be mathematically reconstructed, by a technique called the Radon transform, to produce data in 3D. In the 1950s, the mathematical techniques to perform 3-D reconstructions, including the Fourier Transform, were developed [8]. The first clinical CT system, capable of acquiring 3-D data, was produced in 1963 [8]. Upon the producing CT systems, reconstruction algorithms such as Algebraic Reconstruction Techniques (ART), backprojection, and Fourier

transform based techniques developed [8]. With the ability to acquire and process 3-D data, 3-D modeling from this data began in 1977 with Herman and Liu producing 3-D CT images [9]. Through the 1980s several technologies were developed to interpret CT data and make 3-D computer models, usually as a series of 2-D images [9, 10].

In the 1990s the concept of combining these series of stacked 2-D images with rapid prototyping technology came into being [11]. Rapid prototyping is a technique born in industry for rapidly producing parts from computer aided design (CAD) models. A wide array of rapid prototyping technologies now exist, including: computer controlled milling [11], stereolithography [11], selective laser sintering [11], electron beam melting [12], sheet lamination [13], and two-photon polymerization [14]. In rapid prototyping, objects are formed slice by slice, either by removal, addition, or polymerization of material. The different fabrication processes are compatible with different materials such as metals, polymers, and ceramics [11].

The complexity, power, and precision of modeling software to reconstruct 3-D CAD models from CT data have improved greatly since the 1990s. Presently, specifically designed software packages such as Materialise's Mimics and 3-matic packages (Materialise, Leuven, Belgium) are user-friendly ways that have seen clinical use in designing prostheses from CT data. Mimics is capable of using data from a wide array of imaging modalities to make reconstructive models, including CT, MRI, and microscopy data in a variety of file formats [15]. In addition to importing from a variety of modalities and file formats, Mimics can

export into a variety of file formats, which allows the data to be modified with CAD software or read by rapid prototyping systems [15]. 3-matic is Materialise's software package for manipulating CAD files after they have been converted by Mimics [12]. Sample images of the conversion, design, and resultant implant using Materialise software can be seen in Figure 1. Also, it has recently been shown that widely used commercial CAD programs such as SolidWorks (SolidWorks Corporation, Concord, MA) can be used to form 3-D models from CT data for rapid prototyping applications [16].



From: www.materialise.com

Figure 1. Screenshot of Mimics processing of CT data (left), final prosthesis CAD model design by 3-matic (center), and actual implant produced by electron beam melting (right). ©

2008 Materialise NV.

CT based models have been used to make several prostheses by rapid prototyping. As early as 1992, Nakai *et al.* used academic algorithms to make models from CT images [17]. Their custom modeling software interpolated between CT image slices to make 3-D models with smoother contours than afforded by the 10 mm CT image slice intervals [17]. These models

were used in conjunction with solid object ultraviolet-laser plotting (SOUP) to create prostheses; none of these prostheses were implanted [17].

In 1995, patient-specific craniofacial prostheses designed by academic CT based contouring techniques and fabricated by rapid prototyping were implanted in patients [18]. These prostheses were made by milling rapid prototyping with 0.5 mm step size precision [18].

Materialise medical image conversion and implant design software have been used to make several clinically used prostheses. Chang *et al.* used a combined approach of computed tomography and stereolithography to make patient-specific dentures [19]. Beerens *et al.* used Materialise's Mimics and 3-matic software packages to design a clinically used craniofacial implant that was made by electron beam melting [12]. Spiral CT, Materialise software, and sheet lamination rapid prototyping were used by Dai *et al.* to make 10 patient-specific hemipelvic prostheses that were used in patients [20]. Liu *et al.* reported that between 2007 and 2010 they performed 25 cases of successful production and implantation of oral and maxillofacial implants made by CT-based rapid prototyping [21].

Singare *et al.* used helical CT with 1.3 mm slice thickness, conversion and design by Materialise software, and stereolithography was used to make a prosthetic chin [22]. In this case, rapid prototyping was employed to make a master structure that was then used to make a mold. The mold was then used to make a titanium prosthesis. This same approach of utilizing rapid prototyping to make a master structure, mold forming, and then molding was

used to make auricular prostheses [23]. Employing molding in addition to rapid prototyping allows materials that are not compatible with the desired rapid prototyping technique to still be used. However, there are drawbacks to adopting molding techniques. With CT-based modeling and rapid prototyping, the interior structure of the original organ is preserved. By maintaining the interior structure, native anisotropic properties can be conserved in the prosthesis. When molding is performed, only the exterior structure is replicated, so the mechanical properties are not as accurately replicated.

The prosthetics produced by Gittard *et al.* are one example of the benefits of producing structures based on CT data directly with rapid prototyping [24]. In their study, replicas of human scaphoid and lunate bones were produced by stereolithography. These input STL files were from CT data that was acquired using Materialise software. These structures not only reproduced the exterior architecture, but fracturing of the replicas revealed that the interior structure of these bones was also reproduced.

There are several factors to be taken into consideration with CT modeling-based rapid prototyping. One important factor is precision. There are three factors contributing to prosthesis precision: CT image precision, CAD model precision, and rapid prototyping precision. For CT, layer step size is often maximized in order to minimize patient radiation exposure [17]. Interpolating algorithms in the conversion of CT data to CAD models can attempt to correct this problem [17]. Additionally, CT image artifacts need to be identified and corrected for in order to better replicate the original structure [25]. Lastly the fabrication

precision of the rapid prototyping system must be taken into account. The different rapid prototyping systems have varying degrees of precision, ranging from sub-micron (2PP) [26] to several hundred microns (fused deposition modeling) [23]. Since structures are fabricated layer-by-layer in rapid prototyping, structures with higher precision require longer fabrication times. While the highest precision is desirable, it is an inefficient use of time and resources to perform rapid prototyping fabrication with a smaller precision than what is present in the CAD model. Likewise, there is no reason to use processing to make CAD models with a smaller precision than can be produced by the rapid prototyping system.

Patient-specific prostheses are beginning to be developed and used in clinical settings with success. However, there are still improvements that can be made. Improvements in processing algorithms can help to increase the precision of the prosthesis CAD models. For small bone prostheses, micro CT is a potential technique to produce more precise prostheses. Lastly, combining different imaging modalities can be used to gather data about multiple tissues. With data on a variety of tissues in the natural organ, rapid prototyping could be performed with several materials to better replicate the properties of the natural organ.

References

[1] Learmonth ID, Young C, Rorabeck C. The operation of the century: total hip replacement. *Lancet* 2007; 370:1508-1519.

[2] Karrholm J, Borssen B, Lowenhielm G, Snorrason F. Does early micromotion of femoral stem prostheses matter? *J Bone Joint Surg [Br]* 1994; 76-B: 912-917.

[3] Ingham E and Fisher J. Biological reactions to wear debris in total joint replacement. *Proc. Instn Mech Engrs* 2000; 214 H: 21-37.

[4] Harrysson OLA, Hosni YA, Nayfeh JF. Custom-designed orthopedic implants evaluated using finite element analysis of patient-specific computed tomography data: femoral-component case study. *BMC Musculoskeletal Disorders* 2007; 8: 91-101.

[5] Gailey R, Allen K, Castles J, Kucharik J, Roeder M. Review of secondary physical conditions associated with lower-limb amputation and long-term prosthesis use. *J Rehabil Res Dev* 2008; 45: 15-29.

[6] Hohlweg-Majert B, Schmelzeisen R, Pfeiffer BM, Schneider E. Significance of osteoporosis in craniomaxillofacial surgery: A review of the literature; *Osteoporos Int* 2006; 17: 167-179.

[7] Pitto RP, Mueller LA, Reilly K, Schmidt R. Quantitative computer-assisted osteodensitometry in total hip arthroplasty. *Int Orthop* 2007; 31: 431-438.

[8] Dhawan AP. A review on biomedical image processing and future trends. *Comput Meth Programs Biomed* 1990; 31: 141-183.

[9] Solar P, Ulm C, Lill W, Imhof H, Watzek G, Blahout R, Gruber H, Matejka M. Precision of three-dimensional CT-assisted model production in the maxillofacial area. *Eur Radiol* 1992; 2: 473-477.

[10] Hoffmeister JW, Rinehart GC, Vannier MW. Three-dimensional surface reconstruction using a general purpose image processing system. *Comput Med Imaging Graph.* 1990; 14: 35-42.

[11] McGurk M, Amis AA, Potamianos P, Goodger NM. Rapid prototyping techniques for anatomical modelling in medicine. *Ann R Coll Surg Engl* 1997; 79: 169-174.

[12] Beerens MMA, Laeven P, Poukens J. 3-matic assists in true rapid design and manufacturing of a custom skull implant. Accessed from www.materialise.com
<http://www.materialise.com/materialise/view/en/905210-3-matic+Assists+in+True+Rapid+Design+and+Manufacturing+of+a+Custom+Skull+Implant+.html?cat=266395>; December 4, 2008.

[13] Chua CK, Chou SM, Wong TS. A study of the state-of-the-art rapid prototyping techniques. *Int J Adv Manuf Technol* 1998; 14: 146-152.

- [14] Doraiswamy A, Jin C, Narayan RJ, Mageswaran P, Mente P, Modi R, Auyeung R, Chrisey DB, Ovsianikov A, Chichkov B. *Acta Biomaterialia* 2006; 2: 267-275.
- [15] www.materialise.com; Accessed: December 4, 2008.
- [16] Han J and Jia Y. CT image processing and medical rapid prototyping. BMEI 2008: Proceeding of the International Conference on Biomedical engineering and Informatics 2008; 2: 67-71.
- [17] Nakai T and Marutani Y. Application of UV laser fabrication to organ models interpolated from computed tomography and magnetic resonance images. *Applied Optics* 1992; 31: 5375-5379.
- [18] Eufinger H, Wehmoller M, Machtens E, Heuser L, Harders A, Kruse D. Reconstruction of craniofacial bone defects with individual alloplastic implants based on CAD/CAM-manipulated CT-data. *J Cranio Maxillo-Facial Surg* 1995; 23: 175-181.
- [19] Chang CC, Lee MY, Wang SH. Digital denture manufacturing- an integrated technologies of abrasive computer tomography, CNC machining and rapid prototyping. *Int J Adv Manuf Technol* 2006; 31; 41-49.

- [20] Dai KR, Yan MN, Zhu ZA, Sun YH. Computer-aided custom-made hemipelvic prosthesis used in extensive pelvic lesions. *J Arthroplasty* 2007; 22: 981-986.
- [21] Liu Y, Dong X, Zhu H, Peng W. Study on Application of Rapid Prototyping in Precise Oral and Maxillofacial Surgery. *Adv Mater Res* 2010;102-104:64-68.
- [22] Singare S, Dichen L, Bingheng L, Zhenyu G, Yaxiong L. Customized design and manufacturing of chin implant based on rapid prototyping. *Rapid Prototyping J* 2005; 11: 113-118.
- [23] Subburaj K, Nair C, Rajesh S, Meshram SM, Ravi B. Rapid development of auricular prosthesis using CAD and rapid prototyping techniques. *Int J Oral Maxillofac Surg.* 2007; 36: 938-943.
- [24] Gittard SD, Narayan RJ, Lusk J, Morel P, Stockmans F, Ramsey M, Laverde C, Phillips J, Monteiro-Riviere NA, Ovsianikov A, Chichkov BN. Rapid prototyping of scaphoid and lunate bones. *Biotechnol J* 2009 Jan;4(1):129-134.
- [25] Morris CL, Barber RF, Day R. Orofacial prosthesis design and fabrication using stereolithography. *Australian Dental J* 2000; 45: 250-253.

[26] Ovsianikov A, Chichkov B, Mente P, Monteiro-Riviere NA, Doraiswamy A, Narayan RJ. Two photon polymerization of polymer-ceramic hybrid materials for transdermal drug delivery. *Int J Appl Ceram Technol.* 2007; 4: 22-29.

2.3.2 Micro- and Nanoscale Aspects of Tissue Engineering

Introduction

The fundamental challenges of tissue engineering are ongoing. The issues challenging scientists today have been known since the inception of this field. As stated by Dr. Joseph Vacanti, “The major components of this technique are (1) the use of biodegradable polymers; (2) cell viability supported temporarily by diffusion; (3) proliferation and organization of cells; (4) vascularization of the growing cell mass; and (5) proper cell function in the context of the new structure” [1]. These important factors, known more than 20 years ago, are still the challenges being faced in this field. In the past two decades advances have been made in understanding the importance of some of the underlying factors in tissue engineering, such as geometry, mechanical cues, and chemical factors. It is essential that these factors are taken into account when producing tissue engineering scaffolds by rapid prototyping.

Effects of Scaffold Architecture on Tissue Engineering

A wide range of architectural factors have an effect on the performance of tissue engineering scaffolds. The native extracellular matrix provides chemical and mechanical cues that induce cells to exhibit adhesion, migration, proliferation, and differentiation that is characteristic of that specific tissue [2]. The end goal of tissue engineering scaffold generation from a materials science perspective is to generate a scaffold with the same properties as the natural

extracellular matrix of the tissue being engineered, thus producing an environment in which cells will behave in the same manner as in the natural tissue.

It is well-established that cells behave vastly differently in 2-D and 3-D environments [3]. Cells grown on 2-D surfaces have a flat, spread morphology; different proliferation rates; inhibited differentiation; and significantly different phenotypes [3, 4]. For example, Ma *et al.* found that cells on 2-D surfaces had different cell cycle progression and less differentiation than cells in 3-D surfaces [5]. Sahai and Marshall found that cells in 2-D may have different responses to pharmacological agents than cells in 3-D [4]. These behavioral differences necessitate that tissue engineering utilize 3-D scaffold instead of 2-D substrate for generating new tissues.

Another important architectural factor is surface chemistry and morphology. In tissue engineering, cells must have some sort of cell-substrate adhesion in order to survive, since the majority of mammalian cells are anchorage-dependent [6, 7]. The quality of cell-substrate adhesion is highly dependent on the surface roughness and surface energy of the scaffold material [8-12]. Lampin *et al.* performed cell adhesion and spreading studies on PMMA substrates of varying surface roughnesses that were produced by sand-blasting [8]. Increased surface roughnesses resulted in increased hydrophobicity and improved cell adhesion. In a series of studies by Laser Zentrum Hannover, spike structures were produced in various materials to determine the effects of hydrophobicity and surface roughness on cell adhesion [10, 12-14]. Spike structures were generated by laser ablation and/or micromolding

in silicon, titanium, and silicone elastomer [10, 12-14]. In all of these materials, the presence of a spiked morphology increased the surface roughness and corresponding hydrophobicity of the surface. Interestingly, their studies indicated that the effects of hydrophobicity on proliferation rate was cell-type specific. For example, fibroblasts exhibited decreased proliferation on spiked surfaces while neuroblastoma cells exhibited no change in proliferation rate [10, 12]. This finding indicates that surface roughness may be used to select for a certain cell type, for example inhibiting proliferation of fibroblasts, which are responsible for scar tissue formation. Experiments by Ranella *et al.* with similar spiked structures achieved comparable results [15]. Mouse fibroblasts, grown on silicon surfaces that were flat and of various spiked surface roughnesses, had increased densities and adhesion for low roughness ratios (<3) and low cell density and adhesion for high roughness ratios (>3). Dulgar-Tulloch *et al.* examined the effect of the grain size of ceramics on human mesenchymal stem cell, osteoblast, and fibroblast proliferation [16]. For all three materials, average grain sizes of 200 nm had the greatest cell proliferation, with grain sizes of 1500 nm having slightly reduced proliferation and grain sizes of 50 nm having significantly reduced proliferation. Numerous studies have shown that surface roughness on the microscale can reduce proliferation and adhesion [10, 12-15], whereas surface roughness on the nanoscale can improve cell adhesion and proliferation [17].

In addition to affecting cell adhesion and proliferation, surface features may also be used to control cell orientation. Rebollar *et al.* produced grooves of varying periodicities (200-430 nm) and depths (30-100 nm) in polystyrene by polarized KrF laser light [17]. Human

embryonic kidney cells, Chinese hamster ovary cells, human myoblasts, and rat skeletal myoblasts all aligned parallel to the nanoscale grooves. These modified surfaces also demonstrated enhanced adhesion and proliferation for human embryonic kidney cells. A phase contrast image of human myoblasts aligned parallel to the nanoscale grooves after 2 days of culturing is presented in (Figure 1d). Teixeira *et al.* produced grooves in silicon with pitches of 400, 800, 1200, 1600, 2000, and 4000 nm for examining the effects of surface topography on keratocytes [18]. Smooth silicon has random orientation of cells; the 400 nm pitch surface had approximately 50% of the cells oriented parallel to the grooves; and the rest of the surfaces had greater than 65% of the cells oriented parallel to the grooves. Patterned surfaces also had significantly greater cell elongation than the smooth surface. Cells on the nanoscale surfaces exhibited fewer stress fibers and focal adhesions than the microscale surfaces. The differences in cell stress fiber orientation on these surfaces can clearly be seen in (Figure 1a-c). Cells on smooth silicon (C) have random stress fiber orientation, cells on the 4000 nm surface (B) are strongly aligned parallel to the grooves, and cells on the 400 nm surface are less strongly aligned. Miller *et al.* demonstrated that laser-micromachined lines in silicon may be used to control alignment of human aortic-vascular smooth muscle cells; on these surfaces the cells were aligned perpendicular to these grooves which were spaced approximately 100 μm apart [19]. These findings indicate that cell orientation can be controlled and is highly dependent on the size scale of the surface patterning.

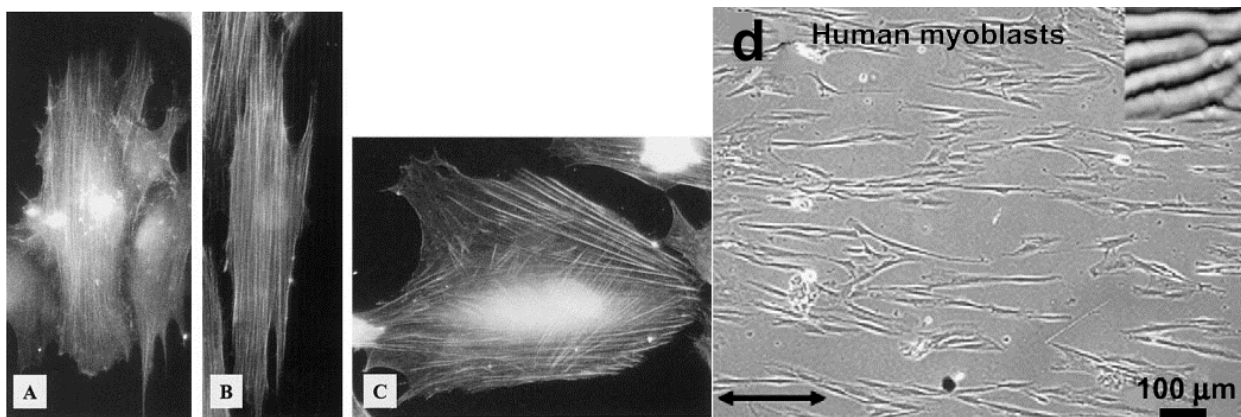


Figure 1. Effect of surface features on cells. Cells align with groves and ridges at the nanometer and micron scale. Keratocytes with stress fibers visible: A) Cell aligned on a 400-nm pitch vertical pattern*; B) cell aligned on a 4000-nm pitch pattern*; C) Cells on a smooth substrate; stress fibers are randomly oriented*. D) Human myoblasts aligned to nano-scale ridges on polystyrene foil**.

*Reprinted with permission from Teixeira AI, Nealey PF, Murphy CJ. Responses of keratocytes to micro- and nanostructured substrates. *J Biomed Mater Res* 2004; 71A: 369-376. © 2004, John Wiley & Sons.

**Reprinted from *Biomaterials*, Volumer 29, Rebollar E, Frischauf I, Olbrich M, et al. Proliferation of aligned mammalian cells on laser-nanostructured polystyrene. 1796-1806, Copyright 2008, Elsevier.

Mass Transport in Tissue Engineering Scaffolds

Mass transport is essential for a successful tissue engineering scaffold. Without a means of receiving nutrients and removing waste, cells in a scaffold cannot survive [20]. In native

tissue, mass transport is achieved via the vasculature. However, producing vascularized *in vitro* scaffolds has been challenging so an alternative approach has generally been preferred. The predominant technique for enabling mass transport in tissue engineering scaffolds has been via porosity. Scaffolds with a high porosity enable nutrients and waste to be transported via diffusion [21]. Research has indicated that 80-90% porosity is ideal for mass transport in scaffolds [22]. However, there is a trade-off between high porosity and mechanical integrity of the scaffold, so an appropriate balance between the two must be maintained.

An alternative solution to the mass transfer issue is to develop scaffolds with vasculature. As native tissue uses vasculature to achieve mass transport, this native transport mechanism can be used in tissue engineering scaffolds. An additional cause for producing pre-vascularized scaffolds is that vascularization aids scaffolds in integrating with the host tissue [23]. It has been established in the literature that endothelial cells in a 3-D environment will spontaneously form tube-like structures [24-28]. Kelm *et al.* produced a vascularized macrotissue structure by assembly of pre-generated microtissues [29]. Myoblast microtissues produced by gravity-enforced self-assembly were coated with vascular endothelial cells, which resulted in development of a vascular structure initiated by the fibroblast VEGF production. A macrotissue was then produced by casting of these macrotissues in an agarose mold. Tsuda *et al.* created pre-vascularized tissue by creating multiple alternating monolayers of fibroblasts or patterned endothelial cells [30]. Unger *et al.* showed that human endothelial cells and osteoblasts in co-culture on scaffolds will distribute and form structures resembling bone tissue, including microcapillary-like structures [31]. *In vivo* implantation of

these scaffolds into immune-deficient mice confirmed integration with the host vasculature and formation of chimeric microcapillaries (containing both human and mouse cells). Both outgrowth of human cell microcapillaries into host tissue and ingrowth of mouse vasculature into the scaffold were observed. In contrast, scaffolds with solely endothelial cells and unseeded scaffolds exhibited poor ingrowth.

Cell Seeding of Tissue Engineering Scaffolds

The maximum distance that cells have been able to migrate to fill an acellular matrix is 1 cm [32]. Therefore, in order to populate acellular scaffolds larger than 1 cm, the scaffolds must be directly seeded with cells. Various seeding methods exist: immersion of a porous scaffold in a cell suspension, pipetting cell suspensions into a scaffold, centrifuging a porous scaffold in a cell suspension, printing into a porous scaffold, and generating a scaffold with cells already contained in the material. Immersion of a scaffold into a cell suspension and pipetting of cell suspensions into scaffolds are the most common methods, due to their ease of use. In order for these techniques to be successful, the scaffolds must be highly porous, which reduces their mechanical stability. Another drawback is that cell suspensions have a low cell density compared to tissue. In 2004, the Atala research group reported a novel cell seeding technique using centrifugal force [33]. Tubes containing the scaffold and a cell suspension were centrifuged, which resulted in deposition of the majority of the cells in the suspension into the scaffold. Centrifugal seeding was approximately 3 times more effective than static seeding. Centrifugation helps to reduce the problem of low cell density in scaffold

seeding, though scaffolds still need to be porous. Inkjet printing and laser bioprinting have been used to print cells into porous scaffolds [34, 35]. The advantage of these techniques is that multiple cells can be printed into the scaffolds in controlled locations. Laser bioprinting has an advantage over inkjet printing in that high cell density can be achieved, since inkjet printing requires dilute suspensions [36]. Additionally, both inkjet printing and laser bioprinting can be used to produce scaffolds with cells already embedded inside [37, 38].

Conclusions

The various rapid prototyping methods have numerous attributes that make them appealing for generation of tissue engineering scaffolds. The most obvious advantage is that all rapid prototyping techniques allow for complete control of scaffold geometry (e.g., porosity, pore location, size, and shape). Some techniques, such as two-photon polymerization and laser ablation have the ability to precisely control the surface features of scaffolds. Printing-based techniques enable precise patterning of cells and generation of multi-material scaffolds. Light-based rapid prototyping generally facilitates higher resolution structures than other rapid prototyping processes. The ability to control many of the factors that affect the performance of tissue engineering scaffolds make rapid prototyping an important tool in advancing the field of tissue engineering.

References

- [1] Vacanti CA. The history of tissue engineering. *J Cell Mol Med* 2006 JUL-SEP;10(3):569-576.
- [2] Yaszemski MJ, Trantolo DJ, Lewandrowski K, Hasirci V, Altobelli DE, Wise DL. *Tissue Engineering and Novel Drug Delivery Systems*. 1st ed. USA: CRC Press; 2004.
- [3] Edelman DB, Keefer EW. A cultural renaissance: in vitro cell biology embraces three-dimensional context. *Exp Neurol* 2005 MAR;192(1):1-6.
- [4] Sahai E, Marshall CJ. Differing modes of tumour cell invasion have distinct requirements for Rho/ROCK signalling and extracellular proteolysis. *Nat Cell Biol* 2003 AUG;5(8):711-719.
- [5] Ma T, Li Y, Yang ST, Kniss DA. Effects of pore size in 3-D fibrous matrix on human trophoblast tissue development. *Biotechnol Bioeng* 2000 DEC 20;70(6):606-618.
- [6] Meredith JE, Fazeli B, Schwartz MA. The Extracellular-Matrix as a Cell-Survival Factor. *Mol Biol Cell* 1993 SEP;4(9):953-961.
- [7] Atala A. Engineering organs. *Curr Opin Biotechnol* 2009 OCT;20(5):575-592.

[8] Lampin M, WarocquierClerout R, Legris C, Degrange M, SigotLuizard MF. Correlation between substratum roughness and wettability, cell adhesion, and cell migration. *J Biomed Mater Res* 1997 JUL;36(1):99-108.

[9] Tesema Y, Raghavan D, Stubbs J. Bone cell viability on collagen immobilized poly (3-hydroxybutrate-co-3-hydroxyvalerate) membrane: Effect of surface chemistry. *J Appl Polym Sci* 2004 SEP 5;93(5):2445-2453.

[10] Fadeeva E, Schlie S, Koch J, Ngezahayo A, Chichkov BN. The hydrophobic properties of femtosecond laser fabricated spike structures and their effects on cell proliferation. *Physica Status Solidi A-Applications and Materials Science* 2009 JUN;206(6):1348-1351.

[11] Fadeeva E, Schlie S, Koch J, Chichkov BN. Selective Cell Control by Surface Structuring for Orthopedic Applications. *J Adhes Sci Technol* 2010;24(13-14):2257-2270.

[12] Schlie S, Fadeeva E, Koch J, Ngezahayo A, Chichkov BN. Femtosecond Laser Fabricated Spike Structures for Selective Control of Cellular Behavior. *J Biomater Appl* 2010 SEP;25(3):217-233.

[13] Koroleva A, Schlie S, Fadeeva E, Gittard SD, Miller P, Ovsianikov A, Koch J, Narayan RJ. Microreplication of laser-fabricated surface and three-dimensional structures. *J Optics* 2010;12(12):124009.

[14] Schlie S, Fadeeva E, Koroleva A, Ovsianikov A, Koch J, Ngezahayo A, Chichkov BN. Laser-based nanoengineering of surface topographies for biomedical applications. *Photonics and Nanostructures - Fundamentals and Applications* ;In Press, Corrected Proof.

[15] Ranella A, Barberoglou M, Bakogianni S, Fotakis C, Stratakis E. Tuning cell adhesion by controlling the roughness and wettability of 3D micro/nano silicon structures. *Acta Biomaterialia* 2010 JUL;6(7):2711-2720.

[16] Dulgar-Tulloch AJ, Bizios R, Siegel RW. Human mesenchymal stem cell adhesion and proliferation in response to ceramic chemistry and nanoscale topography. *Journal of Biomedical Materials Research Part a* 2009 AUG;90A(2):586-594.

[17] Rebollar E, Frischauf I, Olbrich M, Peterbauer T, Hering S, Preiner J, Hinterdorfer P, Romanin C, Heitz J. Proliferation of aligned mammalian cells on laser-nanostructured polystyrene. *Biomaterials* 2008 APR;29(12):1796-1806.

[18] Teixeira AI, Nealey PF, Murphy CJ. Responses of human keratocytes to micro- and nanostructured substrates. *Journal of Biomedical Materials Research Part a* 2004 DEC 1;71A(3):369-376.

- [19] Miller PR, Aggarwal R, Doraiswamy A, Lin YJ, Lee YS, Narayan RJ. Laser micromachining for biomedical applications. *JOM* 2009;61(9):35-40.
- [20] Borenstein JT, Terai H, King KR, Weinberg EJ, Kaazempur-Mofrad MR, Vacanti JP. Microfabrication technology for vascularized tissue engineering. *Biomed Microdevices* 2002 JUL;4(3):167-175.
- [21] Lanza R, Langer R, Vacanti JP. *Principles of Tissue Engineering*. Second ed. Burlington, MA: Academic Press; 1996.
- [22] Karande TS, Ong JL, Agrawal CM. Diffusion in musculoskeletal tissue engineering scaffolds: Design issues related to porosity, permeability, architecture, and nutrient mixing. *Ann Biomed Eng* 2004 DEC;32(12):1728-1743.
- [23] Phelps EA, Garcia AJ. Engineering more than a cell: vascularization strategies in tissue engineering. *Curr Opin Biotechnol* 2010 OCT;21(5):704-709.
- [24] Montesano R, Orci L, Vassalli P. In vitro Rapid Organization of Endothelial-Cells into Capillary-Like Networks is Promoted by Collagen Matrices. *J Cell Biol* 1983;97(5):1648-1652.

[25] Montesano R, Orci L. Tumor-Promoting Phorbol Esters Induce Angiogenesis In vitro. *Cell* 1985;42(2):469-477.

[26] Tsujii M, Kawano S, Tsuji S, Sawaoka H, Hori M, DuBois RN. Cyclooxygenase regulates angiogenesis induced by colon cancer cells. *Cell* 1998 MAY 29;93(5):705-716.

[27] Takei A, Tashiro Y, Nakashima Y, Sueishi K. Effects of Fibrin on the Angiogenesis In Vitro of Bovine Endothelial-Cells in Collagen Gel. *In Vitro Cellular & Developmental Biology-Animal* 1995 JUN;31(6):467-472.

[28] Black AF, Berthod F, L'Heureux N, Germain L, Auger FA. In vitro reconstruction of a human capillary-like network in a tissue-engineered skin equivalent. *Faseb Journal* 1998 OCT;12(13):1331-1340.

[29] Kelm JM, Djonov V, Ittner LM, Fluri D, Born W, Hoerstrup SP, Fussenegger M. Design of custom-shaped vascularized tissues using microtissue spheroids as minimal building units. *Tissue Eng* 2006 AUG;12(8):2151-2160.

[30] Tsuda Y, Shimizu T, Yarnato M, Kikuchi A, Sasagawa T, Sekiya S, Kobayashi J, Chen G, Okano T. Cellular control of tissue architectures using a three-dimensional tissue fabrication technique. *Biomaterials* 2007 NOV;28(33):4939-4946.

[31] Unger RE, Ghanaati S, Orth C, Sartoris A, Barbeck M, Halstenberg S, Motta A, Migliaresi C, Kirkpatrick CJ. The rapid anastomosis between prevascularized networks on silk fibroin scaffolds generated in vitro with cocultures of human microvascular endothelial and osteoblast cells and the host vasculature. *Biomaterials* 2010 SEP;31(27):6959-6967.

[32] Dorin RP, Pohl HG, De Filippo RE, Yoo JJ, Atala A. Tubularized urethral replacement with unseeded matrices: what is the maximum distance for normal tissue regeneration? *World J Urol* 2008 AUG;26(4):323-326.

[33] Godbey WT, Hindy BSS, Sherman ME, Atala A. A novel use of centrifugal force for cell seeding into porous scaffolds. *Biomaterials* 2004 JUN;25(14):2799-2805.

[34] Hollister SJ. Porous scaffold design for tissue engineering. *Nature Materials* 2005 JUL;4(7):518-524.

[35] Ovsianikov A, Gruene M, Pflaum M, Koch L, Maiorana F, Wilhelmi M, Haverich A, Chichkov B. Laser printing of cells into 3D scaffolds. *Biofabrication* 2010 MAR;2(1):014104.

- [36] Koch L, Kuhn S, Sorg H, Gruene M, Schlie S, Gaebel R, Polchow B, Reimers K, Stoelting S, Ma N, Vogt PM, Steinhoff G, Chichkov B. Laser Printing of Skin Cells and Human Stem Cells. *Tissue Engineering Part C-Methods* 2010 OCT;16(5):zs847-854.
- [37] Cohen DL, Malone E, Lipson H, Bonassar LJ. Direct freeform fabrication of seeded hydrogels in arbitrary geometries. *Tissue Eng* 2006 MAY;12(5):1325-1335.
- [38] Gruene M, Deiwick A, Koch L, Schlie S, Unger C, Hofmann N, Bernemann I, Glasmacher B, Chichkov B. Laser Printing of Stem Cells for Biofabrication of Scaffold-Free Autologous Grafts. *Tissue Engineering Part C-Methods* 2011 JAN;17(1):79-87.

3. DRUG DELIVERY VIA MICRONEEDLES AND RELATED TECHNOLOGIES

3.1 Fabrication of Polymer Microneedles Using a Two-Photon Polymerization and Micromolding Process

*The following section is a complete article from the journal: **Journal of Diabetes Science & Technology** © 2009 Diabetes Technology Society*

Source: Gittard SD, Ovsianikov A, Monteiro-Riviere NA, Lusk J, Morel P, Minghetti P, Lenardi C, Chichkov BN, Narayan RJ. Fabrication of Polymer Microneedles Using a Two-Photon Polymerization and Micromolding Process. *J Diabetes Sci Technol* 2009 March; 3(2):304-311.

Note: This article has been reformatted. In particular, the location of figures and spacing may have changed. The references are formatted as in the original manuscript.

Journal of Diabetes Science and Technology

Volume 3, Issue 2, March 2009

© Diabetes Technology Society

ORIGINAL ARTICLES**Fabrication of Polymer Microneedles Using a
Two-Photon Polymerization and Micromolding Process**

Shaun D. Gittard, B.S.,¹ Aleksandr Ovsianikov, D.Sc.,² Nancy A. Monteiro-Riviere, Ph.D.,^{1,3}
Jason Lusk, M.S.,⁴ Pierre Morel, M.S.,⁴ Paola Minghetti, Ph.D.,⁵ Cristina Lenardi, Ph.D.,⁶
Boris N. Chichkov, D.Sc.,² and Roger J. Narayan, M.D., Ph.D.¹

Author Affiliations: ¹Joint Department of Biomedical Engineering, University of North Carolina and North Carolina State University, Raleigh, North Carolina; ²Nanotechnology Department, Laser Zentrum Hannover e.V., Hannover, Germany; ³Center for Chemical Toxicology Research and Pharmacokinetics, North Carolina State University, Raleigh, North Carolina; ⁴ElectroForce Systems Group, Bose Corporation, Eden Prairie, Minnesota; ⁵Faculty of Pharmacy, University of Milan, Milan, Italy; and ⁶Department of Physics, University of Milan, Milan, Italy

Abbreviations: (2PP) two-photon polymerization, (CAD) computer-aided design, (KGM-2) keratinocyte growth medium-2, (PDMS) poly-dimethylsiloxane, (UVB) ultraviolet B

Keywords: microneedle, photopolymer, transdermal drug delivery

Corresponding Author: Roger J. Narayan, M.D., Ph.D., Joint Department of Biomedical Engineering, University of North Carolina and North Carolina State University, 2147 Burlington Engineering Labs, Raleigh, NC 27695 7115; email address roger_narayan@unc.edu

Abstract

Background:

Microneedle-mediated drug delivery is a promising method for transdermal delivery of insulin, incretin mimetics, and other protein-based pharmacologic agents for treatment of diabetes mellitus. One factor that has limited clinical application of conventional microneedle technology is the poor fracture behavior of microneedles that are created using conventional materials and methods. In this study polymer microneedles for transdermal delivery were created using a two-photon polymerization (2PP) microfabrication and subsequent polydimethylsiloxane (PDMS) micromolding process.

Methods:

Solid microneedle arrays, fabricated by means of 2PP, were used to create negative molds from PDMS. Using these molds microneedle arrays were subsequently prepared by molding eShell 200, a photo-reactive acrylate-based polymer that exhibits water and perspiration resistance.

Results:

The eShell 200 microneedle array demonstrated suitable compressive strength for use in transdermal drug delivery applications. Human epidermal keratinocyte viability on the eShell 200 polymer surfaces was similar to that on polystyrene control surfaces. *In vitro* studies demonstrated that eShell 200 microneedle arrays fabricated using the 2PP microfabrication and PDMS micromolding process technique successfully penetrated human stratum corneum and epidermis.

Conclusions:

Our results suggest that a 2PP microfabrication and subsequent PDMS micromolding process may be used to create microneedle structures with appropriate structural, mechanical, and biological properties for transdermal drug delivery of insulin and other protein-based pharmacologic agents for treatment of diabetes mellitus.

J Diabetes Sci Technol 2009;3(2):304-311

Introduction

The article presents a new material, eShell 200, that may be used in microneedle fabrication. There is a need for microneedles with improved mechanical properties to deliver insulin and other peptide drugs. The article also examines the mechanical properties of eShell 200 microneedles. Results suggest that eShell 200 may be an appropriate material for use in microneedle fabrication.

Insulin is a hormone produced by the pancreas that promotes the storage of glucose in the liver and in other locations within the body.¹ The term “diabetes mellitus” includes several metabolic disorders that result from deficiencies in insulin action or insulin secretion. Damage to the eyes, kidneys, nerves, and blood vessels may occur as a result of elevated blood glucose levels (hyperglycemia).² Several techniques for administering insulin to diabetes patients have been considered over the past century. Insulin and other protein-based pharmacologic agents cannot be delivered orally since they can be metabolized in the liver or degraded by proteolytic enzymes (e.g., pepsin) in the gastrointestinal tract.³ Insulin also cannot be delivered using conventional transdermal patches due to its high molecular

weight.² Insulin is currently delivered by means of subcutaneous injection; however, this technique has numerous shortcomings, including pain and trauma at the injection site.⁴

Microneedles, miniaturized needles with at least one dimension under 1 mm in length, may be used to create pores in the stratum corneum layer of the skin and enable diffusion of pharmacologic agents.^{2,5} The delivery of insulin using microneedles has several benefits over conventional subcutaneous delivery processes.¹ For example, no specialized medical training or supervision is required for use of these devices. Pain to the patient and trauma at the injection site is minimized since these devices do not interact with nerve endings located within the dermis layer of the skin.^{6,7} Microneedle delivery and subcutaneous injection of insulin have been shown to reduce blood glucose levels with similar efficiency.⁸

A variety of microfabrication techniques have been previously used for fabrication of microneedles, including wet etching, dry etching, two-photon polymerization (2PP), electroplating, and micromolding.⁹⁻¹⁶ For example, Wilke and colleagues¹² fabricated microneedles by anisotropic wet etching of a silicon substrate; the needle density that may be obtained using this technique is limited since only one row of needles may be fabricated per chip. Kobayashi and Suzuki⁹ and McAllister and associates¹⁵ fabricated electroplated shell structures; these structures demonstrate thin microneedle walls. Chun and coworkers¹⁰ demonstrated fabrication of microcapillaries using deep reactive ion etching; however, the needle density was limited by isotropy of the etch step. Griss and Stemme¹¹ and Gardeniers and colleagues¹³ fabricated single-crystal silicon microneedle arrays. In these studies needle

openings were positioned far from the tip, which necessitated deeper insertion within the skin. Despite these efforts microneedles prepared using conventional microfabrication processes have not been employed in widespread clinical use.

One factor that has limited clinical application of conventional microneedle technology is the poor fracture behavior of microneedles that are prepared using conventional materials and methods. Microneedles undergo mechanical failure by a variety of methods, including tip buckling, tip fracture, and base fracture.^{16,17} Since many biomedical microdevice fabrication technologies originated in the semiconductor industry, silicon is widely used for fabricating microneedles. However, silicon is extremely brittle, and silicon microneedles are prone to catastrophic failure; for example, stress concentration regions at the microneedle tip are susceptible to fracture. Fracture of silicon microneedles during *in vivo* studies has been reported.¹⁸ Metal microneedles produced by electroplating possess thin walls and exhibit poor mechanical properties. These devices are prone to buckling of the tip during insertion; failure of metal microneedles has been reported at less than 1 N compressive force.¹⁷ Microneedles that are attached to a substrate (e.g., Ormocer® microneedles on a glass substrate) are susceptible to detachment from the substrate and retention in the skin.¹⁶ The development of novel materials and fabrication methods for producing microneedles with appropriate mechanical properties for transdermal delivery will enable wider clinical use of this technology.

In this study microneedles containing eShell 200 polymer were created using a 2PP microfabrication and subsequent polydimethylsiloxane (PDMS) micromolding process. LaFratta and associates¹⁹ and Li and Fourkas²⁰ demonstrated that a combination of photopolymerization and micromolding may be used to produce three-dimensional microstructures. eShell 200 is a photo-reactive acrylate-based polymer that is suitable for rapid prototyping of functional medical parts.²¹ It is a rigid, durable polymer produced by Envisiontec (Ferndale, MI) for use in medical applications, including fabrication of thin-walled hearing aid shells. Due to the fact that it exhibits high cross linkage, eShell 200 polymer is suitable for use in environments containing high humidity (e.g., water or perspiration). It exhibits hardness of 83 Shore (D2240 test method), tensile strength of 57.8 MPa (D638M test method), flexural strength of 2300 MPa (D790M test method), Young's modulus of 2400 GPa (D638M test method), elongation at yield of 3.2% (D638M test method), dielectric strength of 14.6 (D149-97a test method), and glass transition temperature of 109 °C (E1545-00 test method).²¹

The structural, mechanical, and biological properties of eShell 200 microneedles created using a 2PP micro-fabrication and subsequent PDMS micromolding process were examined by scanning electron microscopy, energy dispersive x-ray spectroscopy, compressive force failure testing, and MTT cell viability assay. We anticipate that microneedles fabricated using this high-throughput technique may be used for delivery of insulin and other protein-based pharmacologic agents.

Experimental Procedure

A computer-aided design (CAD) program (DeskArtes Oy, Espoo, Finland) was used to prepare an STL format file for fabrication of the microneedle array master structure. The master structure was a 5 x 5 array of 25 identical solid microneedles (needle height = 500 μm ; needle base diameter = 150 μm ; needle center to needle center distance = 500 μm).

The 2PP technique was used to create a microneedle master.^{14,16,22} This process involves nonlinear light absorption, igniting chemical reactions and material hardening within well-defined, highly localized volumes. The 2PP process involves spatial and temporal overlap of photons in order to bring about chemical reactions, which lead to photopolymerization and material hardening within well-defined, highly localized volumes. A titanium:sapphire laser (Kapteyn-Murnane, Boulder, CO) was used to obtain femtosecond laser pulses (60 fs; 94 MHz; <450 mW; 780 nm), which were focused using a 10x plan achromat microscope objective. Nonlinear absorption of laser pulses cleaved chemical bonds of photoinitiator molecules located in a small focal volume within the polymer resin. The radicalized photoinitiator molecules created radicalized polymolecules through interaction with the monomers; reactions were terminated when radicalized polymolecules interacted with other radicalized polymolecules. By moving the laser focus in three dimensions within the photopolymer, material was polymerized along the laser trace. A combination of three C-843 linear translational stages (Physik Instrumente, Karlsruhe, Germany) and a galvo scanner

(Scanlab AG, Puchheim, Germany) was utilized in order to alter the laser focus position in three dimensions.

The original microneedle array was fabricated by 2PP of SR 259 polymer (Sartomer, Paris, France) containing 2 wt % Irgacure 369 photoinitiator (Ciba Specialty Chemicals, Basel, Switzerland) on a glass cover slip. SR 259 is a polyethylene glycol (200) diacrylate that exhibits low volatility, a refractive index of 1.4639, viscosity of 25 cps at 25 °C, surface tension of 41.3 dynes/cm, and a molecular weight of 302.23. The Irgacure® 369 photoinitiator exhibits an absorption peak at $\sim\lambda = 320$ nm. The microneedle array was subsequently sputter coated with gold (coating time = 245 s; coating current = 10 mA) to improve separation of the master structure from the mold. The glass cover slip containing the microneedle array was then fixed to a glass microscope slide using double-sided tape.

A negative mold of the microneedle array was fabricated using PDMS. Sylgard® 184 silicone elastomer and hardening agent (Dow Corning, Midland, MI) were prepared according to manufacturer instructions. The liquid mixture was subsequently degassed under vacuum. After degassing, a 20 mm diameter open center aluminum crimp seal (Sigma Aldrich, St. Louis, MO) was placed on the glass with the microneedle array located in the center of the ring. The unpolymerized silicone elastomer was poured over the microneedle array until the aluminum ring was completely filled. The glass slide with microneedle array, aluminum ring, and silicone elastomer were placed under 100 mbar vacuum in order to remove residual gas voids. The sample, consisting of a glass slide, microneedle array,

aluminum seal, and silicone, was subsequently placed on a hot plate for PDMS cross linking. The hot plate temperature was increased from 25 to 100 °C over 30 min and then maintained at 100 °C for 30 min. Once the polymerized mold had cooled, it was mounted onto a C843 linear translational stage (Physik Instrumente, Karlsruhe, Germany) in order to separate the mold from the master structure. The glass slide was held in place against the table using two metal restraining bars, while the aluminum seal containing the PDMS mold was vertically moved by the stage. A second PDMS mold (depth = 2 mm; diameter = 1 cm) was used for molding the substrate.

Approximately 50 μ l of eShell 200 polymer (Envisiontec, Gladbeck, Germany) was placed on the surface of the PDMS mold over the microneedle array. The mold containing eShell 200 polymer was subsequently degassed under vacuum in order to allow the eShell 200 polymer to completely fill the mold. The cylindrical substrate mold was then filled with eShell 200 polymer, and the microneedle mold was placed on top of it. The two molds were placed in contact, with the substrate mold facing up and the microneedle mold facing down so that the two surfaces with eShell 200 were in contact. The molds were then exposed for 2 min to an ultraviolet curing lamp, which provided visible and ultraviolet light emission (Thorlabs, Newton, NJ). The molds were subsequently inverted; the substrate side was exposed to ultraviolet light for 1 min. After ultraviolet curing, the molds and polymerized microneedle arrays were separated by hand.

Images of the eShell 200 microneedles were obtained using a S3200 scanning electron microscope (Hitachi, Tokyo, Japan), which was equipped with a Robinson back-scattered electron detector. Energy dispersive x-ray spectroscopy was performed to determine the chemical composition of the microneedles. Compression testing of the eShell 200 microneedle arrays was performed using an Electroforce 3100 system (Bose, Eden Prairie, MN). The eShell 200 microneedle arrays were placed directly on the load cell surface. Axial loading was applied to the microneedle array (displacement rate = 10 $\mu\text{m/s}$) until a force of 10 N was achieved. Compression testing of microneedles against hard surfaces such as polytetrafluoroethylene has been used to examine the mechanical properties of microneedle arrays.^{14,16,17}

Human epidermal keratinocyte viability on polymerized eShell 200 material was examined using the MTT assay.²⁴ The MTT assay is based on reduction of a yellow tetrazolium salt (3-[4,5-dimethylthiazol-2-yl] 2,5-diphenyl tetrazolium bromide) to a purple formazan dye by mitochondrial succinic dehydrogenase. The MTT assay uses mitochondria metabolism as a measure of cell viability. Cylindrical pellets of eShell 200 ($n = 3$) were created by exposure of the polymer in PDMS molds (diameter = 6 mm; depth = 1 mm) using the same curing lamp and exposure time that were used to fabricate the microneedle arrays. Prior to conducting the MTT assay, the pellets were sterilized by ultraviolet B (UVB) radiation for 3 h, with both sides of the pellets receiving equal UVB light exposure. Cryopreserved human epidermal keratinocytes (Lonza, Walkersville, MD) were passed twice to initiate propagation, and 285,000 human epidermal keratinocytes were seeded in 10 ml of

keratinocyte growth medium-2 (KGM-2), consisting of serum-free keratinocyte basal media, which is supplemented with bovine pituitary extract, epinephrine, GA-1000 (gentamicin-amphotericin), human epidermal growth factor, hydrocortisone, insulin, and transferrin (Lonza, Basel, Switzerland). The seeded human epidermal keratinocytes were then cultured at 37 °C and 5% CO₂ until 80% confluency was obtained. The cells were then transferred to 96 well plates, in which pellets were placed at the bottom of the wells. The pellets and polystyrene culture wells were washed with 1 ml of KGM-2 prior to seeding. The pellets were held to the bottom of the culture wells by applying a drop of Akwa Tears® (Akorn, Buffalo Grove, IL) to the bottom of the wells prior to pellet placement. The human epidermal keratinocytes were allowed to proliferate for 24 h before the MTT assay was performed. Human epidermal keratinocyte viability was determined by measuring absorbance at $\lambda = 550$ nm using a Multiskan RC ELISA plate reader (Labsystems, Helsinki, Finland). Cell viability on the eShell 200 polymer pellets was normalized to surface area and compared with growth on the surface of polystyrene wells with no pellets.

Human abdominal skin obtained from a surgical abdominoplasty was used to assess skin penetration of the microneedles. The use of this tissue received institutional approval according to the Declaration of Helsinki of the World Health Association. The skin was utilized within 24 h of removal. Subdermal fat was mechanically removed via dermatome to achieve uniform layers of full thickness skin. Stratum corneum and epidermal layers were obtained from full thickness skin by a heat separation method. The skin was immersed in distilled water at 60 ± 1 °C for 1 min. Then the stratum corneum and epidermis was gently

peeled from the dermis using forceps. Isolated stratum corneum and epidermal layers were dried in a desiccator at ~30% relative humidity, wrapped in aluminium foil, and stored at -20 ± 1 °C until use. The integrity of the barrier was visually inspected to ensure that the stratum corneum and epidermal layers were unaltered during this process. This method of skin preparation has previously been used to examine microneedle-mediated drug delivery and other transdermal drug delivery techniques.^{25–28} Microneedles were inserted into the tissue using an electronic texture analyzer (Acquati, Arese, Italy). An eShell 200 microneedle array was placed on the stratum corneum and epidermis sample. The eShell 200 microneedle array was held in place using a polystyrene support and was compressed against the sample using a stainless steel probe (surface area = 1.13 cm²). The probe was moved toward the sample at a rate of 300 mm/min until a maximum load of 4 N was obtained. The microneedles were held in place for 3 s and then removed. Similar protocols for examining microneedle insertion into human stratum corneum and epidermis have been reported in the literature.^{26,29–31} Optical microscopy was used to examine the microneedle–skin interaction.

Results

Scanning electron microscopy was used to examine microscale features of microneedles fabricated using the 2PP microfabrication and subsequent PDMS micromolding process. A scanning electron micrograph of a microneedle array is shown in **Figure 1a**, and an individual microneedle is shown in **Figure 1b**. The microneedles exhibited length values of 500 μm and base diameter values of 150 μm ; good microneedle-to-microneedle uniformity

was observed in the microneedle array. The microneedles exhibited tip angle values of 45°. In some cases microneedles in the microneedle arrays demonstrated slight deviations from the dimensions that were specified in the stereolithography CAD file. For example, the tips of some microneedles in the microneedle arrays were slightly truncated. In other cases sharper needle tips were observed. Iteration of processing parameters, including molding materials and mold fabrication parameters, may enable the development of microneedle arrays containing microneedles with more uniform tip diameters. In general, microscale features in the microneedles were consistent with the dimensions specified in the stereolithography CAD file. Energy-dispersive x-ray spectroscopy studies of the microneedle arrays indicated that eShell 200 is composed of 78% carbon, 20% oxygen, and 2% titanium. No trace amount of other elements, including those with known toxicity, was noted. Carbon and oxygen are common components of organic molecules, and titanium exhibits excellent compatibility with human tissues.³²

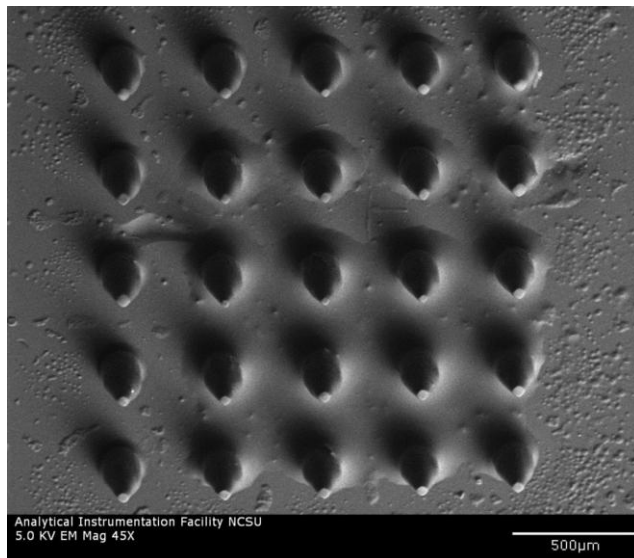


Figure 1a. Scanning electron micrograph of an eShell 200 microneedle array created using the 2PP microfabrication and subsequent PDMS micromolding process.

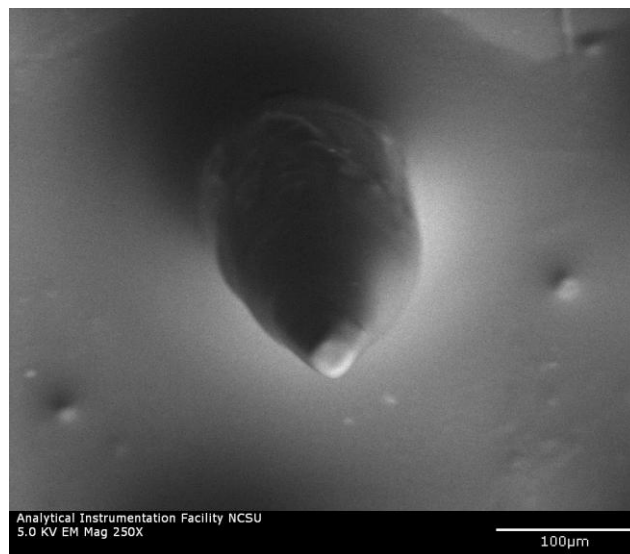


Figure 1b. Scanning electron micrograph of an eShell 200 individual microneedle created using the 2PP microfabrication and subsequent PDMS micromolding process.

Cell growth on the polystyrene control surfaces and the Envisiontec eShell 200 polymer surfaces was examined using an inverted microscope. The Envisiontec eShell 200 polymer surfaces were shown to support human epidermal keratinocyte growth, and 24 h MTT assays indicated that human epidermal keratinocyte growth on the eShell 200 surfaces was similar to that on polystyrene control surfaces (>95%). In addition, these growth values were not significantly different ($p < .05$). These results suggest that Envisiontec eShell 200 polymer processed using micromolding does not decrease cell viability or cell growth.

A plot of force versus displacement for the eShell 200 microneedle array obtained during compression testing is shown in **Figure 2**. None of the 25 eShell 200 microneedles in the microneedle array fractured during axial compression. The 5 x 5 eShell 200 microneedle arrays were able to withstand an axial load of 10 N without fracture, which corresponds to an axial load of 0.4 N per needle. The axial load applied to the Envisiontec eShell 200 microneedle array in this study was more than seven times greater than the force for microneedle insertion into skin that was previously described by Davis and coworkers¹⁷ (1.29 N); their study involved microneedles with similar tip diameters. The force versus displacement curve was linear at axial loads between 4 and 10 N, indicating that the microneedle array exhibited elastic deformation and not plastic deformation over these values. These results suggest that eShell 200 polymer microneedles fabricated using the PDMS micromolding process are able to penetrate through human skin without fracture.

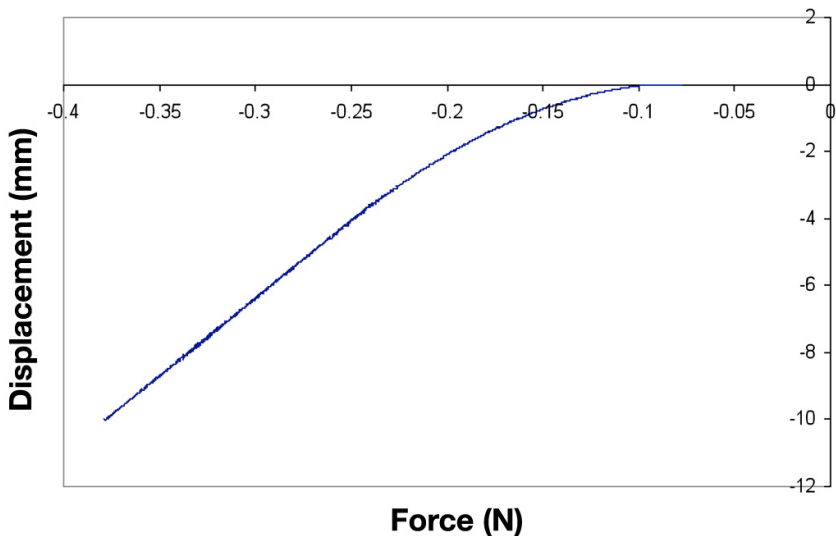


Figure 2. Characteristic plot of force versus displacement for eShell 200 microneedle array obtained during axial compression testing.

The eShell 200 microneedle arrays were successfully able to create pores in human stratum corneum and epidermis. An image of the pores created by microneedle insertion and removal is shown in **Figure 3**. Approximately 58 μm diameter pores were observed in the human stratum corneum and epidermis. The pores are irregular in shape and smaller than the microneedle diameter. These features were attributed to anisotropic tensile forces caused by the collagen and elastic fibers in the skin. These forces can contract the skin and thereby reduce the pore size in the stratum corneum. By adjusting the focal height of the microscope, we were able to verify that the needles created pores that completely passed through the stratum corneum layer and entered the deeper layers of the epidermis. The pores became smaller in size but remained open after removal of the microneedle arrays. These open pores

may serve as conduits for transport of pharmacologic agents after microneedle removal. Park and colleagues²⁶ reported similar results in a poly(L-glycolic acid) microneedle skin penetration study using the human stratum corneum and epidermis model.

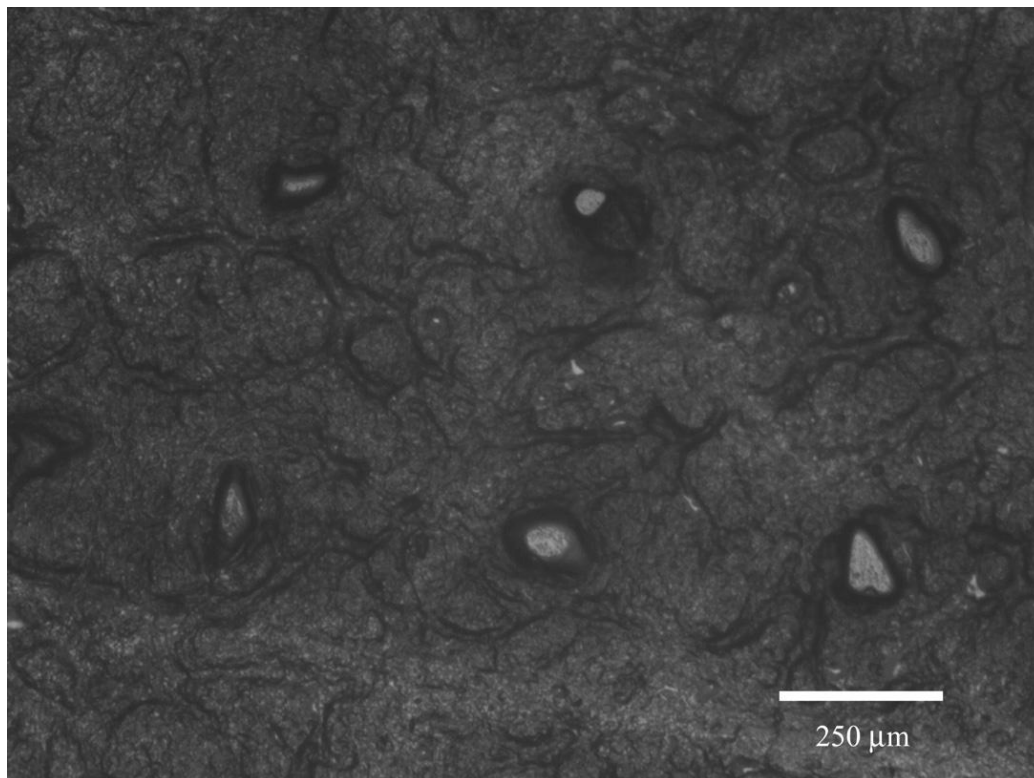


Figure 3. Optical micrograph of human stratum corneum and epidermis sample after eShell 200 microneedle array insertion and removal.

Conclusions

Polymer microneedles for transdermal delivery of insulin or other protein-based pharmacologic agents were created using a combination of 2PP microfabrication and PDMS

micromolding. This approach generally provides high-fidelity reproduction of microscale features; however, some improvement in reproduction of small scale features (e.g., microneedle tips) may be possible. The eShell 200 microneedle array demonstrated suitable compressive strength for use in transdermal drug delivery applications. Human epidermal keratinocyte viability on the eShell 200 polymer surfaces was similar to that on polystyrene control surfaces. *In vitro* studies demonstrated that microneedle arrays fabricated from eShell 200 successfully produced pores in stratum corneum and epidermis. The microscale pores produced by microneedle–skin interaction may be used to facilitate the diffusion of pharmacologic agents through the skin. Our results suggest that a combination of micromolding and 2PP microfabrication represents a high-throughput approach that may be used to create microneedle structures with appropriate structural, mechanical, and biological properties for transdermal drug delivery of insulin and other protein-based pharmacologic agents. *In vitro* and *in vivo* studies are underway to examine whether microneedles prepared using this approach exhibit suitable biological properties for insulin delivery. *In vitro* permeation studies of various pharmacologic agents through animal and human skin models are also being investigated.^{25,27,28} Several medical uses for these devices are anticipated. For example, eShell 200 microneedles may be utilized to deliver incretin mimetics and other novel protein-based pharmacologic agents for treatment of diabetes, which cannot be administered in oral form because they may be metabolized in the gastrointestinal tract or in the liver before reaching systemic circulation.

Funding:

R. J. Narayan acknowledges support from the Jefferson-Pilot Fellowship in Academic Medicine at the University of North Carolina at Chapel Hill. S. D. Gittard acknowledges support from the National Science Foundation (Award 0920997).

Acknowledgments:

The authors thank K. Evaul and A. O. Inman (Center for Chemical Toxicology Research and Pharmacokinetics, North Carolina State University) for their assistance with the MTT assays.

References:

1. Gerstel MS, Place VA. Drug delivery device. U.S. Patent 3,964,482. June 22, 1976.
2. Prausnitz MR, Mitragotri S, Langer R. Current status and future potential of transdermal drug delivery. *Nat Rev Drug Discov.* 2004;3(2):115–24.
3. Gowthamarajan K, Kulkarni GT. Oral insulin—fact or fiction? Possibilities of achieving oral delivery for insulin. *Resonance.* 2003;8(5):38–46.
4. Nordquist L, Roxhed N, Griss P, Stemme, G. Novel microneedle patches for active insulin delivery are efficient in maintaining glycaemic control:an initial comparison with subcutaneous administration. *Pharm Res.* 2007;24(7):1381–8.

5. Brown MB, Martin GP, Jones SA, Akomeah, FK. Dermal and transdermal drug delivery systems:current and future prospects. *Drug Deliv.* 2006;13(3):175–87.
6. Gill HS, Denson DD, Burris BA, Prausnitz MR. Effect of microneedle design on pain in human volunteers. *Clin J Pain.* 2008;24(7):585–94.
7. Kaushik S, Hord AH, Denson DD, McAllister DV, Smitra S, Allen MG, Prausnitz MR. Lack of pain associated with microfabricated microneedles. *Anesth Analg.* 2001;92(2):502–4.
8. Martano W, Davis SP, Holiday NR, Wang J, Gill HS, Prausnitz MR. Transdermal delivery of insulin using microneedles *in vivo*. *Pharm Res.* 2004;21(6):947–52.
9. Kobayashi K, Suzuki H. A sampling mechanism employing the phase transition of a gel and its application to a micro analysis system imitating a mosquito. *Sens. Actuators B.* 2001;80(1):1–8.
10. Chun K, Hashiguchi G, Toshiyoshi H, Fujita H. Fabrication of array of hollow microcapillaries used for injection of genetic materials into animal/plant cells. *Jpn J Appl Phys.* 1999;38(3A):L279–81.

11. Griss P, Stemme G. Side-opened out-of-plane microneedles for microfluidic transdermal liquid transfer. *J Microelectromech Syst.* 2003;12(3):296–301.
12. Wilke N, Mulcahy A, Ye SR, Morrissey A. Process optimization and characterization of silicon microneedles fabricated by wet etch technology. *Microelectron J.* 2005;36(7):650–6.
13. Gardeniers HJGE, Luttge R, Berenschot EJW, De Boer MJ, Yeshurun SY, Hefetz M, Van't Oever R, van den Berg A. Silicon micromachined hollow microneedles for transdermal liquid. *J Microelectromech Syst.* 2003;12(6):855–62.
14. Doraiswamy A, Jin C, Narayan RJ, Mageswaran P, Mente P, Modi R, Auyeung R, Chrisey DB, Ovsianikov A, Chichkov B. Two photon induced polymerization of organic-inorganic hybrid biomaterials for microstructured medical devices. *Acta Biomater.* 2006;2(3):267–75.
15. McAllister DV, Wang PM, Davis SP, Park JH, Canatella PJ, Allen MG, Prausnitz MR. Microfabricated needles for transdermal delivery of macromolecules and nanoparticles: fabrication methods and transport studies. *Proc Natl Acad Sci USA.* 2003;100(24):13755–60.

16. Ovsianikov A, Chichkov B, Mente P, Monteiro-Riviere NA, Doraiswamy A, Narayan RJ. Two photon polymerization of polymer-ceramic hybrid materials for transdermal drug delivery. *Int J Appl Ceramic Technol.* 2007;4(1):22–9.
17. Davis SP, Landis BJ, Adams ZH, Allen MG, Prausnitz MR. Insertion of microneedles into skin: measurement and prediction of insertion force and needle fracture force. *J Biomech.* 2004;37(8):1155–63.
18. Griss P, Tolvanen-Laakso HK, Meriläinen P, Stemme G. Characterization of micromachined spiked biopotential electrodes. *IEEE Trans Biomed Eng.* 2002;49(6):597–604.
19. LaFratta CN, Li L, Fourkas JT. Soft-lithographic replication of 3D microstructures with closed loops. *Proc Natl Acad Sci USA.* 2006;103(23):8589–94.
20. Li L, Fourkas JT. Multiphoton polymerization. *Mater Today.* 2007;10(6):30–7.
21. envisionTEC GmbH. envisionTEC e-Shell 200 Series Technical Data.
http://www.envisiontec.com/fileadmin/pdf/MatSheet_eShell200_en_s.pdf. Accessed November 5, 2008.

22. Serbin J, Egbert A, Ostendorf A, Chichkov BN, Houbertz R, Domann G, Schulz J, Cronauer C, Fröhlich L, Popall M. Femtosecond laser-induced two-photon polymerization of inorganic-organic hybrid materials for applications in photonics. *Opt Lett*. 2003;28(5):301–3.
23. Sartomer Company, Inc. Product bulletin:SR-259.
<http://www.sartomer.com/wpapers/2036.pdf>. Accessed November 5, 2008.
24. Mosmann T. Rapid colorimetric assay for cellular growth and survival: application to proliferation and cytotoxicity assays. *J Immunol Metth*. 1983;65(1-2):55–63.
25. Minghetti P, Cilurzo F, Casiraghi A, Montanari L, Santoro A. Development of patches for the controlled release of dehydroepiandrosterone. *Drug Dev Ind Pharm*. 2001;27(7):711–7.
26. Park JH, Allen MG, Prausnitz MR. Biodegradable polymer microneedles: fabrication, mechanics and transdermal drug delivery. *J Control Release*. 2005;104(1):51–66.
27. Minghetti P, Cilurzo F, Casiraghi A, Montanari L, Fini A. *Ex vivo* study of transdermal permeation of four diclofenac salts from different vehicles. *J Pharm Sci*. 2007;96(4):814–23.

28. Cilurzo F, Minghetti P, Pagani S, Casiraghi A, Montanari L. Design and characterization of an adhesive matrix based on a poly(ethyl acrylate, methyl methacrylate). *AAPS PharmSciTech*. 2008;9(3):748–54.
29. Stumpp OF, Welch AJ, Gill HS, Prausnitz MR. OCT analysis of microneedle and Er:YAG surface ablation for enhanced transdermal delivery of hyperosmotic agents for optical skin clearing. In: Jacques SL, Roach WP, eds. *Lasers with tissue and cells XV*. Proc SPIE. 2004;5319:121–9.
30. Kumar R, Philip A. Modified transdermal technologies: breaking the barriers of drug permeation via the skin. *Tropical J Pharm Res*. 2007;6(1):633–44.
31. Herndon TO, Gonzalez S, Gowrishankar TR, Anderson RR, Weaver JC. Transdermal microconduits by microscission for drug delivery and sample acquisition. *BMC Med*. 2004;2:12.
32. Kuhn SD, Sridharan K, Hao Z, Muir P, Suresh M, Singh A, Raj SV. Biocompatibility of uncoated and diamond-like carbon coated Ti-20%Hf alloy. *Mater Sci Technol*. 2008;24(5):575–8.

3.2 The Effects of Geometry on Skin Penetration and Failure Mechanics of Polymer Microneedles

The following section is a complete article which has been submitted for review to Biomedical Materials

The Effects of Geometry on Skin Penetration and Failure Mechanics of Polymer Microneedles

Shaun D Gittard^{1,2}, Bo Chen¹, Huadong Xu¹, Aleksandr Ovsianikov², Boris N Chichkov², Nancy A Monteiro-Riviere^{1,3}, Roger J Narayan¹

¹Joint Department of Biomedical Engineering, North Carolina State University, Raleigh, NC 27695, USA

²Laser Zentrum Hannover, Hollerithalle 8, 30419 Hannover, Germany

³Center for Chemical Toxicology Research and Pharmacokinetics, North Carolina State University, Raleigh, NC 27695, USA

Email: roger_narayan@msn.com

Abstract:

Microneedles are a rapidly developing class of drug delivery and sensing devices. These devices show promise of reducing much of the pain and trauma that is associated with conventional hypodermic needles. The forces required for mechanical failure and the means of mechanical failure as well as the forces and mechanism of penetration into skin were examined in this study. Microneedles produced from the polymer e-Shell 200 were found to have sufficient strength to penetrate the skin, with failure forces an order of magnitude greater than the forces required to fully inserted into the skin. Bending was the most common form of failure, with increasing aspect ratio and decreasing tip diameter resulting in lower failure forces. Video captured during skin penetration revealed that microneedle penetration into skin occurs by a series of insertions and not a single insertion event. Imaging during and after skin penetration confirmed that microneedles penetrated the skin and were able to deliver dye. These findings provide enlightenment into the mechanisms of microneedle penetration and failure, which will aid in improving the design of polymer microneedles and developing better models of drug delivery via microneedles.

Introduction

Microneedle-mediated drug delivery is a novel parenteral drug delivery technology that holds promise to provide patients with pain-free delivery of drugs to the bloodstream. Numerous applications of this technology have been demonstrated, most particularly in drug delivery, sensing, and cosmetics. Delivery of numerous pharmaceuticals, such as insulin, antibiotics,

DNA, and chemotherapy agents has been demonstrated. Over the past decade, steady progress has been made to bring this technology closer to widespread clinical use.

Due to their exceptionally small size, failure of microneedles during insertion has been a major concern. Fracture of silicon microneedles during *in vivo* use has been previously observed [1, 2]. Also silicon is a brittle material, so when failure does occur, the microneedle buckles or breaks [3, 4]. As a result, several groups have switched from silicon to materials with more favorable mechanical properties such as metals and polymers [3]. Polymer microneedles have remained as one of the most commonly used classes of microneedle materials due to their appealing properties. Polymers can be easily molded via either hot embossing [5, 6], solvent casting [7, 8], or UV lithography [10-12], which enables cost-effective mass production. Polymers are also compatible with rapid manufacturing techniques, such as stereolithography and two-photon polymerization. While polymers are significantly weaker than ceramics, many of them have sufficient strength to penetrate skin [11-14]. However, some polymer microneedles have been reported to not have sufficient strength to penetrate skin [8].

Several investigations of the mechanical properties of microneedles already exist in the literature. Davis *et al.* have investigated the relationship between the fracture force of Nickel microneedles and wall thickness, wall angle, and tip radius [15]. In this study they also examined the relationship between these geometric factors and penetration force. Aoyagi *et al.* measured the effects of tip angle and width on insertion force using PLA microneedles

[16]. Ovsianikov *et al.* investigated the effect of channel positioning on microneedle mechanical properties, reporting that the pointed tips in off-centered channels have a lower penetration force than blunt-tipped microneedles [17]. Doraiswamy *et al.* reported mechanical measurements of compressions of Ormocer® microneedles into porcine skin in a study that used a similar setup to the one presented in this study [18]. Park *et al.* examined the effects of microneedle tip area on the ability to penetrate the stratum corneum, reporting that smaller tip areas required lower penetration forces [13]. This study also examined the effects that several geometric factors have on the mechanical properties of microneedles, namely length, base diameter, and Young's modulus; failure forces were examined in both the axial and transverse directions. Generally, smaller tip diameters and higher aspect ratios have been reported to have lower penetration forces [4, 19]. Larger tip diameters, lower aspect ratios, and thicker walls generally exhibit higher mechanical strengths [4, 19]. While there have been numerous studies examining the mechanical properties of microneedles, there are still several factors that have yet to be examined. Since skin is viscoelastic, bending of the skin occurs during microneedle insertion [15, 20]. Also, the surface of skin is uneven which can effect measurements of penetration depth. The mechanics of skin penetration by microneedles has been an area with a notable lack in research. While several studies have used various techniques to measure the force required to compromise the stratum corneum. Detailed studies on the depth of penetration of microneedles and the mechanics of microneedles entering the skin beyond the stratum corneum are a necessary step for allowing researchers to better understand how drugs are delivered with microneedles.

The most common techniques for determining skin penetration are transepidermal water loss (TEWL) [21-24], electrical resistance [13-15], and post-penetration staining [21, 25]. In TEWL the rate of water loss through the skin is measured; TEWL will increase when the stratum corneum barrier, which prevents diffusion and evaporation of water, is compromised. The stratum corneum is non-conducting since it only contains dead cells and no water; the electrical resistance is greatly lower in the epidermis, which contains water, live cells, and electrolytes. Dyes that will stain cells in the epidermis but not the stratum corneum can be topically applied after application of microneedles to determine stratum corneum penetration. If the stratum corneum has been compromised, the dyes will be able to stain the epidermis in the area surrounding the microneedle-generated pores. Numerous dyes have been used including Trypan Blue, Methylene Blue, and Gentian Violet [8, 21, 24, 25]. These techniques have several shortcomings when used in evaluating microneedle penetration. Most importantly, these techniques verify that the stratum corneum has been passed, but not how deep the needle has penetrated. In many applications, the depth of microneedle penetration and not simply the ability to break the SC is important. For example, Al-Qallaf and Das developed a detailed model of the effects of microneedle array design on drug delivery [26]. In their model they assumed that the needles are completely penetrated into the skin and made their calculations of drug permeation based on such factors as the base radius and length of the needle. If the microneedles are not fully penetrated into the skin, then these values will need to be adjusted to correspond to the apparent radius and apparent length of the needle that is actually in the epidermis.

When using needles for drug delivery, delivery of the drug to the blood stream is generally achieved by diffusion through the epidermis. Thus, the distance from capillaries is extremely important for determining the pharmacokinetics of drug delivery with these devices. Some microneedles may barely pierce the stratum corneum and require longer times to reach the bloodstream than needles that reach directly to the capillaries. Secondly, when performing sensing with microneedles, such as microneedle-based glucose sensors, sampling of blood is required. Therefore, these needles must reach significantly deeper in the skin than simply compromising the stratum corneum barrier. In order to improve performance of microneedle drug delivery and sensing, the mechanics of skin penetration beyond the stratum corneum needs to be better understood.

Indirect rapid prototyping is an ideal technique to use in investigating different microneedle geometries. In indirect rapid prototyping a master structure is made by a rapid prototyping technique which is then used to make replicas by molding. This technique has been used on several occasions to make microneedles by two photon polymerization and UV soft lithography [9-11]. Two-photon polymerization is a rapid prototyping technique that affords excellent spatial resolution and design flexibility, making it an ideal technique for producing microneedles of various geometries [4, 17, 27, 28].

In this study microneedles made from a commercially available stereolithography material, e-Shell 200 (EnvisionTEC, Gladbeck, Germany), were examined. Previous research by the authors had found that this material has a Young's modulus of 2.803 GPa [29]. This material

has previously been used by the authors when they demonstrated that UV soft lithography can be used to make e-Shell 200 microneedles [11]. In this study e-Shell 200 was found to have exceptional mechanical properties, being able to undergo more than 0.35 N of compression with no indication of failure. However, only limited mechanical testing was performed and only one microneedle geometry was used. As a result, in this paper we performed a more in depth mechanical study of microneedles in a variety of geometries. The purpose of this study was two-fold: to better understand the mechanical properties of e-Shell 200 microneedles and to better understand the mechanics of skin penetration by microneedles. Compression of microneedles against stainless steel and into skin was performed while recording force, displacement, and video of the compressions. Delivery of Lucifer Yellow dye from the coated needles into skin was also demonstrated using brightfield fluorescence, laser scanning confocal, and multiphoton microscopy.

Materials and Methods

Master structures of the needles were made using two-photon polymerization, a laser-based rapid prototyping process. In two-photon polymerization microstructures are produced by scanning a femtosecond laser within a photosensitive resin; polymerization of the resin occurs along the trace of the focal point of the laser. A Ti:Sapphire femtosecond laser (Chameleon, Coherent, Santa Clara, CA) operating at 780 nm with 60 fs pulses, was used to selectively polymerize the photosensitive resin. Polyethylene glycol diacrylate (molecular weight 302) (SR259, Sartomer, Paris, France) with 2% wt of the photoinitiator Irgacure 369 (Ciba Specialty Chemicals, Basel, Switzerland) was used as the photosensitive resin.

Structuring was performed by focusing the laser with a 5x objective with a numerical aperture of 0.13 (Zeiss, Jena, Germany). A hurrySCAN® scan head (Scanlabs, Puchheim, Germany) was used to control the lateral dimensions of the laser, a translational stage (C-843, Physik Instrumente, Karlsruhe, Germany) were used to control the height of the focal plane of the laser within the resin. The laser was guided using STL files; custom written software sliced the file into layers and rastered the laser across the contour of each layer. After structuring, the unpolymerized resin was removed by washing in ethanol. Exposure to an ultraviolet lamp after washing ensured that the structures were completely polymerized. Input .stl files for the needles were produced using Solidworks Education Edition 2009 (Dassault Systemes SA, Velizy, France). Microneedles were produced in three different geometries, which are provided in Table 1.

Table 1. Dimensions of the microneedle geometries

Name	Base Diameter	Length	Aspect Ratio	Radius of Curvature
A	250 μm	750 μm	3:1	10.0 μm
B	300 μm	750 μm	2.5:1	14.5 μm
C	250 μm	500 μm	2:1	16.5 μm

Mass replication of the master structures was achieved by UV soft lithography as previously described [11]. The master structures were coated with gold by sputter coating and molded with a thick layer of polydimethylsiloxane (PDMS) (Sylgard® 184, Dow Corning, Midland,

MI). The molds and master structures were separated using a linear translational stage. Replicas out the material e-Shell 200 (Envisiontec GmbH, Gladbeck, Germany) were produced by filling the shape in the mold via greater than 1 mbar vacuum. Polymerization of the needles was achieved using a UV flash oven (Otoflash, Envisiontec GmbH, Gladbeck, Germany). The replicas were manually separated from the mold.

High magnification images of the replicas were obtained using a S3200 (Hitachi, Tokyo, Japan). Images of the microneedles after compression and skin penetration were taken with a dissection scope (EZ 4, Leica, Wetzlar, Germany). Videos during compressions and skin penetrations were captured with a CCD camera focused through a 10x objective.

Compression of the needles was performed using a 20 N load cell (Electroforce 3100, Bose, Eden Prairie, MN) with 1 mN force resolution and 0.001 mm displacement resolution and WinTest® software. Microneedles of all three geometries were compressed to loads of 0.1 N, 0.25 N, 0.5 N, 0.75 N, and 1 N in load controlled mode at a rate of 0.001 N/sec. Load and displacement were recorded during the compressions. Full-thickness porcine skin was used for examining skin penetration of the needles. Microneedles of all three geometries were pressed into full thickness skin using the load cell. Penetration was performed in both displacement controlled mode at a rate of 0.01 mm/sec to a total displacement of at least 1.3 mm.

Drug delivery studies were performed with needles in geometry A that were coated with the dye Lucifer Yellow (Lucifer Yellow, Thermo Fisher Scientific, Waltham, MA). Lucifer Yellow was chosen due to its properties that minimized diffusion in tissue; it is a hydrazine-derivative dye that covalently combines with proteins. Coating was performed by placing a 0.1 mL droplet of a solution of 5% Lucifer Yellow in water onto the needle/substrate and evaporating the solvent by heating at 60 °C for 15 minutes. The microneedles were pressed into porcine skin by hand for 15 minutes and then imaged. Images of the microneedle-produced pores at the surface of the skin were obtained by removing the array and imaging with widefield fluorescence microscopy (TC-5500 Epi-fluorescent, Meiji Techno America, Santa Clara, CA). Confocal microscopy was used to confirm that the dye was delivered below the surface of the skin. Prior to imaging, needles were pressed into the skin for 15 minutes and removed. A Zeiss LSM 710 was used to obtain DIC and fluorescence images of the pores 100 μm below the surface of the skin with excitation with a 458 nm laser and emission collected between 494 and 600 nm. Microneedles in the skin were imaged with multiphoton microscopy via a Zeiss NLO LSM 710 with 740 nm excitation by a femtosecond laser (Chameleon, Coherent, Santa Clara, CA); a beam splitter was used to collect emission below 690 nm. For multiphoton microscopy imaging, the needles were left in the skin while images were obtained. Fluorescence from the dye was imaged from the surface of the skin to 100 μm below the surface of the skin in order to determine how much of the needle was in the skin.

Results

Scanning electron microscopy confirmed that UV soft lithography produced accurate replicas of the structures. A characteristic SEM image of a replicated microneedle (geometry B) is provided in Figure 1. The bodies of all microneedle geometries were smooth; the radii of curvature of the tips are provided in Table 1.

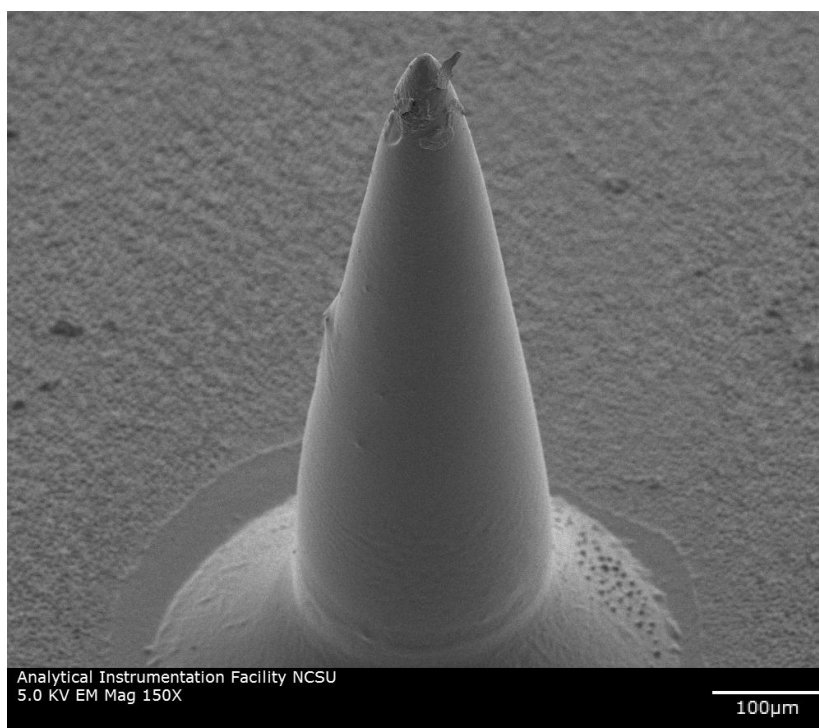


Figure 1. Scanning electron microscopy image of a microneedle replica produced by indirect rapid prototyping using two-photon polymerization and UV soft lithography.

The microneedle geometries underwent compression of forces ranging from 0.1 N to 1.0 N as a means of assessing their mechanical strength. Optical microscopy images of the microneedles after compression to this range of forces are provided in Figure 2. All three

geometries were able to sustain forces up to 0.1 N without any signs of damage. At 0.25 N of force, slight deformation of the tip of geometry A (3:1 aspect ratio) was observed, while geometries B and C had no signs of damage. At forces of 0.5 N and higher, permanent tip deformation of geometries B and C was observed. During 10% of compressions above 0.1 N, microneedle geometry A exhibited fracturing near the tip; the other 90% of the compressions resulted in bending or compressing and then bending. Geometry B exhibited bending of the tip. Microneedle geometry C underwent compression of the tip with bending occurring at forces greater than 0.75 N.

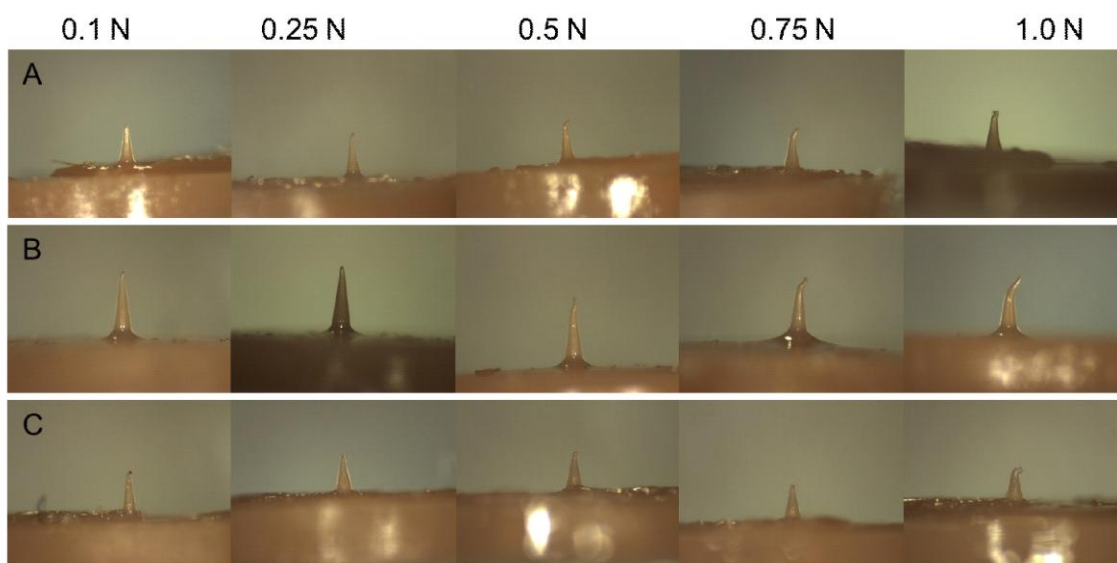


Figure 2. Microneedles after compression testing. All three geometries were able to sustain compressive loads up to 0.1 N without any deformation. At higher loads the most common mode of failure was bending of the needle. Failure by fracturing near the tip occurred 10% of the time and was observed only for geometry A.

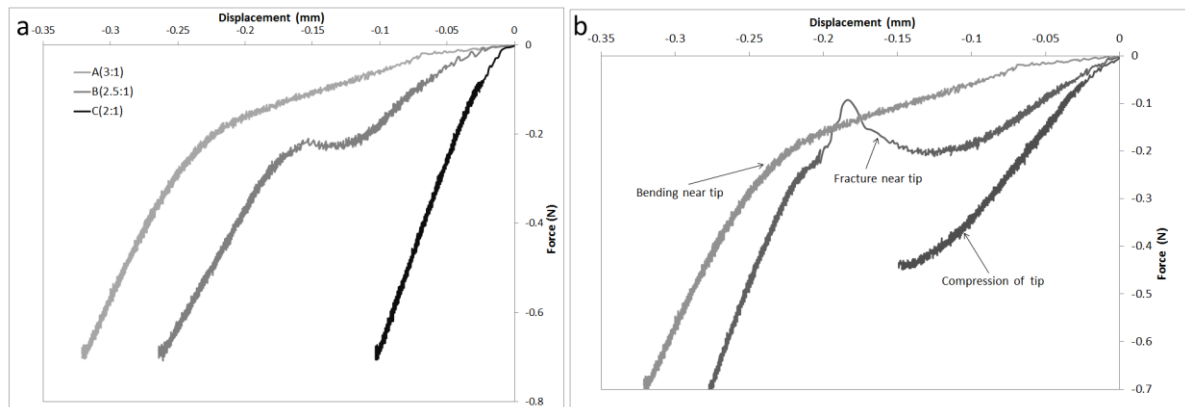


Figure 3. Microneedle compression: (a) force vs. displacement plots of compressed microneedles at varying aspect ratios; (b) characteristic force vs. displacement plots of microneedle failure mechanisms.

A characteristic force versus displacement plot of the three needles is provided in Figure 3a. Mechanical strength of the needles was inversely related to aspect ratio. The 2:1 aspect ratio needles underwent less than 0.1 mm of deformation with 0.75 N of force, whereas the 2.5:1 and 3:1 aspect ratios underwent approximately 0.25 mm and 0.33 mm of deformation at 0.75 N, respectively. Figure 3b contains characteristic plots of the three failure mechanisms occurring in the microneedles, all three of the curves are from compressions of microneedle geometry A. Fracturing of the tip resulted in a sharp spike in the force versus displacement curve. Compression of the tip resulted in an approximately linear relationship, whereas bending produced a shoulder in the force versus displacement plot. Characteristic plots of force and displacement versus time in load controlled mode are provided in Figure 4. A needle (geometry B) undergoing bending is represented in Figure 4a; the load curve is linear

with a shoulder in the displacement curve occurring at the time of bending of the needle. Eventually, displacement becomes linear again as the compression platen reaches a portion of the needle with a sufficiently larger diameter where bending no longer occurs. A microneedle fracturing is presented in Figure 4b, where is shown by a sharp spike in the load curve with a simultaneous jump in displacement.

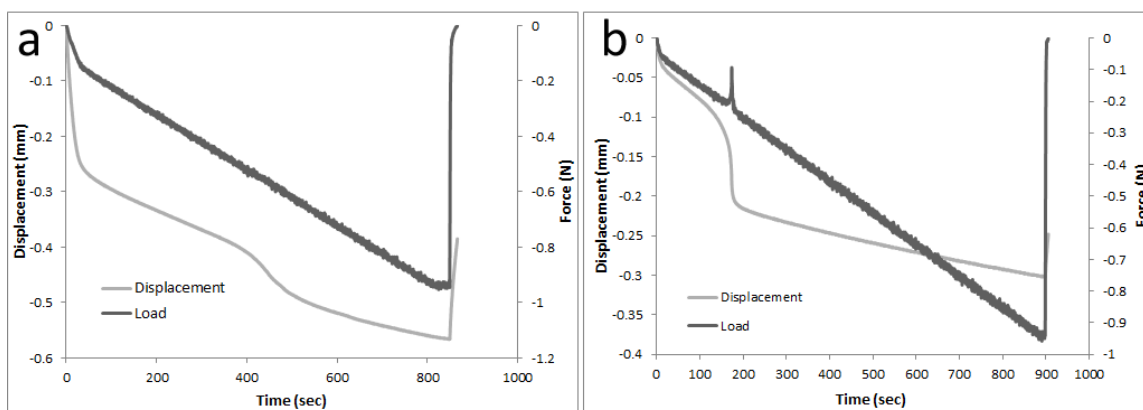


Figure 4. Microneedle failure in force and displacement versus time: (a) bending and (b) fracturing.

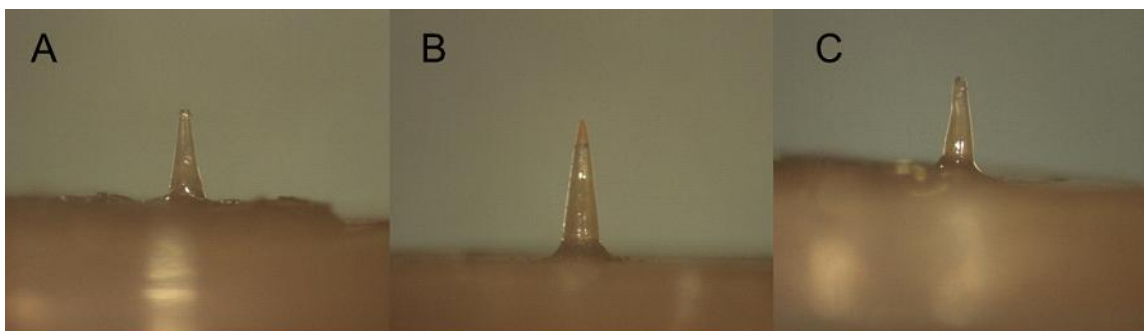


Figure 5. Microneedles after penetrating into skin with 1.0 N of compression. All needle geometries were able to penetrate into skin without damage.

Penetration of microneedles into full-thickness porcine skin was achieved without damage for all three microneedle geometries. Images of the three needle geometries after insertion into skin with 1.0 N of force are presented in Figure 5. Figure 6 contains force versus displacement curves of the three microneedle geometries penetrating skin in displacement control mode. No significant differences between the penetration forces for the three microneedle geometries were observed. Figure 7 provides a characteristic comparison (geometry B) of microneedle penetration into skin versus compression. The microneedles penetrate into the skin with significantly less forces than would damage the needles.

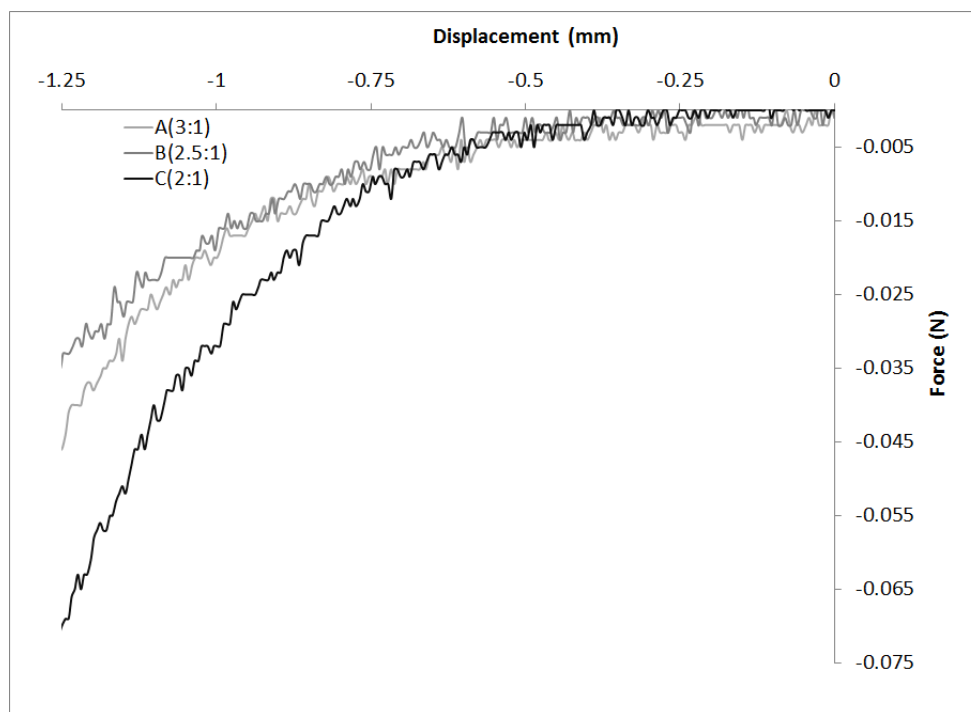


Figure 6. Skin Penetration: force versus displacement of microneedles penetrated into full-thickness porcine skin in displacement control mode.

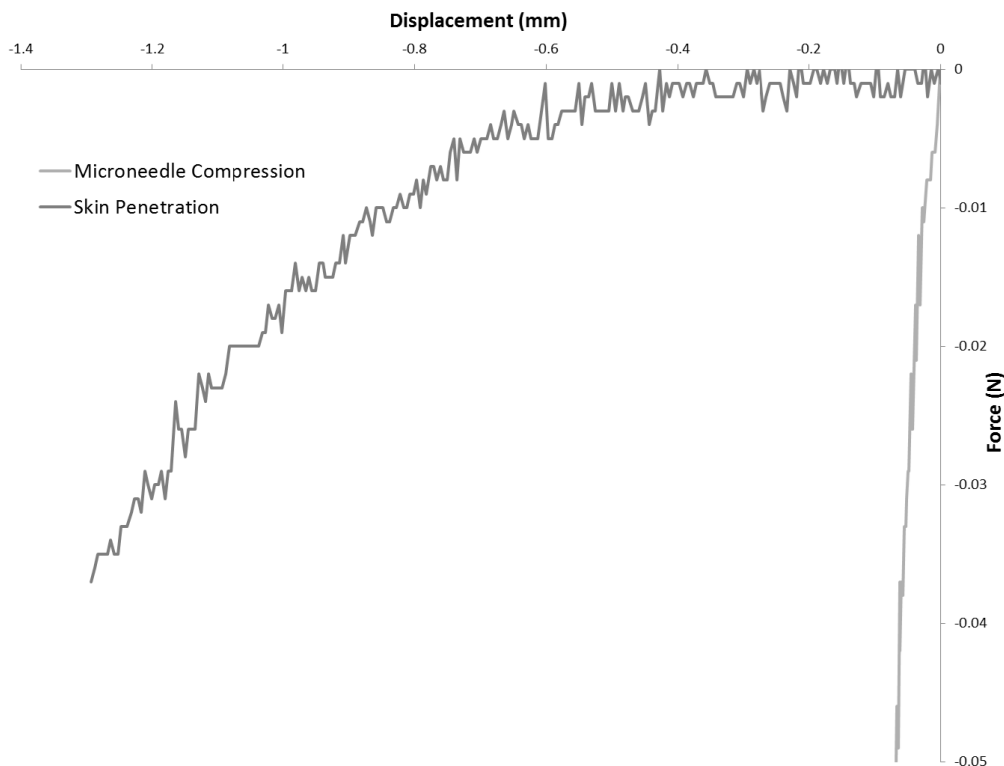


Figure 7. Characteristic example of penetration versus compression (Geometry B).

Microneedle penetration into skin requires forces that have a negligible effect on the microneedles themselves.

Video of microneedle compressions and penetration into skin was collected simultaneously with force and displacement measurements. Screenshots of a microneedle compression and penetration, both with geometry B, were produced from these videos for easier visualization. Figure 8 contains screenshots of a characteristic microneedle compression (geometry B) in load controlled mode with the corresponding displacement and load versus time plots underneath. The needle can be seen to bend at the tip and along the base, with partial

recovery after the force is released. Video screenshots and the corresponding mechanical data for a characteristic microneedle penetration into skin (geometry B) in displacement controlled mode are provided in Figure 9. The mechanical data and video footage both indicate that penetration of the needle into the skin consists of an incremental series of the skin bending and then partially rebounding upon deeper piercing of the needle. The skin can be seen to rebound upward from the 24 second to the 25 second frame.

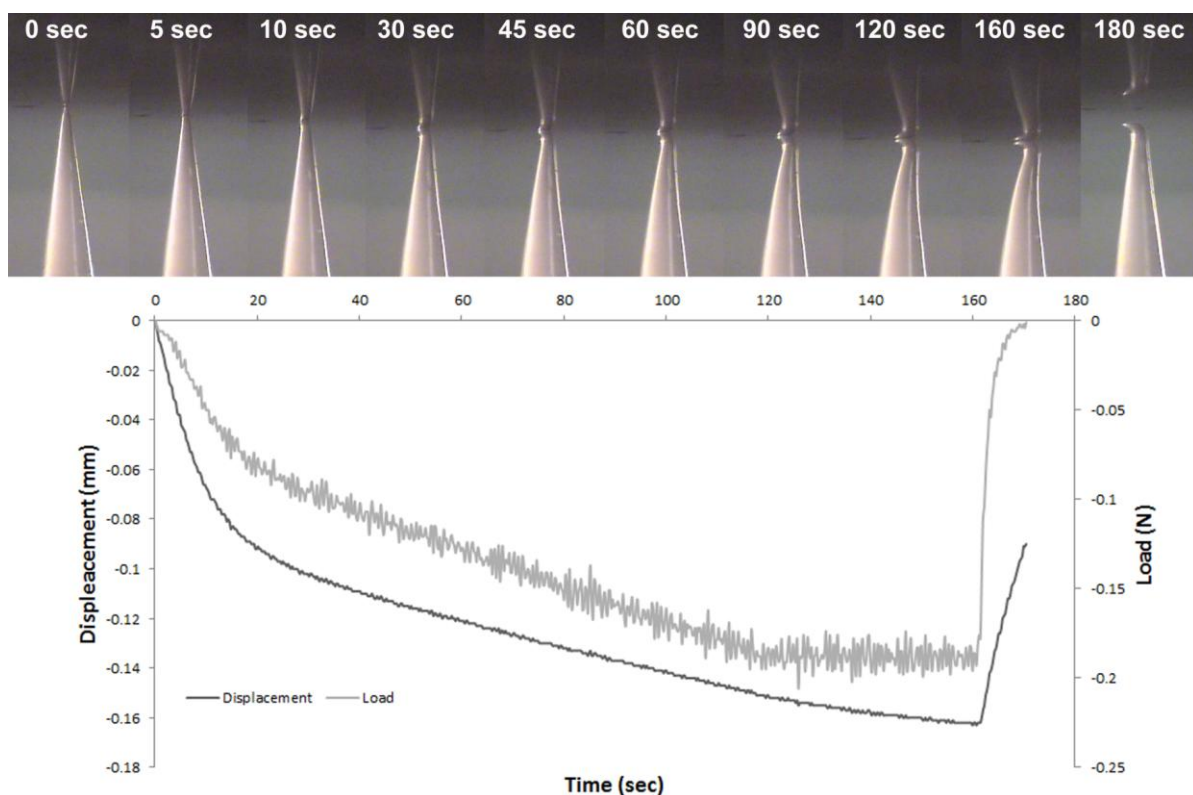


Figure 8: Timeline of microneedle geometry B being compressed in displacement controlled mode. Top: Screenshots of a video recording of the needle being compressed (video available online as supplemental data). Bottom: Force and Displacement versus time during the compression.

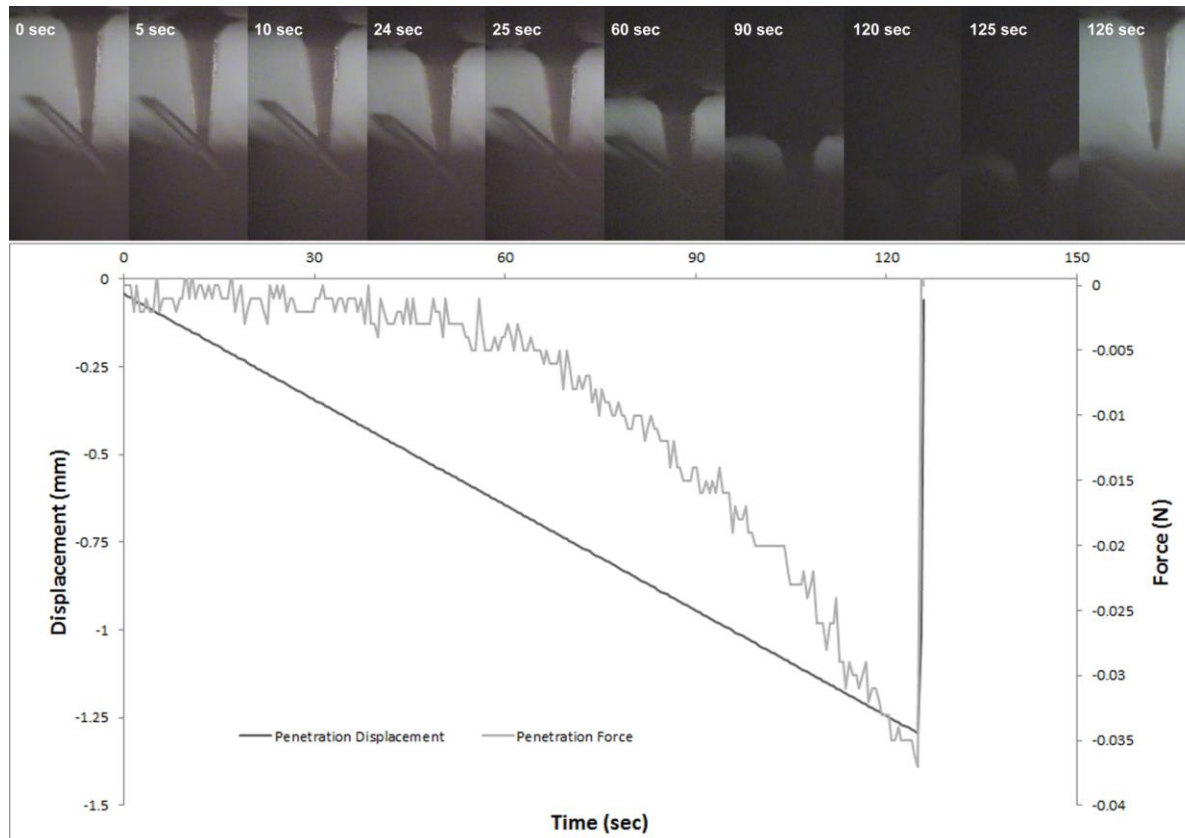


Figure 9. Timeline of microneedle geometry B penetrating skin in displacement controlled mode. Top: Screenshots of a video recording of the needle penetrating the skin (video available online as supplemental data). Bottom: Force and Displacement versus time during the compression.

Fluorescence microscopy confirmed that the coated microneedles created pores in the skin and delivered Lucifer yellow dye. Brightfield fluorescence and confocal microscopy confirmed that pores remained at the surface and 120 μm below the surface of the skin after removal of the needles (Figure 10). The pores were significantly smaller than the needles themselves and were anisotropic. The pore at the surface of the skin was approximately 80

μm in diameter, whereas the pore at 100 μm below the surface of the skin was approximately 80 μm in diameter. Confocal microscopy also confirmed release of the dye into the surrounding area of the skin.

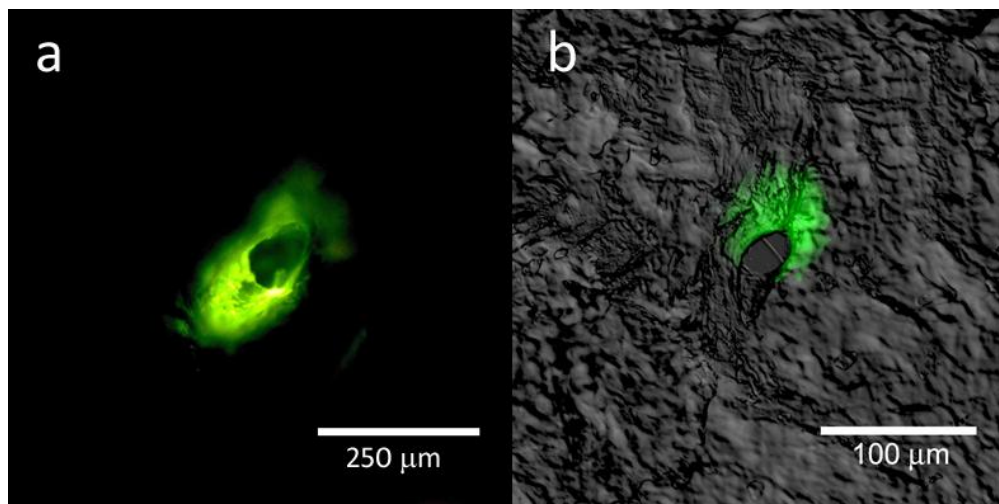


Figure 10: Fluorescence microscopy of Lucifer Yellow delivery at surface of the skin and Confocal and DIC overlay of Lucifer yellow delivery at 120 μm depth.

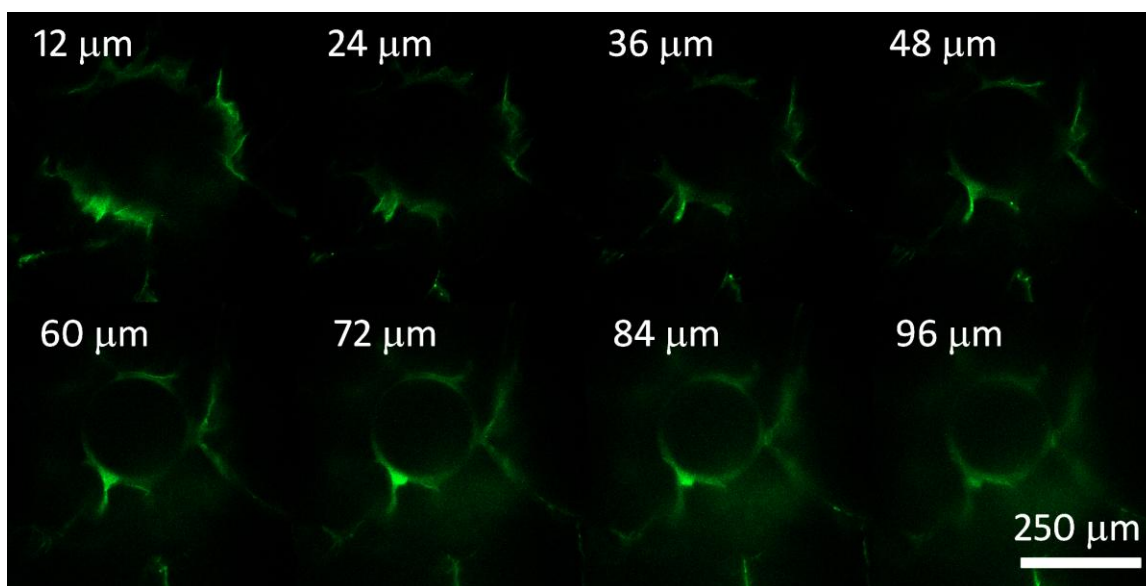


Figure 11: Lucifer Yellow delivery into porcine skin assessed with multiphoton microscopy.

Multiphoton microscopy data was collected from the surface of the skin to 100 μm deep in the skin in order to determine the degree of “tenting” of the skin (Figure 11). The pores have a regular circular shaped from 96 μm deep to 36 μm deep. From 36 μm to the surface of the skin the pores have a more irregular shape. The diameter of the pore at 36 μm from the surface of the skin is 221 μm ; the base diameter of the needle was 250 μm . Needle geometry A has a diameter of 221 μm at 86 μm from the base, indicating that 664 μm or 88.5% of the length of the needle is residing in the skin.

Discussion

Scanning electron microscopy confirmed that UV soft lithography is an appropriate technique for rapidly producing replicas of fine structures, such as those produced by two-photon polymerization. This technique has been used to mass-produce replicas of microstructures that were generated by a variety of techniques, including two-photon polymerization [9-11], laser ablation [30], and reactive ion etching [8].

The microneedles produced from the polymer e-Shell 300 were found to be remarkably strong. All three geometries were able to undergo 0.1 N of compressive force without any permanent deformation of the tip for an individual needle. In comparison, 10x10 Ormocer® microneedle arrays experienced plastic deformation at 0.3 g and fracture at 0.4 g, which corresponds to 0.0294 N and 0.0376 N per needle in the array for plastic deformation and fracture, respectively [18]. Park *et al.* reported failure of PLGA microneedles in similar geometries with failure forces from 0.06 N to 0.25 N [13]. The primary form of failure for

the needles was compression followed by bending. Initially, elastic bending occurred, followed by plastic bending. As aspect ratio increased, the force required for elastic and plastic bending decreased. Tip diameter of the needles increased as aspect ratio decreased. Therefore it is not possible to differentiate between the effects of these two geometric factors. Davis *et al.* have reported that increasing tip diameters and decreasing aspect ratio both result in increased mechanical strength, which is in agreement with our data [15]. Geometry A (3:1 aspect ratio) began plastic bending beyond 0.1 N; geometry B (2.5:1 aspect ratio) exhibited plastic bending beyond 0.25 N; and geometry C (2:1 aspect ratio) exhibited plastic bending beyond 0.75 N. Fracture of the highest aspect ratio needles (3:1) occurred 10% of the time; fracture always occurred after plastic bending had begun. Fracturing always occurred near the tip of the needles at the point where the most bending was occurring. The failure mechanism of polymer needles is favorable in comparison to ceramics. Ceramic microneedles, such as the widely-used material silicon, primarily fail by fracturing.

All microneedle geometries were able to penetrate the skin with exceptionally low forces; all three geometries had displaced more than 0.5 mm into the skin before forces greater than 5 mN were achieved. Beyond a displacement of 0.75 mm the force for geometry C significantly increases, but this increase is due to compression of the skin from the substrate coming in contact with the skin since this needle geometry is shorter. In comparison, blunt-tipped microneedles, such as those investigated by Davis *et al.*, exhibited piercing of the stratum corneum at approximately 0.5 N, as measured by electrical conduction [15]. These blunt-tipped needles also displaced the skin approximately 500 μm before stratum corneum

piercing was achieved. Even though the needles were produced from metal, the failure mechanism of the needles was by fracturing and buckling. Another important factor to note about skin penetration is that the forces applied to the needle during compression and during penetration do not exactly correspond. During compression into a hard surface, the entirety of the applied force is on the surface of the needle. In contrast, forces during skin penetration are distributed over a larger area of the needle, especially after initial penetration has occurred.

No significant differences in the penetration properties of the three microneedle geometries were observed. In comparison, the differences in geometry were found to have a significant effect on the mechanical strength of the needles. Therefore, the 2:1 aspect ratio would be the best geometry to use, due to it having a higher strength without a significantly different penetration force. While the 2:1 aspect ratio needle has the highest margin of safety, all three geometries are safe for use in drug delivery. Even for the 3:1 aspect ratio geometry, the force required for compressing 1 mm into the skin (~ 0.015 N) is an order of magnitude less than the force at which plastic deformation occurs (~ 0.2 N).

The most revealing information about microneedle penetration into skin was a result of the video footage and mechanical measurements taken during microneedle penetration. Both the recorded mechanical data and video indicated that there is not a single force when microneedles penetrate the skin, but a series of increasing forces required to penetrate deeper into the skin. Upon application of microneedles to the skin, the skin will compress until a

threshold where the needle will pierce through the tissue. In our video footage, piercing can be observed as when the skin rebounds towards the needles. Piercing in our mechanical data is shown as a sharp drop in force. In the video of skin penetration (available in online supplementary data), the skin can be seen to rebound frequently during the beginning of skin penetration. The entire skin can be seen to rebound, with hairs aiding in visualization of motion of the skin. These findings indicate that there is not a single force required for a microneedle to penetrate the skin, but rather a threshold force for a microneedle to pierce a certain depth into the skin. Numerous studies have reported a singular force at which the needle is inserted into the skin. Davis *et al.* and Choi *et al.* reported singular forces of insertion, which they determined via the decrease in resistance when the stratum corneum was compromised [14, 15]. Techniques which determine if the stratum corneum has been compromised, such as TEWL measurements and staining, provide only partial information about microneedle penetration. In order to form accurate pharmacological models of drug delivery via microneedles, the depth of release of the drug must be known. Consequently, TEWL and staining are not appropriate techniques for assessing drug delivery into skin. Alternative techniques, such as histology [15, 27, 31], laser scanning confocal [32, 33], and multiphoton microscopy [12], are better suited for determining the depth of penetration into the skin, though additional methods may still be developed.

Microneedle penetration was further confirmed by both with microneedles in the skin and after removal of needles. Fluorescence microscopy also confirmed that a model drug (Lucifer Yellow) had been delivered into the skin. Pores were found to remain in the skin

after removal of the needles. The decrease in size and the anisotropic shape of the microneedle-produced pores is due to tension in the skin, which is anisotropic. Previous studies have reported similar pores shapes in skin after removal of microneedles [11]. Multiphoton microscopy indicated slight tenting of the skin in the area surrounding the base of the needle. Tenting is present in the upper 36 μm where the pore shape is irregular. At lower depths, the pore is seen to be isotropic, indicating that no tenting has occurred at these depths. By measuring the diameter of the pore at the point where tenting no longer occurs, the length of the needle residing in the skin can be determined. 88.5% of the length of microneedle geometry A (86 μm) was found to penetrate the skin. In contrast, blunt-tipped needles have been observed to have tenting on the order of hundreds of microns [15].

Conclusions

Microneedles produced from the material e-Shell 200 were shown to have excellent material properties for use in transdermal drug delivery. All three of the investigated microneedle geometries were able to penetrate skin with forces that were at least an order of magnitude less than the forces where damage to the needles occurred. Geometry had a significant effect on the mechanical strength of the needles, with an increase in aspect ratio corresponding to a decrease in mechanical strength. Observation of skin penetration revealed that there is not a single event when microneedles pierce the skin, but a series of penetrations where the microneedles progressively pierce deeper into the skin. Various methods of fluorescence microscopy confirmed that the needles could deliver a drug into the skin. These findings show that indirect rapid prototyping of polymer microneedles is an effective means of mass

producing microneedles for drug delivery. Further, we have shown that effective means of determining the location of a needle within the skin is necessary since the depth of microneedle penetration into the skin varies depending on the applied force.

References

- [1] Griss P, Tolvanen-Laakso H K, Merilainen P and Stemme G 2002 Characterization of micromachined spiked biopotential electrodes *Biomedical Engineering, IEEE Transactions on* **49** 597

- [2] Smart W H and Subramanian K 2000 The use of silicon microfabrication technology in painless blood glucose monitoring *Diabetes Technol. Ther.* **2** 549-559

- [3] Aoyagi S, Izumi H, Isono Y, Fukuda M and Ogawa H 2007 Laser fabrication of high aspect ratio thin holes on biodegradable polymer and its application to a microneedle *Sensors and Actuators A: Physical* **139** 293-302

- [4] Gittard S D, Ovsianikov A, Chichkov B N, Doraiswamy A and Narayan R J 2010 Two-photon polymerization of microneedles for transdermal drug delivery *Expert Opin. Drug Deliv.* **7** 513-533

- [5] Trautmann A, Heuck F, Mueller C, Ruther P and Paul O 2005 Replication of microneedle arrays using vacuum casting and hot embossing *Solid-State Sensors, Actuators and Microsystems, 2005. Digest of Technical Papers. TRANSDUCERS '05. The 13th International Conference on* **2** 1420-1423 Vol. 2
- [6] Moon S J, Lee S S, Lee H S and Kwon T H 2005 Fabrication of microneedle array using LIGA and hot embossing process *Microsyst. Technol.* **11** 311-318
- [7] Lee J W, Park J and Prausnitz M R 2008 Dissolving microneedles for transdermal drug delivery *Biomaterials* **29** 2113-2124
- [8] Choi S O, Kim Y, Park J W, Hutcheson J, Gill H, Yoon Y K, Prausnitz M, and Allen M 2010 An electrically active microneedle array for electroporation *Biomed. Microdevices* 263-273
- [9] Gittard S D, Ovsianikov A, Akar H, Chichkov B, Monteiro-Riviere N A, Stafslie S, Chisholm B, Shin C, Shih C, Lin S, Su Y and Narayan R J 2010 Two Photon Polymerization-Micromolding of Polyethylene Glycol-Gentamicin Sulfate Microneedles *Advanced Engineering Materials* **12** B77-B82

- [10] Gittard S D, Narayan R J, Jin C, Ovsianikov A, Chichkov B N, Monteiro-Riviere N A, Stafslie S and Chisholm B 2009 Pulsed laser deposition of antimicrobial silver coating on Ormocer® microneedles *Biofabrication* **1** 041001
- [11] Gittard S D, Ovsianikov A, Monteiro-Riviere N A, Lusk J, Morel P, Minghetti P, Lenardi C, Chichkov B N and Narayan R J 2009 Fabrication of Polymer Microneedles Using a Two-Photon Polymerization and Micromolding Process *J. Diabetes Sci. Technol.* **3** 304-311
- [12] Gittard S D, Miller P R, Boehm R D, Ovsianikov A, Chichkov B N, Heiser J, Gordon J, Monteiro-Riviere N and Narayan R J 2011 Multiphoton microscopy of transdermal quantum dot delivery using two photon polymerization-fabricated polymer microneedles *Faraday Discuss.* **149** 171-185
- [13] Park J H, Yoon Y K, Choi S O, Prausnitz M R and Allen M G 2007 Tapered Conical Polymer Microneedles Fabricated Using an Integrated Lens Technique for Transdermal Drug Delivery *Biomedical Engineering, IEEE Transactions on* **54** 903-913
- [14] Choi J W, Park I B, Ha Y M, Jung M G, Lee S D and Lee S H 2006 Insertion Force Estimation of Various Microneedle Array-type Structures Fabricated by a Microstereolithography Apparatus *SICE-ICASE, 2006. International Joint Conference* 3678-3681

- [15] Davis S P, Landis B J, Adams Z H, Allen M G and Prausnitz M R 2004 Insertion of microneedles into skin: measurement and prediction of insertion force and needle fracture force *J. Biomech.* **37** 1155-1163
- [16] Aoyagi S, Izumi H and Fukuda M 2008 Biodegradable polymer needle with various tip angles and consideration on insertion mechanism of mosquito's proboscis *Sens. Actuator A-Phys.* **143** 20-28
- [17] Ovsianikov A, Chichkov B, Mente P, Monteiro-Riviere N A, Doraiswamy A and Narayan R J 2007 Two photon polymerization of polymer-ceramic hybrid materials for transdermal drug delivery *Int. J. Appl. Ceram. Technol.* **4** 22-29
- [18] Doraiswamy A, Jin C, Narayan R J, Mageswaran P, Mente P, Modi R, Auyeung R, Chrisey D B, Ovsianikov A and Chichkov B 2006 Two photon induced polymerization of organic-inorganic hybrid biomaterials for microstructured medical devices *Acta Biomater.* **2** 267-275
- [19] Gittard S D and Narayan R J 2010 Chapter 29: Applications of Microneedle Technology to Transdermal Drug Delivery Monteiro-Riviere N A (ed) *Toxicology of the Skin* (New York, NY: Informa Healthcare) 301-316

- [20] Yang M and Zahn J,D. 2004 Microneedle Insertion Force Reduction Using Vibratory Actuation *Biomed. Microdevices* 177-182
- [21] Verbaan F J, Bal S M, van den Berg D J, Groenink W H H, Verpoorten H, Lüttge R and Bouwstra J A 2007 Assembled microneedle arrays enhance the transport of compounds varying over a large range of molecular weight across human dermatomed skin *J. Controlled Release* **117** 238-245
- [22] Vemulapalli V, Yang Y, Friden P M and Banga A K 2008 Synergistic effect of iontophoresis and soluble microneedles for transdermal delivery of methotrexate *J. Pharm. Pharmacol.* **60** 27-33
- [23] Sivamani R K, Stoeber B, Liepmann D and Maibach H I 2009 Microneedle penetration and injection past the stratum corneum in humans *J. Dermatol. Treat.* **20** 156-159
- [24] Haq M I, Smith E, John D N, Kalavala M, Edwards C, Anstey A, Morrissey A and Birchall J C 2009 Clinical administration of microneedles: skin puncture, pain and sensation *Biomed. Microdevices* **11** 35-47
- [25] Verbaan F J, Bal S M, van den Berg D J, Dijksman J A, van Hecke M, Verpoorten H, van den Berg A, Luttge R and Bouwstra J A 2008 Improved piercing of microneedle arrays in dermatomed human skin by an impact insertion method *J. Controlled Release* **128** 80-88

[26] Al-Qallaf B and Das D B 2008 Optimization of square microneedle arrays for increasing drug permeability in skin *Chemical Engineering Science* **63** 2523-2535

[27] Doraiswamy A, Ovsianikov A, Gittard S D, Monteiro-Riviere N A, Crombez R, Montalvo E, Shen W, Chichkov B N and Narayan R J 2010 Fabrication of Microneedles Using Two Photon Polymerization For Transdermal Delivery of Nanomaterials *J. Nanosci. Nanotechnol.* **10** 6305-6312

[28] Gittard S D and Narayan R J 2010 Laser direct writing of micro- and nano-scale medical devices. *Expert. Rev. Med. Devices* **7** 343-356

[29] Gittard S D, Narayan R J, Lusk J, Morel P, Stockmans F, Ramsey M, Laverde C, Phillips J, Monteiro-Riviere N A, Ovsianikov A and Chichkov B N 2009 Rapid prototyping of scaphoid and lunate bones *Biotechnol. J.* **4** 129-134

[30] Koroleva A, Schlie S, Fadeeva E, Gittard S D, Miller P, Ovsianikov A, Koch J and Narayan R J 2010 Microreplication of laser-fabricated surface and three-dimensional structures *J. Optics* **12** 124009

[31] Li G, Badkar A, Nema S, Kolli C S and Banga A K 2009 In vitro transdermal delivery of therapeutic antibodies using maltose microneedles *Int. J. Pharm.* **368** 109-115

[32] Bal S, Kruithof A C, Liebl H, Tomerius M, Bouwstra J, Lademann J and Meinke M
2010 In vivo visualization of microneedle conduits in human skin using laser scanning
microscopy *Laser Physics Letters* **7** 242-246

[33] Bal S M, Kruithof A C, Zwier R, Dietz E, Bouwstra J A, Lademann J and Meinke M C
2010 Influence of microneedle shape on the transport of a fluorescent dye into human skin in
vivo *J. Controlled Release* **147** 218-224

3.3 Assessing the antimicrobial activity of zinc oxide thin films using disk diffusion and biofilm reactor

*The following section a complete article reprinted from **Applied Surface Science**, Volume 255, Gittard SD, Perfect JR, Monteiro-Riviere NA, Wei W, Jin C, Narayan RJ. 5806-5811, Copyright 2009, with permission from Elsevier*

Note: This article has been reformatted. In particular, the location of figures and spacing may have changed. The references are formatted as in the original manuscript.

Applied Surface Science 255 (2009) 5806–5811

Contents lists available at ScienceDirect

Applied Surface Science

journal homepage: www.elsevier.com/locate/apsusc

doi:10.1016/j.apsusc.2009.01.009

Assessing the antimicrobial activity of zinc oxide thin films using disk diffusion and biofilm reactor

Shaun D. Gittard ^{a,b}, John R. Perfect ^c, Nancy A. Monteiro-Riviere ^{a,b,d}, Wei Wei ^e,
Chunming Jin ^e, Roger J. Narayan ^{a,b,e,*}

^a *Department of Biomedical Engineering, University of North Carolina at Chapel Hill, Chapel Hill, NC, United States*

^b *Department of Biomedical Engineering, North Carolina State University, Raleigh, NC, United States*

^c *Department of Medicine, Division of Infectious Diseases, Duke University, Durham, NC, United States*

^d *Center for Chemical Toxicology Research and Pharmacokinetics, North Carolina State University, Raleigh, NC, United States*

^e Department of Materials Science Engineering, North Carolina State University, Raleigh, NC, United States

ARTICLE INFO

Article history:

Received 4 October 2008

Accepted 7 January 2009

Available online 10 January 2009

Keywords:

Antimicrobial materials

Pulsed laser deposition

Zinc oxide

ABSTRACT

The electronic and chemical properties of semiconductor materials may be useful in preventing growth of microorganisms. In this article, in vitro methods for assessing microbial growth on semiconductor materials will be presented. The structural and biological properties of silicon wafers coated with zinc oxide thin films were evaluated using atomic force microscopy, X-ray photoelectron spectroscopy, and MTT viability assay. The antimicrobial properties of zinc oxide thin films were established using disk diffusion and CDC Biofilm

Reactor studies. Our results suggest that zinc oxide and other semiconductor materials may play a leading role in providing antimicrobial functionality to the next-generation medical devices.

© 2009 Elsevier B.V. All rights reserved.

* Corresponding author at: Joint Department of Biomedical Engineering,
University of North Carolina and North Carolina State University, 8210 Stonetown Ave,
Raleigh, NC 27695-7115, United States. Tel.: +1 919 696 8488; fax: +1 919 513 3814.
E-mail address: roger_narayan@msn.com (R.J. Narayan).

1. Introduction

The growth of bacteria and other microorganisms on synthetic materials, especially materials used in medical devices, is a growing area of scientific inquiry. The National Institutes of Health has stated that microbial biofilms are a contributing factor in more than 80% of human infections [1]. Bacteria can be found in two states, either floating in a liquid medium (as planktonic bacteria) or embedded within a matrix (in a microbial biofilm). Bacteria more commonly exist in the sessile form than in free-floating form [2,3]. While much remains unknown about biofilm formation, organization, and function, it is now understood that bacteria within biofilms exhibit different physiological properties than planktonic bacteria.

They express different genes, exhibit different growth rates, demonstrate different pathogenic properties, and possess different antimicrobial susceptibility rates [4,5]. Infections caused by biofilms are commonly seen in patients with implanted devices or indwelling foreign objects, including catheters, pacemakers, and endoscopes [6–8].

Biofilms consist of a community of microorganisms held together by a matrix, in which the microorganisms cooperate and interact with one another. This matrix is comprised of an extracellular polymeric substance that is produced by microorganisms in the biofilm and is primarily made up of polysaccharides [5–9]. Microorganisms in a biofilm are found along solid–liquid interfaces and liquid–gas interfaces. Biofilms may contain only one organism or a variety of different microorganisms. The main unit of the biofilm is the microcolony, which contains clusters of microorganisms [3–10]. Microcolonies are located throughout the matrix, and contain channels for the transport of oxygen, nutrients, waste, and other particles [11–13]. In some situations, microscale layers within a biofilm contain cells of the same species that exhibit dissimilar phenotypes [14,15]. Oxygen concentration gradients, pH differences, and other environmental variations are created by these microscale layers.

Biofilm formation begins with adhesion of a microorganism to a surface. The initial interaction between the microbial cells and the surface is tenuous [16–18]. It is during this time that biofilms are the most fragile, with cells frequently attaching and detaching from the biofilm surface [5]. Once the cells have attached, they produce an extracellular polysaccharide matrix, which provides stability to the biofilm by enabling cell–surface and

cell–cell interactions [4,16,19]. After stable attachment, the biofilm develops into a more complex environment; additional planktonic cells adhere, microcolonies develop, and complex biofilm architecture forms [2,18,19].

Biofilms are a dynamic environment, in which cells from solution are attaching to the biofilm and are being released into the local environment. Microbial biofilms possess several unique attributes that convey resistance to antimicrobial agents. For example, the dosage of an antimicrobial that would eradicate a bacterium in planktonic form may have a less significant effect on a bacterium within a microbial biofilm. In fact, doses of antimicrobial agents that are thousands of times stronger than the minimum amount required to kill planktonic microorganisms may not be sufficient to eradicate microorganisms within a biofilm [6]. In addition, antibacterial metal ions such as copper and silver are highly effective against planktonic bacteria but are significantly less effective against bacteria in the biofilm state [6]. The same matrix that holds the biofilm together may also act as a diffusion barrier that slows the rate at which antimicrobials reach the microorganisms [20]. It is thought that cells are able to transfer genetic information, allowing resistance properties of one cell to spread to other cells within the biofilm [6]. One theory is that a small percentage of cells in a biofilm, called persister cells, adapt a phenotype that is highly resistant to antibiotics and is similar to that of fungal spores. Little is known about this phenomenon, but it is currently being investigated by several research groups [21,22].

The environmental variations within a biofilm may allow certain regions of a microbial biofilm to be susceptible to a particular antibiotic, while other regions remain impervious. Layering within a microbial biofilm, cells can exist in a variety of metabolic states [7,23]. Cells can be found growing both aerobically and anaerobically in the same biofilm; as a result, antimicrobial agents that only act on aerobic bacteria may not completely eradicate the biofilm [12]. Cells may also have different growth rates depending on their position within the biofilm. For example, b-lactam antimicrobials that only act upon dividing cells (e.g., penicillin) may only kill a portion of the bacteria within a layered biofilm [4– 20]. Local regions within microbial biofilms may possess low pH values due to hindered acidic cell waste removal; as a result, the structure of antimicrobial agents may be altered and rendered harmless [7–24]. Several studies have examined the mechanics and kinetics of initial cell–surface adhesion [17,18]. One unique function of microbial biofilms that makes them unique from their planktonic counterparts is their information-sharing capability. Studies have shown that not only do cells in a biofilm communicate with each other, but also cell–cell communication is necessary for normal biofilm development. Cells in a biofilm secrete chemical signals that are not produced by planktonic bacteria; without these signals, microorganisms within biofilms are more susceptible to antimicrobial agents [24]. Quorum sensing is another microbial communication phenomenon that has received much attention by researchers. It is believed that cells in a biofilm can obtain a census of surrounding cells using chemical signaling [14–24]. Genetic studies of biofilms have shown that microbial cells within biofilms express different genes, with some genes being up regulated and other genes being down regulated [15]. Finally, it has been shown that fluid shear forces have

significant effects on biofilm formation. Increased hydrodynamic forces have been correlated to higher density, higher stability, lower thickness, and increased extracellular polysaccharide production [16].

Developing effective methods to reduce biofilm formation is a growing area of biomaterials research. Several approaches have been taken to combat biofilm infections. One strategy is to disrupt the extracellular polysaccharide component of the microbial biofilm, thereby returning the microorganisms to their antibiotic-susceptible planktonic state [6]. Halogenated furanones are a set of compounds that inhibit quorum sensing. Researchers theorize that by disrupting quorum sensing they can eliminate some of the resistant behavior of microbial biofilms [25]. Another anti-biofilm technique involves the development of materials with antimicrobial properties that destroy the microorganisms on contact before they can develop into an organized biofilm [25]. Other groups are focusing on developing mechanisms to prevent cell adhesion processes that are necessary for microbial biofilm formation [26,27].

Standard methods to quantify antimicrobial efficacy are necessary in order to develop novel approaches for eliminating biofilms. One of the most simple and commonly administered studies is the Kirby-Bauer disk diffusion test [26]. The principle of this method is that when a biomaterial is placed on an inoculated agar plate, its antimicrobial activity will diffuse into the surrounding agar and produce a “zone of inhibition” in which microbial growth does not occur. The shake test is another method to examine antimicrobial susceptibility [28–30]. In

this method, the material of interest is placed in a bacterial suspension. The diffusion of antimicrobial agents from the material into the suspension is examined by measuring the cell density before and after addition of an antimicrobial agent.

Bioreactors have become a frequently used tool for studying microbial biofilms. The common element of these devices is that they provide a controlled environment, which contains both (a) a growth medium and (b) an organism that is to be cultured. A variety of bioreactors have been developed, in which variety of experimental parameters, including temperature, volume, flow rate, hydrodynamic forces, and cell density, may be controlled. One of the first bioreactors used to study biofilm formation is the Robbins device. This device consists of a flow chamber with holes for removable round plugs on which the microbial biofilm grows [31]. Approximately 20 years ago, researchers began creating modifications of the Robbins device, which have been modified to meet various experimental needs [32,33]. Some types of modifications include alterations in the material used, plug type, number of plugs, plug orientation, and flow rate (Tyler Research, Edmonton, AB) [34,35]. Another bioreactor that was developed in the early years of biofilm research was the perfused biofilm fermenter [20– 36]. The advantage of this device is that by regulating the flow rate of media, the growth rate of the biofilm can be controlled. The perfused biofilm fermenter was later modified to provide more efficient examination of antimicrobial susceptibility; for example, a system was developed that enabled multiple biofilms to be exposed to different concentrations of an antimicrobial agent. A scaled-down model of the original perfused biofilm fermenter has been fabricated using Swinnex filter units (Millipore,

Billerica, MA), which allows microbial biofilm studies to be conducted with low quantities of material [37].

Biosurface Technologies (Bozeman, MT) carries several types of bioreactors that may be used to examine microbial biofilms. The annular reactor is a vessel with a rotating cylinder for creating fluid shear and 20 removable coupons for carrying test materials [38,39]. This bioreactor is intended for industrial research of water systems, electronics, and chemical processes. The drip flow reactor consists of channels, which contain surfaces on which the microbial biofilm is grown. Media is dripped onto these channels to create an environment for studying biofilms under low shear stress conditions [23]. For microscopic studies, Biosurface Technologies has prepared a device with five lines of flow cells, which are compatible with fluorescent and confocal imaging under a variety of flow conditions [40]. The rotating disc reactor consists of a continuous flow media vessel, which contains six removable coupons on a rotating disk that can be used to expose microbial biofilms to surface shear stress [41,42]. This device is meant for antimicrobial efficacy studies. Similar to the rotating disc reactor is the CDC Biofilm Reactor. The bioreactor consists of 24 stationary removable coupons in a continuous flow media vessel, in which shear stress is provided by a rotating baffle. This reactor has been designed by the Centers for Disease Control and Prevention to study biocides and medical materials [43]. The Calgary Biofilm Device (Innovotech, Edmonton, AB) is a high-throughput bioreactor that allows for efficient examination of antimicrobial susceptibility. This two-part device consists of a top component containing pegs arranged to fit into a 96-well plate; the bottom component shaped like a 96-

well plate, which is adapted to also serve as a media flow channel [44]. With 96 opportunities to examine material–biofilm interaction, a large amount of data can be collected at once. This device is commercially sold as the MBEC assayTM (Innovotech, Edmonton, AB) [45].

In this study, we have examined microbial biofilm formation on zinc oxide thin films. Researchers have taken significant interest in zinc oxide (ZnO) due to its electrical, piezoelectric, and photocatalytic properties [46–49]. This compound is an n-type semiconductor with a wide direct band gap of 3.3 eV and a free excitation energy of 60 meV [50]. It is naturally found in the wurtzite crystal structure. In the field of nanoelectronics, zinc oxide is one of several semiconductor compounds being used to make nanowires [46]. Due to its ability to be both n-doped and p-doped, zinc oxide has been used to make blue light emitting diodes [47]. Doped zinc oxide has also been used in the fabrication of photovoltaic thin films [51,52]. When exposed to light, valence band holes can be generated in zinc oxide. These holes are able to react with nearby molecules to produce oxidants. The reaction of zinc oxide with water produces the hydroxyl radical (OH[•]). In the case of oxygen, the result is the superoxide molecule, O₂^{•-} [53].

Photocatalytic generation of radicals provides zinc oxide with antimicrobial properties, since the oxidizing agents disrupt microbial cell membranes [49]. Several techniques have been used to make zinc oxide thin films, including filtered vacuum arc deposition, chemical vapor deposition, and pulsed laser deposition [54–58]. The structural and biological properties of silicon wafers coated with zinc oxide thin films by means of pulsed laser deposition were

examined by atomic force microscopy, X-ray photoelectron spectroscopy, and MTT viability assay. In order to examine the effects of light on zinc oxide antimicrobial properties, disk diffusion antimicrobial susceptibility studies were conducted under fluorescent light and in darkness. In addition, a CDC Biofilm Reactor was used to examine the antimicrobial properties of zinc oxide thin films. Zinc oxide thin films and other semiconductors may be used to provide chemical and electronic antimicrobial functionalities to next-generation medical devices.

2. Materials and methods

A high-purity zinc oxide powder (Alfa Aesar, Ward Hill, MA) was pressed into round 2-in. diameter pellets. The pellets were subsequently sintered in an oxygen atmosphere at 1000 °C for 12 h. Zinc oxide thin films were grown on silicon wafers using pulsed laser deposition. A krypton fluoride excimer laser ($\lambda = 248$ nm, repetition rate = 10 Hz) was used to ablate the high-purity zinc oxide target. The thin films were grown under O₂ partial pressure of 5×10^{-5} Torr at room temperature for 5 min. The materials were then cut into approximately 0.5 cm x 0.5 cm squares. The zinc oxide thin film deposition rate using a KrF excimer laser is on the order of 0.01 nm/pulse [59]. A Dimension 3000 AFM (Veeco, Santa Barbara, CA) with an AC160 tip (Olympus, Melville, NY), which was operated at a resonance frequency of 366.304 kHz in tapping mode, was used to determine the surface topography of the zinc oxide-coated silicon wafer. X-ray photoelectron spectroscopy on the zinc oxide-coated silicon wafer was performed with a LAS-3000 spectrometer (Riber, Rueil Malmaison,

France), which utilized Mg K α excitation ($\lambda = 1254$ eV) and a 1 mm spot size. The photoelectron energy was calibrated by referencing to adventitious carbon. In this study, the take off angle was 75° from the surface, the X-ray incidence angle was 20°, and the X-ray source to analyzer angle was 55°. The base pressure of the analysis chamber was maintained at $\sim 10^{-10}$ Torr.

Viability of neonatal human epidermal keratinocytes (HEK) on zinc oxide-coated silicon wafers was examined using the metabolic marker MTT assay. These cryopreserved human epidermal keratinocytes were purchased from a commercial source (Lonza, Walkersville, MD) and then passed twice to propagate and then seeded in 6-well plates at a density of approximately 20,000 human epidermal keratinocytes in keratinocyte growth media (KGM-2). Cells were grown in a humidified environment of 5% CO₂ at 37 °C. Cells were maintained in keratinocyte growth media, consisting of serum-free keratinocyte basal media supplemented with human epidermal growth factor, insulin, bovine pituitary extract, hydrocortisone, transferrin, epinephrine and GA-1000 (gentamicin–amphotericin). Wells, zinc oxide-coated silicon wafers, and uncoated silicon wafers were washed with 2 ml of media. Prior to the experiments, zinc oxide-coated silicon wafers and uncoated silicon wafers were sterilized by exposure to ultraviolet B light for 4 h, flipping the sides after 2 h. During sterilization, the materials were rotated ninety degrees every 30 min. Upon completion of UV sterilization, the materials were placed in 24-well plates. A small amount of Akwa Tears (Akorn, Buffalo Grove, IL) was used to attach the wafers to the bottom of the plate. The wells were rinsed with KGM-2 and the media was changed after 24 h. Sampling was

conducted after the human epidermal keratinocytes were 60% confluent. MTT assay (3-[4,5-dimethyl-2-thiazol]-2,5-diphenyl-2H-tetrazolium bromide) was used to assess viability [60]. Absorbance, directly proportional to cell viability, was determined spectrophotometrically at $\lambda = 550$ nm in a Multiskan RC ELISA plate reader (Labsystems, Helsinki, Finland). The zinc oxide-coated silicon wafers and uncoated silicon wafers were moved to a new plate to prevent cells that had grown on the plate from influencing the data. MTT viability assays were conducted in quadruplicate on zinc oxide-coated silicon wafers and uncoated silicon wafers. Human epidermal keratinocytes (normalized to media control) were statistically compared using ANOVA (SAS 9.1 for Windows) (SAS, Cary, NC). Multiple comparisons were made between different membrane types using the Student's t-test at $p < 0.05$.

A CDC Biofilm Reactor (Biosurface Technologies, Bozeman, MT) was used to examine microbial growth on zinc oxide-coated silicon wafers and uncoated silicon wafers. 0.5 cm x 0.5 cm wafers of the materials were glued to polycarbonate sampling coupons. These coupons were immobilized in the bioreactor media by coupon holder rods. Four samples were used for each biomaterial, with separate experiments being conducted for the uncoated and coated wafers. Tryptic Soy Broth (Teknova, Hollister, CA) was used as the media in the bioreactor. Fluid shear stress was provided by a baffled stir bar, which was rotated at a rate of 120 rpm. A 0.5 McFarland Standard of *Escherichia coli* strain ATCC 25922 (American Type Culture Collection, Manassas, VA) in sterile H₂O was prepared. The bioreactor was inoculated with 1 ml of the bacterial suspension ($\sim 1 \times 10^8$ colony-forming units). Culturing occurred in the bioreactor for 48 h at room temperature under constant fluorescent light

exposure. At 48 h, sterile cotton tipped applicator sticks were used to transfer the biofilms from the surfaces of the to 10 ml vials of sterile water. Serial dilution in sterile water and plating on trypticase soy agar (Teknova, Hollister, CA) was used to determine the cell density of the *E. coli* biofilm on the surface of the material.

Microbial growth on zinc oxide-coated silicon wafers and uncoated silicon wafers was examined using a disk diffusion assay. *E. coli* strain ATCC 25922 was used in this study (American Type Culture Collection, Manassas, VA). The microorganism was cultured on trypticase soy agar plates (Teknova, Hollister, CA). McFarland Standard suspensions made by visual comparison were used to measure cell density. Disk diffusion studies were used to examine the microbial growth properties of zinc oxide-coated silicon wafers and uncoated silicon wafers. A 0.5 McFarland Standard suspension of *E. coli* in sterile H₂O was spread onto Mueller-Hinton II agar plates (BD Diagnostic Systems, Sparks, MD) using sterile cotton tipped applicator sticks. Immediately following inoculation, the zinc oxide-coated silicon wafers and uncoated silicon wafers were placed on the inoculated plates, with the coated side facing the agar. Zinc oxide-coated silicon wafers and uncoated silicon wafers were placed on different plates, with three samples on each plate. Two plates were prepared for each of the materials. One set was left in dark and the other set was constantly exposed to fluorescent light for the duration of the experiment. After 24 h at room temperature, microbial growth on the plates was examined using optical microscopy.

3. Results and discussion

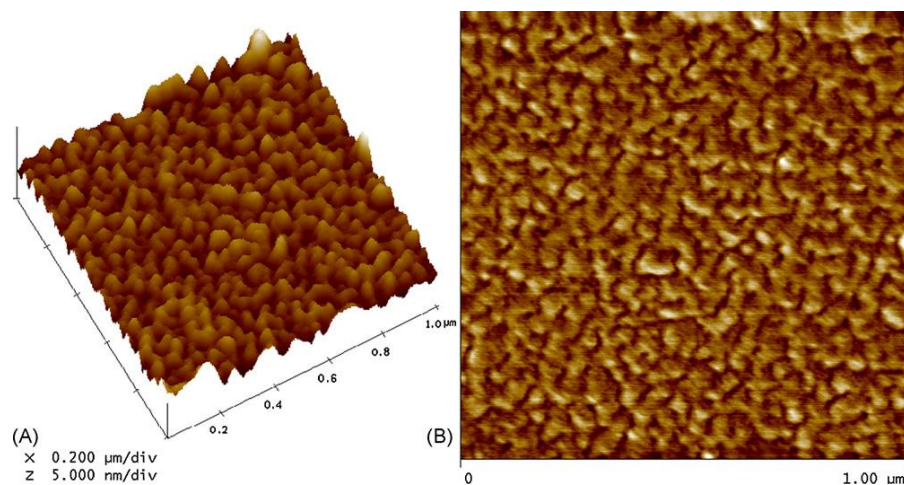


Fig. 1. (A and B) Atomic force micrograph of zinc oxide thin film grown on silicon wafer.

Atomic force micrographs of the zinc oxide-coated silicon wafer are shown in Fig. 1. Root mean squared surface roughness was derived from tapping mode measurements taken over a 1 mm^2 area. The root mean squared value was shown to be 0.4 nm , indicating that splashing is not significant [61]. The average grain size was $\sim 25 \text{ nm}$. These surface properties were similar to those for zinc oxide materials using filtered vacuum arc deposition [55]. The X-ray photoelectron spectrum for the zinc oxide-coated silicon wafer revealed the presence of carbon, oxygen, silicon, and zinc (Fig. 2). A large amount of the oxygen in this spectrum can be attributed to oxygen atoms located in adventitious oxidized carbon on the film surface and in silicon oxide on the substrate. The MTT viability assays after 24 h for both zinc oxide-coated silicon and uncoated silicon are shown in Fig. 3. These results indicate that human epidermal keratinocyte growth on the zinc oxide-coated silicon wafer was similar to that on the uncoated silicon wafer and that zinc oxide thin films processed using pulsed laser deposition do not cause a significant difference in human cell viability or cell growth.

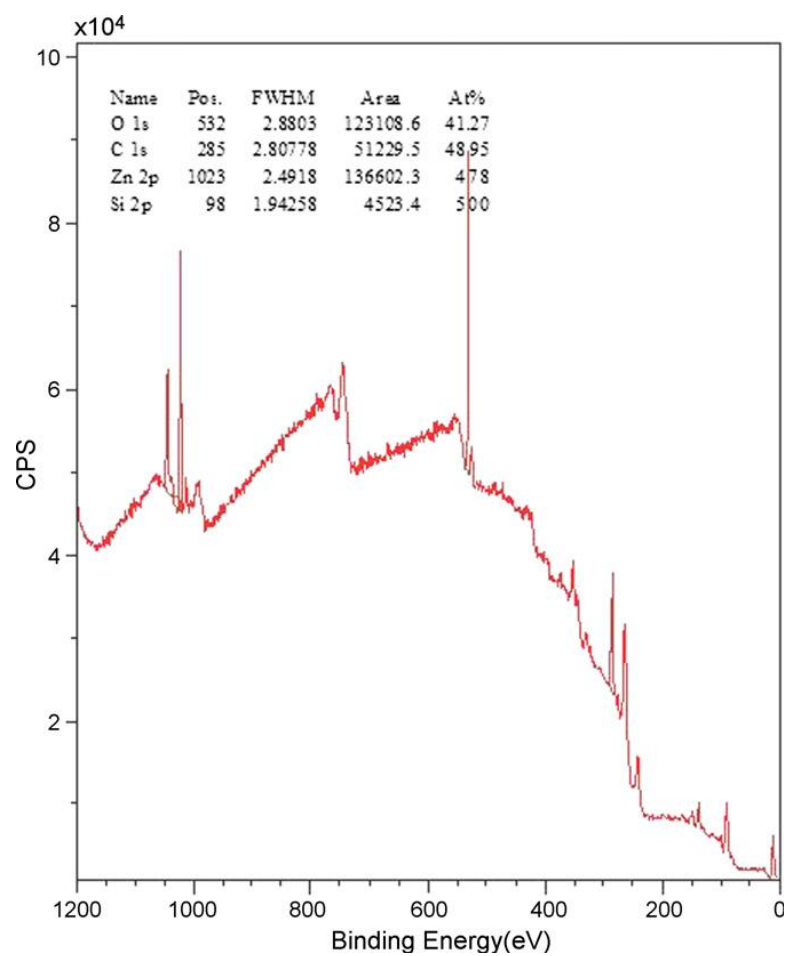


Fig. 2. X-ray photoelectron spectrum of zinc oxide-coated silicon wafer.

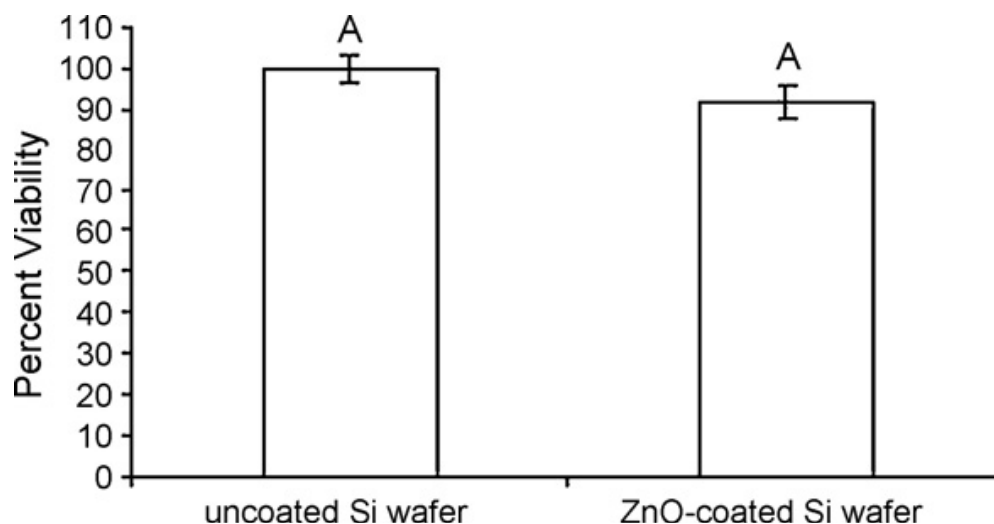


Fig. 3. Twenty-four hours MTT viability assays for zinc oxide-coated silicon wafers and uncoated silicon wafers.

E. coli were able to grow on both zinc oxide-coated silicon wafers and uncoated silicon wafers in the CDC Biofilm Reactor. The cell density on the uncoated silicon was $13.16 \pm 9.44 \times 10^6$ colony forming units/cm² and the cell density on the zinc oxide-coated silicon was $6.28 \pm 3.52 \times 10^6$ colony-forming units/cm². While bacteria were able to grow on both materials, a greater than 50% reduction in cell density was observed from the zinc oxide to the uncoated silicon. Images of disk diffusion results for uncoated silicon wafers and zinc oxide-coated silicon wafers at 24 h can be seen in Fig. 4. After 24 h, the bacteria on the uncoated silicon wafers had grown over the entire plate. No indication of inhibited microbial growth was observed for the uncoated silicon either under constant fluorescent light or in darkness. On the other hand, the zinc oxide-coated wafers exhibited zones of inhibition both under constant fluorescent light and in darkness. Bacteria were inhibited from growing in a region ~1 mm from each edge of the square wafers. Colonies were observed within the zones

of inhibition, but cell density in within the zones was greatly reduced in comparison to areas outside of these zones. Degradation of the zinc oxide thin films was observed in both disk diffusion (Fig. 4) and CDC Biofilm Reactor studies. The results of this study confirm previous findings that zinc oxide does have antimicrobial properties [49,53,54]. The results also indicate that exposure to light is not necessary for zinc oxide thin films to exhibit antibacterial activity. The valence band holes created by the photocatalytic effect of zinc oxide cause the formation of hydroxide and superoxide molecules, both of which are antimicrobial [49]. In addition, the oxidized zinc ion itself may exhibit antimicrobial properties; the observed antibacterial activity may also be caused by the leaching of Zn^{2+} ions from the zinc oxide thin film [62].

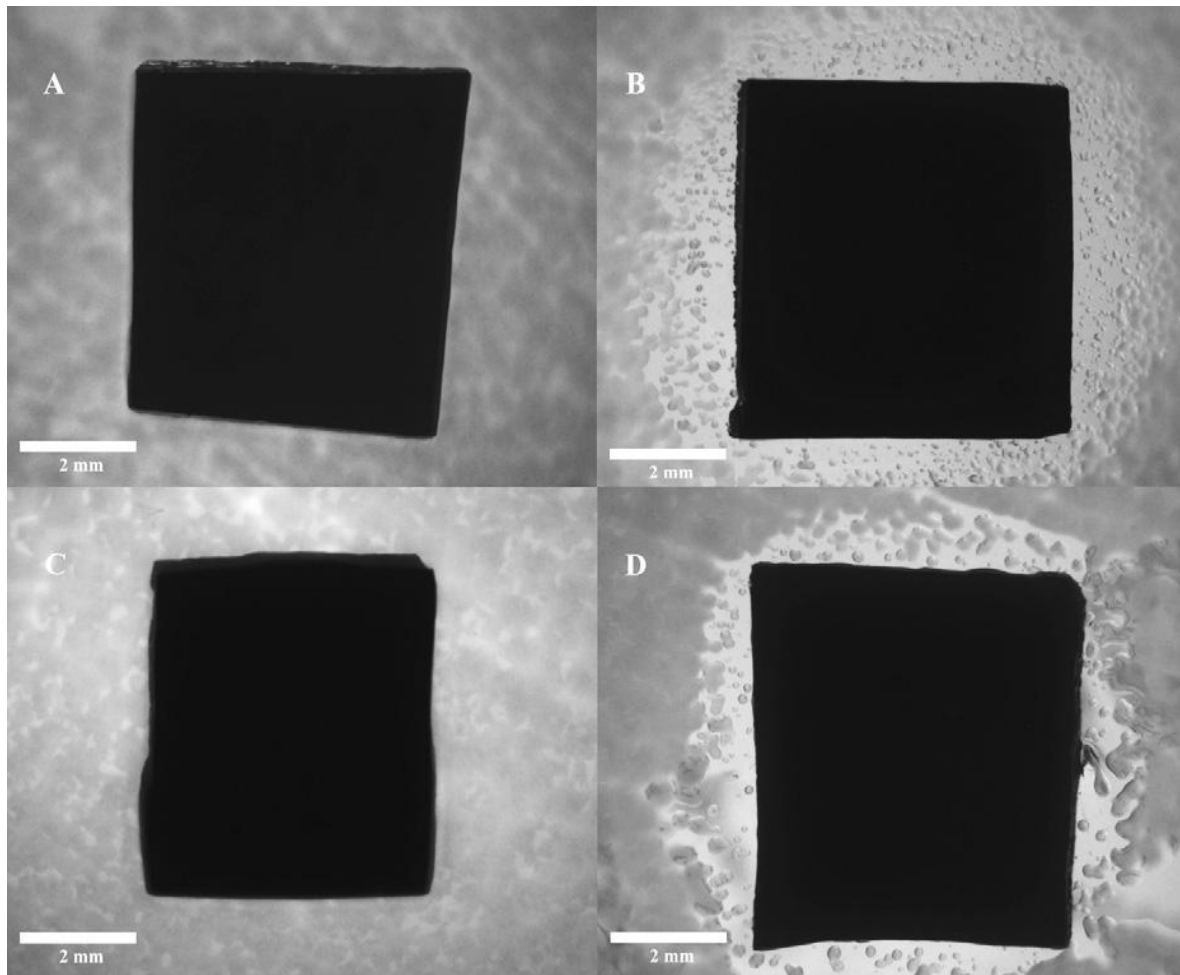


Fig. 4. Light microscopy images of (A) disk diffusion studies of uncoated silicon wafer without light exposure, (B) zinc oxide-coated silicon wafer without light exposure, (C) uncoated silicon wafer with fluorescent light exposure, and (D) zinc oxide-coated silicon wafer with fluorescent light exposure. Both zinc oxide-coated silicon wafers (with fluorescent light and without light exposure) had zones of inhibition that indicate antimicrobial activity. Neither uncoated material inhibited cell growth.

4. Conclusions

Assessing the growth of microbial biofilms on synthetic materials is a growing area of scientific inquiry. In this study, exposure to fluorescent light was shown to be unnecessary for zinc oxide coated silicon wafers to exhibit antimicrobial properties against *E. coli*. Our results indicate that zinc oxide thin films prepared using pulsed laser deposition significantly reduce bacterial growth but do not completely inhibit the growth of *E. coli*. The zinc oxide thin films were also found to degrade upon introduction into an aqueous environment, which allows for diffusion of antimicrobial Zn^{2+} ions into the surrounding environment. Zinc oxide and other semiconductor materials may provide unusual electronic and chemical mechanisms for inhibiting the growth of microorganisms.

Acknowledgement

The authors would like to thank K. Evaul (Center for Chemical Toxicology Research and Pharmacokinetics, North Carolina State University) for her assistance with the MTT assays.

References

- [1] D. Davies, *Nature Reviews Drug Discovery* 2 (2003) 114.
- [2] P. Watnick, R. Kolter, *Journal of Bacteriology* 182 (2000) 2675.

- [3] J.S. Webb, M. Givskov, S. Kjelleberg, *Current Opinion in Microbiology* 6 (2003) 578.
- [4] D.J. Musk, P.J. Hergenrother, *Current Medicinal Chemistry* 13 (2006) 2163.
- [5] D. Lindsay, A. von Holy, *Journal of Hospital Infection* 64 (2006) 313.
- [6] R.M. Donlan, J.W. Costerton, *Clinical Microbiology Reviews* 15 (2002) 167.
- [7] G.S. Baillie, L.J. Douglas, *Antimicrobial Agents and Chemotherapy* 42 (1998) 1900.
- [8] V. Sihorkar, S.P. Vyas, *Pharmaceutical Research* 18 (2001) 1247.
- [9] R.M. Donlan, *Emerging Infectious Diseases* 8 (2002) 881.
- [10] J.W. Costerton, Z. Lewandowski, D. DeBeer, D. Caldwell, D. Korber, G. James, *Journal of Bacteriology* 176 (1994) 2137.
- [11] Z. Lewandowski, P. Stoodley, S. Altobelli, E. Fukushima, *Water Science and Technology* 29 (1994) 223.

[12] D. de Beer, P. Stoodley, F. Roe, Z. Lewandowski, *Biotechnology and Bioengineering* 43 (1994) 1131.

[13] Z. Lewandowski, *Water Research* 34 (2000) 2620.

[14] B. Purevdorj-Gage, W.J. Costerton, P. Stoodley, *Microbiology* 151 (2005) 1569.

[15] P. Tenke, B. Kovacs, M. Jäckel, E. Nagy, *World Journal of Urology* 24 (2006) 13.

[16] Y. Liu, J.H. Tay, *Water Research* 36 (2002) 1653.

[17] W. Teughels, N. van Assche, I. Sliepen, M. Quirynen, *Clinical Oral Implant Research* 17 (2006) 68.

[18] M.C.M. van Looscrecht, J. Lyklema, W. Norde, A.J.B. Zehnder, *Microbiological Reviews* 54 (1990) 75.

[19] L. Hall-Stoodley, J.W. Costerton, P. Stoodley, *Nature Reviews Microbiology* 2 (2004) 95.

[20] P.S. Stewart, *Antimicrobial Agents and Chemotherapy* 40 (1996) 2517.

- [21] M.R. Parsek, C. Fuqua, *Journal of Bacteriology* 186 (2004) 4427.
- [22] I. Keren, N. Kaldalu, A. Spoering, Y. Wang, K. Lewis, *FEMS Microbiology Letters* 230 (2004) 13.
- [23] K.D. Xu, P.S. Steward, F. Xia, C.T. Huang, G.A. McFeters, *Applied and Environmental Microbiology* 64 (1998) 4035.
- [24] D.G. Davies, M.R. Parsek, J.P. Pearson, B.H. Iglewski, J.W. Costerton, E.P. Greenberg, *Science* 280 (1998) 295.
- [25] E.D.L. Pulcini, *Nephrologie* 22 (2001) 439.
- [26] T. Carrel, T. Nguyen, B. Kipfer, U. Althaus, *Journal of Heart and Valve Diseases* 7 (1998) 531.
- [27] B.L. Illingworth, T. Twenden, R.F. Schroeder, J.D. Cameron, *Journal of Heart and Valve Diseases* 7 (1998) 524.
- [28] CLSI performance standards for antimicrobial disk susceptibility tests; approved standard-9th edition M2-A9, Clinical and Laboratory Standards Institute, Wayne, Pennsylvania, 2006.

- [29] W.J. Ye, J.H. Xin, P. Li, K.L.D. Lee, T.L. Kwong, *Journal of Applied Polymer Science* 102 (2006) 1787.
- [30] Corporate Test Method 0923, Dow Corning, Midland, Michigan, 1979.
- [31] W.F. McCoy, J.D. Bryers, J. Robbins, *Canadian Journal of Microbiology* 27 (1981) 910.
- [32] G. Domingue, B. Ellis, M. Dasgupta, J.W. Costerton, *Journal of Clinical Microbiology* 32 (1994) 2564.
- [33] S. Kalmbach, W. Manz, U. Szewzyk, *FEMS Microbiology Ecology* 22 (1997) 265.
- [34] J.L. Adams, R.J.C. McLean, *Applied and Environmental Microbiology* 65 (1999) 4285.
- [35] J. Curtin, M. Cormican, G. Fleming, J. Keelehan, E. Colleran, *Antimicrobial Agents and Chemotherapy* 47 (2003) 3145.
- [36] P. Gilbert, D.G. Allison, D.J. Evans, P.S. Handley, M.R.W. Brown, *Applied and Environment Microbiology* 55 (1989) 1308.
- [37] S. Gander, P. Gilbert, *Journal of Applied Chemotherapy* 40 (1997) 329.

- [38] R.R. Sharp, A.K. Camper, J.J. Crippen, O.D. Schneider, S. Leggiero, *Journal of Environmental Engineering* 127 (2001) 403.
- [39] J.L. Rand, R. Hofmann, M.Z.B. Alam, C. Chauret, R. Cantwell, R.C. Andrews, G.A. Gagnon, *Water Research* 41 (2007) 1939.
- [40] P.A. Suci, B.J. Tyler, *Journal of Microbiological Methods* 53 (2003) 313.
- [41] B. Pitts, A. Willse, G.A. McFeters, M.A. Hamilton, N. Zilver, P.S. Stewart, *Journal of Applied Microbiology* 91 (2001) 110.
- [42] R. Murga, T.S. Forster, E. Brown, J.M. Pruckler, B.S. Fields, R.M. Donlan, *Microbiology* 147 (2001) 3121.
- [43] D.M. Goeres, L.R. Loetterle, M.A. Hamilton, R. Murga, D.W. Kirby, R.M. Donlan, *Microbiology* 151 (2005) 757.
- [44] H. Ceri, M.E. Olson, C. Stemick, R.R. Read, D. Morck, A. Buret, *Journal of Clinical Microbiology* 37 (1999) 1771.
- [45] J.J. Harrison, R.J. Turner, H. Ceri, *Environmental Microbiology* 7 (2005) 981.

- [46] Y.J. Xing, Z.H. Xi, X.D. Zhang, J.H. Song, R.M. Wang, J. Xu, Z.Q. Xue, D.P. Yu, *Applied Physics A* 80 (2005) 1527.
- [47] A. Tsukazaki, M. Kubota, A. Ohtomo, T. Onuma, K. Ohtani, H. Ohno, S.F. Chichibu, M. Kawasaki, *Japan Journal of Applied Physics* 44 (2005) 643.
- [48] A. Kuoni, R. Holzherr, M. Boillat, N.F. de Rooij, *Journal of Micromechanics Microengineering* 13 (2003) S103.
- [49] S.C. Liao, H.F. Lin, S.W. Hung, C.T. Hu, *Journal of Vacuum Science and Technology B* 24 (2006) 1322.
- [50] C. Li, G.J. Fang, Y.Y. Ren, Q. Fu, X.Z. Zhao, *Journal of Nanoscience and Nanotechnology* 5 (2006) 1467.
- [51] L. Stolt, J. Hedstrom, J. Kessler, M. Ruckh, K.O. Velthaus, H.W. Schock, *Applied Physics Letters* 62 (1993) 597.
- [52] O. Kluth, B. Rech, L. Houben, S. Wieder, G. Schope, C. Beneking, H. Wagner, A. Löffl, H.W. Schock, *Thin Solid Films* 351 (1999) 247.

- [53] M. Fang, J.H. Chen, X.L. Xu, P.H. Yang, H.F. Hildebrand, *International Journal of Antimicrobial Agents* 27 (2006) 513.
- [54] Z.W. Zhou, J.J. Liu, L.S. Chu, *Materials Science Forum* 486 (2005) 77.
- [55] E. Cetinorgu , S. Goldsmith, R.L. Boxman, *Surface and Coatings Technology* 201 (2007) 7266.
- [56] X. Li, Y. Yan, T.A. Gessert, C.L. Perkins, D. Young, C. DeHart, M. Young, T.J. Coutts, *Journal of Vacuum Science and Technology A* 21 (2003) 1342.
- [57] K. Minegishi, Y. Koiwai, Y. Kikuchi, K. Yano, M. Kasuga, A. Shimizu, *Japan Journal of Applied Physics* 36 (1997) L1453.
- [58] E.M. Kaidashev, M. Lorenz, H. von Wenckstern, A. Rahm, H.C. Semmelhack, K.H. Han, G. Benndorf, C. Bundesmann, H. Hochmuth, M. Grundmann, *Applied Physics Letters* 82 (2003) 3901.
- [59] H. Yong-Ning, Z. Jing-Wen, Y. Xiao-Dong, X. Qing-An, Z. Chang-Chun, H. Xun, *Science in China Series E: Technological Sciences* 50 (2007) 290.
- [60] T. Mosmann, *Journal of Immunologic Methods* 65 (1983) 55.

[61] S. Stepanovic, D. Vukovic, I. Dakic, B. Savic, M. Svabic-Vlahovic, *Journal of Microbiological Methods* 40 (2000) 175.

[62] E. Szunyogova, D. Mudronova, K. Gyoryova, R. Nemcova, J. Kovarova, L. Piknova - Findorakova, *Journal of Thermal Analysis and Calorimetry* 88 (2007) 355.

3.4 Antifungal Textiles Formed Using Silver Deposition in Supercritical Carbon Dioxide

*The following section a complete article reprinted from **Journal of Materials Engineering and Performance**, Volume 19, Gittard SD, Hojo D, Kyde GK, Narayan RJ, Parsons GN. 368-373, Copyright 2010, with permission from Springer*

Note: This article has been reformatted. In particular, the location of figures and spacing may have changed. The references are formatted as in the original manuscript.

JMEPEG (2010) 19:368–373

©ASM International

DOI: 10.1007/s11665-009-9514-7

1059-9495/\$19.00

Antifungal Textiles Formed Using Silver Deposition in Supercritical Carbon Dioxide

Shaun D. Gittard, Daisuke Hojo, G. Kevin Hyde, Giovanna Scarel, Roger J. Narayan, and Gregory N. Parsons

(Submitted May 25, 2009)

The antifungal properties of two silver-coated natural cotton fiber structures prepared using a supercritical carbon dioxide (scCO₂) solvent were examined. Scanning electron microscopy confirmed that the scCO₂ process may be used to produce cotton fiber textiles with uniform silver nanoparticle coatings. A version of the Kirby-Bauer disk diffusion test was used to assess the ability of these textiles to inhibit fungal growth. Cotton fabric samples modified with Ag(hepta) and Ag(cod)(hfac) exhibited measurable zones of inhibition. On the other hand, the uncoated fabric had no zone of inhibition. Possible applications of antifungal textiles prepared using scCO₂ processing include use in hospital uniforms and wound dressings.

Shaun D. Gittard and **Roger J. Narayan**, Joint Department of Biomedical Engineering, University of North Carolina/North Carolina State University, Raleigh, NC 27695; and

Daisuke Hojo, G. Kevin Hyde, Giovanna Scarel, and Gregory N. Parsons, Department of Chemical and Biomolecular Engineering, North Carolina State University, Raleigh, NC 27695. Contact e-mail: roger_narayan@msn.com.

Keywords antifungal materials, disk diffusion test, silver, supercritical carbon dioxide

1. Introduction

Textiles are appealing materials for use in several medical applications, including hospital uniforms and linens; prosthetic valves; and wound dressings (Ref 1-5). One promising innovation is to impart these textiles with antimicrobial properties. Noble metals such as copper, gold, and silver have broad-spectrum antimicrobial activity. For example, silver has several effects on microorganisms, including impeding the electron transport system and preventing DNA replication (Ref 6-8). Nanocrystalline silver provides Ag^0 and Ag^+ ions to the surrounding environment (Ref 9-12). As silver ions are depleted, an equilibrium shift allows additional Ag^0 and Ag^+ ions to be liberated from nanocrystalline silver. In previous studies, silver has demonstrated antimicrobial activity against a broad range of fungi, viruses, and bacteria (Ref 12-15). Processes such as electroless plating (Ref 16), master batch impregnating (Ref 16), IBAD SPI-ARGENT (Ref 3), layer-by-layer deposition (Ref 17), RF-plasma-mediated deposition (Ref 18), dip-pad-dry (Ref 19-21), sol-gel coating (Ref 22, 23),

soaking in silver nanosols (Ref 24), and sonochemical coating (Ref 25) have previously been used to fabricate textiles that contain antimicrobial metals.

Supercritical CO₂ (scCO₂) is an attractive process for imparting antimicrobial functionality to textile materials. It is a “green” technology, which does not produce any harmful byproducts (Ref 26). In addition, scCO₂ processing is relatively inexpensive and is amenable to scale-up for industrial production. Supercritical CO₂ processing is widely used for industrial-scale extraction of chemicals, including coffee decaffeination and fragrance collection (Ref 26). Supercritical CO₂ has also been used for disinfection of medical fabrics (Ref 27). While most commercial applications of scCO₂ processing involve the extraction of chemicals, scCO₂ processing may also be used to modify the surface (Ref 28) and impregnate the bulk (Ref 29, 30).

At temperatures and pressures above 31.1 °C and 73.8 bar, carbon dioxide exhibits properties of both liquid and gas (Ref 31-34). Supercritical fluids exhibit low viscosity and high diffusivity values similar to gases, but exhibit density values comparable to liquids. Supercritical CO₂ has recently been utilized for producing silver nanoparticle suspensions (Ref 35-37). It is also known that scCO₂ can be used as a solvent to dissolve metal-organic precursors to form thin films of metals and metal oxides (Ref 31-34). In previous studies, scCO₂ processing has been used to impart polymers (Ref 29) and porous structures (Ref 30) with antimicrobial functionality by impregnating these materials with silver nanoparticles.

The use of scCO₂ processing to impregnate textiles with antimicrobial materials has not been previously investigated.

Candida albicans is a pathogenic yeast that may infect the skin, mucous membranes, nails, and gastrointestinal tract. The incidence of candidal infection is rising due to the growing number of individuals with suppressed immune function caused by malignancy, HIV infection, antibiotic use, steroid use, or chemotherapy (Ref 38). In addition, common health problems, including diabetes mellitus and obesity, can also predispose an individual to candidal skin infection (Ref 38). *Candida albicans* is major cause of nosocomial infections (infections acquired during medical care); contaminated health care workers and biomaterials are common sources of these infections (Ref 39). For example, *C. albicans* is the most common fungus isolated from surgical wounds; Giandoni et al. demonstrated that asymptomatic candidal infection may delay wound healing (Ref 40, 41). In addition, *C. albicans* is the most commonly isolated fungal species in intensive care unit (ICU) patients; candidal infection is associated with ICU patient mortality (Ref 42). It is interesting to note that *C. albicans* may also cause enzymatic degradation of common textile dyes (Ref 43). For example, Vitor et al. demonstrated degradation of Direct Violet 51 azo dye by *C. albicans*, which resulted in removal of color (Ref 43).

In this study, we examined the antifungal properties of two silver-coated cotton fiber structures that were prepared using silver precursors dissolved in scCO₂. Two different silver precursor materials, Ag(hepta) and Ag(cod)(hfac), were investigated. A variation of the

Kirby-Bauer disk diffusion test was utilized to assess the ability of these textiles to inhibit growth of *C. albicans*. The Kirby-Bauer disk diffusion test is a National Committee on Clinical Laboratory Standards (Wayne, PA) procedure for assessing antimicrobial activity of materials (Ref 44), which has previously been used to assess the antimicrobial performance of textile materials (Ref 45). The prescribed method of the Kirby-Bauer assay was followed with the exception that silver-coated fabric was used instead of disks containing antibiotic agents. The results of this study suggest that scCO₂ process may be used to coat textiles with antifungal silver for a variety of medical applications.

2. Experimental Procedure

In this work, modification of cotton fabrics using scCO₂ was investigated. The silver precursors dissolved in scCO₂ were able to diffuse into the dense fiber network of the woven cotton structures and react with the cotton to deposit thin films and particles of silver. The size and density of the deposited particles may be controlled by altering the deposition conditions. A schematic of the scCO₂ system used for deposition of the silver nanoparticles can be seen in Fig. 1. Pressurized CO₂ (99.99% purity) was pumped into a stainless steel cylindrical-shaped reactor, which was heated with heating tape. The volume of the reactor used in this study was ~110 mL. Hydrogen was also introduced into the reactor to reduce the precursor material to metal. The inside of the reactor was observed through a sapphire viewing window. The pressure and temperature of the scCO₂ were monitored with a pressure gage and a thermocouple, respectively.

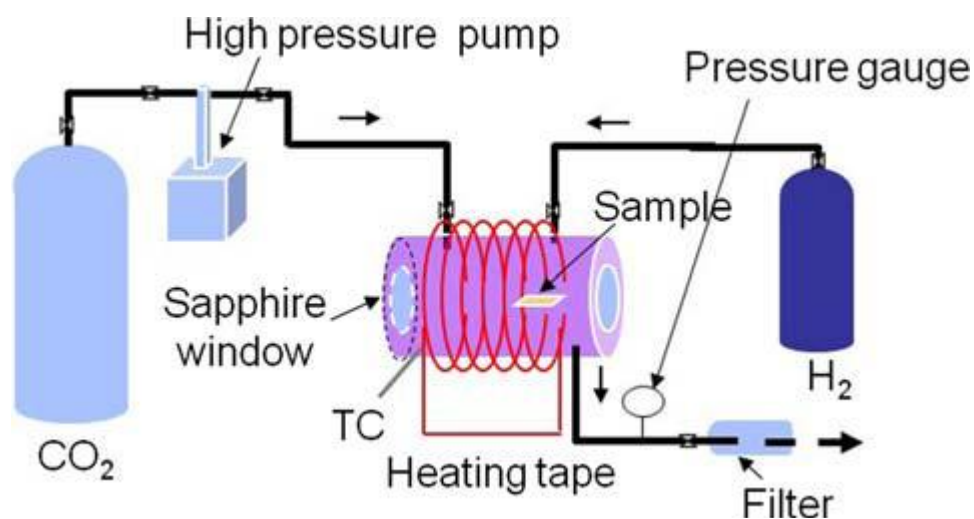


Fig. 1 Schematic of the scCO₂ system

The experimental procedure for the fabrication of silver-coated cotton fabrics is shown in Fig. 2. 2.0 cm x 2.0 cm cotton pieces and either 10 mg of Ag(hepta) or 2.1×10^{-4} mol/ L of Ag(cod)(hfac) were placed in the preheated reactor before it was filled with pressurized CO₂. The pressure and temperature of the dissolution process were 21 MPa and 40 °C, respectively. The supercritical fluid color remained clear after dissolution of the precursor. The cotton fabric samples were left in the chamber with the dissolved precursor for between 10 and 15 h, allowing the dissolved precursor to diffuse into the individual cotton fibers. After the diffusion process, the reaction chamber was allowed to vent. The temperature was then raised to 80 °C. Supercritical CO₂ with hydrogen gas (0.7 MPa) was introduced into the reaction chamber for reduction of the impregnated precursor. The decomposition time was 6 h. The decomposition pressure and temperature utilized in this study were 22 MPa and 80 °C, respectively. After the reaction chamber was vented, the scCO₂ fluid was replaced with fresh

compressed CO₂, which was used for rinsing the materials. Scanning electron microscopy of the silver-coated cotton fabrics was performed using a S3200 system (Hitachi, Tokyo, Japan), which was equipped with a Robinson backscattered electron detector and an energy-dispersive X-ray spectrometer.

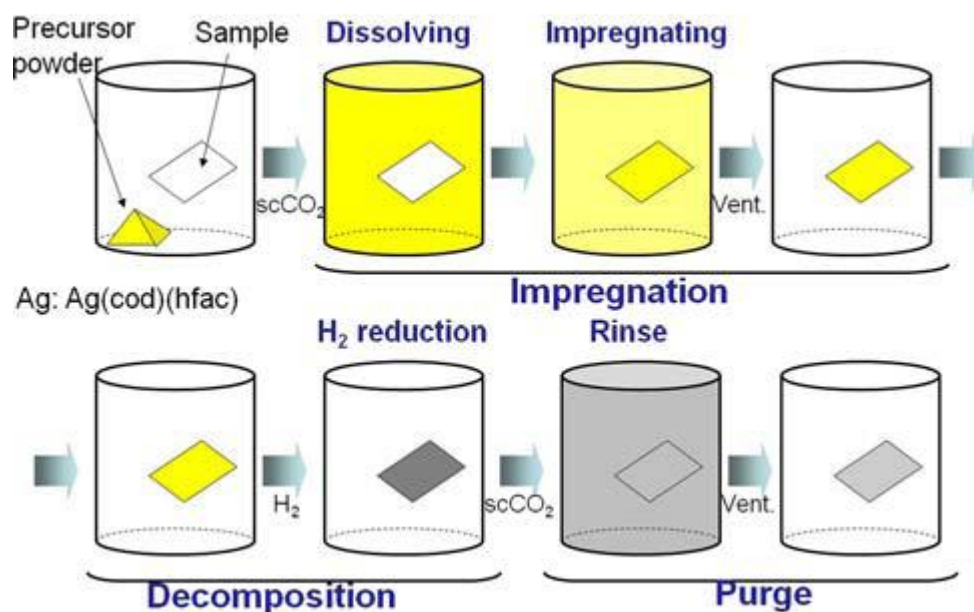


Fig. 2 Procedure for fabrication of silver-coated cotton fabrics

The antifungal properties of the Ag(hepta)- and Ag(cod)- (hfac)-coated fabrics were examined using *C. albicans*. The prescribed method of the Kirby-Bauer assay was followed with the exception that silver-coated fabric was used instead of disks containing antibiotic agents (Ref 44). Untreated cotton fabric was used as a negative control in these experiments. All fabrics were cut into ~0.50 cm x ~0.25 cm rectangles. 1% w/v Bacto yeast extract (BD Diagnostics, Sparks, MD), 2% w/v Bacto peptone (BD Diagnostics, Sparks, MD), 2% w/v dextrose (Mallinckrodt Chemical, St. Louis, MO), and 2% w/v granulated agar (BD

Diagnostics, Sparks, MD), commonly known as YPD agar, were used as growth media. The microorganism used in this study was *C. albicans* strain DUMC 117.00 (Duke University Medical Center, Durham, NC). A 0.5 McFarland Standard of *C. albicans* in sterile deionized water was prepared. The turbidity was verified using a Stasar II spectrophotometer (Gilford Instruments, Oberlin, OH). Sterile cotton-tipped applicator sticks were used to spread the cell suspension onto the agar plates. A different applicator stick was used for each plate. The fabrics were placed on the plates after inoculation. Triplicates of the same type of fabric were placed on each plate. Different types of fabrics were placed on separate plates. After the fabrics were placed on the plates, the plates were incubated at 37 °C for the duration of the study. The plates were examined at 0, 12, 24, 36, and 48 h after inoculation. Examination consisted of measuring zones of inhibition of cell growth on the agar and obtaining images of the fabrics to detect growth on the fabrics. An EZ4 D dissection stereo-microscope (Leica Microsystems, Bannockburn, IL) was used for imaging of the samples.

3. Results and Discussion

Scanning electron microscopy images of the three fabrics can be seen in Fig. 3. The silver-coated fabrics demonstrated both (a) a thin layer of silver over the entire fabric surface and (b) a scattering of silver aggregates on regions of the fabric surface. The appearance of streaks on the fibers was caused by electron beam-initiated swelling of the cotton fibers. A increase in volume of the cotton fiber caused fissures to form in the silver film; these features appear as streaks in the electron micrographs.

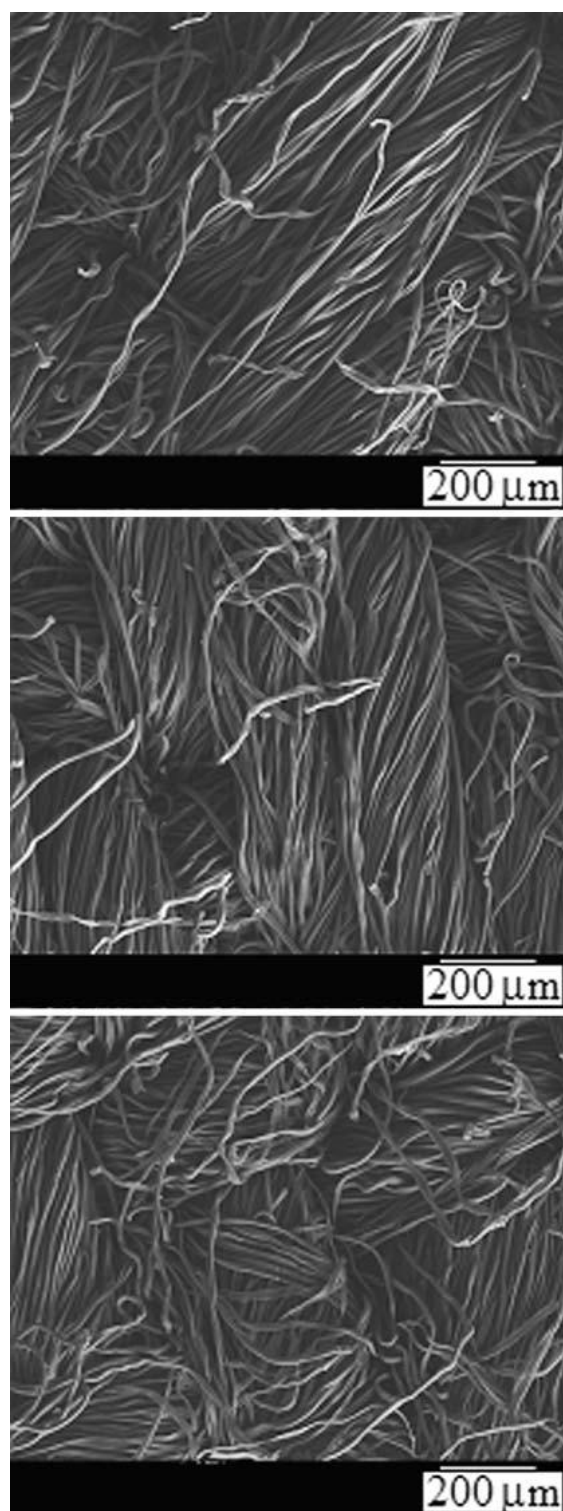


Fig. 3 Scanning electron micrographs of Ag(hepta)-modified fabric (top), Ag(cod)(hfac)-modified fabric (middle), and uncoated fabric (bottom)

Additional scanning electron microscopy images of the silver-coated fabrics showing both silver aggregates and electron beam-induced fissures are provided in Fig. 4. In this figure, the Ag(hepta)-modified fabric exhibited a greater number of silver crystals on its surface than the Ag(cod)-(hfac)-modified fabric. The energy dispersive X-ray spectra for Ag(hepta)-modified fabric, Ag(cod)(hfac)-modified fabric, and uncoated fabric can be seen in Fig. 5. All three fabrics exhibited trace amounts of copper and aluminum. The energy dispersive X-ray spectra of the uncoated cotton demonstrated that the material contained no silver. Energy dispersive X-ray spectra also indicated that the Ag(hepta)-modified fabric and Ag(cod)(hfac)-modified fabric contain similar amounts of silver. The cotton is primarily made up of cellulosic polymer, which contains a significant amount of hydroxyl groups on the surface. In the presence of hydrogen, it is likely that the silver precursors reacted at the surface to reduce the metal to Ag⁰ and oxidize the functional ligands. This mechanism is often found in other deposition techniques, including chemical vapor deposition and atomic layer deposition. The oxidized ligands were subsequently dissolved in the scCO₂ and removed from the system, resulting in silver coatings on the fibers (Ref 24-27). The formation of particles could result from either (a) surface diffusion of silver atoms or small clusters or (b) preferred oxidation/reduction of the precursors at deposited silver sites, which promoted formation of clusters and nanoparticles.

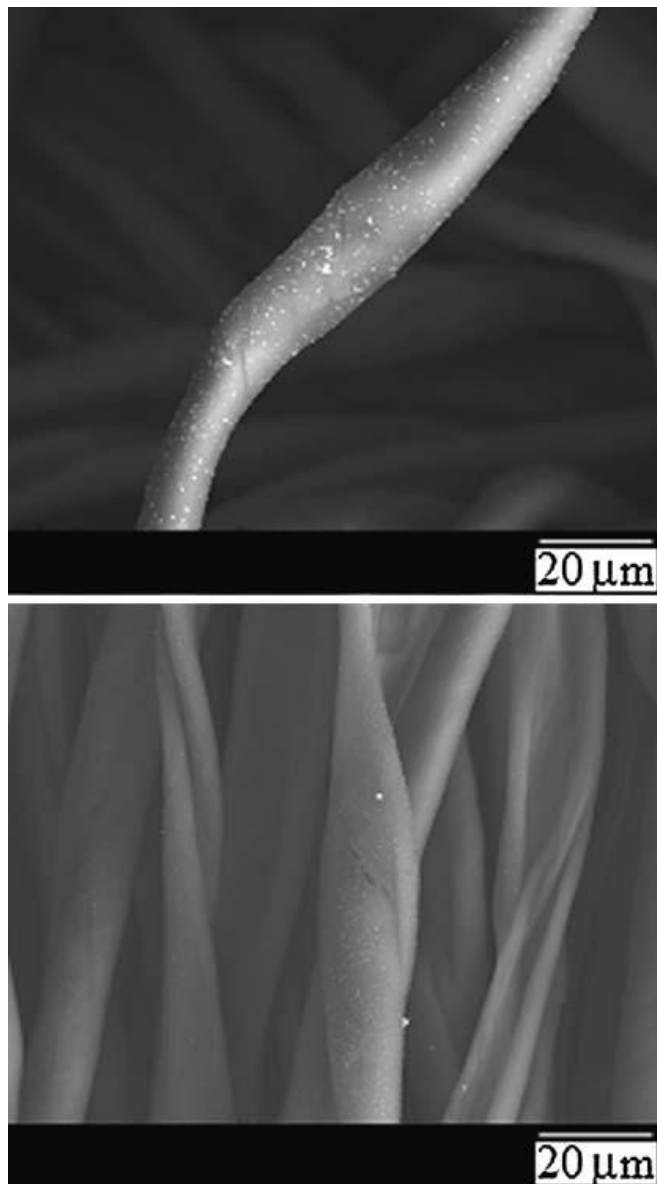


Fig. 4 Scanning electron micrographs of Ag(hepta)-modified fabric (top) and Ag(cod)(hfac)-modified fabric (bottom). The lighter-colored regions on the silver-modified fibers represent silver aggregates.

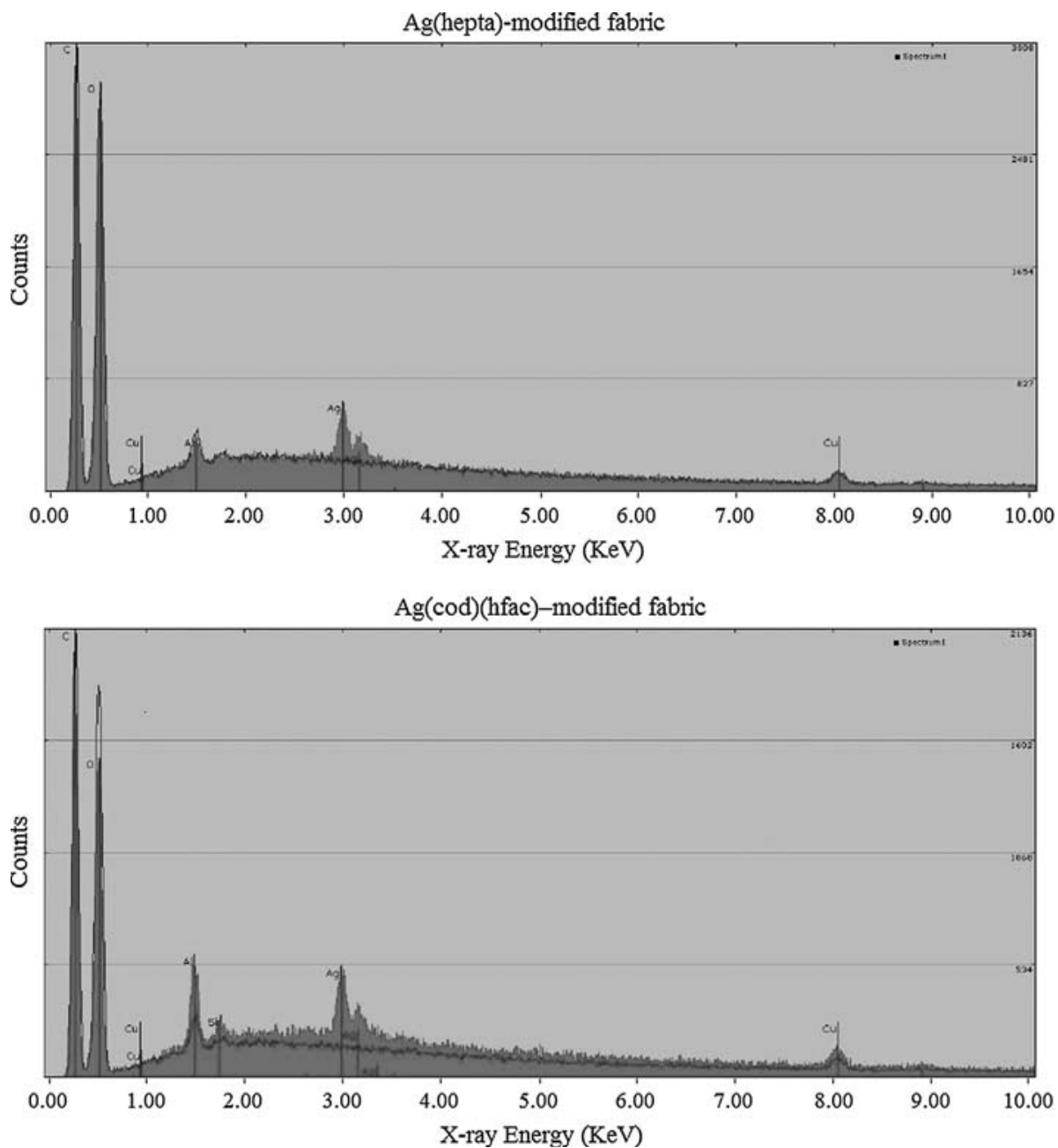


Fig. 5 Energy dispersive X-ray spectra overlay of Ag(hepta)-modified fabric (top) and Ag(cod)(hfac)-modified fabric (bottom). The spectra of the coated fabrics are in gray, and spectrum of the uncoated fabric is in black.

Images were obtained at 0, 12, 24, 36, and 48 h after initiation of the antimicrobial susceptibility assay. Images of the silver-coated and uncoated fabrics at these times are shown in Fig. 6. At 12 h, a confluent layer of small colonies formed on the agar. Zones of inhibition of fungal growth were observed in Ag(hepta)-modified and Ag(cod)(hfac)-modified fabrics. Enlarged images of the zones of inhibition of the three fabrics at 12 h are shown in Fig. 7. Zones of inhibition were measured from the edge of the fabric to the first sign of growth. The average radius of inhibited growth was 1.2 mm for both Ag(hepta)-modified and Ag(cod)(hfac)-modified fabrics. The uncoated cotton had no observed zone of inhibition. At 24 h, some fungal cells began to appear within the zones of inhibition for Ag(hepta)-modified and Ag(cod)(hfac)-modified fabric samples. The Ag(hepta)-modified surface exhibited a smaller number of colonies than the Ag(cod)(hfac)-modified surface; this result may be attributed to the arrangement of silver crystals on the fabric surface.

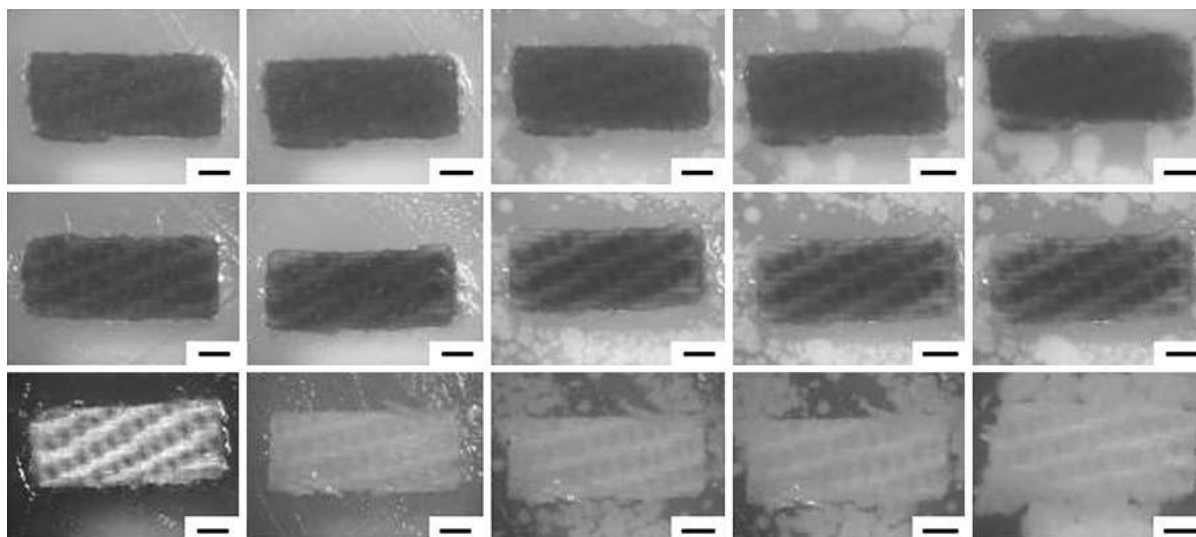


Fig. 6 Ag(hepta)-modified fabric (top), Ag(cod)(hfac)-modified fabric (center), and uncoated fabric (bottom). Images obtained at 0, 12, 24, 36, and 48 h after initiation of the experiment are shown from left to right. Scale bar = 1 mm

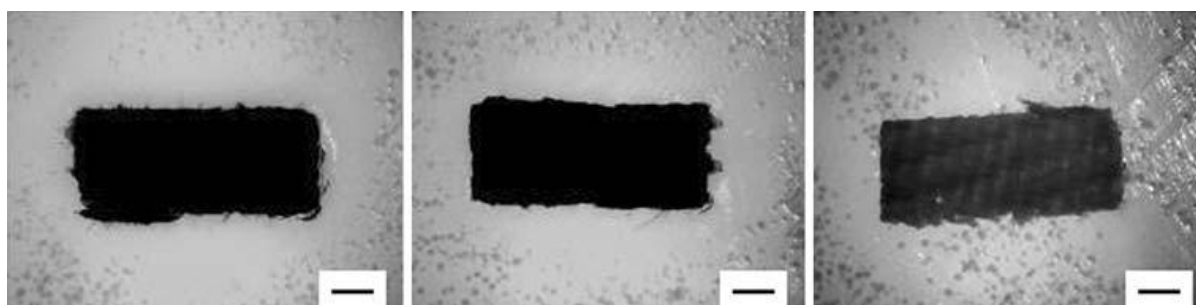


Fig. 7 Optical micrographs showing zones of inhibition for Ag(hepta)-modified fabric (left) and Ag(cod)(hfac)-modified fabric (center) at 12 h. An optical micrograph of the uncoated fabric at 12 h (right) is provided for comparison purposes. Scale bar = 1 mm

4. Summary

In this study, scCO₂ processing was shown to be a viable technique for producing antifungal textiles that may be used in medical applications. While the samples examined in this study were small in size, scCO₂ processing can easily be scaled up for commercial production of silver-coated textiles. After exposure to *C. albicans*, fabrics modified with Ag(hepta) and Ag(cod) (hfac) demonstrated measurable zones of inhibition. On the other hand, the uncoated fabric exhibited no zone of inhibition. Use of scCO₂ for imparting antimicrobial functionality to materials has several advantages, including relatively low processing temperatures, nonflammable processing materials, and nontoxic reactants. Supercritical CO₂ processing may be used to impart antifungal functionality to textiles used in wound dressings. Hospital uniforms containing antifungal textiles may be used to prevent the spread of fungal infections in hospitals, nursing homes, and other healthcare settings.

Acknowledgments

One of the authors (GNP) acknowledges support from the International Lead Zinc Research Organization, Inc., and support from the National Science Foundation under cooperative agreement CHE-9876674 and under project CTS-0626256.

References

1. S. Petrulyte, *Advanced Textile Materials and Biopolymers in Wound Management*, *Dan. Med. Bull.*, 2008, 55, p 72–77
2. X. Chen and H.J. Schluesener, *Nanosilver: A Nanoproduct in Medical Application*, *Toxicol. Lett.*, 2008, 176, p 1–12
3. K.S. Tweden, J.D. Cameron, A.J. Razzouk, and R.W. Bianco, *Silver Modification of Polyethylene Terephthalate Textiles for Antimicrobial Protection*, *ASAIO J.*, 1997, 43, p M475–M481
4. A. Gauger, M. Mempel, A. Schekatz, T. Schäfer, J. Ring, and D. Abeck, *Silver-Coated Textiles Reduce Staphylococcus aureus Colonization in Patients with Atopic Eczema*, *Dermatology*, 2003, 207, p 15–21
5. S. Haug, A. Roll, P. Schmid-Grendelmeier, P. Johansen, B. Wüthrich, T.M. Kündig, and G. Senti, *Coated Textiles in the Treatment of Atopic Dermatitis*, *Curr. Probl. Dermatol.*, 2006, 33, p 144–151
6. P.D. Bragg and D.J. Rainnie, *The Effect of Silver Ions on the Respiratory Chain of Escherichia coli*, *Can. J. Microbiol.*, 1974, 20, p 883–889

7. M.S. Modak and C.L. Fox, Binding of Silver Sulfadiazine to the Cellular Components of *Pseudomonas aeruginosa*, *Biochem. Pharmacol.*, 1973, 22, p 2391–2404
8. H.S. Rosenkranz and S. Rosenkranz, Silver Sulfadiazine: Interaction with Isolated Deoxyribonucleic Acid, *Antimicrob. Agents Chemother.*, 1972, 22, p 373–383
9. C.R. Ricketts, E.J. Lowbury, J.C. Lawrence, M. Hall, and M.D. Wilkins, Mechanism of Prophylaxis by Silver Compounds Against Infection of Burns, *Br. Med. J.*, 1970, 2, p 444–446
10. P. Spacciapoli, D. Buxton, D. Rothstein, and P. Friden, Antimicrobial Activity of Silver Nitrate Against Periodontal Pathogens, *J. Periodontal Res.*, 2001, 36, p 108–113
11. P.A. Maple, J.M. Hamilton-Miller, and W. Brumfitt, Comparison of the In Vitro Activities of the Topical Antimicrobials Azelaic Acid, Nitrofurazone, Silver Sulphadiazine and Mupirocin Against Methicillin- Resistant *Staphylococcus aureus*, *J. Antimicrob. Chemother.*, 1992, 29, p 661–668
12. P.K. Stoimenov, R.L. Klinger, G.L. Marchin, and K.J. Klabunde, Metal Oxide Nanoparticles as Bactericidal Agents, *Langmuir*, 2002, 18, p 6679–6686

13. R.M. Slawson, M.I. Van Dyke, H. Lee, and J.T. Trevors, Germanium and Silver Resistance, Accumulation, and Toxicity in Microorganisms, *Plasmid*, 1992, 27, p 72–79
14. G.J. Zhao and S.E. Stevens, Multiple Parameters for the Comprehensive Evaluation of the Susceptibility of *Escherichia coli* to the Silver Ion, *Biometals*, 1998, 11, p 27–32
15. J.A. Spadaro, T.J. Berger, S.D. Barranco, S.E. Chapin, and R.O. Becker, Antibacterial Effects of Silver Electrodes with Weak Direct Current, *Antimicrob. Agents Chemother.*, 1974, 6, p 637–642
16. J. Gabbay, G. Borkow, J. Mishal, E. Magen, R. Zatzoff, and Y. Shemer- Avni, Copper Oxide Impregnated Textiles with Potent Biocidal Activities, *J. Ind. Textiles*, 2006, 35, p 323–335
17. S.T. Dubas, P. Kumlangdudsana, and P. Potiyaraj, Layer-by-Layer Deposition of Antimicrobial Silver Nanoparticles on Textile Fibers, *Colloid Surf. A*, 2006, 289, p 105–109
18. T. Yuranova, A.G. Rincon, A. Bozzi, S. Parra, C. Pulgarin, P. Albers, and J. Kiwi, Antibacterial Textiles Prepared by RF-Plasma and Vacuum-UV Mediated Deposition of Silver, *J. Photochem. Photobiol. A*, 2003, 161, p 27–34

19. H.J. Lee, S.Y. Yeo, and S.H. Jeong, Antibacterial Effect of Nanosized Silver Colloidal Solution on Textile Fabrics, *J. Mater. Sci.*, 2003, 38, p 2199–2204
20. H.J. Lee and S.H. Jeong, Bacteriostasis and Skin Innoxiousness of Nanosize Silver Colloids on Textile Fabrics, *Textile Res. J.*, 2005, 75, p 551–556
21. S.H. Jeong, Y.H. Hwang, and S.C. Yi, Antibacterial Properties of Padded PP/PE Nonwovens Incorporating Nano-Sized Silver Colloids, *J. Mater. Sci.*, 2005, 40, p 5413–5418
22. B. Mahltig, D. Fiedler, and H. Boëtcher, Antimicrobial Sol-Gel Coatings, *J. Sol-Gel Sci. Technol.*, 2004, 32, p 219–222
23. J.J. Blaker, S.N. Nazhat, and A.R. Boccaccini, Development and Characterisation of Silver-Doped Bioactive Glass-Coated Sutures for Tissue Engineering and Wound Healing Applications, *Biomaterials*, 2004, 25, p 1319–1329
24. E. Falletta, M. Bonini, E. Fratini, A. Lo Nostro, G. Pesavento, A. Becheri, P. Lo Nostro, P. Canto, and P. Baglioni, Clusters of Poly(acrylates) and Silver Nanoparticles: Structure and Applications for Antimicrobial Fibers, *J. Phys. Chem. C*, 2008, 121, p 11758–11766

25. I. Perelshtein, G. Applerot, N. Perkas, G. Guibert, S. Mikhailov, and A. Gedanken, Sonochemical Coating of Silver Nanoparticles on Textile Fabrics (Nylon, Polyester and Cotton) and their Antibacterial Activity, *Nanotechnology*, 2008, 19, p 245705-1–245705-6
26. C. Aymonier, A. Erriguible, S. Marre, A. Serani, and F. Cansell, Processes Using Supercritical Fluids: A Sustainable Approach for the Design of Functional Nanomaterials, *Int. J. Chem. Reactor Eng.*, 2007, 5, p A77
27. C. Cinquemani, C. Boyle, E. Bach, and E. Schollmeyer, Inactivation of Microbes Using Compressed Carbon Dioxide—An Environmentally Sound Disinfection Process for Medical Fabrics, *J. Supercritical Fluids*, 2007, 42, p 392–397
28. C. Aymonier, C. Elissalde, H. Reveron, F. Weill, M. Maglione, and F. Cansell, Supercritical Fluid Technology of Nanoparticles Coating for New Ceramic Materials, *J. Nanosci. Nanotechnol.*, 2005, 5, p 980–983
29. F. Furno, K. Morley, B. Wong, B.L. Sharp, P.L. Arnold, S.M. Howdle, R. Bayston, P.D. Brown, P.D. Winship, and H.J. Reid, Silver Nanoparticles and Polymeric Medical Devices: A New Approach to Prevention of Infection?, *J. Antimicrob. Chemother.*, 2004, 54, p 1019–1024

30. K.S. Morley, P.C. Marr, P.B. Webb, A.R. Berry, F.J. Allison, G. Moldovan, P.D. Brown, and S.M. Howdle, Clean Preparation of Nanoparticulate Metals in Porous Supports: A Supercritical Route, *J. Mater. Chem.*, 2002, 12, p 1898–1905
31. Q. Peng, J.C. Spagnola, and G.N. Parsons, Self-Catalyzed Hydrogenolysis of Ni(cp)₂: Functional Metal Coating of Three-Dimensional Nanosystems at Low Temperature, *J. Electrochem. Soc.*, 2008, 155, p D580–D582
32. Q. Peng, D. Hojo, K.J. Park, and G.N. Parsons, Low Temperature Metal Oxide Film Deposition and Reaction Kinetics in Supercritical Carbon Dioxide, *Thin Solid Films*, 2008, 516, p 4997–5003
33. Q. Peng, J.C. Spagnola, H. Daisuke, K.J. Park, and G.N. Parsons, Conformal Metal Oxide Coatings on Nanotubes by Direct Low-Temperature Metal-Organic Pyrolysis in Supercritical Carbon Dioxide, *J. Vac. Sci. Technol. B*, 2008, 26, p 978–982
34. T. Gougousi and Z.Y. Chen, Deposition of Yttrium Oxide Thin Films in Supercritical Carbon Dioxide, *Thin Solid Films*, 2008, 516, p 6197–6204
35. M. Ji, X. Chen, C.M. Wai, and J.L. Fulton, Synthesizing and Dispersing Silver Nanoparticles in a Water-In-Supercritical Carbon Dioxide Microemulsion, *J. Am. Chem. Soc.*, 1999, 121, p 2631–2632

36. H. Ohde, F. Hunt, and C.M. Wai, Synthesis of Silver and Copper Nanoparticles in a Water-In-Supercritical-Carbon Dioxide Microemulsion, *Chem. Mater.*, 2001, 13, p 4130–4135
37. P.S. Shah, S. Husain, K.P. Johnston, and B.A. Korgel, Nanocrystal Arrested Precipitation in Supercritical Carbon Dioxide, *J. Phys. Chem. B*, 2001, 105, p 9433–9440
38. B. Havlickova, V.A. Czaika, and M. Friedrich, Epidemiological Trends in Skin Mycoses Worldwide, *Mycoses*, 2008, 51, p 2–15
39. M.A. Pfaller, Nosocomial Candidiasis: Emerging Species, Reservoirs, and Modes of Transmission, *Clin. Infect. Dis.*, 1996, 22, p S89–S94
40. D. Kaya, C.A. Agartan, and M. Yucel, Agents as a Cause of Surgical Wound Infections: An Overview of Host Factors, *Wounds*, 2007, 19, p 218–222
41. M.B. Giandoni and W.J. Rabski, Cutaneous Candidiasis as a Cause of Delayed Surgical Wound Healing, *J. Am. Acad. Dermatol.*, 1994, 30, p 981–984
42. J.J. Picazo, F. Gonzalez-Romo, and F.J. Candel, Candidemia in the Critically Ill Patient, *Int. J. Antimicrob. Agents*, 2008, 32, p S83–S85

43. V. Vitor and C.R. Corso, Decolorization of Textile Dye by *Candida albicans* Isolated from Industrial Effluents, *J. Ind. Microbiol. Biotechnol.*, 2008, 35, p 1353–1357

44. Laboratory and Clinical Standards Institute, Approved Standard: M2-A9, Performance Standards for Antimicrobial Disk Susceptibility Tests, 9th ed., Clinical and Laboratory Standards Institute, Wayne, PA, 2006

45. U.C. Hipler, P. Elsner, and J.W. Fluhr, Antifungal and Antibacterial Properties of a Silver-Loaded Cellulosic Fiber, *J. Biomed. Mater. Res. B Appl. Biomater.*, 2006, 77, p 156–163

3.5 Pulsed laser deposition of antimicrobial silver coating on Ormocer® microneedles

*The following section a complete article reprinted from **Biofabrication**, Volume 1, Gittard SD, Narayan RJ, Jin C, Ovsianikov A, Chichkov BN, Monteiro-Riviere NA, Staflien S, Chisholm B.041001, Copyright 2009, with permission from IOP Publishing*

Note: This article has been reformatted. In particular, the location of figures and spacing may have changed. The references are formatted as in the original manuscript.

IOP Publishing

doi:10.1088/1758-5082/1/4/041001

Biofabrication **1** (2009) 041001 (5pp)

COMMUNICATION

Pulsed laser deposition of antimicrobial silver coating on Ormocer® microneedles

S D Gittard¹, R J Narayan^{1,5}, C Jin¹, A Ovsianikov², B N Chichkov², N A Monteiro-Riviere^{1,3}, S Stafslie⁴ and B Chisholm⁴

¹ Joint Department of Biomedical Engineering, North Carolina State University, Raleigh, NC 27695, USA

² Laser Zentrum Hannover, Hollerithallee 8, 30419 Hannover, Germany

³ Center for Chemical Toxicology Research and Pharmacokinetics, North Carolina State University, Raleigh, NC 27695, USA

⁴ Center for Nanoscale Science and Engineering, North Dakota State University, 1805 Research Park Drive, Fargo, ND 58102, USA

⁵ Author to whom any correspondence should be addressed

E-mail: roger.narayan@msn.com

Received 29 July 2009

Accepted for publication 12 November 2009

Published 30 November 2009

Online at stacks.iop.org/BF/1/041001

© 2009 IOP Publishing Ltd Printed in the UK

Abstract

One promising option for transdermal delivery of protein- and nucleic acid-based pharmacologic agents involves the use of microneedles. However, microneedle-generated pores may allow microorganisms to penetrate the stratum corneum layer of the epidermis and cause local or systemic infection. In this study, microneedles with antimicrobial functionality were fabricated using two-photon polymerization–micromolding and pulsed laser deposition. The antibacterial activity of the silver-coated organically modified ceramic (Ormocer®) microneedles was demonstrated using an agar diffusion assay. Human epidermal keratinocyte viability on the Ormocer R® surfaces coated with silver was similar to that on uncoated Ormocer® surfaces. This study indicates that coating microneedles with silver thin films using pulsed laser deposition is a useful and novel approach for creating microneedles with antimicrobial functionality.

Microneedles are small-scale medical devices (<1 mm in length) used for delivery of protein-based pharmacologic agents, nucleic acid-based pharmacologic agents and other pharmacologic agents that are unable to be administered in oral form [1]. These devices create small pores in the stratum corneum layer of the epidermis of the skin that enable the delivery of pharmacologic agents into deeper layers of the skin and into the bloodstream [2]. Unlike conventional hypodermic needles, microneedle administration of a pharmacologic agent does not require medical training. Due to their smaller dimensions, microneedles are associated with less injection site damage and less patient pain than conventional hypodermic needles [1]. One concern that limits microneedle usage is the risk of infection associated with a compromised stratum corneum [3–5].

The stratum corneum layer serves as the outermost limiting barrier that prevents foreign objects, including microorganisms, from entering the body. Pathogenic microorganisms such as *Staphylococcus aureus* may be transferred through the stratum corneum by microneedles. One approach to reduce the risk of infection associated with microneedles is to fabricate microneedles that have antimicrobial properties. For example, antimicrobial microneedles may be fabricated by coating microneedles with thin films of antimicrobial materials such as silver. Silver exhibits broad-spectrum antimicrobial properties against viruses, fungi and bacteria, including *S. aureus*. These properties have been attributed to interruption of DNA replication and disruption of electron transport [3–10]. Silver also serves to reduce local matrix metalloproteinase levels, reduce inflammatory activity in wounds and facilitate

healing in wounds [11–13]. Recent work by Demling *et al* suggests that silver acts to increase re-epithelialization compared to a conventional antimicrobial solution [13].

Antimicrobial coatings may be applied to microneedle surfaces using a physical vapor deposition technique known as pulsed laser deposition [14]. Pulsed laser deposition involves vaporization of a solid target using a high energy laser; the average kinetic energy of atomic and molecular species generated by excimer laser ablation is between 100 kT and 1000 kT. In comparison, the equilibrium energy of species generated in thermal deposition techniques is on the order of kT [15, 16]. The high energy of laser-ablated species enhances film adhesion and promotes chemical reactions between the substrate and the film [17]. Pulsed laser deposition is ideally suited for deposition on biomedical polymeric substrates since deposition of many coating materials can take place at room temperature; other methods may involve deposition temperatures close to or above the glass transition temperatures of many biomedical polymers. Thin films prepared using pulsed laser deposition exhibit useful properties for many biomedical applications due to the high adhesion strength and the high-density/low-porosity nature of deposited films.

In this study, microneedle arrays were created from organically modified ceramic (Ormocer®) materials using a two-photon polymerization–micromolding technique. Ormocer® materials are organic–inorganic hybrid materials originally developed by Fraunhofer Institut für Silicatforschung, which contain organically modified silicon alkoxides and organic monomers [1]. Interactions between organic methacrylate groups and inorganic

silicon– oxygen–silicon networks create a three-dimensional network. These interactions between the ceramic and polymer components provideOrmocer® materials with chemical and thermal stability as well as prevent separation of Ormocer® material into separate phases. In previous work, Ormocer® surfaces fabricated using two-photon polymerization exhibited acceptable cell viability and cell growth profiles against neuroblast-like cells and epithelial cells [18]. In this study, pulsed laser deposition was used to deposit silver thin films on Ormocer® microneedle arrays. An agar diffusion assay was used to determine the antimicrobial activity of silver-coated Ormocer® microneedles.

Five-by-five arrays of out-of-plane microneedles were fabricated with Ormocer® materials using a two-photon polymerization–micromolding technique. In the first step, two-photon polymerization was used to fabricate a master structure of the microneedle array on a silanized glass coverslip (figure 1). The microneedle array was fabricated using SR 259 polyethylene glycol dimethacrylate (Sartomer, Paris, France) with 2% weight Irgacure® 369 initiator (Ciba Specialty Chemicals, Basel, Switzerland). Femtosecond laser pulses (60 fs, 300 mW, 780 nm) from a titanium:sapphire laser (Kapteyn-Murnane, Boulder, CO) were focused using a 5× microscope objective. Three C-843 linear translational stages (Physik Instrumente, Karlsruhe, Germany) were used to direct the laser focus position in three dimensions. A HurrySCAN galvo-scanner (Scanlab AG, Puchheim, Germany) was used to control polymerization of the photosensitive resin in the X–Y plane. Control of the laser was determined by an .STL format drawing of the microneedle. The .STL format drawing that was used to fabricate the microneedle arrays contained microneedles with a base diameter

value of 200 μm and length of 500 μm . In addition, the microneedles demonstrated 500 μm microneedle center-to-microneedle center spacing. Arrays of microneedles enable delivery of pharmacologic agents to be provided over a wider area and at higher rates than solitary needles [19].

In the second step, replication of the microneedle array was performed by means of a micromolding process. The master structure was sputter-coated with gold in order to improve separation of the mold from the master structure. Sylgard® 184 silicone elastomer and curing agent (Dow Corning, Midland, MI) were mixed in a 10:1 weight ratio. This silicone elastomer-curing agent mixture was degassed in vacuum and poured into an aluminum seal, which had been placed over the master microneedle array. The unpolymerized mold was placed under vacuum in order to eliminate residual air pockets in the mold. After degassing, the liquid mold was placed on a hotplate in order to initiate polymerization of the silicone elastomer. The hotplate temperature was increased from 25 °C to 100 °C over 30 min. The hotplate temperature was subsequently maintained at 100 °C for an additional 30 min. The master structure substrate was then clamped to a table. The silicone mold was attached to a vertical actuator. By raising the vertical actuator, the silicone mold was separated from the polyethylene glycol master structure.

In the third step, Ormocer® microneedle arrays were photopolymerized within the silicone mold. Ormocore® (Ormocer b59) (Microresist Technology, Berlin, Germany) is a commercially available Ormocer® material with 1.8% Irgacure 369 photoinitiator (Ciba

Specialty Chemicals, Basel, Switzerland). 50 μL of liquidOrmocer[®] material was placed in the silicone mold. The silicone mold containing the liquidOrmocer[®] was placed under vacuum in order to remove air pockets and completely fill all mold parts with Ormocer[®] material. The mold with Ormocer[®] material was subsequently pressed against a glass slide and attached to the vertical actuator. The construct was subsequently exposed for 2 min to a curing lamp that provides visible and ultraviolet light emission (Thorlabs, Newton, NJ) in order to polymerize the Ormocer[®] material. The silicone mold and the Ormocer[®] microneedle array were then separated from one another using the vertical actuator. In addition, silicone culture wells were utilized as molds in order to fabricate cylindrical (6 mm diameter \times 1 mm thick) Ormocer[®] wafers for use in the MTT assay.

Lastly, silver thin films were grown on Ormocer[®] microneedle arrays and Ormocer[®] wafers using pulsed laser deposition. A high-purity silver target was obtained from a commercial source (Alfa Aesar, Ward Hill, MA). A krypton fluoride (KrF) excimer laser ($\lambda = 248$ nm, repetition rate = 10 Hz) was used to ablate the high-purity silver target. The thin films were grown under a background pressure of 5×10^{-6} Torr at room temperature for 2 min. Recent work by Warrender *et al* indicates that the deposition rate for silver thin films using a KrF laser under similar conditions is ~ 0.06 nm s⁻¹ [15].

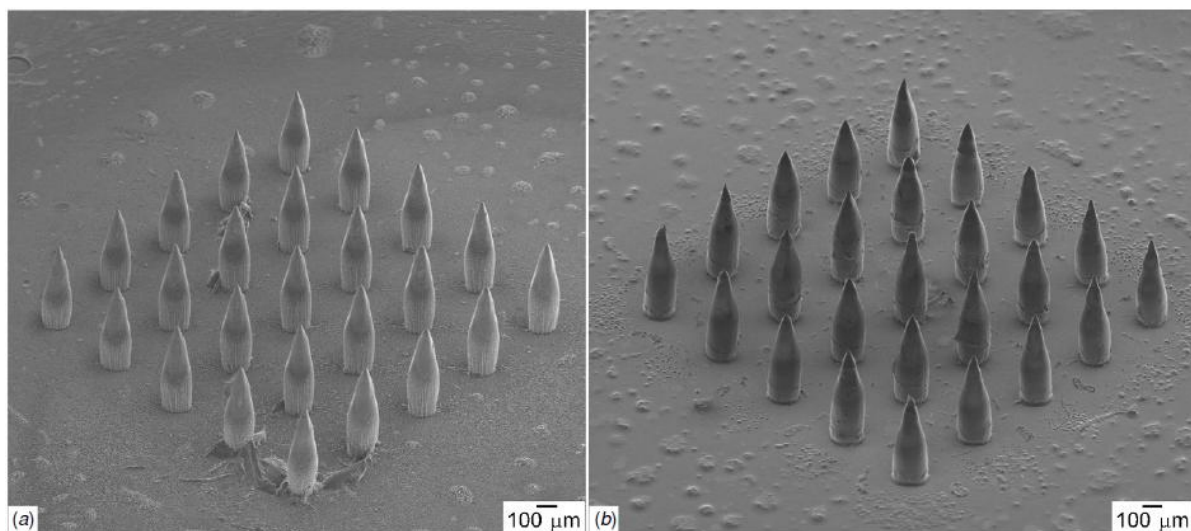


Figure 1. (a) Scanning electron micrograph of a SR 259 polyethylene glycol dimethacrylate microneedle array, which served as a master structure in the two-photon polymerization–micromolding process. (b) Scanning electron micrograph of a silver-coated Ormocer® microneedle array fabricated using two-photon polymerization–micromolding and pulsed laser deposition.

Cell proliferation on silver-coated and uncoated Ormocer® materials was examined using neonatal human epidermal keratinocytes (HEKs). The MTT assay (3-(4,5-dimethylthiazol-2-yl)2,5-diphenyl tetrazolium bromide) test was used to assess cell viability [20]. In the MTT assay, reduction of a yellow tetrazolium salt (MTT) to a purple formazan dye by mitochondrial succinic dehydrogenase is observed. Four silver-coated Ormocer® wafers and four uncoated Ormocer® wafers were placed in a 96-well plate and exposed to ultraviolet-B light for 3 h in order to sterilize the surfaces prior to seeding with HEKs. The wafers were rinsed with 200 μ l of keratinocyte growth media (KGM-2). The HEKs (Lonza, Walkersville, MD) were seeded onto the wafers and grown to 80% confluency in a humidified environment

containing 5% CO₂ at 37 °C. Twenty-four hours later, the HEKs were incubated in the MTT medium (0.5 mg ml⁻¹ KGM-2) for 3 h, the formazan dye was extracted with isopropyl alcohol and the extracted solution in each well was transferred to a new plate in order to prevent the physical presence of the wafers from influencing the data. The absorbance of the solutions was quantified on a Multiskan RC ELISA plate reader (Labsystems, Helsinki, Finland) at $\lambda=550$ nm. The silver-coated Ormocer® data was normalized to the uncoated Ormocer® (control) data. Mean values for percent viability were calculated and significant differences ($p < 0.05$) were determined using the PROC GLM Procedure (SAS 9.1 for Windows) (SAS Institute, Cary, NC). When significant differences were found, multiple comparisons were performed using Tukey's Studentized Range (HSD) test at $p < 0.05$ level of significance.

An agar plating method was used to assess microbial growth on the silver-coated microneedle array as well as the uncoated microneedle array. *S. aureus* ATCC 25923 (American Type Culture Collection, Manassas, VA) was cultured overnight in tryptic soy broth (VWR International, West Chester, PA). The cell suspensions were then centrifuged at 4500 rpm for 10 min. The cell pellet was then resuspended in 1X phosphate-buffered saline (VWR International, West Chester, PA) in order to obtain a cell density of $\sim 10^8$ CFU ml⁻¹. Tryptic soy agar plates (VWR International, West Chester, PA) were inoculated with a lawn of *S. aureus* suspension using a sterile swab. Glass cover slips with uncoated and silver-coated microneedle arrays were placed on the inoculated plates with the needles projecting into the agar. The plates were then incubated at 37 °C for 24 h. The microneedle arrays were

subsequently removed. Optical microscopy was performed in order to determine the extent of microbial growth.

Silver-coated microneedles within the arrays demonstrated sharp ($<10\ \mu\text{m}$ diameter) tips, tip angle values of 45° and good microneedle-to-microneedle uniformity (figure 1(b)). A few deviations from the dimensions specified in the STL file were observed. For example, the base diameter of the microneedles ($181.3 \pm 4.7\ \mu\text{m}$) was slightly smaller than the base diameter that was specified in the .STL format drawing. This decrease in diameter is due to shrinkage of the Ormocer® material during polymerization [21]. Shrinkage of the Ormocer® material is beneficial in the micromolding component of the two-photon polymerization–micromolding process since it enhances separation between the mold and the fabricated device. Iteration of microneedle materials and processing parameters may enable the development of microneedle arrays with more uniform features. In general, these images indicate that the features observed in the microneedles were consistent with the dimensions specified in the .STL format drawing. No pinholes, pores or nonuniformities in the silver thin film were noted in the scanning electron micrograph of the individual silver-coated microneedle (figure 2). Energy-dispersive x-ray spectra indicated that silver was present on the microneedles and the glass substrate. Silicon and carbon were also identified in the spectra; these elements were attributed to the glass substrate and the Ormocer® microneedle. No trace amounts of other elements were observed.

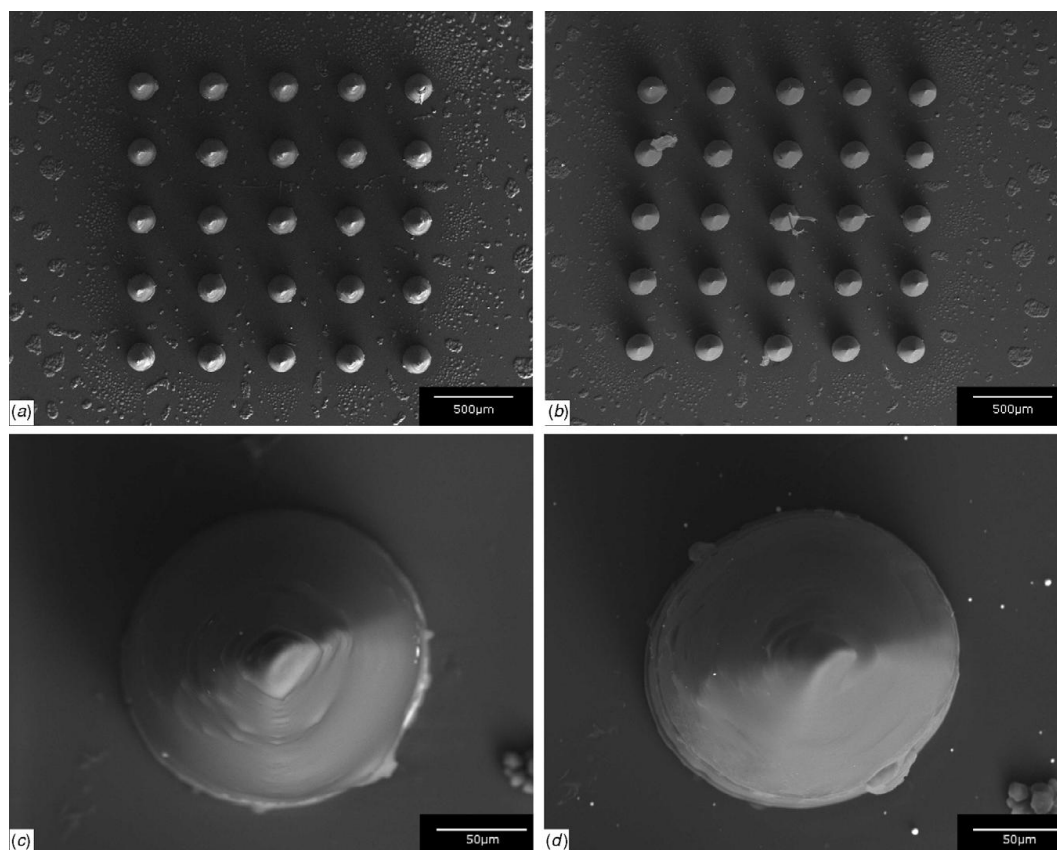


Figure 2. (a) Scanning electron micrograph of an uncoated Ormocer® microneedle array. (b) Scanning electron micrograph of a silver-coated Ormocer® microneedle array. (c) Scanning electron micrograph of an individual uncoated Ormocer® microneedle. (d) Scanning electron micrograph of an individual silver-coated Ormocer® microneedle.

The 24 h MTT assay (figure 3(a)) indicated that the silver-coated Ormocer® and uncoated Ormocer® wafers supported HEK growth. No significant differences were noted between HEK growth on the test surfaces. These results suggest that silver-coated Ormocer® processed using two-photon polymerization–micromolding and pulsed laser deposition does not impair cell growth or decrease cell viability. Previous studies have indicated that cell

growth on Ormocer® surfaces is similar to that on polystyrene control surfaces [22]. The agar plating method provides qualitative data regarding susceptibility of microorganisms to a given antimicrobial agent. This protocol is similar to one that is outlined by the National Committee for Clinical Laboratory Standards [23]. Results of the agar plating study for the uncoated microneedle array and the silver-coated microneedle array are shown in figures 3(b)–(e). On the plate containing the uncoated Ormocer® microneedle array, *S. aureus* growth was present directly under the microneedle array; no zone of growth inhibition was observed (figure 3(c)). The plate containing the silver-coated Ormocer® microneedle array exhibited an absence of *S. aureus* growth under the array. In addition, inhibited growth surrounding the microneedle array was noted (figure 3(e)). The presence of a zone of inhibition suggests that silver was released into agar adjacent to the microneedle array.

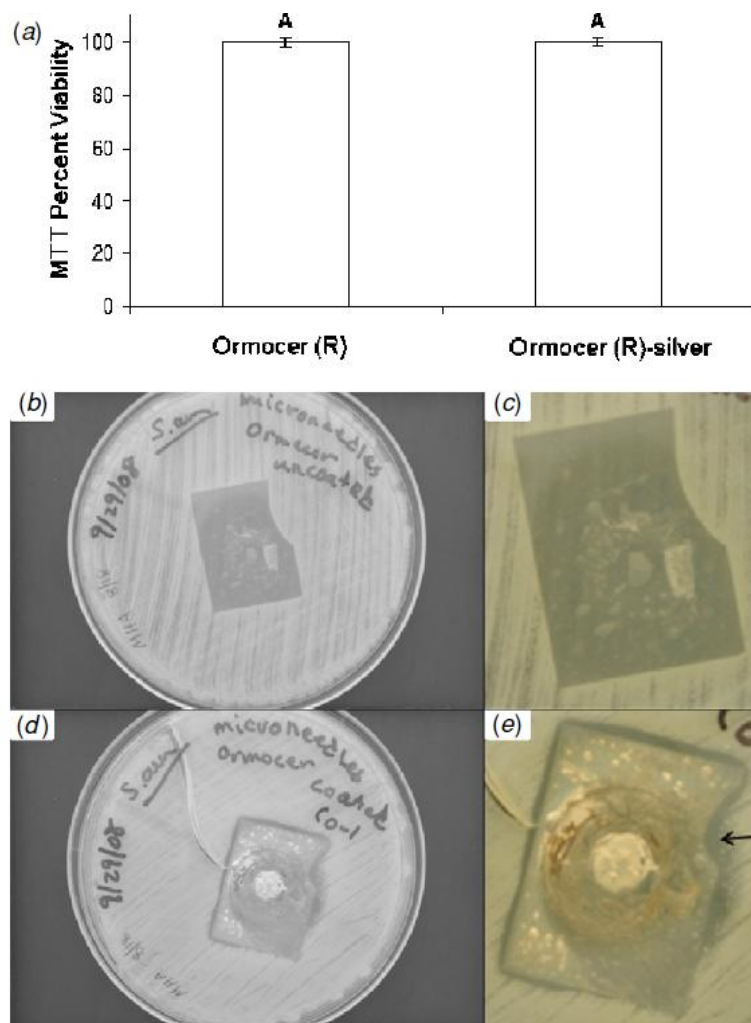


Figure 3. (a) MTT viability of human epithelial keratinocytes on uncoated Ormocer and silver-coated Ormocer wafers. (b) Low magnification and (c) high magnification agar diffusion assay results for the uncoated Ormocer® microneedle array. (d) Low magnification and (e) high magnification agar diffusion assay results for the silver-coated Ormocer® microneedle array. The arrow indicates an absence of growth under the microneedle array as well as inhibited growth surrounding the microneedle array. (This figure is in colour only in the electronic version)

The results of this study indicate that coating microneedles with silver thin films using pulsed laser deposition is a useful approach for creating microneedles with antimicrobial functionality. Two-photon polymerization–micromolding is an indirect rapid prototyping technique that is compatible with high throughput production of microscale medical devices. Pulsed laser deposition produced a pinhole-free, pore-free silver film on an Ormocer® microneedle array. Microneedles fabricated using two-photon polymerization– micromolding and pulsed laser deposition were shown to inhibit growth of *S. aureus*. It is anticipated that microneedles with antimicrobial functionality may find wider uses than conventional microneedles for transdermal delivery of protein and nucleic-acid-based pharmacologic agents.

Acknowledgment

We thank Mr Al Inman at the Center of Chemical Toxicology Research and Pharmacokinetics at North Carolina State University for technical assistance.

References

- [1] McAllister D V, Wang P M, Davis S P, Park J H, Canatella P J, Allen M G and Prausnitz M R 2003 Microfabricated needles for transdermal delivery of macromolecules and

nanoparticles: fabrication methods and transport studies *Proc. Natl Acad. Sci. USA* **100**

13755–60

[2] Gittard S D, Ovsianikov A, Monteiro-Riviere N A, Lusk J, Morel P, Minghetti P, Lenardi C, Chichkov B N and Narayan R J 2009 Fabrication of polymer microneedles using a two-photon polymerization and micromolding process *J. Diabetes Sci. Technol.* **3** 304–11

[3] Lee S H, Jeong S K and Ahn S K 2006 An update of the defensive barrier function of skin *Yonsei Med. J.* **47** 293–306

[4] Banga A K 2007 Theme section: transdermal delivery of proteins *Pharm. Res.* **24** 1357–9

[5] Birchall J C 2006 Microneedle array technology: the time is right but is the science ready? *Exp. Rev. Med. Dev.* **3** 1–4

[6] Bragg P D and Rainnie D J 1974 The effect of silver ions on the respiratory chain of *Escherichia coli* *Can. J. Microbiol.* **20** 883–9

[7] Rosenkranz H S and Rosenkranz S 1972 Silver sulfadiazine: interaction with isolated deoxyribonucleic acid *Antimicrob. Agents Chemother.* **2** 373–83

- [8] Stoimenov P K, Klinger R L, Marchin G L and Klabunde K J 2002 Metal oxide nanoparticles as bactericidal agents *Langmuir* **18** 6679–86
- [9] Slawson R M, Van Dyke M I, Lee H and Trevors J T 1992 Germanium and silver resistance, accumulation, and toxicity in microorganisms *Plasmid* **27** 72–9
- [10] Zhao G and Stevens S E Jr 1998 Multiple parameters for the comprehensive evaluation of the susceptibility of *Escherichia coli* to the silver ion *BioMetals* **11** 27–32
- [11] Trengove N J, Stacey M C, Macauley S, Bennett N, Gibson J, Burslem F, Murphy G and Schultz G 1999 Analysis of the acute and chronic wound environments: the role of proteases and their inhibitors *Wound Repair Regen.* **7** 442–52
- [12] Wright J B, Lam K, Buret A G, Olson M E and Burrell R E 2002 Early healing events in a porcine model of contaminated wounds: effects of nanocrystalline silver on matrix metalloproteinases, cell apoptosis, and healing *Wound Repair Regen.* **10** 141–51
- [13] Demling R H and DeSanti L 2002 The rate of re-epithelialization across meshed skin grafts is increased with exposure to silver *Burns* **28** 264–6

- [14] Morrison M L, Buchanan R A, Liaw P K, Berry C J, Brigmon R, Riester L, Jin C and Narayan R J 2006 Electrochemical and antimicrobial properties of diamond like carbon-metal composite films *Diamond Related Mater.* **15** 138–46
- [15] Warrender J M and Aziz M J 2007 Kinetic energy effects on morphology evolution during pulsed laser deposition of metal-on-insulator films *Phys. Rev B* **75** 085433
- [16] Willmott P R 2004 Deposition of complex multielemental thin films *Prog. Surf. Sci.* **76** 163–217
- [17] Lackner J M 2005 Industrially-scaled large-area and high-rate tribological coating by pulsed laser deposition *Surf. Coat. Technol.* **200** 1439–44
- [18] Doraiswamy A, Jin C, Narayan R J, Mageswaran P, Mente P, Modi R, Auyeung R, Chrisey D B, Ovsianikov A and Chichkov B 2006 Two photon polymerization of microneedles for drug delivery *Acta Biomater.* **2** 267–75
- [19] Davis S P, Landis B J, Adams Z H, Allen M G and Prausnitz M R 2004 Insertion of microneedles into skin: measurement and prediction of insertion force and needle fracture force *J. Biomech.* **37** 1155–63

- [20] Monteiro-Riviere N A, Inman A O and Zhang L W 2009 Limitations and relative utility of screening assays to assess engineered nanoparticle toxicity in a human cell line *Toxicol. Appl. Pharmacol.* **234** 222–35
- [21] Yap A U J and Soh M S 2004 Post-gel polymerization contraction of ‘low shrinkage’ composite restoratives *Oper. Dent.* **29** 317–24
- [22] Ovsianikov A, Chichkov B N, Mente P, Monteiro-Riviere N A, Doraiswamy A and Narayan R J 2007 Two photon polymerization of polymer-ceramic hybrid materials for transdermal drug delivery *Int. J. Appl. Ceramic Technol.* **4** 22–9
- [23] 1997 Performance standards for antimicrobial disk susceptibility tests (M2-A6), National Committee for Clinical Laboratory Standards, Wayne, PA

3.6 Two Photon Polymerization-Micromolding of Polyethylene Glycol-Gentamicin Sulfate Microneedles

*The following section is a pre-peer reviewed version of an article from **Advanced Engineering Materials**, Volume 12, Gittard SD, Ovsianikov A, Akar H, Chichkov B, Monteiro-Riviere NA, Stafslien S, Chisholm B, Shin CC, Shih CM, Lin SJ, Su YY, Narayan RJ.B77-B82, Copyright 2010, with permission from Wiley-VCH Verlag BmhH & Co. KGaA*

Two Photon Polymerization-Micromolding of Polyethylene

Glycol-Gentamicin Sulfate Microneedles

By Shaun D. Gittard, Aleksandr Ovsianikov, Hasan Akar, Boris Chichkov, Nancy A. Monteiro-Riviere, Shane Stafslie, Bret Chisholm, Chun-Che Shin, Chun-Ming Shih, Shing-Jong Lin, Yea-Yang Su and Roger J. Narayan*

The use of microneedles for transdermal drug delivery is limited due to the risk of infection associated with formation of channels through the stratum corneum layer of the epidermis. The risk of infection associated with use of microneedles may be reduced by imparting these devices with antimicrobial properties. In this study, a photopolymerization-micromolding technique was used to fabricate microneedle arrays from a photosensitive material containing polyethylene glycol 600 diacrylate, gentamicin sulfate, and a photoinitiator. Scanning electron microscopy indicated that the photopolymerization-micromolding process produced microneedle arrays that exhibited good microneedle-to-microneedle uniformity. An agar plating assay revealed that microneedles fabricated with polyethylene glycol 600 diacrylate containing 2 mg mL⁻¹ gentamicin sulfate inhibited growth of *Staphylococcus aureus* bacteria. Scanning electron microscopy revealed no platelet aggregation on the surfaces of platelet rich plasma-exposed undoped polyethylene glycol 600 diacrylate microneedles and gentamicin-doped polyethylene glycol 600 diacrylate microneedles. These efforts will enable wider adoption of microneedles for transdermal delivery of pharmacologic agents.

[*] R. J. Narayan, S. D. Gittard, N. A. Monteiro-Riviere

Joint Department of Biomedical Engineering, University of North Carolina, and North Carolina State University Chapel Hill, Raleigh, NC 27599-7115, USA

E-mail: roger_narayan@msn.com

A. Ovsianikov, H. Akar, B. Chichkov

Department of Nanotechnology, Laser Zentrum Hannover Hollerithalle 8, 30419 Hannover, Germany

N. A. Monteiro-Riviere

Center for Chemical Toxicology Research and Pharmacokinetics, North Carolina State University, Raleigh, NC 27695, USA

S. Stafslie, B. Chisholm

Center for Nanoscale Science and Engineering, North Dakota State University, 1805 Research Park Drive, Fargo, ND, 58102, USA

C.-C. Shih, S.-J. Lin, Y.-Y. Su

Institute of Clinical Medicine, School of Medicine, National Yang-Ming University, Taipei 112, Taiwan

C.-C. Shih

Division of Cardiovascular Surgery, Taipei Veterans General Hospital, Taipei 112, Taiwan

C.-C. Shih, S.-J. Lin

Cardiovascular Research Center, National Yang-Ming University, Taipei 112, Taiwan

C.-M. Shih

Graduate Institute of Medical Sciences, School of Medicine, Taipei Medical University,
Taipei 110, Taiwan

S.-J. Lin

Division of Cardiology, Taipei Veterans General Hospital, Taipei 112, Taiwan

One novel mechanism for transdermal delivery of pharmacologic agents involves the use of microneedles.^[1] Microneedles are structures that are similar in shape to hypodermic needles or lancets; these devices exhibit at least one dimension that is less than 1 mm in length. Bal *et al.* recently demonstrated that hollow and solid metal microneedles were able to penetrate ventral forearm skin in human volunteers; these devices were shown to disrupt the stratum corneum layer of the epidermis with minimal irritation and absence of pain.^[2] Bacteria such as *Staphylococcus aureus* reside on the skin surface; a pore in the stratum corneum created by a microneedle could enable microorganisms to enter the circulatory system and cause systemic infection.^[3] Sato *et al.* demonstrated that pathogenic microorganisms may be transferred from the surface of the skin to deeper regions of the skin with conventional

hypodermic needles.^[4] Birchall described the risk of infection associated with penetration of the stratum corneum by a microneedle.^[5] He suggested that damage to the stratum corneum is transient and is relatively minor in nature; however, he also noted that mechanisms of skin repair in response to microneedle insertion are not completely understood.

Antimicrobial microneedles may be fabricated by combining biocompatible polymers such as polyethylene glycol with conventional antimicrobial agents such as gentamicin sulfate.

One common method for fabricating polyethylene glycol structures involves free-radical photopolymerization of polyethylene glycol diacrylate macromers using ultraviolet light or visible light photoinitiators.^[6] Miyano *et al.* demonstrated that polyethylene glycol microneedles penetrated a living human skin model, which suggested that the needles exhibited sufficient mechanical strength to form conduits through the stratum corneum.^[7] Takano *et al.* recently demonstrated insertion of polyethylene glycol microneedles into a wet cultured human skin model that was placed under biaxial tension; in their study, shortening of inserted microneedles due to hydrolysis was observed.^[8]

Gentamicin sulfate is utilized as a broad spectrum antimicrobial agent for treatment of pyodermas and other skin infections due to its efficacy against Gram negative organisms as well as some Gram positive organisms. For example, Changez *et al.* demonstrated that gentamicin is active against *Staphylococcus*, a pathogenic organism that is commonly found on the skin.^[9] They demonstrated that the minimum inhibitory concentration, the lowest concentration showing no visible growth after incubation at 37 °C for 18 h, of gentamicin for

S. aureus (ATCC 259523) was 0.4 mg ml^{-1} ; they also determined that the minimum bactericidal concentration (MBC) and the break point sensitivity of gentamicin for *S. aureus* were 0.6 and 1 mg ml^{-1} , respectively. Several biomedical polymers, including poly (methyl methacrylate), polylactic acid, polyglycolic acid, and polyethylene glycol, have been combined with gentamicin sulfate.^[10,11] Gentamicin is extremely hydrophilic, which enables aqueous suspensions containing polyethylene glycol and gentamicin to be readily produced.^[12]

Gentamicin-doped polyethylene glycol was made by mixing SR 610 polyethylene glycol 600 diacrylate (Sartomer, Paris, France) with 2 wt% Irgacure 369 photoinitiator (Ciba Specialty Chemicals, Basel, Switzerland). Aqueous 10 mg mL^{-1} gentamicin sulfate (MP Biomedicals, Solon, OH) was subsequently added to this mixture in order to obtain a 2 mg mL^{-1} concentration. A mixture containing only polyethylene glycol and 2 wt% Irgacure 369 photoinitiator was also prepared for comparison purposes. A photopolymerization-micromolding process was used to fabricate microneedle arrays from undoped polyethylene glycol 600 diacrylate and gentamicin-doped polyethylene glycol 600 diacrylate.

Details on the photopolymerization-micromolding process have been previously reported in ref.^[13,14] A microneedle array master structure was fabricated with SR 259 polyethylene glycol dimethacrylate (Sartomer, Paris, France) containing 2 wt% Irgacure 369 photoinitiator on a silanized glass cover slip substrate using two photon polymerization. In two photon polymerization, temporal and spatial overlap of photons enables polymerization and material

hardening within well-defined and highly localized volumes. Femtosecond laser pulses (60 fs, 94 MHz, <450mW, 780 nm) from a titanium: sapphire laser (Kapteyn-Murnane, Boulder, CO) were focused using a 5x microscope objective. The position of the laser focus was moved using a galvanoscanner and three translational stages. A HurrySCAN galvo-scanner (Scanlab AG, Puchheim, Germany) was used to control the laser focus position in the X-Y plane and three C-843 linear translational stages (Physik Instrumente, Karlsruhe, Germany) were utilized to control the laser focus position in three dimensions. A computer-aided design program was used in order to create stereolithography (STL) files, which guided the two photon polymerization process. The master structure was a fiveby- five array of solid microneedles, in which the microneedles were separated by a 500 μm needle center-to-needle center spacing. Each microneedle in the array was designed with a length of 500 μm , a base diameter of 150 μm , and a tip angle of 45°. Due to their larger surfaces, arrays of microneedles provide drug delivery in higher amounts and over larger regions than solitary needles.^[15] Microneedle arrays may be designed^[15] with redundant structures in case some of the microneedles are fractured or obstructed during insertion into the skin. The microneedle array was sputtered with a gold coating (sputter time = 245 s, sputter current = 10mA) in order to enhance separation of the mold from the master structure. It was subsequently attached to a glass microscope slide with double-sided tape.

This master structure was subsequently used to fabricate polydimethylsiloxane (PDMS) mold. Sylgard/ 184 silicone elastomer and curing agent (Dow Corning, Midland, MI) were mixed in a 10:1 weight ratio. This mixture was degassed under vacuum. A 20 mm diameter

aluminum seal (Sigma Aldrich, St. Louis, MO) was positioned over the master structure. The mixture was poured over the array until the seal was completely filled. 100 mbar vacuum was applied to the glass slide containing the master structure, aluminum seal, and unpolymerized PDMS mixture. The glass slide was subsequently placed on a heat plate. Thermal curing of the PDMS mixture was obtained by increasing the heat plate temperature from room temperature to 100 °C over 30 min and then maintaining the heat plate temperature at 100 °C for 30 min. After the polymerized PDMS mold had cooled, the glass slide clamped to a table using two metal restraining bars. The aluminum seal was attached to a vertical actuator using screws. The PDMS mold and aluminum seal were separated from the master structure by lifting the PDMS mold away from the table using the vertical actuator. The polymethylsiloxane mold was ultrasonically cleaned in ethanol for 15 min.

Microneedle arrays were fabricated from the PDMS mold using a micromolding process. ~50 mL of either gentamicin-doped polyethylene glycol 600 diacrylate or undoped polyethylene glycol 600 diacrylate was placed on the surface of the PDMS mold. The PDMS mold containing the unpolymerized polymer mixture was placed under 100 mbar vacuum for ~5 min. The mold containing the unpolymerized polymer mixture was degassed under vacuum in order to enable the mixture to completely fill the mold. This degassing step removed air from the unpolymerized polymer mixture in the PDMS mold; trapped air may result in the formation of incomplete microneedles, missing microneedle tips, and other microneedle defects. The PDMS mold containing the unpolymerized polymer mixture was then pressed against a glass cover slip, which in turn was attached to a microscope slide using double-

sided tape. The mold and the slide were fitted into a vertical actuator. The unpolymerized polymer mixture was then exposed to an ultraviolet curing lamp, which provided visible and ultraviolet light emission (Thorlabs, Newton, NJ). ATR-FTIR studies by Witte *et al.* have shown that complete photopolymerization of polyethylene glycol 600 diacrylate occurs with less than 3 min of ultraviolet light exposure.^[16] After ultraviolet curing was complete, the microneedle array was separated from the PDMS mold using the vertical actuator.

A S3200 scanning electron microscope (Hitachi, Tokyo, Japan) equipped with a Robinson back scattered electron detector was used to examine microneedle arrays fabricated with gentamicin-doped polyethylene glycol 600 diacrylate and undoped polyethylene glycol 600 diacrylate. Fourier transform infrared spectroscopy (FTIR) was performed on cylindrical wafers of gentamicin-doped polyethylene glycol 600 diacrylate or undoped polyethylene glycol 600 diacrylate using a Nexus 470 system equipped with an OMNI sampler and a continuum microscope (Thermo Fisher, Waltham, MA). Analysis of the absorption spectra was performed using OMNICTM software (Thermo Fisher, Waltham, MA). Platelet adhesion testing is an *in vitro* technique that is commonly used for examining adsorption of platelets, proteins, and other blood components to the surface of a biomaterial.^[17] Fresh whole blood was obtained from a healthy adult volunteer. The blood was evaluated for the presence of anticoagulants and other pharmacologic agents that could affect protein-biomaterial or platelet-biomaterial interaction using platelet function, prothrombin time, and partial thromboplastin time studies. Sodium citrate was added to the fresh whole blood in order to prevent coagulation. The blood was centrifuged using a Plasma Saver

system (Hemonetics, Braintree, MA) at 25 °C for 10 min, 25 °C for 10 min, and then at 4 °C for 1 h (operating speed 43500 rpm). In this multiple-step centrifugation process, the first spin process served to separate low-platelet concentrated plasma from platelet rich plasma and red blood cells.^[18] The mixture of platelet rich plasma and red blood cells was separated, and the platelet rich plasma was subsequently collected at the bottom of the test tube because of its high specific gravity. The platelet rich plasma was incubated at 37 °C for 10 min and then frozen until testing. Microneedle arrays fabricated with gentamicin-doped polyethylene glycol 600 diacrylate or undoped polyethylene glycol 600 diacrylate were immersed in the platelet rich plasma solution and incubated at 37 °C for 10 min. Weakly adherent platelets were removed by rinsing the microneedle arrays with 0.9% saline solution. The platelet rich plasma-exposed microneedle arrays were subsequently fixed in 4% glutaraldehyde and critical point dried. Scanning electron microscopy and energy dispersive X-ray spectroscopy were performed to examine protein and platelet adhesion on the platelet rich plasma-exposed microneedle arrays.

The antimicrobial properties of microneedle arrays fabricated with gentamicin-doped polyethylene glycol 600 diacrylate or undoped polyethylene glycol 600 diacrylate were evaluated using an agar plating method. The agar plating method is similar to a method that was outlined by the National Committee for Clinical Laboratory Standards and is used in clinical laboratories across the world, in which an antimicrobial agent diffuses outward from a disk over 18 h and the zone of inhibition is subsequently determined.^[19] The agar plating

method is appropriate for most pathogenic bacteria and provides qualitative data regarding susceptibility

of microorganisms to a given antimicrobial agent. Overnight cultures of *S. aureus* ATCC 25923 (American Type Culture Collection, Manassas, VA) in tryptic soy broth (TSB) (VWR International, West Chester, PA) were centrifuged at 4500 rpm for 10 min. The resulting pellets were resuspended in 1X phosphate-buffered saline (PBS) in order to obtain a final cell density of $\sim 10^8$ cells ml^{-1} . 1X phosphate-buffered saline solution was prepared by diluting 10X phosphate-buffered saline (VWR International, West Chester, PA) using deionized water. A sterile swab was used in order to inoculate a lawn of the bacterium on tryptic soy agar plates (VWR International, West Chester, PA). Microneedle arrays fabricated with gentamicin-doped polyethylene glycol 600 diacrylate or undoped polyethylene glycol 600 diacrylate were then placed on the inoculated plates, in which the needles were projected into the agar. The plates were inverted and incubated for 24 h at 37 °C. The microneedle arrays were subsequently removed from the agar. Inhibition of microbial growth was determined using optical microscopy.

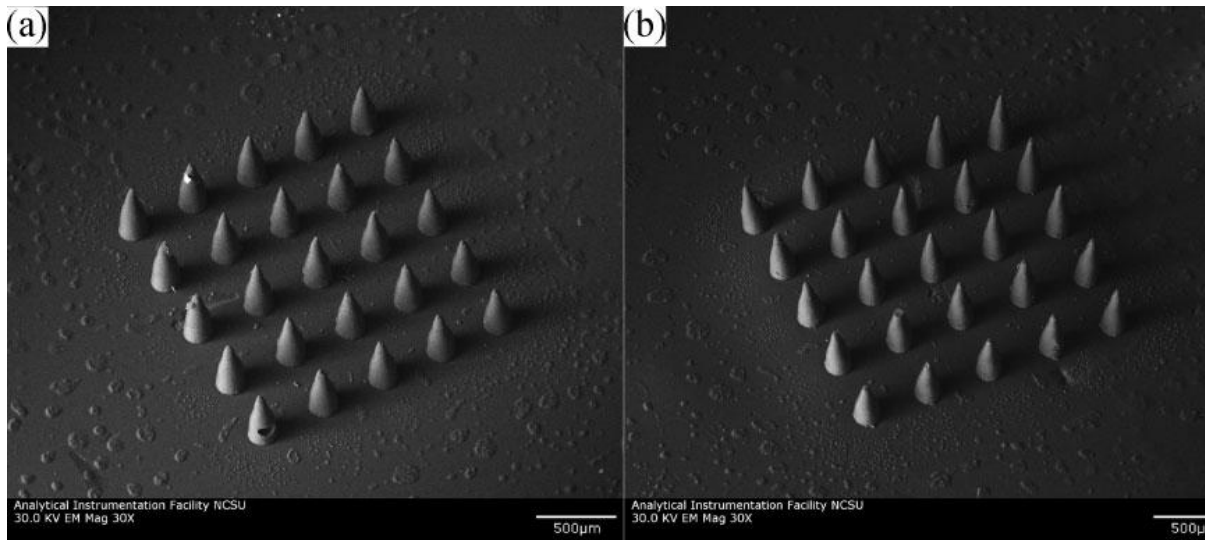


Fig. 1. Scanning electron micrographs of microneedle arrays. (a) Microneedle array fabricated with undoped polyethylene glycol 600 diacrylate. (b) Microneedle array fabricated with gentamicin-doped polyethylene glycol 600 diacrylate.

Scanning electron micrographs of microneedle arrays fabricated with undoped polyethylene glycol 600 diacrylate and gentamicin-doped polyethylene glycol 600 diacrylate are shown in Figure 1(a) and 1(b), respectively. The microneedles in both arrays exhibited good correspondence with the CAD microneedle designs; in addition, good microneedle-to-microneedle uniformity was observed in both arrays. The microneedle arrays fabricated by photopolymerization micromolding also exhibited good correspondence with the master structure. The microneedles in both arrays demonstrated base diameters of 150 μm , lengths of 500 μm , tip angles of 45° , and $>10 \mu\text{m}$ tip diameters. Voids within microneedles and truncated microneedle tips were observed in a small fraction of the microneedles within the microneedle arrays; these features were attributed to incomplete degassing of the unpolymerized polyethylene glycol solution. Energy dispersive X-ray spectroscopy found

that gentamicin-doped polyethylene glycol 600 diacrylate microneedle arrays and undoped polyethylene glycol 600 diacrylate microneedle arrays were comprised of carbon, oxygen, and hydrogen. This finding confirms that other elements were not introduced during the photopolymerization-micromolding process.

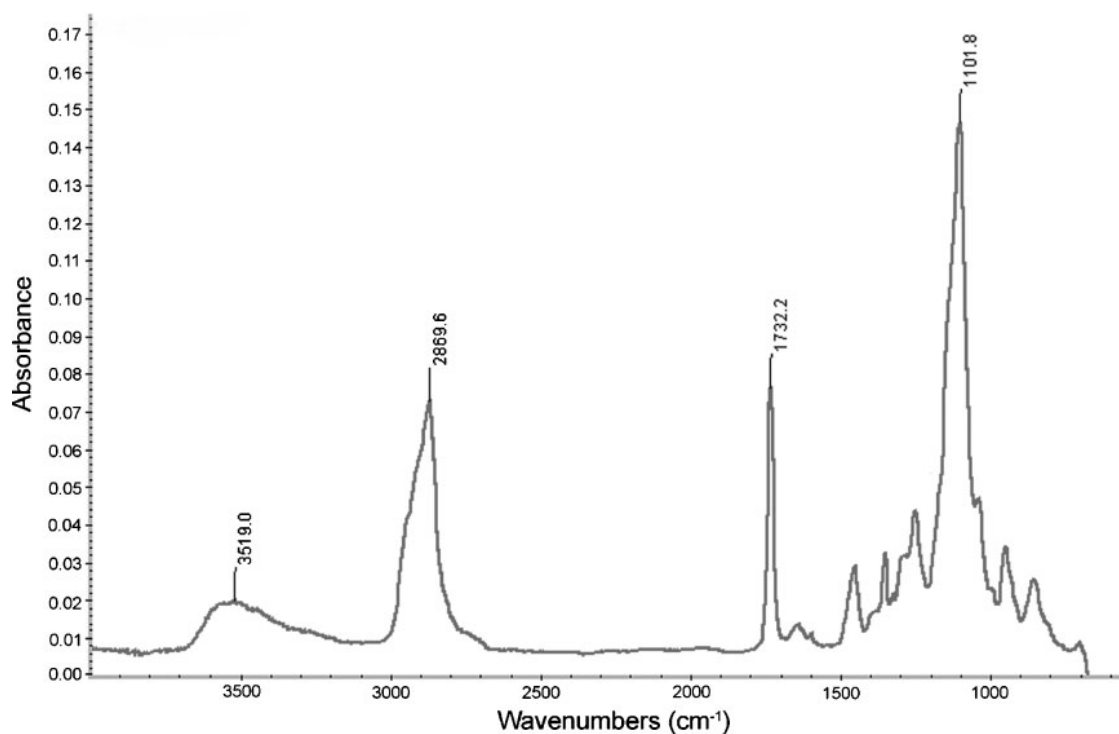


Fig. 2. Fourier transform infrared spectrum of gentamicin-doped polyethylene glycol 600 diacrylate.

The FTIR spectrum of photo-initiated polymerization of polyethylene glycol 600 diacrylate in the presence of Irgacure 369 photoinitiator (2-benzyl-2-dimethylamino-1-(4-

morpholinophenyl)-butanone-1) contained large sharp peaks at 2870, 1732, and 1102 cm^{-1} as well as a broad peak at 3519 cm^{-1} ; this spectrum showed good correspondence with absorption spectra of polyethylene glycol 600 diacrylate prepared by other methods (e.g., redox initiation).^[20-22] The addition of gentamicin sulfate to polyethylene glycol 600 diacrylate did not significantly alter the absorption spectrum (Fig. 2). Peaks at 1740 and 1102 cm^{-1} were attributed to stretching vibration of the aliphatic carbonyl groups and the ether groups, respectively.^[22,23] Irgacure 369 photoinitiator forms radicals by means of a Norrish type I mechanism, which involves homolytic alpha cleavage between the carbonyl group and the α carbon atom upon photoexcitation.^[24]

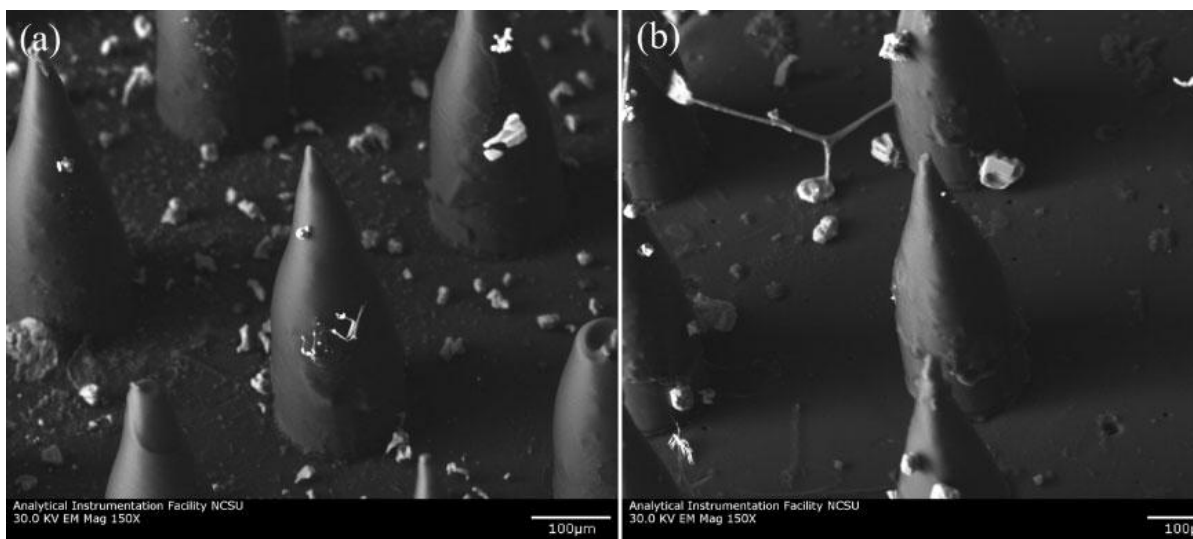


Fig. 3. Scanning electron micrographs of microneedle arrays after exposure to platelet rich plasma. (a) Microneedle array fabricated with undoped polyethylene glycol 600 diacrylate. (b) Microneedle array fabricated with gentamicin-doped polyethylene glycol 600 diacrylate.

Scanning electron micrographs of microneedle arrays fabricated using undoped polyethylene glycol 600 diacrylate and gentamicin-doped polyethylene glycol 600 diacrylate after exposure to platelet rich plasma are provided in Figure 3(a) and 3(b), respectively. No protein aggregation was observed on the gentamicin-doped polyethylene glycol 600 diacrylate microneedle array and the undoped polyethylene glycol 600 diacrylate microneedle array. In addition, no platelet aggregation was observed on the gentamicin-doped polyethylene glycol 600 diacrylate microneedle array and the undoped polyethylene glycol 600 diacrylate microneedle array. Metal-containing materials exposed to platelet rich plasma under similar conditions demonstrated a dense fibrin network with aggregated platelets.^[17] Small, widely scattered crystals were observed on the surfaces of the gentamicin-doped polyethylene glycol 600 diacrylate microneedle array and the undoped polyethylene glycol 600 diacrylate microneedle array. The presence of sodium, chlorine, and phosphorus in the energy dispersive X-ray spectra suggests that sodium chloride crystals precipitated from the platelet rich plasma. Precipitation of sodium chloride crystals from platelet rich plasma appears to be autonomous from platelet and protein adsorption processes. Previous studies have shown that polyethylene glycol is resistant to adhesion of cells and adsorption of proteins; for example, Moon *et al.*, DeLong *et al.*, and Nagaoka *et al.* demonstrated that polyethylene glycol diacrylate-based materials exhibit nonspecific resistance to adhesion of cells, adsorption of proteins, and formation of thrombi.^[25-27] The ability of polyethylene glycol surfaces to resist proteins and other biological molecules is attributed to formation of hydrogen bonds with water molecules and is enhanced by steric stabilization.^[28] Steric stabilization is a repulsive force that results from: (i) the loss in conformational freedom of polyethylene glycol chains

when proteins move closer to polyethylene glycol surfaces and (ii) osmotic interactions between proteins and polyethylene glycol surfaces.^[29] These properties are appealing for microneedle-based devices, since protein fouling and cell adhesion can impede transport of pharmacologic agents from the microneedle to the surrounding tissues.

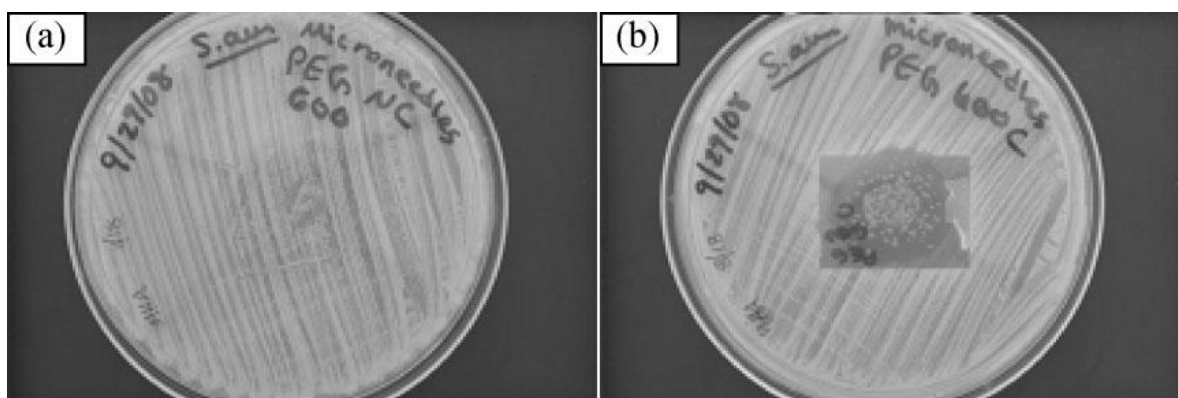


Fig. 4. Agar plating assay results. (a) Microneedle array fabricated with undoped polyethylene glycol 600 diacrylate against Staphylococcus aureus. (b) Microneedle array fabricated with gentamicin-doped polyethylene glycol 600 diacrylate against Staphylococcus aureus. The zone of inhibition for the microneedle array fabricated with gentamicin-doped polyethylene glycol 600 diacrylate was 26.8mm in diameter. The bubble-like structures were acellular and were attributed to hydrogel degradation.

The agar plating assay results for microneedle arrays fabricated using undoped polyethylene glycol 600 diacrylate and gentamicin-doped polyethylene glycol 600 diacrylate are shown in Figure 4(a) and 4(b), respectively. The microneedle arrays were removed from the agar plates in order to facilitate imaging of microbial growth. No zone of inhibition was observed for the microneedle array fabricated with undoped polyethylene glycol 600 diacrylate; S.

aureus growth was observed over the entire agar plate, including underneath the microneedle array. The microneedle array fabricated with gentamicin-doped polyethylene glycol 600 diacrylate had a circular zone of inhibition (diameter = 26.8 mm). The zone of inhibition indicated that gentamicin sulfate was released from polyethylene glycol 600 diacrylate during the agar plating assay. Acellular bubble-like structures were observed on the agar surface, which were attributed to hydrogel degradation. Previous work by Matsuda *et al.* demonstrated that PEG-based microneedles and other microstructures undergo degradation at the surface and in the bulk due to absorption of water.^[30] According to Miyano *et al.*, there are minimal concerns regarding fracture of polyethylene glycol microneedles during insertion since hydrolytic degradation of polyethylene glycol microneedles may occur on the skin surface.^[7] Takano *et al.* describe retention of polyethylene glycol microneedles on the skin surface for extended periods of time; for example, hydrolysis of polyethylene glycol microneedles on the skin surface may allow for gradual release of antimicrobial agents as well as other pharmacologic agents.^[8] Disposal of polyethylene glycol microneedles may be performed by means of boiling or other low cost procedures.^[7]

In this study, microneedle arrays with antimicrobial properties were fabricated using a photosensitive material containing polyethylene glycol 600 diacrylate, gentamicin sulfate, and a photoinitiator. The photopolymerization- micromolding process was used to produce microneedle arrays that exhibited good microneedle-to-microneedle uniformity. An agar plating assay revealed that the microneedle array fabricated using gentamicin-doped polyethylene glycol 600 diacrylate inhibited growth of *S. aureus* bacteria. A 26.8 mm

diameter zone of inhibition was observed, which indicated that gentamicin sulfate was released from the microneedle array. In addition, no platelet aggregation was observed on the surface of the platelet rich plasma-exposed undoped polyethylene glycol 600 diacrylate microneedles and gentamicin-doped polyethylene glycol 600 diacrylate microneedles. The results of this study suggest that gentamicin- doped polyethylene glycol 600 diacrylate may be used to fabricate microneedles and other medical devices that exhibit antimicrobial functionality.

[1] A. Arora, *Int. J. Pharm.* 2008, 364, 227.

[2] S. M. Bal, *Eur. J. Pharm. Sci.* 2008, 35, 193.

[3] Y. N. Kalia, *J. Invest. Dermatol.* 1998, 111, 320.

[4] S. Sato, *Anesthesiology* 1996, 85, 1276.

[5] J. C. Birchall, *Exp. Rev. Med. Dev.* 2006, 3, 1.

[6] S. Gabler, *Int. J. Mater. Eng. Innov.* 2009, 1, 1.

[7] T. Miyano, *Solid-State Sensors, Actuators and Microsystems Conference, IEEE, Los Alamitos, CA, 2007.*

- [8] N. Takano, *J. Solid Mech. Mater. Eng.* 2009, 3, 604.
- [9] M. Changez, *Biomaterials* 2004, 25, 139.
- [10] K. D. Kuhn, *J. Pharm. Biomed. Anal.* 2008, 48, 612.
- [11] Y. S. Brin, *J. Biomater. Sci.* 2009, 20, 1081.
- [12] P. K. Naraharisetti, *J. Control. Rel.* 2005, 102, 345.
- [13] A. Doraiswamy, *Acta Biomater.* 2006, 2, 267.
- [14] S. D. Gittard, *J. Diabetes Sci. Tech.* 2009, 3, 304.
- [15] H. J. G. E. Gardeniers, *J. Microelectromech. Syst.* 2003, 12, 855.
- [16] R. P. Witte, *J. Biomed. Mater. Res.* 2004, 71A, 508.
- [17] M. Andara, *Diamond Relat. Mater.* 2006, 15, 1941.
- [18] J. L. Lozada, *J. Oral Implantol.* 2001, 27, 38.

[19] Performance standards for antimicrobial disk susceptibility tests (M2-A6), National Committee for Clinical Laboratory Standards, Wayne, PA 1997.

[20] G. X. Tan, *Polymer Bull.* 2008, 61, 91.

[21] M. Imani, *Iranian Polymer J.* 2007, 16, 13.

[22] X. Zhang, *Int. J. Biol. Macromol.* 2008, 43, 456.

[23] J. R. Dyer, in *Applications of absorption spectroscopy of organic compounds*, Prentice Hall, Englewood Cliffs, NJ 1965, 1.

[24] R. Houbertz, *Appl. Surf. Sci.* 2005, 247, 504.

[25] S. A. DeLong, *Biomaterials* 2005, 26, 3227.

[26] J. J. Moon, *Tissue Eng. A* 2009, 15, 579.

[27] S. Nagaoka, *Biomaterials* 1990, 11, 119.

[28] J. D. Andrade, *Adv. Chem. Ser.* 1996, 248, 51.

[29] D. H. Atha, *J. Biol. Chem.* 1981, 256, 2108.

[30] T. Matsuda, *J. Biomed. Mater. Res.* 2002, 62, 395.

3.7 Pulsed Laser Deposition of Antimicrobial Metal Thin Film Coatings on Microneedles Produced by Visible Light Dynamic Mask Micro-stereolithography

Pulsed Laser Deposition of Antimicrobial Metal Thin Film Coatings on Microneedles Produced by Visible Light Dynamic Mask Micro-stereolithography

Shaun D Gittard, Philip R Miller, Chunming Jin, Timothy N Martin, Ryan D Boehm, Bret J Chisholm, Shane J Stafslie, Justin W Daniels, Nicholas Cilz, Roger J Narayan

Abstract

Microneedles are small projections that are used to provide painless drug delivery via the parenteral or transdermal route. One requirement for advancing the use of this drug delivery technique is the development of cost effective production methods. In this study, dynamic mask stereolithography, a variation of the well-established rapid prototyping technique that utilizes digital light projection to illuminate a pattern, was used to produce microneedles array. One concern associated with drug delivery via microneedles is the risk of infection. In addition to producing polymer microneedles via dynamic mask stereolithography, pulsed

laser deposition was also used to deposit antimicrobial coatings of the surface of the microneedle arrays. The ability to rapidly produce microneedles with antimicrobial properties will advance the progress of this technology by reducing the cost and increasing the safety of their use.

Introduction

Microneedles are a rapidly developing parenteral drug delivery technique that shows promise to greatly reduce the pain associated with injections and minimize many of the safety concerns pertaining to injections. Microneedles are defined as sharp projections with at least one lateral dimension less than 500 μm . Also, they are generally less than 1000 μm in length. Their small sizes allows them to penetrate the skin with minimal forces while only penetrating a few hundred μm into the skin, therefore not reaching pain sensing nerve bundles located in the lower dermis. While not penetrating to a depth where pain sensations occur, microneedles still greatly improve transdermal delivery rates by both providing conduits to bypass the diffusion resistant stratum corneum layer and directly reaching capillary beds located in the upper dermis [1-2]. Previous studies confirmed that the pain associated with microneedle use is significantly less than with conventional hypodermic needles [3-6].

In their development, microneedles have been produced by a number of methods including glass, silicon, metals, and numerous polymers [1]. Production of ceramic microneedles, such as glass and silicon, require production processes that are high cost, have limited geometries,

and use hazardous chemicals, such as reactive ion etching [2]. Also, while they are exceptionally hard, ceramics are also brittle which can result in catastrophic failure (fracture) when in use [1-2]. Unlike ceramics, metals generally do not undergo catastrophic failure and bend rather than shatter. However, like ceramics, production of metal microneedles is rather limited in geometries. Production of metal microneedles has been limited to two techniques: ablating metal sheets to allow segments to be bent at 90 degrees to form a microneedle array and using electroplating of a conical master structure to make a thin walled hollow shell structure [7-12]. The first technique does not allow for hollow microneedles while the second technique results in weak structures due to the thin walls. While polymers are the least stiff of these materials, they are the most appealing material from a commercial perspective due to their ease of production and flexibility in geometry.

Polymer microneedles are predominantly produced by three methods: micromolding, two photon polymerization, and micro-stereolithography. In micromolding, a microneedle master structure is used to create a negative mold from a material with a low friction coefficient, such as polydimethylsiloxane (PDMS). Two methods can then be used to create replicas, depending on the desired material to be used. If the material to be used is already in its solid state, the material can be melted to fill the shape of the mold and the cooled to allow it to solidify before separating [13-16]. If the material is still in some liquid precursor state, the mold can be filled without any modification and crosslinking is induced, such as by exciting photoinitiators or thermal crosslinkers, to polymerize the material [17-20]. In both methods,

vacuum pressure is often used to remove air from voids in the mold to allow the polymer to completely fill the shape of the master structure [18-21].

Both of the other two polymer microneedle fabrication techniques, two-photon polymerization and micro-stereolithography, are rapid prototyping techniques. In these techniques, an input file, which is generally an STL file type, is used to guide the machine that is being used to build the part. STL files, which are structures composed of numerous triangles, can be generated by CAD software, facilitating robust component design. Most commonly, parts are produced in a layer by layer fashion, though this is not always the case.

Two-photon polymerization is a laser based rapid prototyping technique that utilizes nonlinear optics to induce polymerization of photosensitive resins. In this technique, ultra-short laser pulses (generally femtosecond) interact with photoinitiator molecules in a process called multiphoton absorption which results in the release of free radicals. This process is also utilized in the super-resolution fluorescence microscopy technique, multiphoton microscopy [22]. Due to the non-linear nature of this process, there is no diffraction limit and resolutions smaller than the wavelengths of light can be achieved [23-26]. Further, since the focusing optics are standard microscope objectives, the resolution is easily scalable to reduce production time if high resolution is not needed [22, 27]. Even though this technique is capable of exceptional resolutions while still being scalable, there are drawbacks. In particular the high cost of femtosecond laser systems (several hundred thousand dollars) and the low throughput of production make this process prohibitive for commercial production of

medium to low cost devices. Since polymerization only occurs along the trace of the laser, structuring must occur by rastering over the entire three-dimensional structure.

In microstereolithography, guided light is used to selectively cure a layer photosensitive polymer in a desired pattern. In this manner, microscale structures can be built up layer by layer. Two variations of microstereolithography exist. The first, laser scanning stereolithography, uses a scanning laser to polymerize the pattern [28-31]. This process uses single photon absorption, which is diffraction limited, and less expensive lasers (e.g. Ar, Nd:YAG) [28, 30]. Like 2PP this process requires rastering and is rather time consuming. In the second technique, dynamic mask stereolithography, the light source is a lamp and the pattern is generated by selectively controlling how light passes through a mask. One of the major benefits of dynamic mask stereolithography is that an entire layer is polymerized at once, which significantly reduces the production time. While having a lower resolution than 2PP, microstereolithography is a significantly faster process, making it a more appealing technique for direct fabrication of microneedles.

The microstereolithography system used in this study was the Perfactory® SXGA+ Standard UV system. This commercially available system uses digital light projection (DLP) technology to create the light pattern, the same technology used in DLP high definition televisions. In DLP technology, created by Texas Instruments, millions of tiny mirrors are used to selectively reflect light from a lamp to create pixels that can not only turn on or off but can also be used to regulate the brightness of each pixel. With an approximately

100x75mm build envelope size, multiple structures can be built in parallel to greatly reduce production time.

DLP based microstereolithography systems have been used in several studies to make microscale biomedical devices. Our research group has previously used a Perfactory® microstereolithography system to make replicas of human scaphoid and lunate carpal bones [32]. The Micro-stereolithography group at University of Warwick produced electrochemical flow cells and a microfluidic odor detector using a Perfactory® system [33-34]. A research group at Pusan National University in Korea has a custom-built microstereolithography system that uses DLP projection and focusing optics to make high resolution structures including microlens arrays, tissue engineering scaffolds, and microneedle arrays [35-38].

The need for and benefits of transdermal delivery of antimicrobial agents has been thoroughly described in the patent by Lane [39]. For example, Lane et al state that transdermal delivery will enable easier maintenance of minimum inhibitory concentrations for prolonged periods of time, thus reducing the emergence of drug resistant microbes [39]. The ability to maintain drug concentrations of greater than 100% of the MIC will also decrease therapy duration. Further, transdermally delivered drugs are expected to have better patient compliance than intravenously or orally delivered drugs [39]. Drugs delivered via the transdermal or parenteral route also directly enter the bloodstream so the metabolism concerns associated with oral delivery are avoided [1].

A study by Donnelly et al has investigated the risk of infection associated with microneedle mediated drug delivery [40]. They found that while microneedles had a significantly lower microbial permeation rate than hypodermic needles, microbes were still able to pass through the punctured barrier. Also, microneedles residing in the skin resulting in a higher permeation rate than microneedles that were removed after puncturing [40]. After removal from the skin, microneedles had more organisms adhered to their surface than was the case with hypodermic needle use [40]. These results all indicate the while the risk of infection from microneedle mediated delivery is lower than with hypodermic needles, it is still a concern that needs to be addressed.

Two previous studies by our research group have demonstrated the use of microneedles for delivering antimicrobial agents. In the first study, a master structure of a microneedle array was produced by 2PP. Ormocer® microneedles were then made by micromolding with a PDMS mold. These microneedle arrays were then coating with Ag by pulsed laser deposition. The coated needles were shown to be effective at inhibiting growth of *Staphylococcus aureus* while the uncoated needles showed no inhibition [19]. In the second study, micromolding was again used to produce microneedle arrays but a different material was used, a solution of polyethylene glycol diacrylate and 2 mg/ml of the antibiotic gentamicin sulfate [20]. In this case the release of the drug was from diffusion out of the hydrogel and not from washing off of the surface. These microneedles were also shown to

be effective against *Staphylococcus aureus* while microneedles of pure polyethylene glycol diacrylate had no effect.

One technique that can be used to produce antimicrobial coatings is pulsed laser deposition [19, 41-42]. In this physical vapor deposition process material from a solid target is vaporized using a high energy laser, most commonly excimer lasers. The average kinetic energy of species generated by excimer laser ablation is 100-1000 kT as opposed to single kT for thermal deposition techniques; the higher energy of the deposited species improves the adhesion of the film to the substrate [43-45]. Due to the ability to perform depositions at room temperature, pulsed laser deposition is better suited for producing coatings on polymer substrates than thermal deposition techniques since thermal techniques may exceed the glass transition temperature of the polymer. Thin films deposited by pulsed laser deposition also have high density and low porosity.

As previously mentioned, pulsed laser deposition has been used to produce Ag coatings on microneedles that were produced by the two step process of two-photon polymerization and micromolding [19]. In another previous study, pulsed laser deposition was used to produce thin film coatings on silicon wafers. These coatings were found to be effective against *Escherichia coli* with exposure to light increasing the antimicrobial performance [42]. Silver is a broad-spectrum antimicrobial agent that has been shown to be effective against bacteria, fungi, and viruses [46-54]. Silver has also been shown to reduce inflammation in wounds by lowering the local levels of matrix metalloproteinases [55-57]. Zinc oxide is another widely

used antimicrobial agent, particularly as used as component of endodontic sealants [58]. In addition to zinc oxide molecules having intrinsic antimicrobial properties from generation of reactive oxygen species on their surface, studies have shown that the exposure to light enhances the antimicrobial properties of zinc oxide [42, 59-60]. The exposure of this photovoltaic semiconductor compound to light produces valence band holes which react with neighboring molecules to produce radicals such as hydroxyl (OH^\cdot) and superoxide (O_2^\cdot) [61]. These radicals enhance the antimicrobial activity by disrupting the cell membranes of microbes [62]. ZnO has also been found to have stronger antibacterial activity against Gram-positive than Gram-negative bacteria [63].

In the present study, the use of microstereolithography combined with pulsed laser deposition to make antimicrobial microneedles was investigated. First, tests were performed to determine the resolution of the microstereolithography system. Next, solid microneedles of four different geometries were produced, of which one of them was selected for mass production. In addition to square arrays, needles in a cross shape, which may be used for wound closure, were created. Pulsed laser deposition was then used to coat four microneedle arrays at a time with a layer of silver or zinc oxide. Scanning electron microscopy, atomic force microscopy, and profilometry were used to analyze the microneedles and coatings. Penetration of the needles into porcine skin was confirmed by Trypan blue staining. Lastly, agar diffusion assays were performed with *Escherichia coli*, *Staphylococcus epidermidis*, and *Staphylococcus aureus* to test the effectiveness of the coatings on microneedle arrays and cylindrical wafers. Our findings show that dynamic mask microstereolithography combined

with pulsed laser deposition is a fast and effective way to make microneedle arrays with antimicrobial properties.

Methods:

Stereolithography

An Envisiontec Perfactory® SXGA Standard UV stereolithography system was used to produce structures from a commercially available photosensitive acrylate polymer, eShell 200 (Envisiontec GmbH, Ferndale, MI). The Perfactory® system was equipped with a halogen bulb and a filter for visible light exposure. Building of structures was performed at 550 mW with a 3.5 second exposure time and a z-direction step size of 30 μm . eShell 200 was used as received per manufacturer specifications. The build area of the system was 96.54 mm x 72.41 mm. Perfactory® RP software (Envisiontec GmbH, Ferndale, MI) was used to specify the layout of the parts in the build area, an example of a batch of input STL files is presented in Figure 1a. Structures are produced in a layer by layer fashion on the build platform in the layout specified in Perfactory® RP. After building, the build platform with structures attached is removed from the basin of resin. An image of the resulting structures attached to the build platform after production which correspond to the input batch is provided in Figure 1b. After removal from the basement, the substrates were removed from the build platform and the parts were separated from their support structures. Next, polymerized resin was washed off of the structures using a rinse in isopropanol (Fisher Scientific, Waltham, MA), followed by a second rinse in acetone (Fisher Scientific,

Waltham, MA). After rinsing, the samples were placed in a UV flash oven (Otoflash, Envisiontec GmbH, Ferndale, MI) for 50 seconds to ensure complete polymerization.



Figure 1: a) layout of input STL files that are sent to the Perfactory® machine to produce, b) image of the resulting structures on the build platform, and c) STL drawing of the input STL file for making microneedles which consists of four microneedle arrays held onto a substrate by support structures.

Stereolithography Resolution

Five different types of structures were produced to measure the resolution of the Perfactory® system. Two different structures were produced to determine the hole resolution, which we will define as resolution of a hole produced in a 2 mm thick flat substrate. The first hole resolution structure, shown in Figure 2a, is an array of circular holes having 5 replicates in the y-direction and in the x-direction having descending diameters of 800 μm , 700 μm , 600 μm , 550 μm , 500 μm , 450 μm , and 400 μm . The second hole resolution structure, shown in Fig 2b, is an array of square holes having 5 replicates in the y-direction and in the x-direction

having descending hole side-lengths of 800 μm , 700 μm , 600 μm , 550 μm , 500 μm , 450 μm , and 400 μm . A third structure was produced to determine the line resolution of the Perfactory® system; this structure is shown in Fig 2c. This structure consisted of lines of input widths ranging from 140 μm to 30 μm in 10 μm increments spanning gaps of 500, 300, 250, 200, and 150 μm . After production, the structures were imaged with a Leica EZ4 optical microscope and LAS EZ software (Leica Microsystems, Wetzlar, Germany) to determine the resolution of the features.

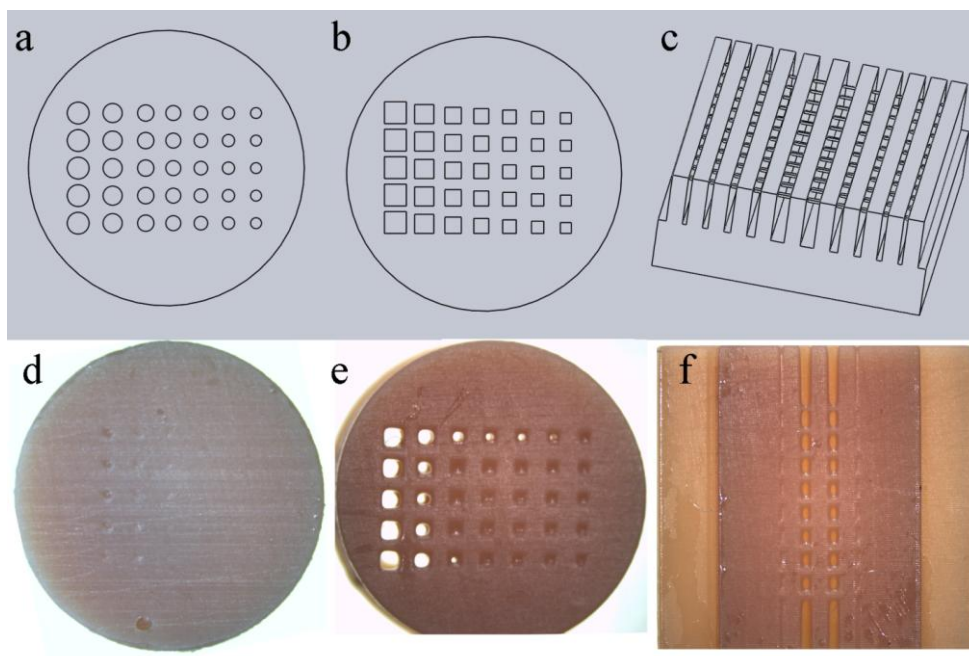


Figure 2: Drawings of input files for testing resolution of making circular holes (a), square holes (b), and line width (c) and the resulting structures that were produced by the Perfactory® system (d-f).

Microneedle Production

Microneedle arrays of four different geometries were produced using the Perfactory® system, consisting of two different heights and two different base geometries as shown in Table 1. The microneedles were in a rectangular pyramid shape. Two different input pyramid heights were produced, 1000 μm and 1250 μm tall. The two different base geometries were 500 x 250 μm and 750 x 250 μm . The tips of all four geometries were 90 x 30 μm . The input files for the stereolithography system consisted of a 1.0 mm thick and 18 x 18 mm substrate upon which four replicas of the 3 x 3 microneedle arrays were attached by support structures (Fig 1c). All of the input STL structures were designed using Solidworks (Dassault Systemes S.A., Velizy, France) and support structures for the structures were produced using Magics RP 13 (Materialise NV, Leuven, Belgium). 8 substrates, for a total of 32 arrays, were produced in a single batch. Microneedles with 1000 μm height and a 750 x 250 μm base were also produced on a cross-shaped substrate (Figure 6b).

Table 1: Microneedle Input and Actual Geometries

Geometry	Input Height (μm)	Actual Height (μm)	Input Width (μm)	Actual Width (μm)	Input Depth (μm)	Actual Depth (μm)
A	1000	828 +/- 19	750	805 +/- 24	250	311 +/- 17
B	1000	665 +/- 40	500	510 +/- 9	250	285 +/- 15
C	1250	831 +/- 9	750	817 +/- 6	250	332 +/- 21
D	1250	748 +/- 31	500	571 +/- 25	250	347 +/- 11

Skin Penetration

The ability of the microneedle devices to penetrate skin was tested via dyes and optical microscopy. The microneedle arrays were manually pressed against full-thickness porcine skin. Immediately after removal of the needles, Trypan blue was applied to the surface of the skin at the insertion site. The dye was then wiped away with isopropanol swabs. Needles were examined before and after penetration with a Leica EZ4 to confirm that the needles were not damaged during application to the skin. Optical microscopy was also used to examine the dyed, micro-needle produced pores in the skin.

Pulsed Laser Deposition

Pulsed laser deposition was performed using a KrF excimer laser operating at a wavelength of 248 nm with 450 mJ energy, 25 ns pulse duration, and 10 Hz repetition rate. The spot size of the laser was a 1 x 3 mm rectangle, resulting in a fluence of 0.0015 J/cm². The coatings were deposited at room temperature and 10⁻⁵ Torr for 5 minutes. Two coatings, Ag and ZnO, were deposited via PLD using these settings. For the silver deposition, a 99.99% purity target was obtained from a commercial source (Alfa Aesar, Ward Hill, MA). For the zinc oxide deposition target, 99.99% purity ZnO powder (Alfa Aesar, Ward Hill, MA) was pressed into round 2 inch diameter pellets and then sintered at 900 °C in an oxygen atmosphere for 12 hours.

Two substrates (8 arrays) of the 250 x 500 µm base, 1250 µm height microneedle geometries were coated for each of the two coating materials. Also, four of the cylindrical wafers (one

substrate) were coated for each coating material using the same conditions. In order to measure coating thickness and roughness, silicon wafers were masked on one half of the surface and coatings were applied using the same settings for the two coating materials.

Scanning Electron Microscopy

A Hitachi S-3200 (Hitachi, Tokyo, Japan) scanning electron microscope operating in vacuum mode was used to image the microneedle devices. The PLD coated samples were imaged as is; the uncoated samples were sputter coated with gold-palladium to enable imaging in the SEM.

Atomic Force Microscopy and Stylus Profilometry

Atomic force microscopy was performed to determine the surface topography and roughness of the PLD deposited coatings on silicon. A Dimension 3000 AFM with NanoScope analysis software (Veeco, Santa Barbara, CA) and an AC160 tip (Olympus, Melville, NY) operating in tapping mode with a resonance frequency of 366.304 kHz was used. A Tencor Alpha Step 200 stylus profilometer (PLA-Tencor, Milpitas, CA) was used to measure the thicknesses of the PLD deposited coatings on silicon wafers. For each coating, scans were performed in triplicate over a 400 μm range containing both the coated and uncoated surface with a 20mg stylus scanning at 10 $\mu\text{m}/\text{second}$.

Agar Diffusion Assay

Antimicrobial activity of the PLD deposited coatings was assessed using an agar diffusion assay. *Escherichia coli* ATCC 12435, *Staphylococcus aureus* ATCC 6548, and *Staphylococcus epidermidis* ATCC 35984 (American Type Culture Collection, Manassas, VA) were cultured overnight in tryptic soy broth (VWR International, West Chester, PA). The cell suspensions were then centrifuged at 4500 rpm for 10 min. A cell suspension with a density of $\sim 10^8$ CFU/ml was then made by resuspending the pellet in 1x phosphate-buffered saline (VWR International, West Chester, PA). Mueller Hinton agar plates (VWR International, West Chester, PA) were inoculated with a lawn of the respective bacteria using a sterile swab. Microneedle arrays and cylindrical wafers were placed on the inoculated plates with the coated side facing the agar (microneedles projecting into the agar). After incubating at 37 °C for 24 hours, the surfaces of the plates were imaged with optical microscopy to determine the extent of microbial growth.

Results

Stereolithography Resolution

Optical microscopy images of the structures produced by the Perfactory® system to determine the resolution are provided in Figure 2D-F. In these images, the largest input holes (800 μm) are on the left for the hole resolution images and the widest input line width (140 μm) is at the bottom for the line width image. As can be seen in these images, the lateral resolutions of the actual structures are significantly larger than dimensions in the input files.

Also, the system was better at producing holes that were a square input as opposed to a circular input, though the holes produced by the square input file has rounded corners, making the holes look nearly circular. While the square input file was able to consistently produce holes for the 800 μm and 700 μm input holes, the circular input file produced no open holes. While some holes were able to be produced for smaller input sizes, these holes were not consistently produced. The actual and input values for the square and circular holes are provided in Table 2. All holes were more than 140 μm smaller than their input dimensions, with the hole size error ranging from 144-354 μm . As can be seen from the line width resolution test image, only input trench widths 500 μm or greater resulted in trenches being produced. A plot of the actual line width values and input values across the largest gap (500 μm) for the line width resolution structure is provided in Figure 3a; the actual values were determined by averaging the actual line widths of 4 different structures with the error bars indicating the standard deviation. While the actual line widths followed the general trend of the input dimensions, the actual line widths were more than twice the input dimensions with the size discrepancy increasing with increasing input width. It is interesting to note that the 60 μm wide input line resulted in the projector producing a line, indicating that a pixel does not need to be completely filled to result in the software selecting to illuminate that pixel. However, the lines less than 60 μm wide did not result in illumination of pixels.

Table 2: Hole Resolution Results

Hole Resolution					
Input (μm)	Square		Input (μm)	Circle	
	Actual (μm)	% Holes Open		Actual (μm)	% Holes Open
800	656.25 +/- 15.83	100%	800	No Open Holes	0%
700	429.2 +/- 42.5	100%	700	No Open Holes	0%
600	245.9 +/- 94.3	40%	600	No Open Holes	0%
550	245.5	20%	550	No Open Holes	0%
500	219.4	20%	500	No Open Holes	0%
450	199.6	20%	450	No Open Holes	0%
400	No Open Holes	0%	400	No Open Holes	0%

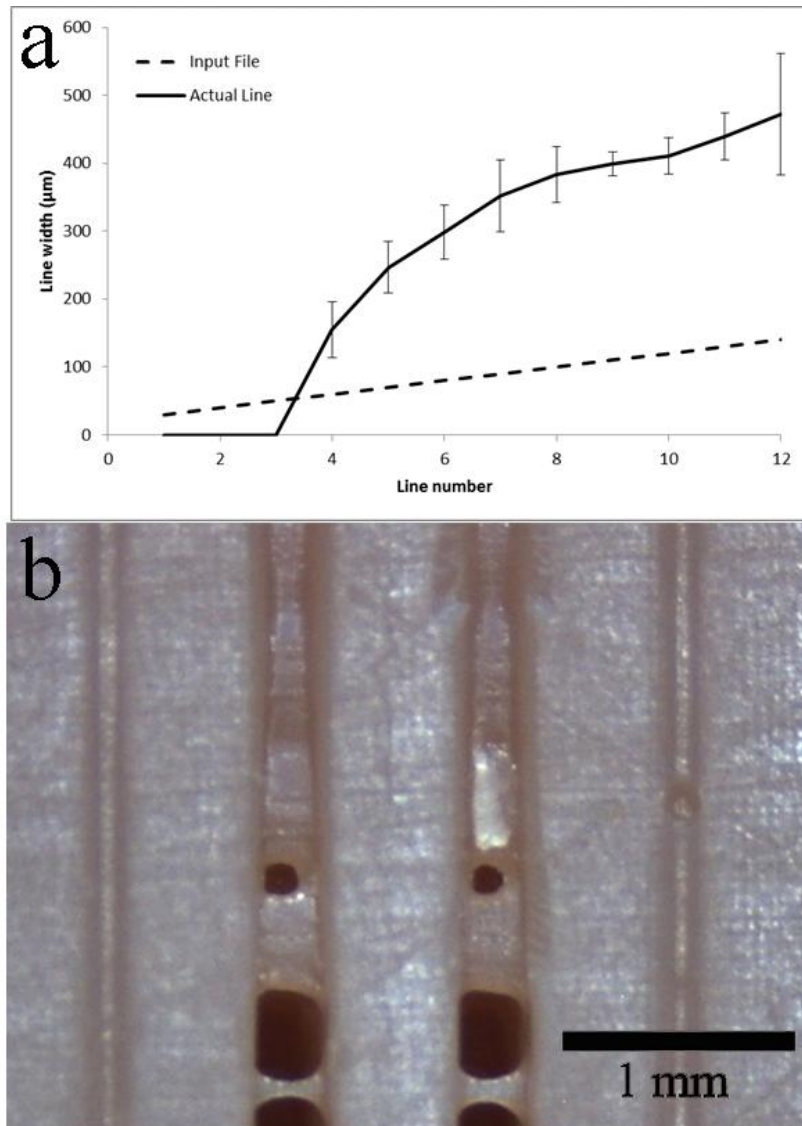


Figure 3: Input line width and average actual line width dimensions for the line width resolution test (a). Error bars are standard deviation. Image of diffusion driven polymerization on a line resolution test structure (b).

Stereolithography-produced Microneedles

Scanning electron micrographs of the uncoated four different geometries are shown in Figure 4. The microneedles were imaged from three views: facing the thin face, facing the wide

face, and at a perspective view; all images of the uncoated samples are at a 60° tilt. Quantitative analysis of the input and actual dimensions of the needles are provided in Table 1. For all of the microneedle geometries, the actual lateral dimensions (width and depth) were larger than the input dimensions. In contrast, the actual vertical dimensions were shorter than the input dimensions. Additionally the $750\ \mu\text{m}$ wide structures were taller than their $500\ \mu\text{m}$ wide structures with the same input heights.

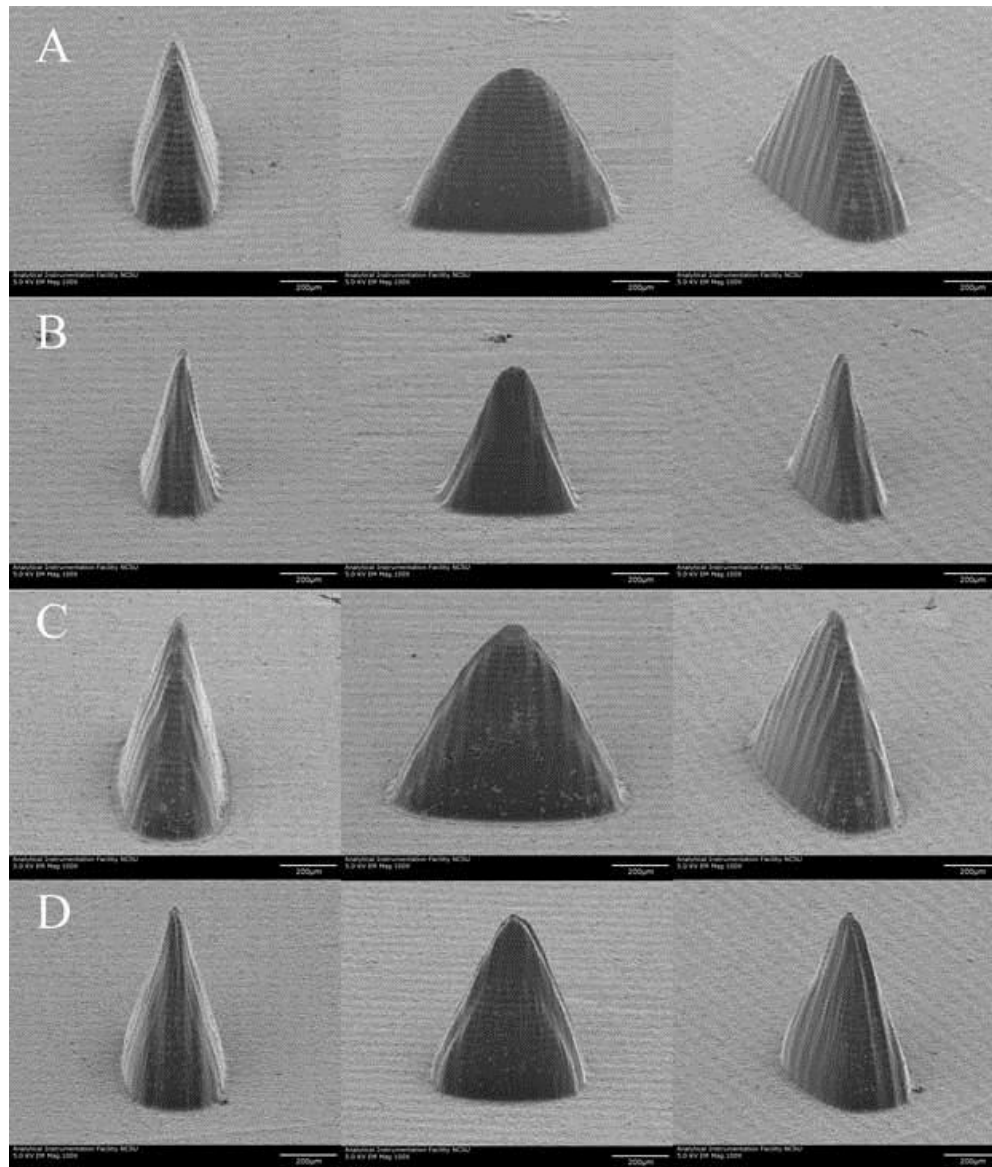


Figure 4: Scanning electron microscopy images of eShell 200 microneedles produced in varying geometries by stereolithography. The geometries of the input STL file were A) 750x250 μm base and 1000 μm height, B) 500x250 μm base and 1000 μm height, C) 750x250 μm base and 1250 μm height, D) 500x250 μm base and 1250 μm height. Views from left to right are facing the 250 μm wide side, facing the wider side, and a perspective view. All images are taken at a 60° tilt.

The z-direction build layers and also the lateral pixel array can clearly be seen in the scanning microscopy images of the microneedles. Higher magnification top-down and side views were used to measure the z-step size, tip radius of curvature, and aspect ratio (Figure 5). The z-direction step size was measured to be $29.89 \pm 0.61 \mu\text{m}$. The radius of curvature was measured to be $18 \mu\text{m}$. The aspect ratio of wide face of the D geometry for each layer was measured by dividing the average z-step size by twice the x and y step distance from layer to layer (via the top-down image) over the entire length of the needle. The average aspect ratio measured layer by layer along the entire length of the needle was 2.4 ± 0.3 to 1 whereas the net aspect ratio (total height divided by width) was measured to be 2.2 to 1.

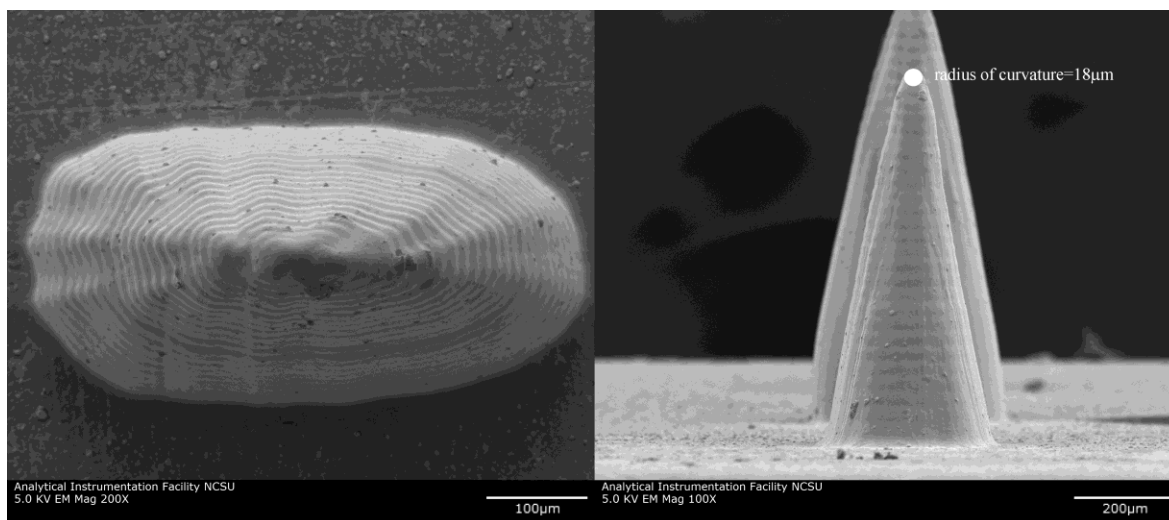


Figure 5: SEM images of geometry D (input dimensions $250 \times 500 \mu\text{m}$ base and $1250 \mu\text{m}$ height) from top down view at 200x magnification (left) and at a 90 degree tilt facing the $250 \mu\text{m}$ wide side at 100x magnification. In the side view image the radius of curvature of the tip is marked.

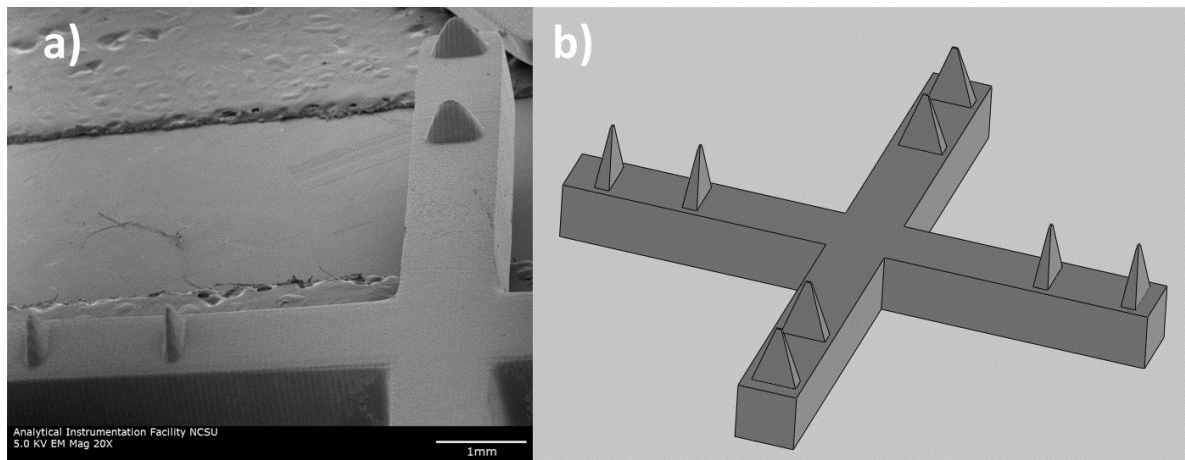


Figure 6: a) SEM image of microneedles on a cross-shaped substrate produced by SLA; b) CAD drawing of the input file used to produce the device by SLA.

Cross-shaped microneedle devices were also able to be produced with the dynamic mask SLA process. A scanning electron microscopy image showing two arms of the cross-shaped device is provided in Figure 6b. The STL file used to make this device is shown in Figure 6a. Trypan blue staining confirmed that the SLA-produced microneedles were capable of penetrating the stratum corneum. This blue dye is absorbed by epidermal tissue but not by the stratum corneum; this dye has previously been used to confirm microneedle penetration beyond the stratum corneum [64]. Figure 7c shows Trypan blue staining of the pores produced in the skin by the cross-shaped microneedle device. A higher magnification image of the pores produced in the skin is shown in Figure 7d. The pores are larger in one direction than the other, in accordance with the cross-sectional shape of the needles. Optical microscopy images of the needles before (Figure 7a) and after (Figure 7b) confirmed that the needles were able to penetrate the skin without damage.

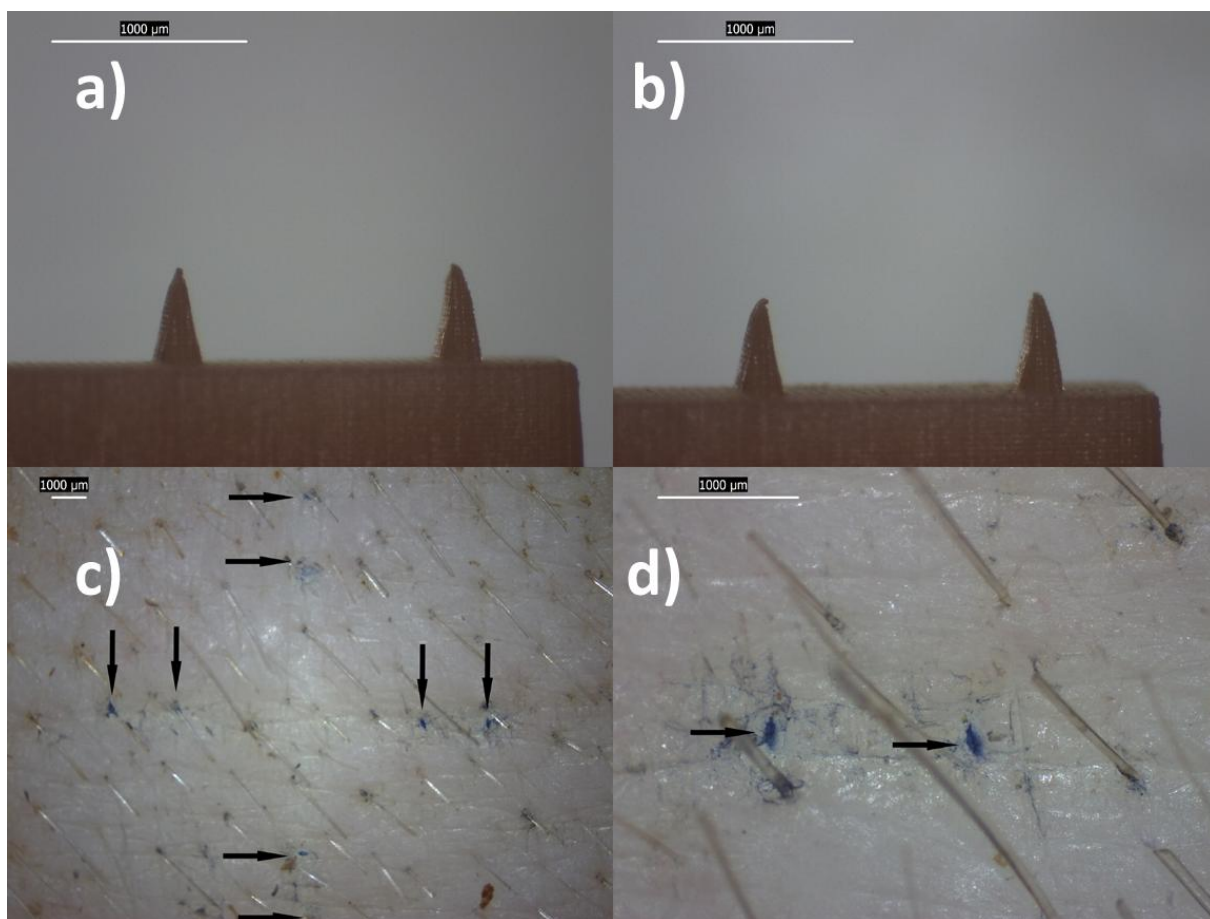


Figure 7. Trypan blue staining of pores in skin produced by application of SLA-produced microneedles: a) microneedles before skin penetration, b) microneedles after skin penetration, c) pattern of entire cross shape, d) close up view of pores.

Pulsed Laser Deposition-coated Microneedles

Optical microscopy images of the coated samples show the distinct color changes that occur from the PLD deposited coatings (Figure 8a,b). The Ag coating resulted in a metallic grey finish and the ZnO coating resulted in metallic brown finish as opposed to the opaque pink of the eShell 200 polymer. High magnification (500x) images of the needles at an angle

perpendicular to the substrate show the differences in surface morphology after coating by pulsed laser deposition was performed (Figure 8c,d). The ZnO coating is visibly rougher than the Ag coating.

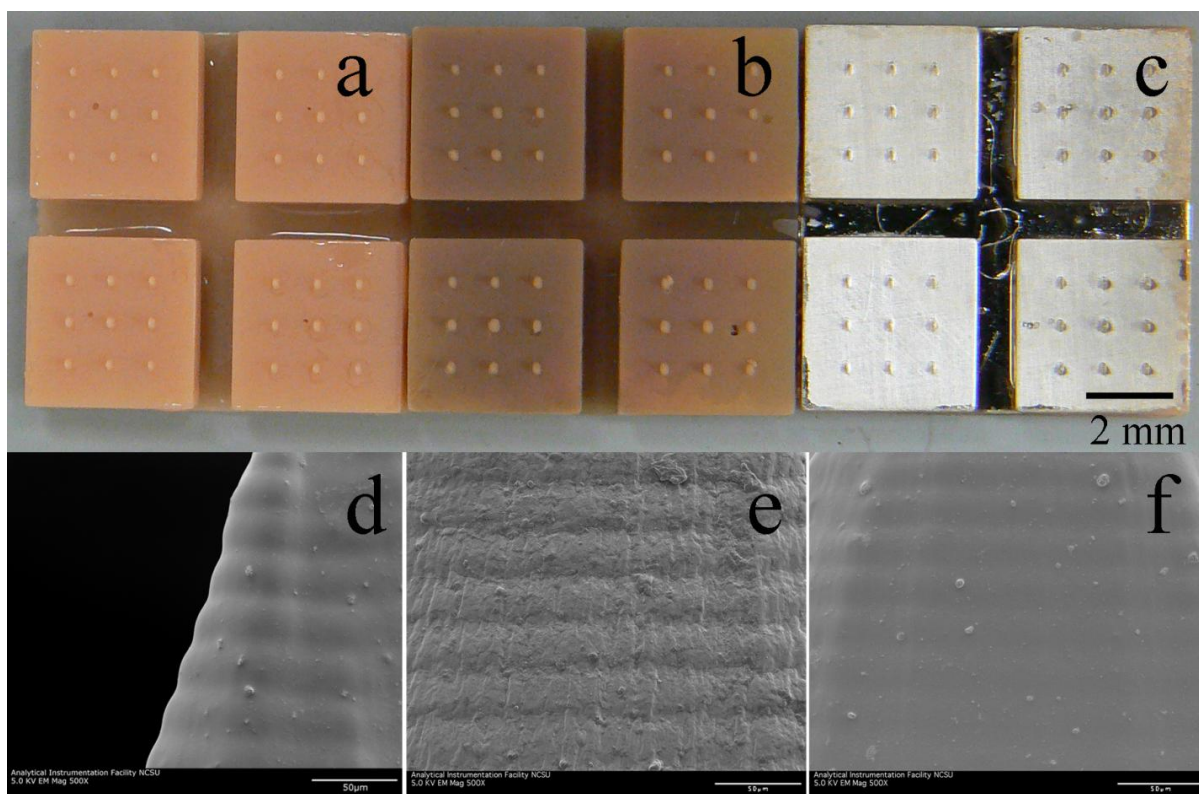


Figure 8: Optical microscopy images (a-c) and high magnification SEM images (d-f) of uncoated (a,d), zinc oxide coated (b,e), and silver coated microneedle arrays (c,f).

AFM topographical data of the two coatings on silicon wafers are shown in Figure 9. AFM revealed that the Ag and ZnO surfaces had R_a roughness values of 1.401 nm and 1.338 nm, respectively. The grain sizes of the coatings were approximately 26.2 ± 4.6 nm and 111.3

+/- 13.4 nm for Ag and ZnO, respectively. The thicknesses of the coatings were measured by profilometry to be 53.5 +/- 8.8 nm for Ag and 287.2 +/- 30.3 nm for ZnO. With the coating thickness, pulse rate, and deposition time known, the deposition rate can be calculated. The deposition rate is 0.018 nm/pulse for Ag and 0.10 nm/pulse for ZnO.

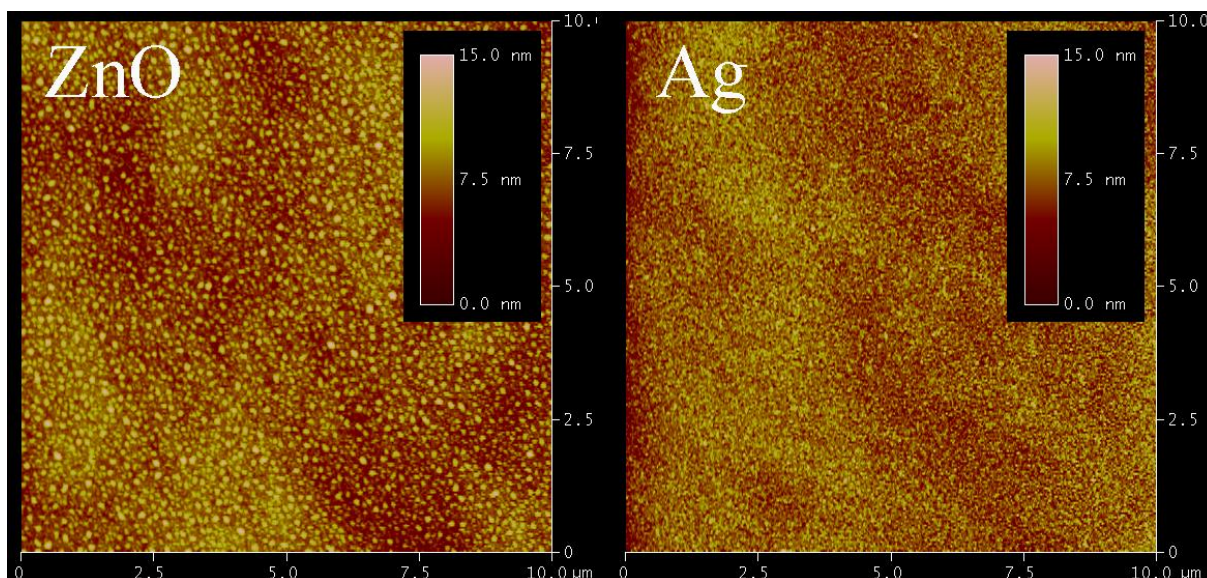


Figure 9: AFM height data of ZnO (left) and Ag (right) PLD-deposited coatings on silicon over a 10 μm scan range.

Agar Diffusion Antibacterial Assay

Images of the agar diffusion assay against microneedle arrays are presented in Figure 10. The agar diffusion assay indicated that both the Ag and ZnO coatings provided the arrays with antibacterial properties. Both coatings had noticeable effects against *S. epidermidis* and *S. aureus* but not significant effects against *E. coli*. The Ag coated microneedle arrays produced a zone void of growth while the ZnO coated samples produced a zone of inhibited

or reduced growth. Some of the coating was still remaining on both the Ag and ZnO coated arrays after 24 hours of contacting the agar.

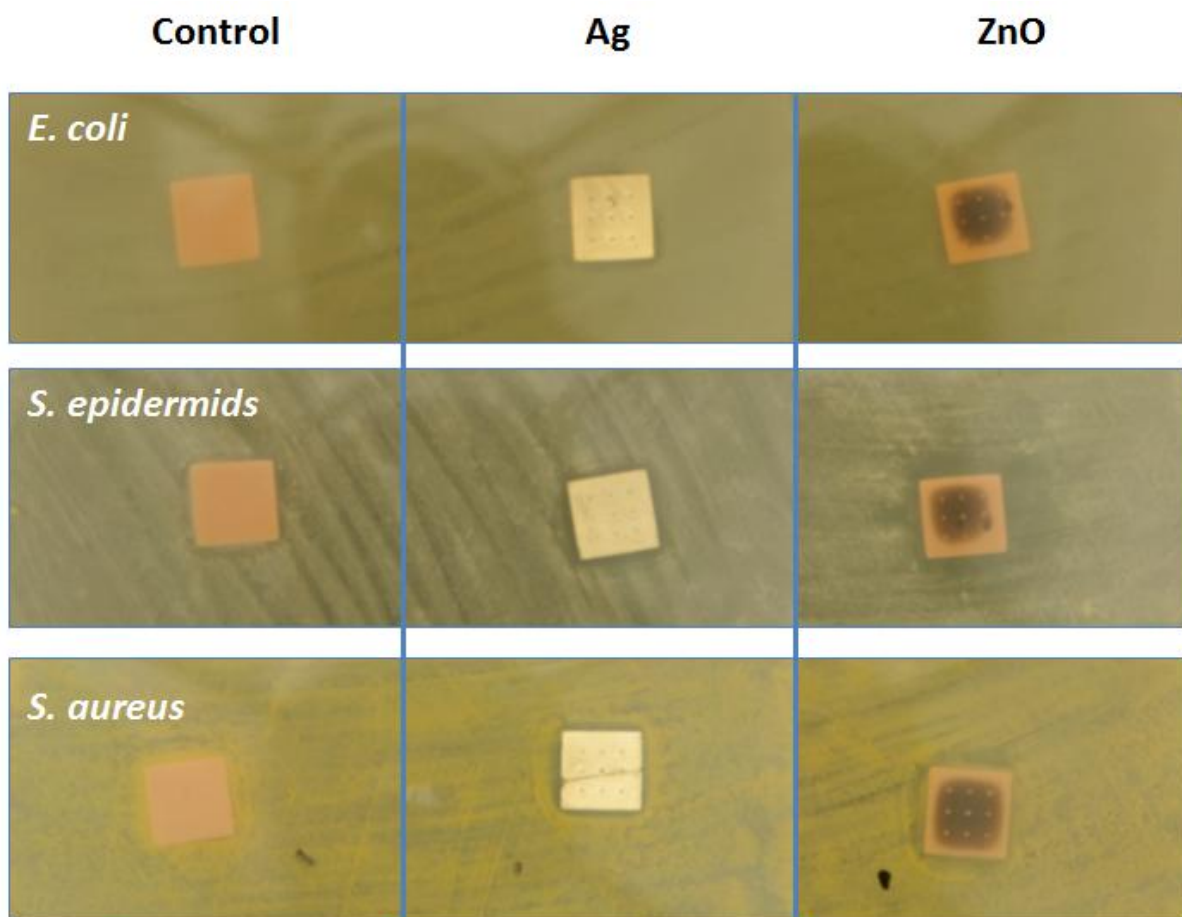


Figure 10: Agar diffusion results of uncoated (left), Ag coated (center), and ZnO (right) coated D geometry microneedles against *E. coli* (top), *S. epidermidis* (center), and *S. aureus* (bottom). Microneedle arrays are 18 x 18 mm wide.

Discussion

Stereolithography Resolution

The discrepancy between lateral input and actual dimensions can be attributed to three factors: projector resolution limits, voxel size, and layer blending. As indicated by the production of the 60 μm input width line, projector controlling software may select to illuminate a pixel even though the pixel is only partially containing a structure. Therefore, a feature of the size of one pixel, but lying between four pixels, can result in the illumination of four pixels, greatly increasing the actual size of the feature. For example, a 120 x 120 μm sized input feature may illumination four pixels, resulting in a 140 x 140 μm illumination area. Since the actual voxel size (measured to be 155 μm wide) is larger than the pixel size (70 μm), the resulting polymerized voxel is larger than the illuminated pixel. Thus, structures will be larger than their input dimensions due to the larger voxel size. Some of the factors that can contribute to the increased size of the voxel are diffraction, refraction, and photoinitiator diffusion [28, 65]. As light coming from the projector passes through the numerous layers of glass the light will diffract and spread the spot size [65]. Quantitative analysis of the spreading of the actual voxel size due to diffraction has been performed by Sun et al [64]. In the Perfactory® system, a lamp which emits a spectrum of light wavelengths (range) is used instead of a single wavelength laser. Therefore the different light wavelengths will refract different amounts as they pass through the various layers of material in the system, with low wavelengths refracting more than high wavelengths. Since a significant portion of the light spectrum is emitted by the lamp and the photoinitiator can be excited by a wavelength range, refraction is a signification factor. (Not the case if the filter

makes it a very narrow range) Diffusion driven polymerization can result in fusing of nearby features. In diffusion driven polymerization, excited photoinitiator molecules diffuse out of the voxel and produce membrane-like features between nearby features. The membrane-like features of diffusion driven polymerization could be clearly seen in some of the line resolution structures between the larger lines as shown in Figure 3b. This phenomenon has been observed in other photopolymerization processes [26]. As seen in the SEM images of the structures, the different layers, while visible, are not exceptionally distinct from each other. This indicates that there is significant overlap between the voxels due to their height being greater than the step size. Exposure of an already polymerized area to light will result in swelling of the polymerization voxel due to diffusion of photoinitiator. Also, light passing through already polymerized material will refract differently, resulting in a localized change in refractive index when exposing already polymerized areas to light. The localized refractive index change can disperse light and increase the voxel size further. This change in voxel size has been observed and theoretically quantified in photopolymerization processes [66].

Stereolithography-produced Microneedles

The Perfactory® system was able to produce 32 microneedle arrays in a single, approximately four hour batch when using a 30- μm layer spacing. This results in a production rate of approximately 7.5 minutes per microneedle array. In comparison, the two photon polymerization process requires each needle to be produced individually, resulting in a production time of 1-20 minutes per needle (depending on resolution and writing speed).

Thus, a single 25 needle array would require a minimum of 25 minutes, not including the production time required to make the substrate. Further, the cost of a Perfactory® system is in the range significantly less expensive than a two-photon polymerization system. Both the lower cost and higher production rate make the Perfactory® system a more appealing method for commercial scale production of microneedles.

As shown in Table 1, the lateral dimensions of the microneedles were larger than the input file while the height of the needles was shorter than the input file. The discrepancy in lateral dimensions can be attributed to the lateral voxel size. The voxel size - which was measured to be 155 μm by the resolution test - adds to the actual lateral dimensions, thus making them larger than the input dimensions. There are two possible causes of the reduction in height in the actual structures. Firstly, the pixel size in the projection mask corresponds to approximately 70 μm . Therefore, a point exists where features below a certain size result in the projection mask software not illuminating the pixel containing the feature. Secondly, small features may not have enough illumination energy to result in polymerization. Longer exposure times and higher energies may improve the resolution of the small tapering features. The combination of these two factors results in small vertically tapering features being significantly smaller than their input dimensions.

The radius of curvature was measured to be 18 μm . Microneedles produced by Choi et al via stereolithography had tip radii ranging from 30-80 μm [36]. They reported an insertion force of 0.08-3.04 N for their 12 needle array of microneedles. E-shell 200 microneedles with

significantly sharper tips produced by 2PP and micromolding were able to undergo compressive forces of greater than 10 N for a 5 x 5 microneedle array [18]. The close correlation of the net aspect ratio and average layer aspect ratio as well as the low standard deviation value of 0.3 shows that the aspect ratio remained quite consistent over the entire length of the needle, which confirms that even though the actual structure is significantly shorter than the input file the structure still tapers to a point as opposed to having a truncation at the tip.

Skin penetration testing confirmed that e-Shell 200 microneedles produced by stereolithography are capable of penetrating the stratum corneum. Applying Trypan blue dye to the surface of the skin after microneedle penetration resulted in staining of pores in the exact locations of the microneedles. Visual observation of the needles confirmed previous studies indicating the e-Shell 200 microneedles have sufficient mechanical strength to penetrate skin [18].

Production of microneedles on a cross-shaped as well as a square substrate illustrates one of the benefits of dynamic mask stereolithography. Microneedles can be produced in a timely manner on substrates with complex shapes. Devices like the cross-shaped microneedle device may be used as a wound healing device that assists in holding the skin together. The design flexibility of stereolithography enables microneedles to be produced on substrates matching the contour of the wound. Coating of the wound closure devices with antimicrobial agents could assist in reducing the risk of infection at the wound site.

Pulsed Laser Deposition-Coated Microneedles

The low roughness values of the coatings – less than 2 nm - indicate that splashing was not significant ([42, 67]. While the two coatings had similar roughnesses, the grain size of the ZnO coating was significantly higher than the Ag coating. Profilometry confirmed that the PLD-deposited coatings were thin films. The Ag coating was significantly thinner than the ZnO coating, with thicknesses of 53.5 nm and 287.2 nm for Ag and ZnO, respectively. The silver coating also had a more consistent coating thickness – standard deviation of 8.8nm - while the ZnO coating had a coating thickness with a standard deviation of 30.3 nm. The deposition rates were calculated to be 0.018 nm/pulse for Ag and 0.10 nm/pulse for ZnO. Choi et al found had a ZnO deposition rate of 0.017-0.033 nm/pulse with a 0.5 J/cm² ArF excimer laser, 3x10⁻⁷ Torr, and a temperature of 400 °C [68]. Warrender et al had an Ag deposition rate of 0.0018-0.006 nm/pulse for a 248 nm KrF excimer with fluence of 6 J/cm², a 30 ns pulse duration, and a base pressure of 2x10⁻⁸ Torr [43]. Variations in deposition rate can be attributed to a number of factors, including but not limited to fluence, target temperature, and pressure [43, 68-70].

Agar Diffusion Antibacterial Assay

The agar diffusion assay confirmed previous findings that PLD-deposited coatings of both Ag and ZnO provide antibacterial properties [19, 42]. In comparison, the uncoated arrays had no antimicrobial effect. Both coatings had strong effects against *S. epidermidis* and *S. aureus* but not significant effects against *E. coli*. Sawai et al have reported that ZnO has a weaker antimicrobial response to Gram-negative bacteria than to Gram-positive bacteria [63]. The

Ag coating had a stronger antibacterial response, produced a zone void of growth as opposed to a zone of reduced growth for the ZnO coatings. Both coating types were only partially released into the agar. Complete release of the coatings would be expected in an environment with a higher water content, such as the epidermis and dermis. Release of the entire coating would result in higher concentration of the metal ions and a more pronounced antimicrobial effect.

Conclusion

In this study we have demonstrated that dynamic mask stereolithography is an appropriate technical for large scale production of microneedle arrays for drug delivery applications. Experiments to determine the resolution found that the line width of this stereolithography system under our conditions was approximately 150 μm . Microneedles were produced in a number of geometries, highlighting the versatility of the system in modifying part design. An in depth analysis of the accuracy of the produced microneedles found that while the Perfactory® system is rather accurate in reproducing lateral dimensions, the lengths of these tapering structures was significantly reduced. In addition to demonstrating large scale production of microneedle array, we established that by designing a substrate that holds four microneedle array, simultaneous pulsed-laser deposition of antimicrobial coatings could be performed on four arrays. Agar diffusion assays confirmed that these inorganic coatings indeed have antimicrobial properties. The combination of dynamic mask stereolithography with pulsed laser deposition enables rapid and cost-effective production of polymer microneedle arrays with antimicrobial properties. The ability to efficiently produce

microneedle arrays that reduce the risk of infection is a promising step towards bringing microneedle technology into wider use.

Acknowledgements

Portions of the research in this paper were funded from Office of Naval Research grant N00014-07-1-1099.

References

[1] Gittard S D and Narayan R J 2010 *Toxicology of the Skin*, ed N A Monteiro-Riviere (New York, NY: Informa Healthcare) p 301

[2] Gittard S D, Ovsianikov A, Chichkov B N, Doraiswamy A and Narayan R J 2010 Two-photon polymerization of microneedles for transdermal drug delivery *Expert Opin. Drug Deliv.* **7** 513-533

[3] Haq M I, Smith E, John D N, Kalavala, M, Edwards C, Anstey A, Morrissey A and Birchall J C 2009 Clinical administration of microneedles: skin puncture, pain and sensation *Biomed. Microdev.* **11** 35-47

[4] Bal S M, Caussin J, Pavel S and Bouwstra J A 2008 In vivo assessment of safety of microneedle arrays in human skin *Eur. J. Pharm. Sci.* **35** 193-202

- [5] Sivamani R K, Stoeber B, Wu G C, Zhai H, Liepmann D and Maibach H 2005 Clinical microneedle injection of methyl nicotinate: stratum corneum penetration *Skin Res. Technol.* **11** 152-156
- [6] Gill H S, Denson D D, Burris B A and Prausnitz M R 2008 Effect of microneedle design on pain in human volunteers *Clin. J. Pain* **24** 585-594
- [7] Gill H S and Prausnitz M R 2007 Coated microneedles for transdermal delivery *J. Control. Release* **117** 227-237
- [8] Shikida M, Hasada T and Sato K 2006 Fabrication of a hollow needle structure by dicing, wet etching and metal deposition *J. Micromech. Microeng.* **16** 2230-2239
- [9] McAllister D V, Wang P M, Davis S P, Park J H, Canatella P J, Allen M G and Prausnitz M R 2003 Microfabricated needles for transdermal delivery of macromolecules and nanoparticles: Fabrication methods and transport studies *Proc. Natl. Acad. Sci. U S A* **100** 13755-13760
- [10] Kim K and Lee J 2007 High aspect ratio tapered hollow metallic microneedle arrays with microfluidic interconnector *Microsyst. Technol.* **13** 231-235

- [11] Chandrasekaran S, Brazzle J D and Frazier A B 2003 Surface micromachined metallic microneedles *J. Microelectromech. Syst.* **12** 281-288
- [12] Chandrasekaran S and Frazier A B 2003 Characterization of surface micromachined metallic microneedles *J. Microelectromech. Syst.* **12** 289-295
- [13] Park J H, Allen M G and Prausnitz M R 2005 Biodegradable polymer microneedles: Fabrication, mechanics and transdermal drug delivery *J. Controlled Release* **104** 51-66
- [14] Park J H, Allen M G and Prausnitz M R 2006 Polymer microneedles for controlled-release drug delivery *Pharm. Res.* **23** 1008-1019
- [15] Park J H, Choi S O, Kamath R, Yoon Y K, Allen M G and Prausnitz M R 2007 Polymer particle-based micromolding to fabricate novel microstructures *Biomed. Microdev.* **9** 223-234
- [16] Han M, Hyun D H, Park H H, Lee S S, Kim C H and Kim C G 2007 A novel fabrication process for out-of-plane microneedle sheets of biocompatible polymer *J. Micromech. Microeng.* **17** 1184-1191
- [17] Trautmann A, Heuck F, Mueller C, Ruther P and Paul O 2005 Replication of microneedle arrays using vacuum casting and hot embossing *Solid-State Sensors, Actuators*

and Microsystems, 2005 Digest of Technical Papers TRANSDUCERS '05 The 13th International Conference on vol 2 (IEEE: New York) p 1420

[18] Gittard, S D, Ovsianikov, A, Monteiro-Riviere, N A, Lusk, J, Morel P, Minghetti P, Lenardi C, Chichkov B N and Narayan R J 2009 Fabrication of polymer microneedles using a two-photon polymerization and micromolding process *J. Diabetes Sci. Technol.* **3** 304-311

[19] Gittard, S D, Narayan, R J, Jin, C, Ovsianikov, A, Chichkov B N, Monteiro-Riviere N A, Stafslie S and Chisholm B 2009 Pulsed laser deposition of antimicrobial silver coating on Ormocer® microneedles *Biofabrication* **1** 041001

[20] Gittard, S D, Ovsianikov, A, Akar, H, Chichkov, B, Monteiro-Riviere N A, Stafslie S, Chisholm B, Shin C C, Shih C M, Lin S J, Su Y Y and Narayan R J 2010 Two photon polymerization-micromolding of polyethylene glycol-gentamicin sulfate microneedles *Adv. Eng. Mater.* **12** B77-B82

[21] Paik S J, Kim S H, Wang P C, Wester B A and Allen MG 2010 Dissolvable-tipped, drug-reservoir integrated microneedle array for transdermal drug delivery *Micro Electro Mechanical Systems (MEMS), 2010 IEEE 23rd International Conference on* (IEEE: New York) p 312

- [22] Gittard, S D, Miller, P R, Boehm, R D, Ovsianikov, A, Chichkov B N, Heiser J, Gordon J, Monteiro-Riviere N A and Narayan R J 2010 Multiphoton microscopy of transdermal quantum dot delivery using two photon polymerization-fabricated polymer microneedles *Faraday Discuss.* 2010 DOI: 101039/C005374K
- [23] Serbin J, Egbert A, Ostendorf A, Chichkov B N, Houbertz R, Domann G, Schulz J, Cronauer C, Fröhlich L and Popall M 2003 Femtosecond laser-induced two-photon polymerization of inorganic-organic hybrid materials for applications in photonics *Opt .Lett* **28** 301-303
- [24] Serbin J, Ovsianikov, A and Chichkov B 2004 Fabrication of woodpile structures by two-photon polymerization and investigation of their optical properties *Opt. Express* **12** 5221-5228
- [25] Gittard S D and Narayan R J 2010 Laser direct writing of micro- and nano-scale medical devices *Exp. Rev. Med. Dev.* **7** 343-356
- [26] Ovsianikov A, Malinauskas M, Schlie S, Chichkov B, Gittard S, Narayan R, Löbler M, Sternberg K, Schmitz KP and Haverich A 2010 Three-dimensional laser micro- and nano-structuring of acrylated poly(ethylene glycol) materials and evaluation of their cytotoxicity for tissue engineering applications *Acta Biomater.* **7** 967-974

- [27] Ovsianikov A, Chichkov B, Adunka O, Pillsbury H, Doraiswamy A and Narayan R J
2007 Rapid prototyping of ossicular replacement prostheses *Appl. Surf. Sci.* **253** 6603-6607
- [28] Lee I H and Cho D W 2004 An investigation on photopolymer solidification considering
laser irradiation energy in micro-stereolithography *Microsyst. Technol.* **10** 592-598
- [29] Lee I H and Cho D W 2003 Micro-stereolithography photopolymer solidification
patterns for various laser beam exposure conditions *Int. J. Adv. Manuf. Technol.* **22** 410-416
- [30] Stampfl J, Baudis S, Heller C, Liska R, Neumeister A, Kling R, Ostendorf A and
Spitzbart M 2008 Photopolymers with tunable mechanical properties processed by laser-
based high-resolution stereolithography *J. Micromech. Microeng.* **18** 125014
- [31] Neumeister A, Himmelhuber R, Materlik C, Temme T, Pape F, Gatzert HH and
Ostendorf A 2008 properties of three-dimensional precision objects fabricated by using laser
based micro stereo lithography *J. Laser Micro Nanoeng.* **3** 67-72
- [32] Gittard S D, Narayan R J, Lusk J, Morel P, Stockmans F, Ramsey M, Laverde C,
Phillips J, Monteiro-Riviere N A, Ovsianikov A and Chichkov B N 2009 Rapid prototyping
of scaphoid and lunate bones *Biotechnol. J.* **4** 129-134

- [33] Snowden M E, King P H, Covington J A, Macpherson J V and Unwin P R 2010 Fabrication of versatile channel flow cells for quantitative electroanalysis using prototyping *Anal. Chem.* **82** 3124-3131
- [34] Covington J A, Gardner J W, Hamilton A, Pearce T C and Tan S L 2007 Towards a truly biomimetic olfactory microsystem: An artificial olfactory mucosa *IET Nanobiotechnol.* **115**-21
- [35] Choi J W, Wicker R, Lee S H, Choi K H, Ha CS and Chung I 2009 Fabrication of 3D biocompatible/biodegradable micro-scaffolds using dynamic mask projection microstereolithography *J. Mater. Process. Technol.* **209** 5494-5503
- [36] Choi J W, Park I B, Ha Y M, Jung M G, Lee S D and Lee S H 2007 Insertion force estimation of various microneedle array-type structures fabricated by a microstereolithography apparatus *SICE-ICASE, 2006 International Joint Conference 2006*, 3678-3681 (doi: 10.1109/SICE.2006.315024)
- [37] Park, I, Ha, Y, Kim, M, Lee, S 2010 Fabrication of a micro-lens array with a nonlayered method in projection microstereolithography *Int. J. Precision Eng. Manuf.* **11** 483-490

- [38] Park I, Ha Y and Lee S 2010 Cross-section segmentation for improving the shape accuracy of microstructure array in projection microstereolithography *Int. J. Adv. Manuf. Technol.* **46** 151-161
- [39] Lane, EM, Method for transdermal administration of antimicrobial medications US Patent US20080085301A1 2008
- [40] Donnelly R F, Singh T R R, Tunney M M, Morrow D I J, McCarron P A, O'Mahony C O and Woolfson A D 2009 Microneedle arrays allow lower microbial penetration than hypodermic needles in vitro *Pharm. Res.* **26** 2513-2522
- [41] Morrison M L, Buchanan R A, Liaw P K, Berry, C J, Brigmon R L, Riester L, Abernathy H, Jin C and Narayan R J 2006 Electrochemical and antimicrobial properties of diamondlike carbon-metal composite films *Diamond Related Mater.* **15** 138-146
- [42] Gittard S D, Perfect J R, Monteiro-Riviere N A, Wei W, Jin C and Narayan R J 2009 Assessing the antimicrobial activity of zinc oxide thin films using disk diffusion and biofilm reactor *Appl. Surf. Sci.* **255** 5806-5811
- [43] Warrender J M and Aziz M J 2007 Kinetic energy effects on morphology evolution during pulsed laser deposition of metal-on-insulator films *Phys. Rev. B* **75** 085433

- [44] Willmott P R 2004 Deposition of complex multielemental thin films *Prog. Surf. Sci.* **76** 163-217
- [45] Lackner J M, Waldhauser W and Ebner R 2004 Large-area high-rate pulsed laser deposition of smooth $\text{TiC}_x\text{N}_{1-x}$ coatings at room temperature—mechanical and tribological properties *Surf. Coat Technol.* **188-189** 519-524
- [46] Lee S H, Jeong S K and Ahn S K 2006 An update of the defensive barrier function of skin *Yonsei Med. J.* **47** 293-306
- [47] Banga A K 2007 Theme section: Transdermal delivery of proteins *Pharm. Res.* **24** 1357-1359
- [48] Birchall J C 2006 Microneedle array technology: the time is right but is the science ready? *Expert Rev. Med. Dev.* **3** 1-4
- [49] Bragg P D and Rainnie, D J 1974 The effect of silver ions on the respiratory chain of *Escherichia coli* *Can. J. Microbiol.* **20** 883-889
- [50] Rosenkranz H S and Rosenkranz S 1972 Silver sulfadiazine: interaction with isolated deoxyribonucleic acid *Antimicrob. Agents Chemother.* **2** 373-383

- [51] Stoimenov P K, Klinger R L, Marchin G L and Klabunde K J 2002 Metal oxide nanoparticles as bactericidal agents *Langmuir* **18** 6679-6686
- [52] Slawson R M, Van Dyke M I, Lee H and Trevors J T 1992 Germanium and silver resistance, accumulation, and toxicity in microorganisms *Plasmid* **27** 72-79
- [53] Zhao G and Stevens S E 1998 Multiple parameters for the comprehensive evaluation of the susceptibility of *Escherichia coli* to the silver ion *Biometals* **11** 27-32
- [54] Gittard S D, Hojo D, Hyde G K, Scarel G, Narayan R J and Parsons G N 2010 Antifungal textiles formed using silver deposition in supercritical carbon dioxide *J. Mater. Eng. Perform.* **19** 368-373
- [55] Trengove N J, Stacey M C, MacAuley S, Bennett N, Gibson J, Burslem F, Murphy G and Schultz G 1999 Analysis of the acute and chronic wound environments: the role of proteases and their inhibitors *Wound Repair Regen.* **7** 442-452
- [56] Wright J B, Lam K, Buret A G, Olson M E and Burrell R E 2002 Early healing events in a porcine model of contaminated wounds: effects of nanocrystalline silver on matrix metalloproteinases, cell apoptosis, and healing *Wound Repair Regen.* **10** 141-151

- [57] Demling R H and DeSanti M D L 2002 The rate of re-epithelialization across meshed skin grafts is increased with exposure to silver *Burns* **28** 264-266
- [58] Leonardo M R, da Silva L A, Tanomaru Filho M, Bonifacio K C and Ito I Y 2000 In vitro evaluation of antimicrobial activity of sealers and pastes used in endodontics *J. Endod.* **26** 391-394
- [59] Padmavathy, N and Vijayaraghavan, R 2008 Enhanced bioactivity of ZnO nanoparticles- An antimicrobial study *Sci. Technol. Adv. Mater.* **9** 035004
- [60] Hernández-Sierra J F, Ruiz F, Pena D C, Martínez-Gutiérrez F, Martínez A E, Guillén Ade J, Tapia-Pérez H and Castañón G M 2008 The antimicrobial sensitivity of *Streptococcus mutans* to nanoparticles of silver, zinc oxide, and gold *Nanomed.* **4** 237-240
- [61] Fang M, Chen J H, Xu X L, Yang P H and Hildebrand H F 2006 Antibacterial activities of inorganic agents on six bacteria associated with oral infections by two susceptibility tests *Int. J. Antimicrob. Agents* **27** 513-517
- [62] Liao S, Lin H, Hung S and Hu C 2006 dc thermal plasma synthesis and properties of zinc oxide nanorods *Journal of Vacuum Science & Technology B: Microelectronics and Nanometer Structures* **24** 1322-1326

- [63] Sawai J, Igarashi H, Hashimoto A, Kokugan T and Shimizu M 1995 Evaluation of growth inhibitory effect of ceramics powder slurry on bacteria by conductance method *J. Chem. Eng. Japan* **28** 288-293
- [64] Choi S O, Kim Y, Park J W, Hutcheson J, Gill H, Yoon Y K, Prausnitz M, and Allen M 2010 An electrically active microneedle array for electroporation *Biomed. Microdevices* 263-273
- [65] Sun C, Fang N, Wu D M and Zhang X 2005 Projection micro-stereolithography using digital micro-mirror dynamic mask *Sensor Actuat. A* **121** 113-120
- [66] Miwa M, Juodkazis S, Kawakami T, Matsuo S and Misawa H 2001 Femtosecond two-photon stereo-lithography *Appl. Phys. A* **73** 561-566
- [67] Szunyogova E, Mudronova, D, Gyoryova, K, Nemcova, R, Jana Kovářová J and Píknová-Findoráková L 2007 The physicochemical and biological properties of zinc(II) complexes *J. Therm. Anal. Calorim.* **88** 355-361
- [68] Choi J H, Tabata H and Kawai T 2001 Initial preferred growth in zinc oxide thin films on Si and amorphous substrates by a pulsed laser deposition *J. Cryst. Growth* **226** 493-500

[69] Bae S H, Lee S Y, Jin B J and Im S 2000 Pulsed laser deposition of ZnO thin films for applications of light emission *Appl. Surf. Sci.* **154-155** 458-461

[70] Aziz M J 2008 Film growth mechanisms in pulsed laser deposition *Appl. Phys. A* **93** 579-587

3.8 Delivery of Radioactive Isotope Tracer in a Porcine Model via a Microneedle Patch System

Summary

The transdermal patch design consists of five primary components: hollow microneedle array, base, cap, interface pad and inlet component. Refer to Figure 1. An array of hollow microneedles was integrated into the base component. The base component incorporates a means to facilitate the delivery of the agent through the hollow microneedles. One of the innovative features of the base component is the protruding geometry of the base structure. The novel geometry of the base applies tension to the underlying skin at the location of the microneedle penetration, thereby enabling a more uniform penetration of the microneedle array into the skin. In addition, the base geometry serves to focus and sustain the micro-structure insertion force to ensure that penetration is maintained. The cap structure is designed to interface with and affix to the base component, interface with and affix to an inlet component and provide a path for the delivery of the agent from the inlet component to the microneedle array. The inlet component is designed to serve as an interface between the transdermal patch and a portable, adjustable drug delivery pump. The base and cap are inserted into the interface pad, with the protruding geometry of the base, and by relation the hollow microneedle array, extending outward. The interface pad is another innovative feature of the transdermal patch as it functions to reduce relative motion between the base and the underlying skin (maintaining the micro-structure penetration and protecting the micro-

structures from shear forces) and serves as a means to protect the underlying skin from the edges of the relatively ridged patch components (reducing the force concentration on the skin in the event that additional pressure is applied to the patch).

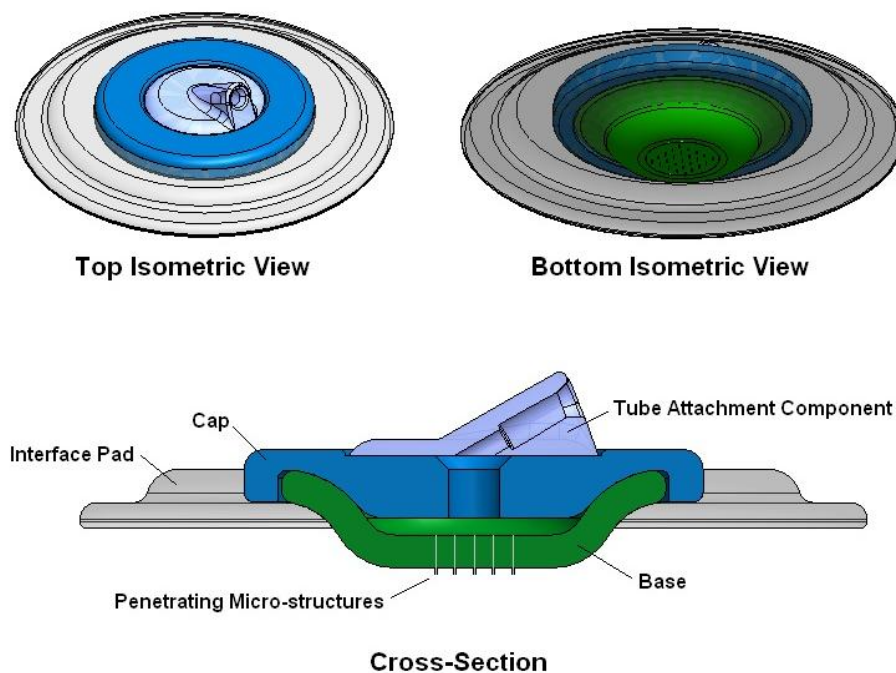


Figure 1. Components of the microneedle patch.

Mechanical evaluations of the e-Shell 200 fabricated microneedle arrays were performed via compression and shear tests. These tests were performed on the needles to assess the deformation and fracture characteristics of the devices. The compression and shear tests were performed using a Bose ElectroForce® 3100. Tests were conducted on single needles fabricated with an Envisiontec Perfactory® Standard UV system.

For the compression testing, the goal was to determine whether the needles deformed or fractured, the associated forces for these events, and how the different needle designs behaved. During the testing, substrates with single needles were placed onto the compression platens, with the needle oriented perpendicular to the platens. Each needle was preloaded with 0.5 N of force to ensure that each tested needle was in contact with the platen prior to the test run. The needle was compressed using a ramp function in displacement control at 0.05 mm/sec to half of the needle length or until the force limit (15 N) was reached. Force data were recorded with respect to time. Furthermore, video of the compression tests was captured using a CCD camera to visualize needle behavior during testing. Needle fracture and deformation was confirmed visually and corresponded to a deviation in force on the output plot from the Electroforce® system.

An *in vivo* study was performed to evaluate the functional aspects of the microneedle patch system in actual physiological conditions. The objectives of the animal study with Gottingen miniswine (pig) were to assess the microneedle patch's ability to deliver a traceable drug proxy through the skin and into the blood stream and to determine how the microneedle patch interacts with live skin. [3H]3-O-Methyl-D-glucose ([3H]OMG) was selected as the traceable drug proxy, based on Ceramatec's previous experience with using the radioactive isotope tracer (tracer) and the detection method.

In order to determine the delivery characteristics *in vivo*, the pharmacokinetic parameters for the miniswine needed to be established. Two pharmacokinetic studies were performed where a bolus volume of tracer was delivered to each of the pigs in a subcutaneous injection. Blood samples were then drawn in accordance with Table 1 and analyzed to determine the elimination rate and effective volume of distribution for the respective pigs. Three pigs were used in the *in vivo* study to provide the minimum number of test animals to achieve an orthogonal experimental design balance. However, due to illness, one of the pigs needed to be replaced and the replacement was not available for the pharmacokinetic study.



Figure 2. Optical micrograph of a single microneedle from array 1.



Figure 3. Optical micrograph of a single microneedle from array 2.

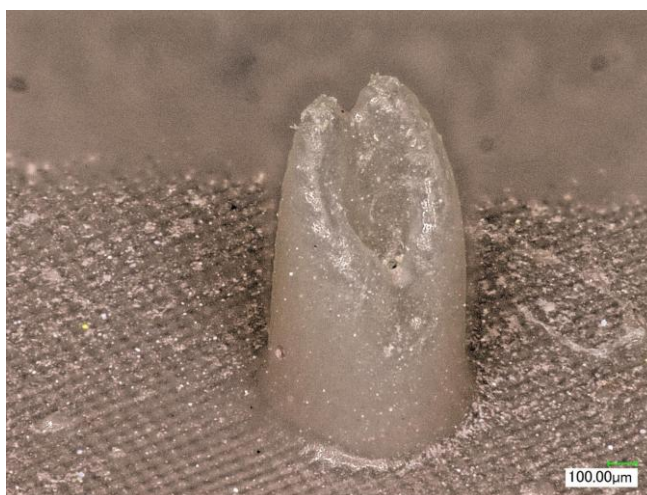


Figure 4. Optical micrograph of a single microneedle from array 3.

Microneedle Devices

Figure 2, Figure 3, and Figure 4 contain optical micrographs of a single microneedle from array 1, array 2, and array 3, respectively. Figure 5, Figure 6, and Figure 7 show scanning electron micrographs of microneedles from array 1, array 2, and array 3, respectively. The needle heights for Array types 1-3 were acquired using SEM images and the measurement

tool within Revolution™ imaging software (4pi, Durham, NC). Array type 1 has a measured needle height of approximately 1342 μm . Array type 2 has a measured needle height of approximately 1398 μm . Array type 3 has a measured needle height of approximately 1138 μm . Height measurements were taken from the base of the needle to the tallest peak on the needle prongs. The inter-needle spacing for the Array types 1 and 3 were determined using optical micrographs acquired using a Leica EZ4 D stereo-microscope (Leica Microsystems, Switzerland), with scale bars applied using LAS EZ software (Leica Microsystems, Switzerland). Array types 1 and 2 have 5 needles in a 5-dice pattern, with four needles composing the corners of a 6 mm x 6 mm square, and a single needle at the center of the square. The needle array configuration for Array type 3 has nine needles, equally spaced in three rows and three columns to form a 6 mm x 6 mm square pattern.

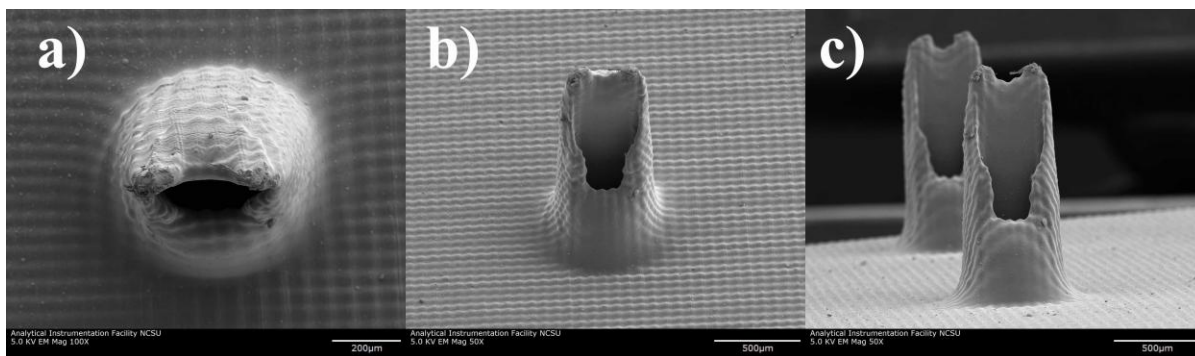


Figure 5. Scanning electron micrographs of microneedles from array 1. (a) Image of a single microneedle obtained at 0° tilt. (b) Image of a single microneedle obtained at 45° tilt. (c) Image of microneedles obtained at 90° tilt.

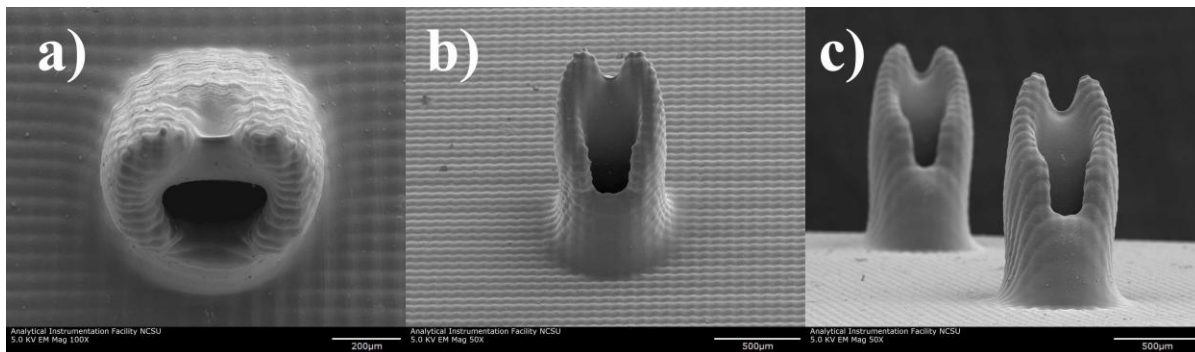


Figure 6. Scanning electron micrographs of microneedles from array 2. (a) Image of a single microneedle obtained at 0° tilt. (b) Image of a single microneedle obtained at 45° tilt. (c) Image of microneedles obtained at 90° tilt.

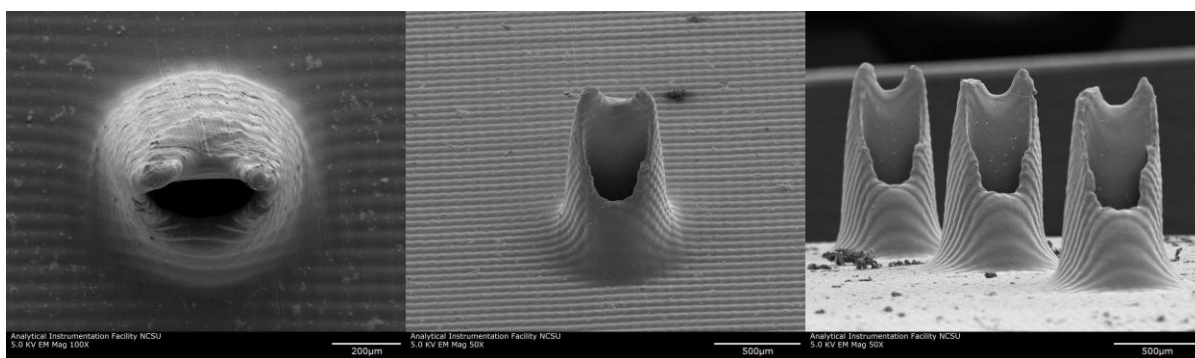


Figure 7. Scanning electron micrographs of microneedles from array 3. (a) Image of a single microneedle obtained at 0° tilt. (b) Image of a single microneedle obtained at 45° tilt. (c) Image of microneedles obtained at 90° tilt.

The center-to-center inter-needle spacing for Array type 1 from the needles at the corners of the 5-dice pattern diagonally to the needle at the center of the 5-dice pattern is ~ 4.24 mm. The center-to-center inter-needle spacing for Array type 2 from the needles at the corners of the 5-dice pattern diagonally to the needle at the center of the 5-dice pattern is ~ 3.24 mm.

The center-to-center inter-needle spacing for Array type 3 in the x- and y-directions is ~2.89 mm.

Microneedle Mechanical Properties

For the compression testing, fracture force averages and standard deviations are reported for needles that fractured. For the purpose of these tests, fractures are defined as having occurred when a component of the needle breaks away from the rest of the structure. The other phenomena observed were bending and splitting of the prongs of the needles. These occurrences are being termed deformations to the needles. For needles that only deformed without fracture, the maximum force of 15 N compression was applied (exception being one run for a needle from Array 1, which had deformation resulting in a maximum applied force of 9.60 N before the maximum displacement for the test was reached).

None of the Array 1 test samples fractured. Two of the samples withstood a force of 15 N before the end of the test. However, the third needle from Array 1 deformed in a manner which imparted 9.6 N of force on the needle before the maximum displacement was reached for the test. All 3 of the Array 2 needles fractured. These needles fractured at an average force of 9.45 ± 2.55 N. Only one of three tested needles fractured for Array 3. This needle fractured at a force of 7.356 N. The other Array 3 needles only deformed and had a maximum load of 15 N applied without fracture.

Observations during the compression testing did not indicate movement or deformation in the substrate. No fracture between the needle and the substrate was observed. There was a tendency for the needles to either split at the prongs or fracture at the tips, rather than break away from the substrates.

For the shear testing, again the goal was to determine whether the needles deformed or fractured, the associated forces for these events, and how the different needle designs behaved. During the testing, substrates with single needles were clamped into the Electroforce® system and shear force was applied to the needle with a metallic bracket oriented parallel to the substrate surface. Each needle was preloaded with 0.5 N of force to ensure that each tested needle was in contact with the shearing apparatus prior to the test run. The needle was then subjected to shear force at 90° using a ramp function in displacement control at 0.05 mm/sec for a displacement distance greater than the needle diameter. Force data were recorded with respect to time. Furthermore, video of the shear testing was captured using a CCD camera to visualize needle behavior during testing. Needle fracture and deformation was confirmed visually and corresponded to a deviation in force on the force output plot from the Electroforce® system.

For the shear testing, fracture forces are reported for needles that fractured. All needles that were tested were fractured during the shear testing. Array 1 had an average fracture force of 4.155 ± 1.165 N. Array 2 had an average fracture force of 7.601 ± 1.421 N. Array 3 had an average fracture force of 6.412 ± 1.224 N.

For needles from Array types 2 and 3, needles were sheared from the substrate. For needle Array 1, the needles fractured on the needle shaft as opposed to breaking away from the substrate. This result may have occurred from the shear apparatus having been shifted slightly toward the needle tip, resulting in force being applied less uniformly, and consequently resulting in a different fracture mechanism and lower fracture values than needle types 2 and 3. Observations during the shear testing did not indicate movement or deformation in the needle substrate.

Radiotracer Pharmacokinetics

The results from the first pharmacokinetic study (PK1) are shown in Figure 8. A preliminary analysis of the results indicated that the tracer was rapidly eliminated to a level that was within the background of the detection method.

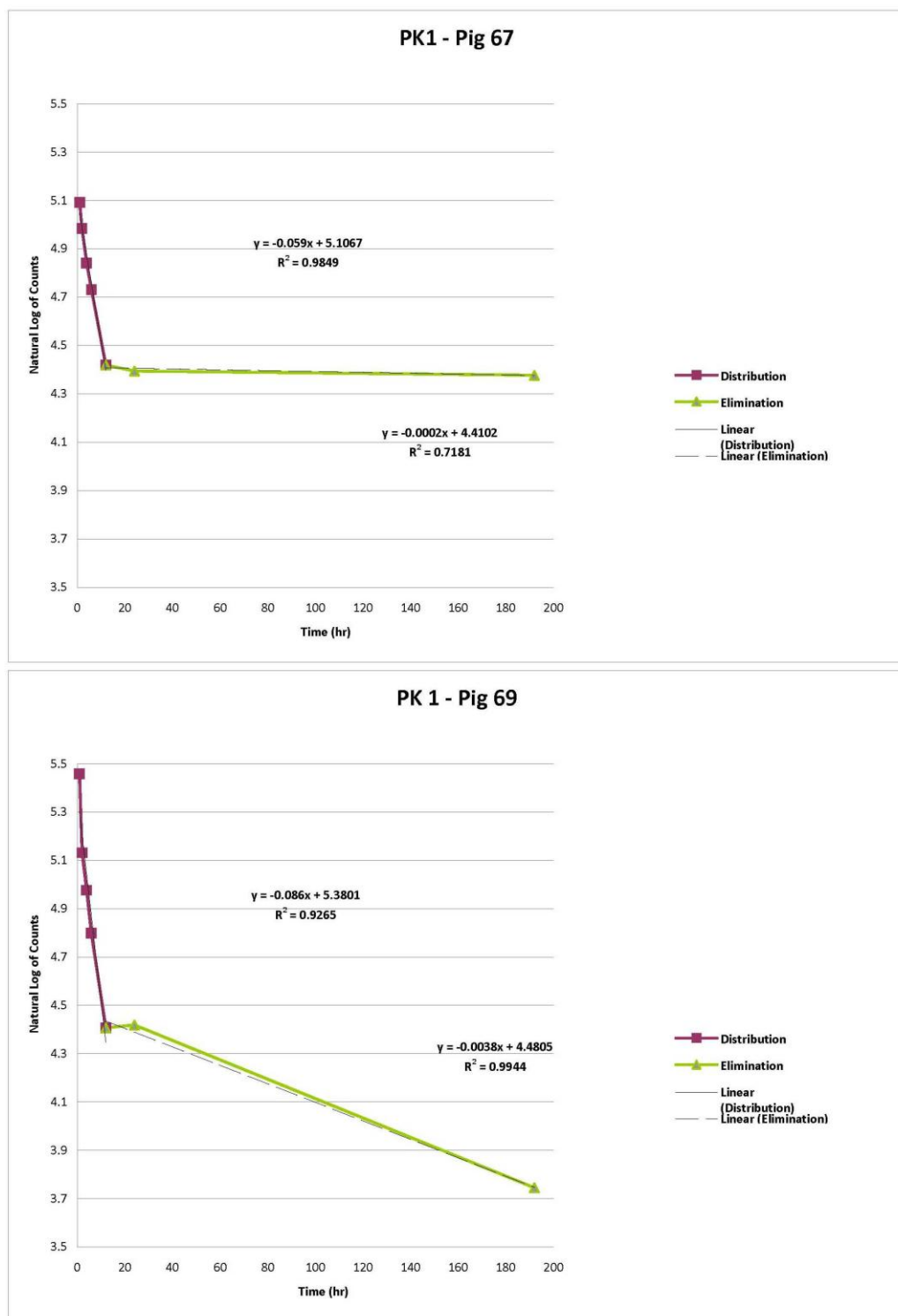


Figure 8. Pharmacokinetic test #1 results.

The volume of tracer was increased for the second pharmacokinetic study (PK2). The tracer was delivered to each of the pigs in a subcutaneous injection and blood samples were drawn in accordance with Table 1. The results from the PK2 are shown in Figure 9.

Table 1. Day/time associated with time points for pharmacokinetic studies.

PK #1							PK #2						
Mon.	Tues.	Wed.	Thur.	Fri.	Sat.	Sun.	Mon.	Tues.	Wed.	Thur.	Fri.	Sat.	Sun.
0 hr	24 hr	48 hr	72 hr	96 hr	120 hr	144 hr	0 hr	24 hr	48 hr	72 hr	96 hr	120 hr	144 hr
0.5 hr							0.5 hr						
1 hr							1 hr						
2 hr							2 hr						
4 hr							4 hr						
6 hr	36 hr						6 hr	36 hr					
9 hr							9 hr						
12 hr							12 hr						
18 hr							18 hr						

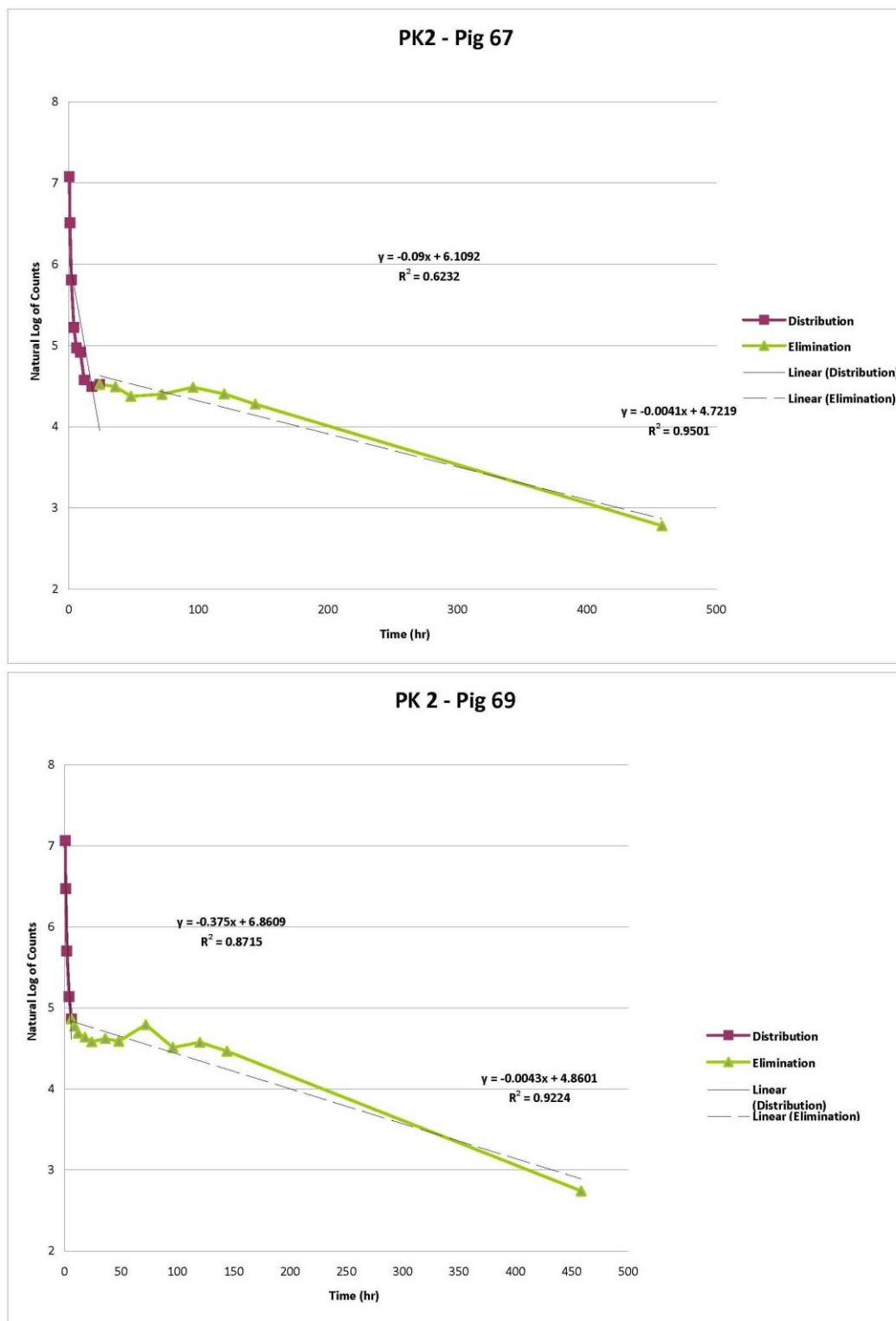


Figure 9. Pharmacokinetic test #2 results.

An analysis of the PK results was performed to determine the elimination rate and effective volume of distribution for the respective pigs. The results are shown in Table 2.

Table 2. Summary of pharmacokinetics analysis.

PK Summary	Pig 67		Pig 69	
	PK #1	PK #2	PK #1	PK #2
ke (Distribution)	0.0590	0.1880	0.0860	0.3750
ke (Elimination)	0.0002	0.0039	0.003	0.0043
Volume of Distribution (L)	31.4	59.8	25.4	43.0

PK Averages	Pig 67	Pig 69
A	501	586
ke (Distribution)	0.1235	0.2305
B	95	109
ke (Elimination)	0.0021	0.0041
Volume of Distribution (L)	46	34

Pig Weight (kg)	32.8	28.2
Volume of Distribution / Weight (L/kg)	1.4	1.2

In vivo Drug Delivery via Microneedle Patch

The microneedle patch system was then tested *in vivo* to determine the delivery capabilities and evaluate the interaction with live skin. Microneedle patch prototypes were produced with three different microneedle arrays. The microneedle delivery tests were performed in accordance with Table 3; where three pigs were tested, such that each pig had all three arrays and each array had all three locations. Each test consisted of two phases: a 7 day delivery

phase and a 6 day non-delivery phase. During the delivery phase, the microneedle patch was placed on the ventral side of the pig in the locations shown in Figure 10. Each microneedle patch was secured in place using a semi-occlusive adhesive film with a low moisture vapor transmission rate, as shown in Figure 11. The microneedle patch and adhesive film was then covered with a jacket and elastic bellyband to further protect the test site and allow for the attachment of the portable pump.

Table 3. Microneedle delivery test matrix.

	Pig 67		
Test	1	2	3
Microneedle Array	1	2	3
Site	1	2	3

	Pig 69		
Test	1	2	3
Microneedle Array	2	3	1
Site	3	1	2

	Pig 86		
Test	1	2	3
Microneedle Array	3	1	2
Site	2	3	1

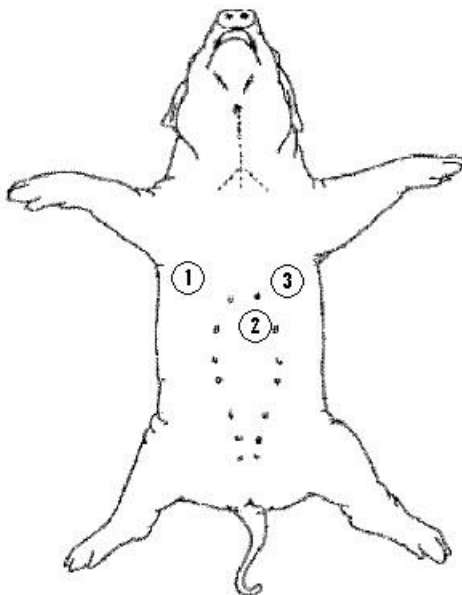


Figure 10. Microneedle patch test sites.



Figure 11. Microneedle patch application.

The microneedle patch was connected to a portable, adjustable drug delivery pump. The pump was set to deliver the tracer solution through the microneedle patch at a rate of 0.34 ml/day. The tracer solution was delivered for seven days. Blood was drawn at specific time-points and analyzed to detect the presence of the tracer in the pig's blood stream.



Figure 12. Image of test site during the removal of the microneedle patch.

After the 7th day of the delivery phase, the microneedle patch was removed, thus ceasing the flow of tracer to the skin site. The pictures in Figure 12 were taken when the patch was removed at the end of the Test #1 delivery phase. Observations confirm the penetration of the skin by the microneedle array. The slight depression in the skin surrounding the penetration site was caused by the protruding geometry of the base, which focused and sustained the micro-structure insertion force to ensure that the microneedle penetration was maintained. In addition, only one set of marks was present for each patch, further indicating that the microneedles did not disengage and re-penetrate. The microneedle arrays were inspected and all microneedles appeared undamaged and intact. No signs of skin irritation were noted, as the interface pad protected the underlying skin from the edges of the ridged patch components. The adhesive film remained adhered to skin and firmly secured patch in place for duration of the delivery phase. In addition, no pooling or leaking was noted during the study, indicating that the solution was delivered into and absorbed by the skin.

Blood samples were drawn at specific time-points during each 7 day delivery phase and 6 day non-delivery phase. The blood samples were spun down in a centrifuge and the plasma

was removed from the red blood cells. 0.25 ml of plasma was then placed in a scintillation vial and mixed with 0.34 ml of ethyl alcohol to reduce the possibility of error resulting from variations in sample color. 3.4 ml of scintillation solution was then added to the vial and the samples were held for a 4 hour minimum stabilization period. This hold period allowed the samples to stabilize and helped to ensure that the samples had a consistent opaqueness prior to beginning the analysis. Three analysis samples were prepared from each blood draw. The samples were then analyzed on a liquid scintillation analyzer and the counts were recorded. The counts were plotted with respect to time, as shown in Figures 13, 14 and 15.

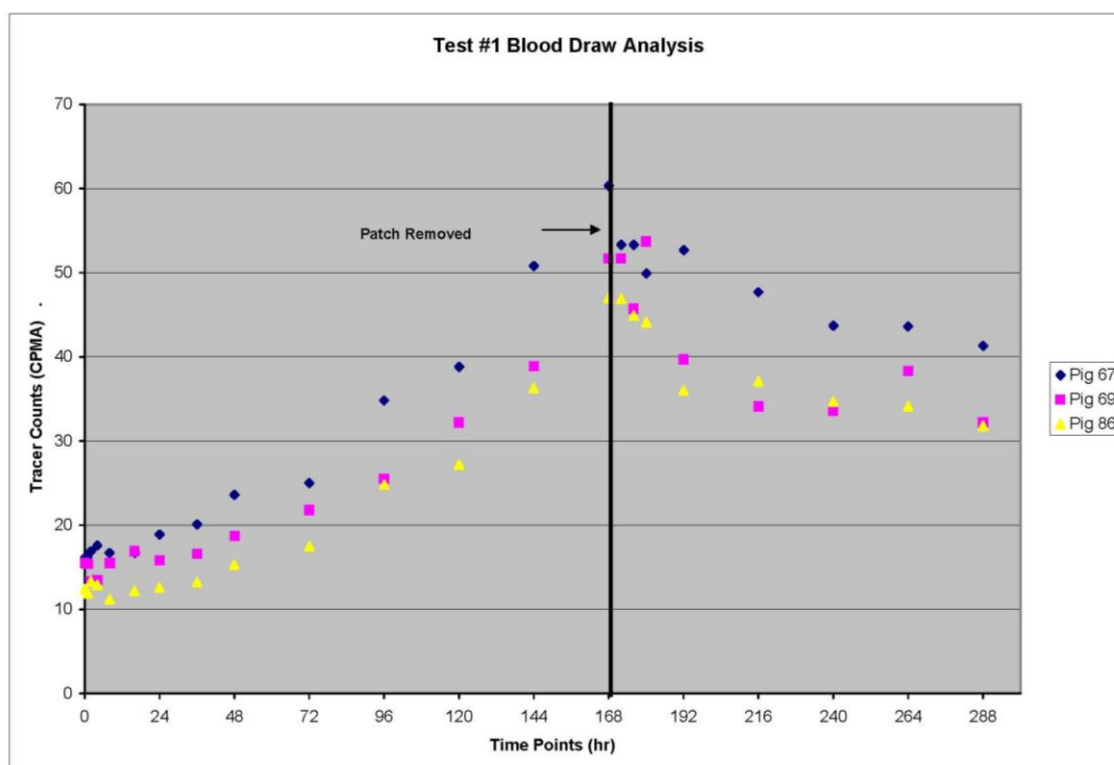


Figure 13. Test #1 counts with respect to time.

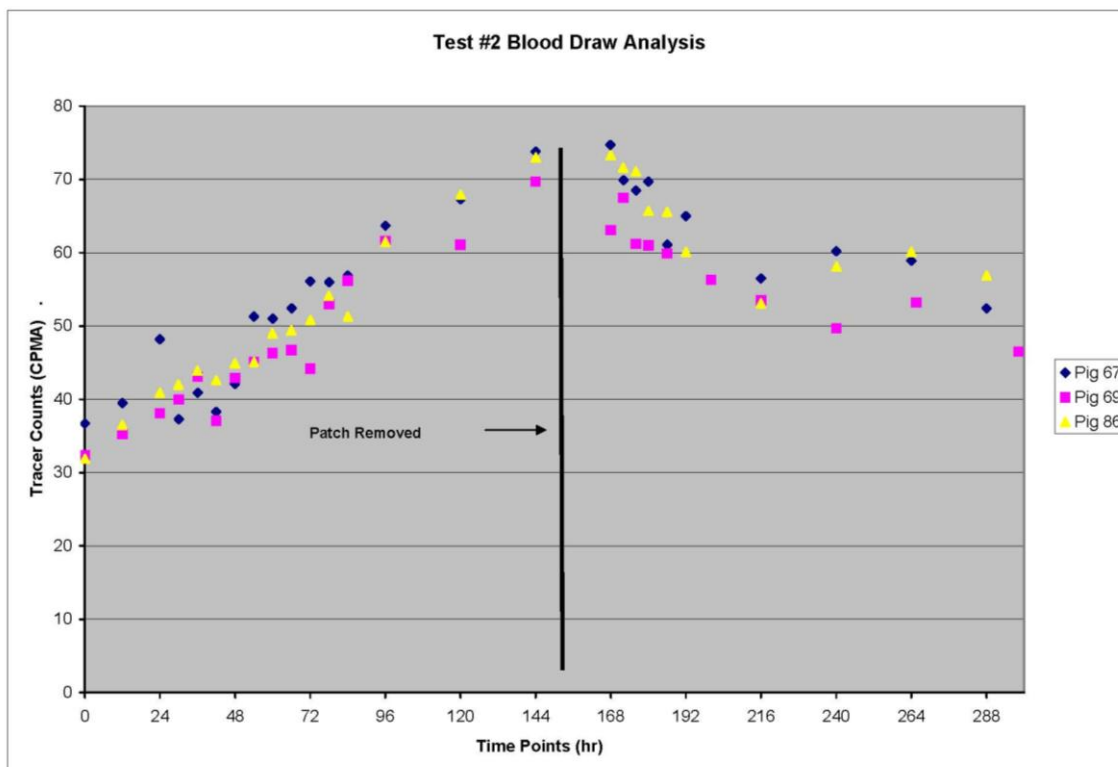


Figure 14. Test #2 counts with respect to time.

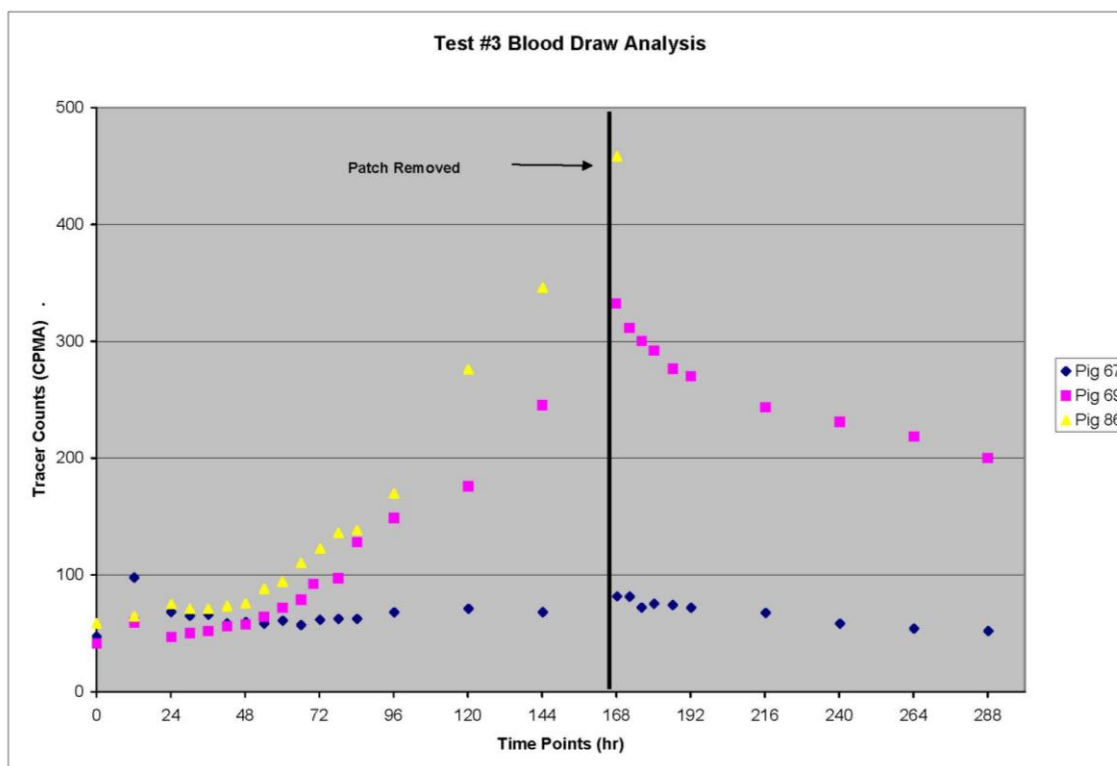


Figure 15. Test #3 counts with respect to time.

It should be noted that several complications were experienced during Test #3. The first complication was associated with Pig 67. The tubing that connected the microneedle patch to the pump was severed. It is assumed that the incident occurred within the first 12 hours. Pig 69 removed its front legs from the jacket and pushed the belly band and jacket down off of the patch. This incident occurred just prior to the 120th hour of the test. The patch appeared to remain secured to the animal, so the jacket and belly band were resituated and the test was continued. The third complication was associated with Pig 86. Pig 86 became

ill and experienced an extreme decrease in appetite and did not readily drink fluids. Pig 86 was removed from the study following day 7 of the delivery phase.

The data in Figures 13, 14, and 15 confirms that the microneedle patch is capable of delivering a solution into the skin, such that it can be readily absorbed into the bloodstream. The graphs also show that the removal of the microneedle patch resulted in a decrease in the level of tracer in the bloodstream.

The data from Pig 67 and Pig 69 was analyzed with respect to the elimination rate and the effective volume of distribution, as determined during the PK studies. Pig 86 was not included in the analysis, since the animal was not available for the PK study. The results for Test #3 were not analyzed as a result of the complications associated with the test. The expected maximum of tracer counts for each test and the expected steady state maximum of tracer counts were calculated using the elimination rate, effective volume, radioactive level of the delivered solution and the set rate of the delivery. Graphs are shown in Figure 16 for Pig 67 and Figure 17 for Pig 69.

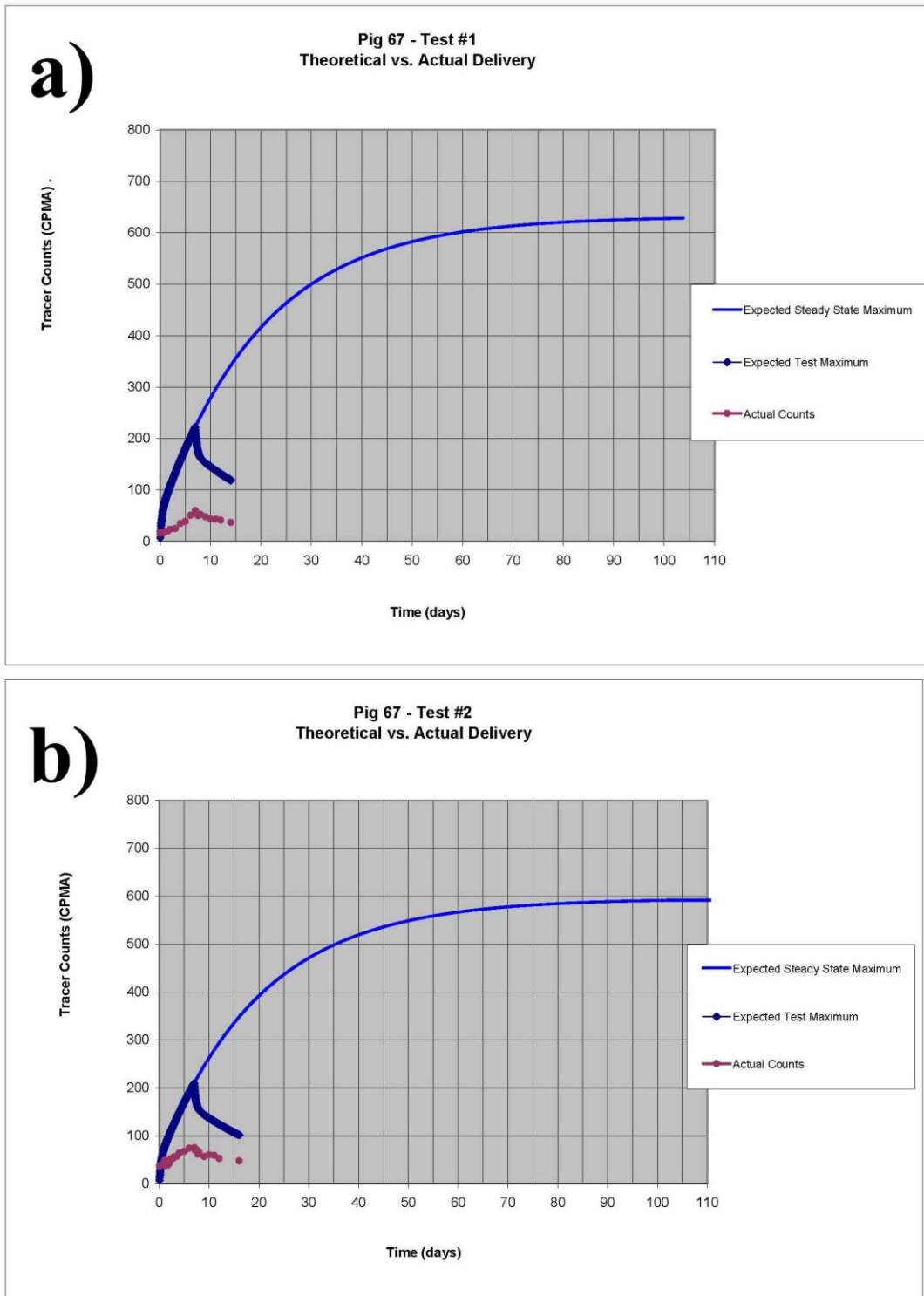


Figure 16. Expected vs. actual counts for pig 67.

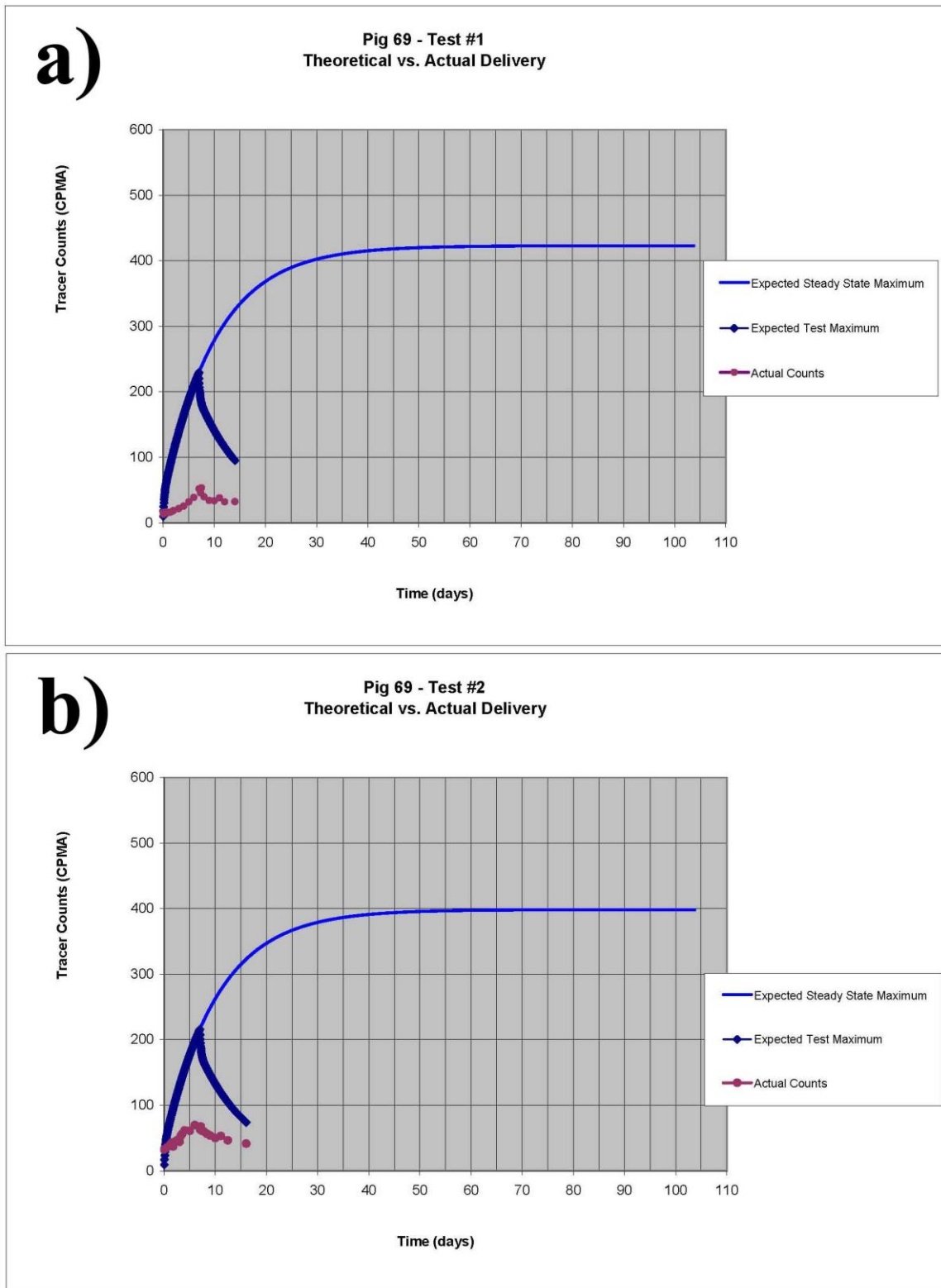


Figure 17. Expected vs. actual counts for pig 69.

As shown in Figure 16 and 17, the test duration was insufficient for achieving a steady state plateau in the delivery phase, as observed by comparing the Expected Test Maximum curve with the Expected Steady State Maximum curve. A comparison of the Actual Counts to the Expected Steady State Maximum curve and the Expected Test Maximum curve, as shown in Figure 16 and 17, illustrated that only a portion of the tracer was delivered into the blood stream. Table 4 summarizes the delivery results and presents the percentage of the expected delivery that actually occurred. The differences in pharmacokinetics between microneedle patch and subcutaneous delivery may be due to the increased diffusion distance through tissue required for the drug delivered with microneedles to reach the bloodstream.

Table 4. Delivery results.

	Pig #67		Pig #69	
	Test 1	Test 2	Test 1	Test 2
Concentration (Counts / ml)	95.5M	90.0M	95.5M	90.0M
Delivery Rate (ml/day)	0.34	0.34	0.34	0.34
Steady State Expected Max (CMPA)	628	592	423	398
Time to 99% of Max (Days)	82.8	82.7	46.3	46.5
% of Steady State Max Delivered	9.6%	12.6%	12.2%	15.8%
Time-point 168 Expected Max (CMPA)	216	203	220	207
% of Time-point 168 Expected Max	28.0%	36.8%	23.5%	30.4%

Conclusions

A pharmacokinetic study was performed in which the elimination rate and effective volume of distribution was determined for Pig 67 and Pig 69. The pharmacokinetic parameters were

then used to determine the expected maximum for the delivery and non-delivery phases of the *in vivo* study.

A microneedle patch system was designed and produced. The functional aspects of the microneedle patch system were evaluated in an *in vivo* study. The *in vivo* study confirmed that the skin was penetrated by the microneedle array and that the microneedle patch was capable of sustaining the micro-structure insertion force, thereby ensuring that the microneedle penetration was maintained throughout the duration of use. The microneedle patch system was proven capable of delivering a traceable drug proxy through the skin and into the blood stream. In addition, the level of radioactive isotope tracer detected in the bloodstream decreased following the removal of the microneedle patch. At the end of the *in vivo* delivery phase, the microneedle patch delivered an average of 29.7% of the radioactive isotope tracer, as compared to the expected maximum.

The microneedle patch proved to be a minimally invasive means to continually deliver a solution over a prolonged period of time, as no adverse events or signs of skin irritation were noted and the radioactive isotope tracer was detected in the blood stream.

Acknowledgments

Jeremy Heiser, John Gordon, Curtis Jensen, Philip R Miller, Ryan D Boehm, and Roger J Narayan contributed to this work.

3.9 Multiphoton microscopy of transdermal quantum dot delivery using two photon polymerization-fabricated polymer microneedles

*The following section a complete article reprinted from **Faraday Discussions**, Volume 149, Gittard SD, Miller PR, Boehm RD, Ovsianikov A, Chichkov BN, Heiser J, Gordon J, Monteiro-Riviere NA, Narayan RJ.171-185, Multiphoton microscopy of transdermal quantum dot delivery using two photon polymerization-fabricated polymer microneedles. Copyright 2010. Reproduced by permission of The Royal Society of Chemistry DOI: **10.1039/c005374k***

Note: This article has been reformatted. In particular, the location of figures and spacing may have changed. The references are formatted as in the original manuscript.

Multiphoton microscopy of transdermal quantum dot delivery using two photon polymerization-fabricated polymer microneedles

Shaun D. Gittard,^a Philip R. Miller,^a Ryan D. Boehm,^a Aleksandr Ovsianikov,^b Boris N. Chichkov,^b Jeremy Heiser,^{cd} John Gordon,^{cd} Nancy A. Monteiro-Riviere^{ae} and Roger J. Narayan^{*a}

Received 18th May 2010, Accepted 22nd June 2010

DOI: 10.1039/c005374k

Due to their ability to serve as fluorophores and drug delivery vehicles, quantum dots are a powerful tool for theranostics-based clinical applications. In this study, microneedle devices for transdermal drug delivery were fabricated by means of two-photon polymerization of an acrylate-based polymer. We examined proliferation of cells on this polymer using neonatal human epidermal keratinocytes and human dermal fibroblasts. The microneedle device was used to inject quantum dots into porcine skin; imaging of the quantum dots was performed using multiphoton microscopy.

^aJoint Department of Biomedical Engineering, University of North Carolina State University, Campus Box 7115, Raleigh, NC, 27695-7115, USA. E-mail: roger_narayan@ncsu.edu; Fax: +1 509 696 8481

^bDepartment of Nanotechnology, Laser Zentrum Hannover, Hollerithalle 8, 30419 Hannover, Germany

^cCeramatec Inc., 2425 South 900 West, Salt Lake City, UT, 84119, USA

^dMicroLin LLC & Technology Holding LLC, 350 West 800 North, Suite 250, Salt Lake City, UT, 84103, USA

^eCenter for Chemical Toxicology Research & Pharmacokinetics, North Carolina State University, Raleigh, NC, 27606, USA

This journal is © The Royal Society of Chemistry 2010 Faraday Discuss.

Introduction

Theranostics, the combination of therapeutic and diagnostic technologies into a single platform, is a rapidly developing technology for treating a variety of medical conditions. For example, theranostics technologies may provide disease imaging and chemotherapy delivery for treatment of cancer, a group of conditions in which cells exhibit uncontrolled growth and invasion.¹⁻⁵ Other applications of theranostics that are being investigated include use in diabetes, ocular disease, obesity, cardiovascular diseases, and infectious diseases.^{1,3,6}

Quantum dots (QD) are 2–10 nm diameter fluorescent semiconductor nanostructured materials that are being considered for use in several theranostics applications. Due to the fact that the exciton Bohr radius (average electron-hole distance) is larger than the

nanoparticle radius, these materials undergo quantum confinement. As a result, quantum dots demonstrate characteristic excitation states as well as larger bandgap values than bulk material. In addition, emission wavelength in these materials is size dependent; bandgap values for quantum dots increase as the nanoparticle radius decreases.⁷⁻¹⁰ Core-shell quantum dots are composed of a core material with a smaller bandgap than the surrounding shell material; zinc sulfide shells surrounding cadmium telluride cores, zinc sulfide shells surrounding cadmium selenide cores, and cadmium sulfide shells surrounding cadmium selenide cores are some examples of this type of quantum dots.^{7,11-13}

Quantum dots exhibit unique photoluminescence behavior; some advantages of quantum dots over conventional fluorophores include greater resistance to light-dependent oxidation (photobleaching) and higher brightness, which is attributed to high quantum yield values and large molar extinction coefficient values.¹⁴ Passive mechanisms (e.g., preferential retention of quantum dots within tumor cells) may be utilized. Quantum dots may also be conjugated with peptides, antibodies, aptamers, pharmacologic agents, and other tumor-specific molecules that allow for specific tumor-cell interactions.¹⁵⁻²⁰ For example, Derfus *et al.* conjugated tumor-homing peptides and small interfering RNA molecules to PEGylated quantum dots. They demonstrated that the F3 tumor-homing peptide enabled tumor cell internalization.¹⁶ When F3 tumor-homing peptide/small interfering RNA-quantum dots were delivered to enhanced green fluorescent protein-transfected HeLa cells, knockdown of the enhanced green fluorescent protein signal was observed. Bagalkot *et al.* demonstrated processing of conjugates containing A10 aptamer (an RNA molecule that recognizes the

extracellular domain of prostate-specific membrane antigen), doxorubicin (an anthracycline antineoplastic agent), and fluorescent quantum dots; in vitro studies demonstrated that these multifunctional nanoparticles may be used for simultaneous targeted imaging, therapy, and sensing of prostate cancer cells.¹⁹ Tada *et al.* conjugated trastuzumab to quantum dots coated with polyethylene glycol amine; these structures were subsequently labeled with monoclonal anti-HER2 antibody. The antibody-conjugated therapeutic nanoparticles were successfully demonstrated using a dorsal skinfold chamber in a murine model.¹⁵ Cai *et al.* conjugated a thiolated arginine-glycine-aspartic acid (RGD) peptide with polyethylene glycol-coated quantum dots; these structures were successfully utilized for in vivo tumor imaging in a murine model.²⁰

It should be noted that quantum dots and other nanoscale pharmacologic agents cannot be administered in enteral form since they may be sequestered within the intestine, kidneys, liver, or lungs prior to entering systemic circulation.^{21,22} Intravenous delivery is the most common mechanism for quantum dot administration at this time because it enables instantaneous delivery of the quantum dots into the bloodstream. However, use of hypodermic needles is associated with several shortcomings, including injection site trauma, patient pain, and difficulty in providing sustained administration over an extended period of time. One option for quantum dot delivery involves the use of microneedles, which are needle-, lancet-, or thorn-shaped structures in which one dimension is less than 500 μm . These devices penetrate the stratum corneum layer of the epidermis; this 15 μm layer contains keratinized dead cells and serves as a barrier against transdermal movement of

pharmacologic agents through the skin. Quantum dots may subsequently enter dermal blood vessels by passing through the lower part of the epidermis. Hollow microneedles enable pressure-driven or diffusion-driven delivery of quantum dots through the skin to be modulated over an extended period of time. In addition, microneedles may be used both for delivery of quantum dots as well as for withdrawal of blood and/or interstitial fluid. Microneedle devices commonly contain several microneedles; use of microneedle arrays is associated with injection at higher rates as well as injection over wider areas than use of solitary microneedles.²³ Furthermore, redundant microneedles within the microneedle arrays may be utilized if some of the microneedles within the array are obstructed or damaged during use. Use of microneedles is associated with minimal tissue compression, nerve ending interaction, pain sensation, injection site trauma, and injection site inflammation.²⁴⁻²⁷

Recent studies have demonstrated delivery of nanomaterials by means of microneedles. For example, Coulman *et al.* used microneedles prepared by means of wet-etch techniques for delivery of fluorescent nanospheres across human epidermal membranes.²⁸ McAllister *et al.* demonstrated that pores in the stratum corneum layer of human cadaver abdomen or back skin created by a solid microneedle array enabled transport of polystyrene latex nanoparticles.²⁹ Bal *et al.* recently utilized laser scanning microscopy to visualize movement of sodium fluorescein dye through conduits in human skin, which were created by 300 μm long DermaStamp[®] microneedles.³⁰ They proposed that laser scanning microscopy may be used to observe the dimensions of microneedle-fabricated conduits in viable human skin over time.

Microneedles with various geometries as well as microneedle arrays may be fabricated using a laser-based rapid prototyping process known as two photon polymerization.³¹⁻³⁷ Two-photon polymerization involves temporal and spatial overlap of photons, which enables highly localized polymerization of a photosensitive resin. Nearly simultaneous absorption of two photons creates a so-called virtual state; this electronic excitation is analogous to excitation by a single photon with a higher energy. A diagram of the two-photon polymerization process is provided in Fig. 1a. The minimum feature size obtained using two-photon polymerization is can be altered by changing the optics (e.g., the objective used to focus the laser beam). Two-photon polymerization provides several advantages over conventional microelectronics- based techniques for fabrication of microneedles and other small-scale medical devices. The photosensitive materials used in two photon polymerization are widely available and are obtained at low cost. In contrast with cleanroom-based microfabrication techniques, photon polymerization can be performed in conventional environments. As opposed to conventional multiple-step microfabrication methods, two-photon polymerization can create microneedles and other complex small-scale structures in a single-step process. Two-photon polymerization has been used to fabricate a variety of small-scale medical devices, including scaffolds for regenerative medicine, ossicular replacement prostheses, and microneedles.³¹⁻³⁸ For example, Doraiswamy *et al.* showed that organically-modified ceramic (Ormocer[®]) microneedles did not exhibit fracture during compression load testing with porcine skin.³¹ Ovsianikov *et al.* fabricated off-center microneedles using two photon polymerization; these off-center microneedles were created by altering the position of

the bore relative to the central axis.³² The off-center microneedle arrays successfully penetrated porcine adipose tissue; no fracture was observed. Doraiswamy *et al.* recently demonstrated delivery of a quantum dot solution using microneedles fabricated using two photon polymerization in a porcine skin model.²⁵ In this study, Ormocer[®] microneedles were produced on perforated glass substrates by two photon polymerization. Quantum dot dispersion was observed by sectioning, differential interference contrast (Nomarski) microscopy, and widefield fluorescence microscopy over a period of one hour. The two photon polymerization-fabricated organically-modified ceramic microneedles enabled more rapid distribution of polyethylene glycol-amine quantum dot solution to the deep epidermis and the dermis of porcine skin than topical administration.

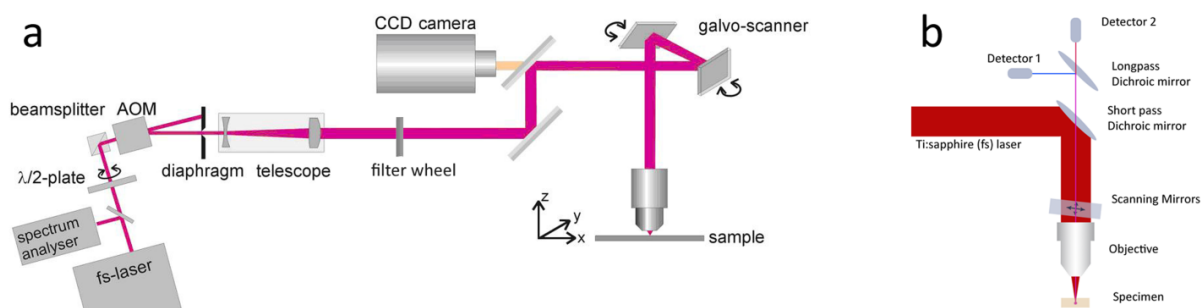


Fig. 1 (a) Schematic of the two-photon polymerization system. Femtosecond laser pulses pass through a beam expander and a filter wheel before being focused on the objective. Scanning mirrors control the location of the laser spot in the focal plane. Polymerization of the resin occurs at the focal point. A charge-coupled device camera behind a dichroic mirror is used for visualizing the two photon polymerization process. (b) Schematic of multiphoton microscopy system. Femtosecond laser pulses pass through the objective before being focused on the specimen, where excitation occurs at the focal point. Scanning mirrors control the location of the laser spot in the focal plane. Dichroic mirrors are used to separate excitation and emission light and to separate emitted light into two channels.

Multi-photon fluorescence microscopy is a microscopy technique that may be used for imaging quantum dots as well as other fluorophores.³⁹ Multi-photon fluorescence microscopy involves nearly simultaneous absorption of two long-wavelength photons from a femtosecond laser by a fluorophore; unlike traditional fluorescence microscopy, the excitation wavelength is longer than the emission wavelength. A diagram of the multi-photon microscopy technique is provided in Fig. 1b. This technique enables imaging with depth resolutions of 800 μm , three-dimensional data acquisition from differentially labelled fluorescent structures, as well as imaging of living structures for extended periods of time at

high spatial resolutions. For example, Wang *et al.* used multi-photon confocal microscopy to observe microscopic holes created by a microneedles in skin biopsy samples.⁴⁰ Kim *et al.* used multiphoton microscopy to observe surfactant (N-lauroyl sarcosine)-mediated enhancement of fluorescein penetration into human cadaver skin.⁴¹ Choi *et al.* observed delivery of calcein into DU145 human prostate cancer cells by means of a microneedle array with electroporation functionality.⁴² The non-invasive nature, absence of significant phototoxicity, and tissue penetration depth provided by multi-photon microscopy make it an appealing tool for theranostics applications. For example, Maffia *et al.* have used multiphoton microscopy to examine immune cell behavior in an artery disease model.⁴³ In their study, multiphoton microscopy was used to image fluorescently tagged lymphocyte migration within the adventitia of intact carotid arteries in apolipoprotein-E-deficient mice. Stroh *et al.* used quantum dots to label bone marrow-derived precursor cells; multiphoton intravital microscopy was used to observe movement of bone marrow-derived precursor cells to tumor vessels.⁴⁴

Quantum dots are appealing fluorophores for use in conjunction with multiphoton microscopy in theranostic applications. According to Larson *et al.*, quantum dots exhibit multi-photon excitation cross-sections of up to 47 000 Goeppert-Mayer units.⁴⁵ They examined cadmium selenide–zinc sulfide quantum dots, which were located inside capillaries hundreds of micrometres deep within the skin of living mice; no fluorescence intermittency (“blinking”) over nanosecond–millisecond time scales was observed. Lee *et al.* examined infusion of COOH-coated QD and QD-PEG in isolated perfused skin by means of

inductively coupled plasma emission spectrometry as well as fluorescence spectroscopy.⁴⁶ Unlike arterial extraction of conventional pharmacologic agents (e.g., carboplatin, cisplatin, lidocaine, and testosterone), arterial extraction of quantum dots showed unique periodic behavior.

In this study, hollow microneedle devices for transdermal delivery of quantum dots and other nanoscale pharmacologic agents were fabricated out of a commercial acrylic polymer by means of two-photon polymerization. Cell viability of the acrylate-based polymer was evaluated using neonatal human epidermal keratinocytes and human dermal fibroblasts. Nanoindentation was performed to obtain the hardness and Young's modulus of the acrylate-based polymer. The ability to perform two-photon polymerization of this material was demonstrated; appropriate structuring parameters for producing microneedle devices were determined. Hollow microneedle arrays with several geometries were prepared using two-photon polymerization. Finally, hollow microneedles devices were used to inject quantum dots into porcine skin; imaging of quantum dot delivery was performed using multiphoton microscopy. This study suggests that two photon polymerization may provide a unique approach for fabricating polymeric microneedle arrays, which may be used for transdermal delivery of quantum dots for theranostics and other medical applications.

Methods

An ultraviolet light-sensitive acrylate-based polymer, e-shell 300 (EnvisionTEC, Gladbeck, Germany), was examined in this study. This rigid, tough, perspiration-resistant material is processed using single-photon polymerization for use in a variety of medical applications, including hearing aid shells and other Class IIa medical devices. Class IIa medical devices include non-invasive active medical devices for channeling and/or storing liquids for administration to the human body.⁴⁷ Information provided by the supplier indicates that e-shell is comprised of 10–25 wt% urethane dimethacrylate (CAS 72869-86-4) and 10–20% tetrahydrofurfuryl-2-methacrylate (CAS 2455-24-5).

The two photon polymerization process was used to produce several types of microneedle structures from the acrylate-based polymer. Femtosecond pulses (60 fs, $\lambda = 780$ nm) from a Chameleon titanium:sapphire laser (Coherent, Santa Clara, CA) were used to polymerize the liquid acrylate-based polymer resin. The resin was polymerized along the trace of the laser focus, which was moved in three dimensions. A hurrySCAN® galvano scan head (Scanlabs, Puchheim, Germany) was used to control laser writing in lateral (X- and Y-) dimensions. Movement in the height (Z-) dimension and movement from one structure to another structure were achieved using three C-843 linear translation stages (Physik Instrumente, Karlsruhe, Germany). Fabrication of the microneedle structures was guided by input stererolithography (STL) files, which were prepared using Solidworks Education Edition 2009 commercial software (Dassault Systemes SA, Velizy, France). The unpolymerized

acrylate-based polymer resin was placed in between two glass cover slips; the resin was enclosed using a 1 mm thick polydimethylsiloxane ring. The structures were washed using isopropanol in order to remove the unirradiated resin. The structures were subsequently exposed to an ELC-410 ultraviolet curing lamp (Electro- Lite, Bethel, CT).

Solid microneedles were initially fabricated using several processing parameters in order to obtain appropriate conditions for subsequent fabrication of hollow microneedles. Above an upper threshold of laser intensity, burning of the resin will occur. Below a lower threshold of laser intensity, polymerization of the resin will not occur. Processing parameters also alter voxel height and voxel width; these parameters affect shape and integrity of two photon polymerization-fabricated structures. An array of solid microneedles was initially fabricated using two photon polymerization; structures were fabricated with an input file height of 750 μm and base diameter of 125 μm . The objective, laser energy, laser wavelength, layer spacing, raster spacing, and mark speed were maintained at 10x, 320 mW, 780 nm, 10 μm , 1.5 μm , and 50–250 (arbitrary units) respectively. Hollow microneedles were subsequently fabricated on glass cover slips by means of two photon polymerization. One set of microneedles was produced using an input file height of 375 μm , base diameter of 250 μm , and channel diameter of 30 μm . Another set of microneedles was produced using an input file height of 500 μm , base diameter of 250 μm , and channel diameter of 30 μm . The objective, laser energy, laser wavelength, layer spacing, raster spacing, and mark speed were maintained at 10x, 320 mW, 780 nm, 10 μm , 1.5 μm , and 100 respectively. Freestanding microneedle arrays, containing both the substrate and the microneedles, were then fabricated

using two-photon polymerization. The 5x objective was used instead of the 10x objective due to limitations associated with radial laser intensity degradation in the focal plane. Changing the objective resulted in a reduction in two photon processing resolution; however, changing the objective was necessary in order to fabricate the large freestanding microneedle array structure. Freestanding microneedle arrays were fabricated in three steps due to radial laser intensity degradation. The border was initially fabricated; this structure enables handling of the freestanding microneedle array without damage to the microneedles. The objective, laser energy, laser wavelength, layer spacing, raster spacing, and mark speed were maintained at 5x, 570 mW, 780 nm, 25 μm , 2 μm , and 40 respectively. The substrate was then fabricated; it exhibited a three-by-three array structure with 500 μm spacing. The objective, laser energy, laser wavelength, layer spacing, raster spacing, and mark speed were maintained at 5x, 370 mW, 780 nm, 25 μm , 1.4 μm , and 60 respectively. A 100 μm overlap between the border and the substrate was used to ensure good bonding between structures. An array of microneedles was subsequently fabricated on the substrate. A computer-aided design drawing of the microneedle structure is shown in Fig. 2a. Microneedles were produced with a conical opening at the base; structures were fabricated with an input file cylindrical base height of 250 μm , cylindrical base diameter of 400 μm , needle height of 608 μm , needle base diameter of 200 μm , and channel diameter of 110 μm . The objective, laser energy, laser wavelength, layer spacing, raster spacing, and mark speed were maintained at 5x, 370 mW, 780 nm, 25 μm , 1.4 μm , and 60 respectively. A 60 μm overlap between the substrate and the microneedles was used to ensure a strong bonding between structures. The structures were subsequently exposed to an ultraviolet curing lamp. The structures were subsequently

removed from the glass cover slips. The structures were washed using isopropanol in order to remove the unirradiated resin. Details on fabrication of freestanding microneedle arrays are provided in Fig. 2b. To confirm the unobstructed nature of the channels, 200 mbar vacuum suction was applied; isopropanol was placed on the array and pulled through the microneedles.

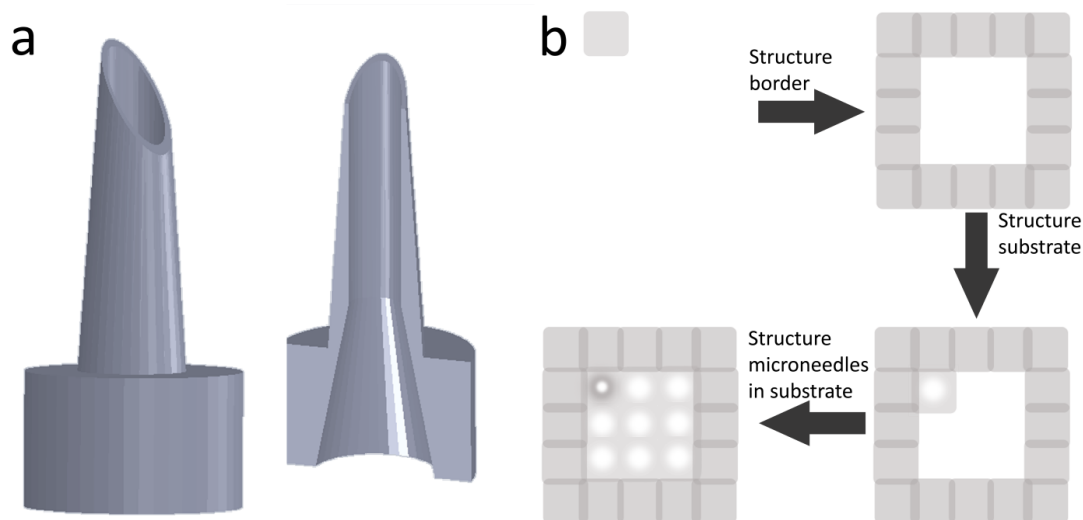


Fig. 2 (a) Input computer-aided design drawing of hollow microneedles processed via two-photon polymerization. (b) Diagram of hollow microneedle device fabrication by means of two-photon polymerization.

Scanning electron microscopy imaging of the microneedle arrays was performed using an S-3200 variable pressure instrument (Hitachi, Tokyo, Japan) with a RobinsonTM backscattered electron detector. Energy dispersive X-ray spectroscopy was used to obtain the elemental composition of the acrylate-based polymer microneedle arrays. Fourier transform infrared spectroscopy (FTIR) was performed using a Nexus 470 system with a continuum microscope

and an OMNI sampler (Thermo Fisher, Waltham, MA); spectral analysis was performed with OMNICTM software (Thermo Fisher, Waltham, MA). Material for Fourier transform infrared spectroscopy was prepared by sandwiching resin between two glass cover slips with a polydimethylsiloxane spacer (thickness = 1 mm, diameter = 5 mm); the resin was polymerized using an ELC-410 ultraviolet curing lamp.

Elastic modulus (relative stiffness of a material against elastic deformation) and hardness (resistance of a material to penetration and/or plastic deformation) are critical parameters for materials used in fabrication of microneedle devices. Material for nanoindentation testing was prepared by sandwiching resin between two glass cover slips with a polydimethylsiloxane spacer (thickness = 1 mm, diameter = 5 mm); the resin was polymerized using an ELC-410 ultraviolet curing lamp. An Ultra Nano Hardness Tester (CSM Instruments, Needham, MA) containing an indenter tip with Berkovitch geometry was used to obtain elastic modulus and hardness data for the acrylate-based polymer. Ten indentations were performed; the indenter tip was driven into the surface of the material with up to 2 mN normal load, 4 mN min⁻¹ loading rate, and 4 mN min⁻¹ unloading rate. Partial or complete relaxation was achieved by reducing the load after the maximum load had been achieved. Indentation hardness and elastic modulus were obtained from the load-displacement data using the Oliver and Pharr method.⁴⁸

Proliferation of cells on the acrylate-based polymer was assessed by the MTT (3-(4,5-dimethylthiazol-2-yl)2,5-diphenyl tetrazolium bromide) assay; this assay is based on reduction of a yellow tetrazolium salt (MTT) to a purple formazan dye by the succinic dehydrogenase enzyme within mitochondria.⁴⁹ Glass cover slips (diameter = 12.5 mm) ($n = 4$), empty wells within γ -irradiated sterile polystyrene plates ($n = 4$) (Sigma-Aldrich, St. Louis, MO), and e-shell 300 acrylate-based polymer wafers ($n = 4$) were evaluated. Cylindrical wafers (thickness = 1.5 mm, diameter = 14.0 mm) of the acrylate-based polymer were prepared using a Perfactory® Standard SXGA+ UV (EnvisionTEC, Gladbeck, Germany) stereolithography system. This system uses stereolithography (STL) files to guide an ultraviolet light beam over the acrylate-based polymer resin. Illumination in the X- and Y-dimensions was regulated by directed light projection (DLP) optics (Texas Instruments, Dallas, TX); the chip used for wafer fabrication exhibits 1280 x 1024 pixel resolution. Acrylate-based polymer samples were subsequently washed in isopropanol and post-cured using the ELC-410 UV curing lamp. The acrylate-based polymer wafers and glass cover slips were rinsed twice in 70% ethanol for thirty minutes and then exposed to ultraviolet B light for two hours. The acrylate-based polymer wafers and glass cover slips were subsequently rinsed twice in Hanks' Balanced Salt Solution (HBSS) and once in culture medium. The acrylate-based polymer wafers and glass cover slips were then placed in 2 mL of medium and stored in an incubator until seeding. Cryopreserved neonatal human epidermal keratinocytes (HEK) and human dermal fibroblasts (HDF) were purchased from a commercial source (Lonza, Walkersville, MD). Cells were propagated in 75 cm² flasks, grown to 75% confluency, harvested, and seeded (40 000 cells per well) on acrylate-based

polymer wafers, on glass cover slips, and in polystyrene well plates. Culturing was performed with keratinocyte growth media (KGM-2) (Lonza, Walkersville, MD) and fibroblast growth media (FGM-2) (Lonza, Walkersville, MD). The acrylate-based polymer wafers were compared to both empty polystyrene well plates and glass cover slips. Since aspiration of solutions was associated with detachment of cells from the test materials, all media changes and material rinsing were accomplished by moving the test materials from one solution to the other with forceps. Aspiration was performed for evaluation of cell proliferation within the empty wells. Test materials were placed in fresh medium after forty-eight hours, which correlated with 80% confluency of both neonatal human epidermal keratinocytes and human dermal fibroblasts; cell proliferation on test materials was assessed twenty-four hours later. The test materials were rinsed with Hanks' Balanced Salt Solution, desorbed with isopropyl alcohol, and agitated. 100 μ l of isopropyl alcohol was transferred to a new twenty-four well plate; absorbance was spectrophotometrically evaluated ($\lambda = 550$ nm) using a Multiskan RC plate reader (Labsystems Inc, Franklin, MA).

Since human skin is similar to porcine skin, an *ex vivo* porcine skin model was used to evaluate quantum dot delivery.⁵⁰ Full thickness skin was obtained from euthanized female weanling Yorkshire pigs. The back area of the pig was clipped; two days later, full thickness skin was surgically removed. The skin was refrigerated until the quantum dot injection, which occurred one day after surgical removal. Animal care and experimental use were performed according to approved guidelines by the local Animal Care and Use Committee (North Carolina State University, Raleigh, NC).

A LSM-710 multiphoton microscope (Carl Zeiss AG, Oberkochen, Germany) was used for imaging delivery of quantum dots into porcine skin. Qdot[®] 565 ITK[™] carboxyl quantum dots (amount 250 μ L, concentration 8 μ M, pH 9.0) were obtained from a commercial source (Invitrogen, Carlsbad, CA). Information provided by the supplier indicates that the quantum dots contained a CdSe core and a crystalline ZnS shell; an amphiphilic carboxyl coating enables dispersion of quantum dots in aqueous solutions and may serve to minimize generation of free cadmium.

The freestanding microneedle array was initially pressed into the skin. A piece of polydimethylsiloxane containing a hole that was larger than the microneedle array but smaller than the substrate was placed on the backside of the microneedle array in order to obtain a seal. A syringe was filled with the quantum dot solution. A piece of polydimethylsiloxane with a Luer-lock fitting was attached in order to completely seal the connection between the array and the syringe. 250 μ L of 8 μ M quantum dot solution was diluted in deionized water to a total volume of 1 mL prior to injection; 250 μ L of this diluted solution was injected via the microneedle array prior to imaging. The microneedle array was kept in the skin during imaging. Quantum dot solution was topically applied to the surface of a separate porcine skin for comparison purposes.

The microneedles and the quantum dots were simultaneously imaged since multiphoton excitation occurs for both the e-shell 300 acrylate based polymer and the Qdot[®] 565 ITK[™]

carboxyl quantum dots at 1 800 nm. Multiphoton microscopy was performed with a femtosecond laser ($\lambda = 800$ nm) (Chameleon, Coherent, Santa Clara, CA); a pixel dwell time of 1.58 ms were used for imaging. A 20x plan-apochromat water immersion objective was utilized in this study; a droplet of water was placed on the backside of the microneedle array. Water was the only medium between the objective and the sample. Z-stack images were obtained of (a) a porcine skin section containing topically applied quantum dot solution, (b) a porcine skin section containing a freestanding microneedle array without injection of quantum dots, and (c) a porcine skin section containing a freestanding microneedle array immediately after quantum dot injection; image acquisition was completed less than fifteen minutes after quantum dot injection. Imaris 7.0 image analysis software (Bitplane AG, Zurich, Switzerland) was used to produce surface rendering images of the microneedles and maximum projection images of the quantum dots from the Z-stack data; these images provide enhanced visualization of quantum dot delivery.

Results and discussion

The Fourier transform infrared spectrum of e-shell 300 acrylate based polymer is shown in Fig. 3b. Sharp peaks located at 2960.8 cm^{-1} , 1721.5 cm^{-1} , 1509.9 cm^{-1} , 1454.6 cm^{-1} , 1296.6 cm^{-1} , 1248.8 cm^{-1} , 1160.8 cm^{-1} , 1135.8 cm^{-1} , 1065.3 cm^{-1} , and 831.7 cm^{-1} were observed. The peak at $\sim 2961\text{ cm}^{-1}$ was attributed to aliphatic hydrocarbon bond asymmetric stretching. The peak at $\sim 1721\text{ cm}^{-1}$ was attributed to C=O bond stretching. The broad peak at $\sim 3373\text{ cm}^{-1}$ was attributed to N-H bond stretching.⁵¹ The energy dispersive X-ray spectrum of the e-shell

300 acrylate based polymer indicates that it contains carbon and oxygen; other elements, including those with known toxicity, were not observed. Nanoindentation testing of e-shell 300 acrylate based polymer provided hardness and Young's modulus values of 162.9 ± 2.3 MPa and $2.8 \text{ GPa} \pm 0.0$, respectively. Park *et al.* indicated that microneedles produced from materials with a Young's modulus values greater than ~ 1 GPa possess fracture forces that surpass skin insertion forces.⁵² Park *et al.* recently demonstrated fabrication of microneedles out of poly-lactic-co-glycolic acid, which exhibits a Young's modulus of 3 GPa; they described the relationship between Young's modulus, aspect ratio, and failure force.⁵³

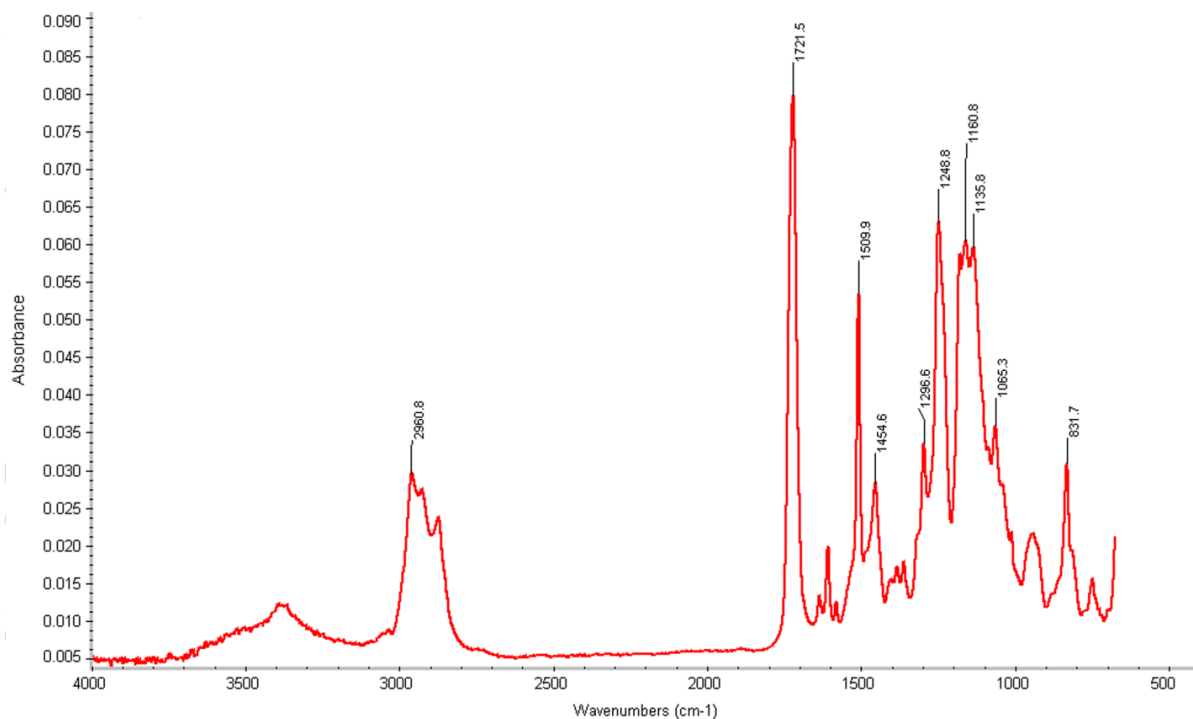


Fig. 3 Fourier transform infrared spectrum of e-shell 300 acrylate-based polymer.

The twenty-four hour MTT assay for proliferation of neonatal epidermal keratinocytes and human dermal fibroblasts on e-shell 300 acrylate based polymer are shown in Fig. 4. Statistical analysis of the cell proliferation data was performed using the Student's t-test ($p < 0.05$). The test materials remained stable and intact in the cell culture media. MTT viability of neonatal human keratinocytes was significantly higher for e-shell 300 acrylate-based polymer than for glass. MTT viability of neonatal human keratinocytes was significantly lower for e-shell 300 acrylate-based polymer than for polystyrene well plates. MTT viability of human dermal fibroblasts on e-shell 300 was significantly lower than on glass or on polystyrene well plates.

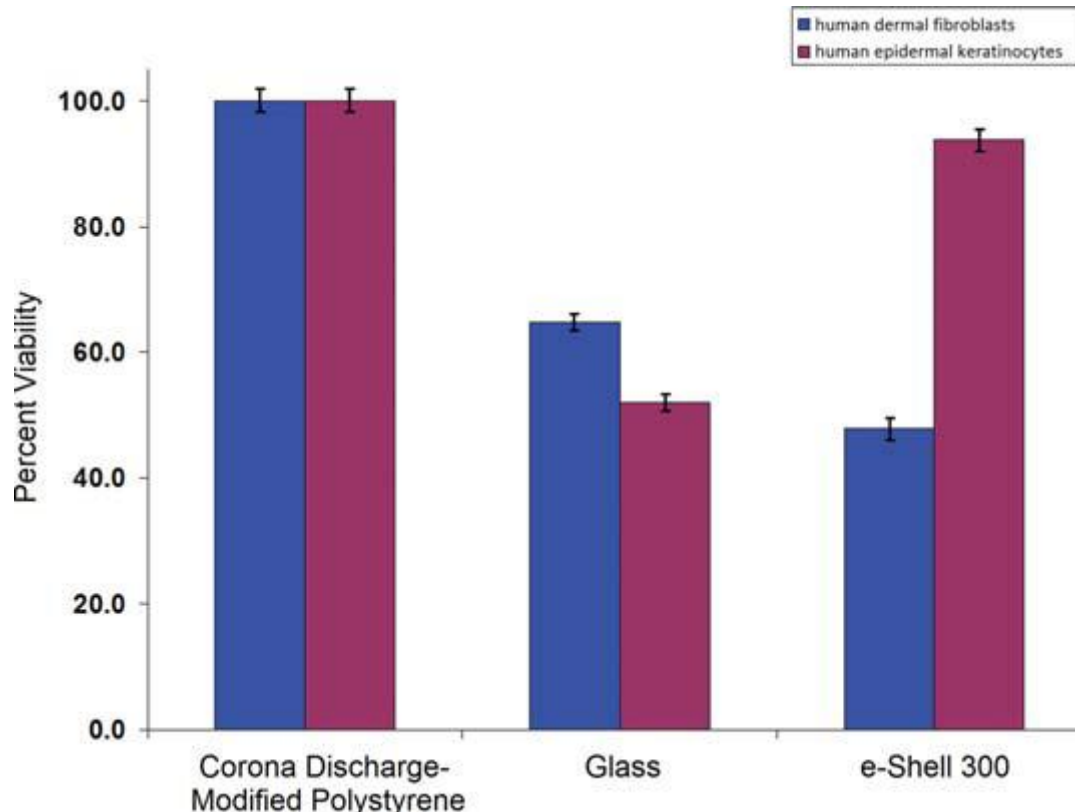


Fig. 4 MTT viability of neonatal human epidermal keratinocytes and human dermal fibroblasts on e-shell 300 acrylate-based polymer, polystyrene well plate, and glass is shown.

Error bars indicate standard error of the mean.

Information provided by the supplier indicates that the surfaces of the polystyrene wells were modified with corona discharge in order to incorporate oxygen-containing chemical groups within surface polystyrene chains; increase surface hydrophilicity; and enhance cell spreading and attachment. The glass cover slips were not modified to enhance cell spreading and attachment. The acrylate-based polymer did not exhibit cytotoxicity in a manner that would raise concerns regarding potential in vivo use in a microneedle device.

A limitation on the writing speed of the two photon polymerization process for e-shell 300 acrylate-based polymer microneedle fabrication was obtained from scanning electron microscopy images of solid microneedles, which were prepared using an input file height of 750 μm and an input file base diameter of 125 μm . As shown in Fig. 5, microneedles processed using write speeds above 150 exhibited tips with insufficient structural integrity; bending of the microneedle tips was observed.

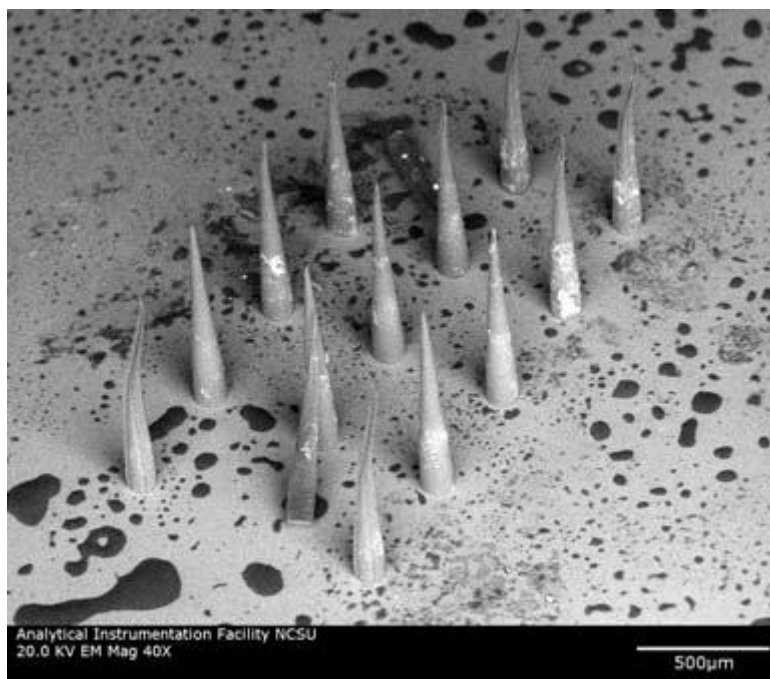


Fig. 5 Scanning electron microscopy image obtained at 45° tilt of solid e-shell 300 microneedles, which were created by means of two photon polymerization. Mark speeds (from front to back) of 250, 50, 100, 150, and 200 are shown.

A scanning electron microscopy image of a hollow microneedle array on a glass cover slip is shown in Fig. 6. The measurements of the microneedles are slightly larger than those of the

input stereolithography (STL) files. For example, one set of microneedles was produced using an input file height of 375 μm , base diameter of 250 μm , and channel diameter of 30 μm ; these microneedles exhibited a measured height of $614 \pm 12 \mu\text{m}$ (Fig. 6a). Another set of microneedles was produced using an input file height 500 μm , base diameter of 250 μm , and channel diameter of 30 μm ; these microneedles exhibited a measured height of $710 \pm 10 \mu\text{m}$ (Fig. 6b and 6c). Unlike some of the microneedles processed using more rapid write speeds (Fig. 5), the microneedles processed using a write speed of 100 (Fig. 6d) exhibited tips that remained upright.

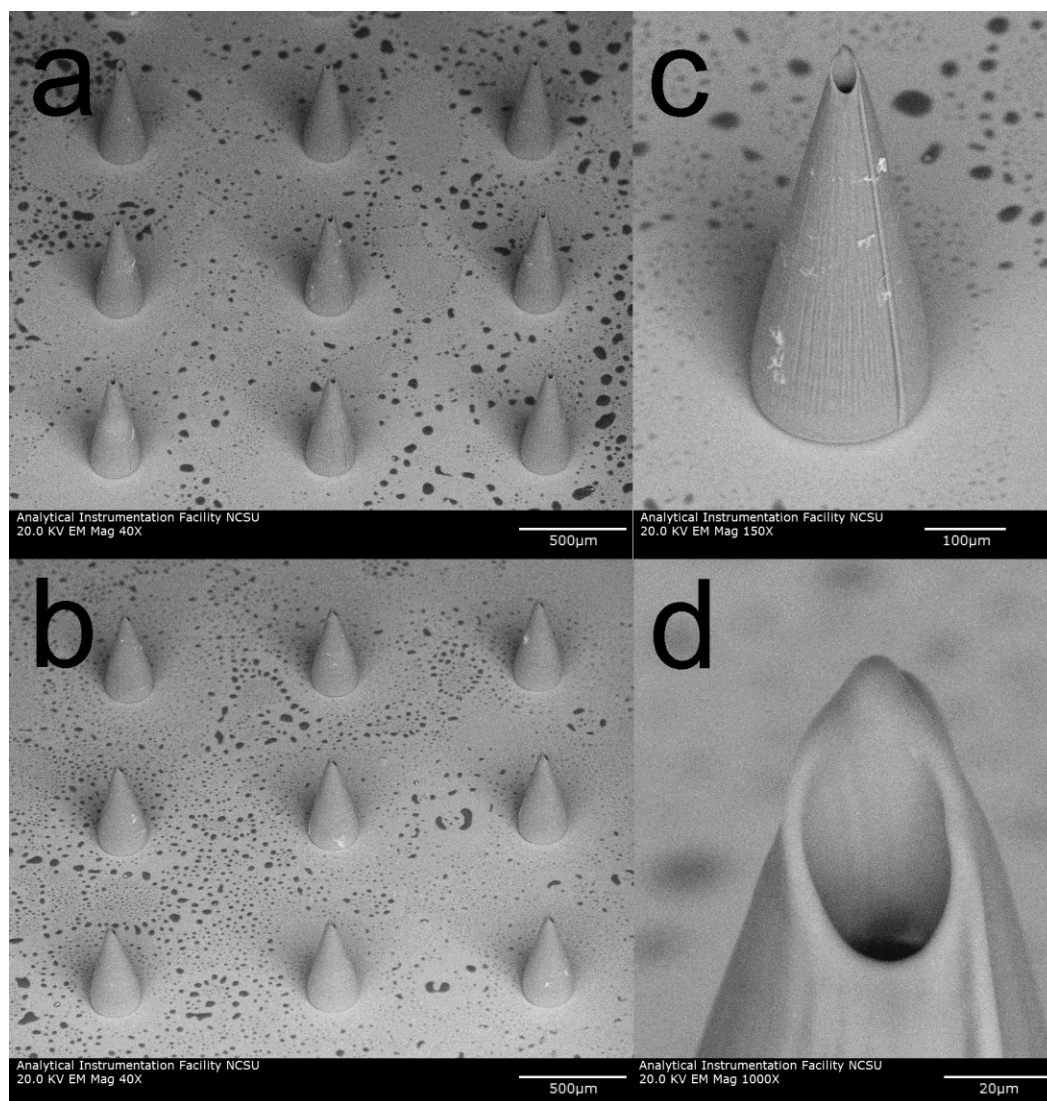


Fig. 6 Scanning electron microscopy images obtained at 45° tilt of e-shell 300 hollow microneedles on glass substrates, which were produced using two photon polymerization. (a) Image of $614 \pm 12 \mu\text{m}$ long microneedle array. (b) Image of $710 \pm 10 \mu\text{m}$ long microneedle array. (c) Image of $710 \pm 10 \mu\text{m}$ long individual microneedle. (d) Image of $710 \pm 10 \mu\text{m}$ long individual microneedle. The base diameter of these microneedles is $226 \pm 5 \mu\text{m}$. Dimensions are shown as average \pm standard deviation.

It should be noted that the 10x objective is not well suited for making large structures (e.g., a freestanding microneedle array, containing both the substrate and the microneedles) due to radial laser energy degradation. Due to refraction and aberration, the intensity at the focal point in the resin decreases as distance from the focal plane center increases. The radial laser energy degradation between the edge and the center of a large structure (e.g., a freestanding microneedle array) was so great that the structure could not be fabricated using a 10x objective. In moving from the 10x objective to the 5x objective, the radial laser energy degradation was reduced by approximately half.

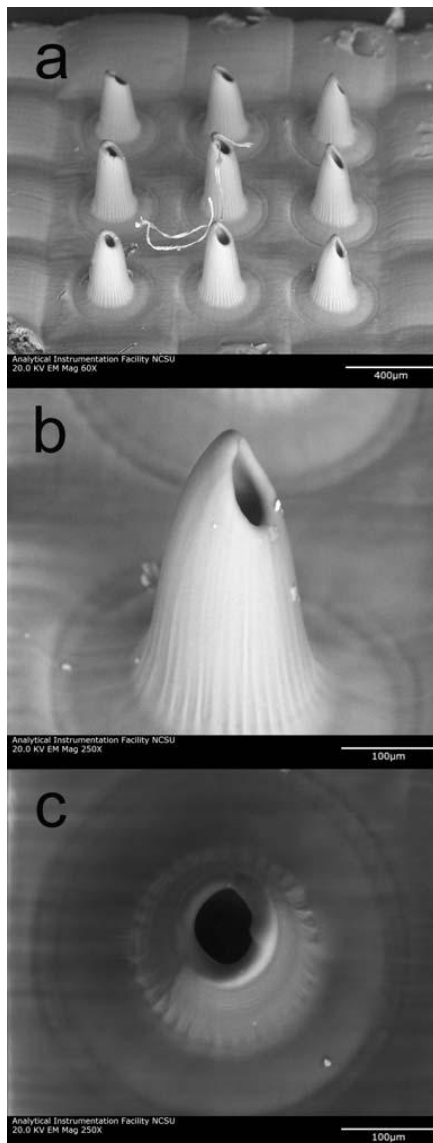


Fig. 7 Scanning electron microscopy images of e-shell 300 hollow microneedle array, which was produced using two photon polymerization. (a) Image of microneedle array obtained at 45° tilt. (b) Image of individual microneedle obtained at 45° tilt. (c) Image of individual microneedle obtained at 0° tilt. The length and base diameters of these microneedles are $508 \pm 33 \mu\text{m}$ and $212 \pm 3 \mu\text{m}$, respectively. Dimensions are shown as average \pm standard deviation.

Fig. 7 contains scanning electron microscopy images of a freestanding microneedle array, containing both the substrate and the microneedles. These microneedles exhibited a measured height of $508 \pm 33 \mu\text{m}$ and a measured diameter of $212 \pm 3 \mu\text{m}$ (Fig. 7a and 7b). No discontinuities were observed at the interfaces between the microneedles and the substrate (Fig. 7c). It should be noted that the microneedle structure shown in Fig. 7a, which was produced with a 5x objective, exhibits less precise small-scale features than the microneedle structure shown in Fig. 6a, which was produced with a 10x objective. It is interesting to note that the measured base diameter obtained using the 10x objective was smaller than the input file base diameter; this finding was attributed to shrinkage of the material during polymerization. On the other hand, the measured base diameter obtained using the 5x objective was larger than the input file base diameter; this finding was attributed to the fact that the voxel size exceeds the material shrinkage. The nonuniform “pillow top”-like morphology of the substrate was attributed to radial laser energy degradation. Minimized processing time and minimized processing cost are obtained by performing two-photon polymerization using the most rapid possible write speed. Objective election and mark speed are two of several laser-material interaction parameters that can be readily altered to produce structures with optimized geometries using two-photon polymerization.

Multiphoton microscopy was used to observe quantum dot delivery into porcine skin via a two-photon polymerization-fabricated e-shell 300 microneedle array as well as via topical application. Z-stack images of a microneedle in porcine skin prior to quantum dot injection (Fig. 8a), a microneedle in porcine skin after quantum dot injection (Fig. 8b), and quantum

dots topically applied to porcine skin (Fig. 8c) are shown. The microneedles are presented as surface renderings (in gray) and the quantum dots are presented as maximum projections (in red). Thresholding values for surface renderings were $62.800 \mu\text{m}^2$ for the Z-stack images of the microneedle in porcine skin prior to quantum dot injection and $35.040 \mu\text{m}^2$ for the Z-stack images of the microneedle in porcine skin after quantum dot injection.

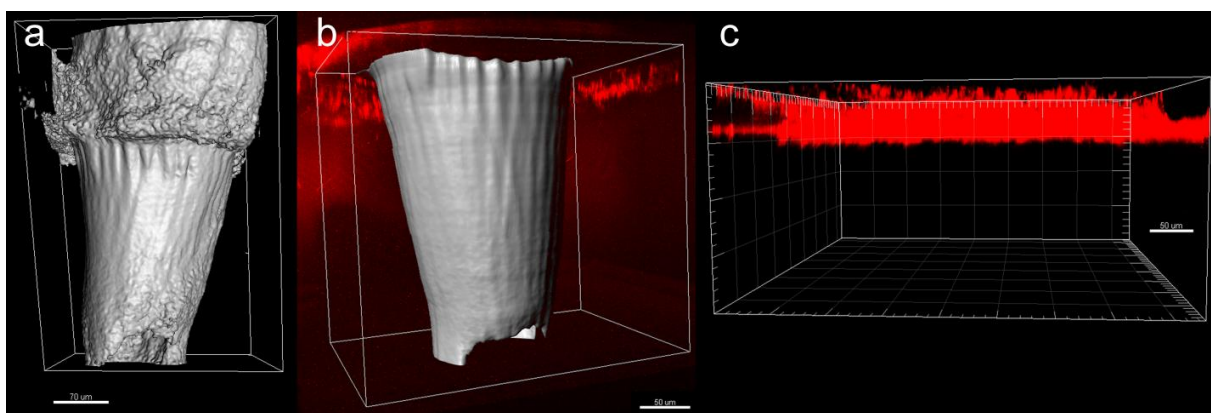


Fig. 8 Multiphoton microscopy images of quantum dot injection via two-photon polymerization-fabricated e-shell 300 microneedle array as well as via topical application. The microneedles are presented as surface renderings (in gray) and the quantum dots are presented as maximum projections (in red). (a) Microneedle in porcine skin prior to quantum dot injection. (b) Microneedle in porcine skin after quantum dot injection. A broad distribution of the quantum dots in the deep epidermis and dermis was observed. (c) Quantum dots topically applied to porcine skin. The topically applied quantum dots exhibited poor penetration and remained in the topmost $50 \mu\text{m}$ region of the epidermis.

The e-shell 300 acrylate-based polymer was noted to fluoresce under multiphoton excitation; the use of e-shell 300 or similar materials may be beneficial for transdermal theranostics activities involving multiphoton microscopy. Since time is needed to acquire Z-stack image data and adjust image acquisition settings, quantitative time-dependent data on quantum dot movement over time was unable to be obtained.

Another drawback of the multiphoton microscopy setup involved the use of a water immersion lens, which required a water column between the objective and the sample. Water was placed on the backside of the microneedle array. It is possible that capillary forces in the channels pulled some of the water through the microneedles and even into the skin, resulting in dilution of quantum dot solution. Refraction from the skin resulted in reduced image quality from deep tissue regions; neither the e-shell 300 acrylate-based microneedles nor the quantum dots could be imaged beyond a depth of $\sim 500 \mu\text{m}$ from the skin surface. Levene *et al.* recently demonstrated the use of gradient index lenses with needle-like dimensions for multiphoton microscopy with subcellular resolution; in vivo images of quantum dots within tissues that were several millimetres within an anesthetized, intact murine model (e.g., hippocampal tissue and cortical layer tissue) were obtained.⁵⁵

The topically applied quantum dots exhibited poor penetration; they remained in the topmost 50 μm region of the epidermis. Ryman-Rasmussen *et al.* investigated topical administration of Qdot® 565 ITK™ carboxyl quantum dots; the carboxyl quantum dots were shown to penetrate the stratum corneum and primarily localize in the epidermis by eight hours;

fluorescence intensity maps suggested that penetration occurred by means of a passive diffusion mechanism.⁵⁴ They suggested that quantum dot penetration by carboxylic acid-coated quantum dots (hydrodynamic size = 14 nm) occurred by means of diffusion within the intracellular space. After being pressed against the skin, the microneedles penetrated to nearly their full length. After quantum dot injection via the microneedle array, broad distribution of the quantum dots in the deep epidermis and dermis was observed. Quantum dots administered via microneedle injection were well distributed within fifteen minutes. Quantum dots were also observed in between the microneedles and the skin; this finding was attributed to migration of the quantum dot solution along the microneedle-created pores. In previous work, Gittard *et al.* used solid e-Shell 200 acrylate-based polymer microneedle arrays to create pores in human stratum corneum and epidermis. Optical imaging of the microneedle-created pores revealed that they were irregular in shape and were smaller than the microneedle dimensions; this finding was attributed to anisotropic tensile forces associated with collagen and other skin tissue components.³³ The small microneedle channel dimensions may enable precise delivery of a theranostics agent.

Conclusions

In this study, we demonstrated that two-photon polymerization can be used to produce a freestanding microneedle array, containing both the substrate and the microneedles. The e-shell 300 acrylate-based polymer microneedles successfully created pores in the stratum corneum layer, which enabled administration of the quantum dot solution to the deep

epidermis and dermis. Microneedles enabled more rapid distribution of quantum dots to deep epidermal and dermal layers of porcine skin than topical administration. Multiphoton microscopy enabled imaging of quantum dots as well as microneedles within the skin; this approach may be useful for theranostics applications involving a variety of tissues. The ability to transdermally deliver quantum dots by means of microneedles is advantageous for theranostics applications due to the fact that microneedles are associated with minimal pain sensation, injection site trauma, and injection site inflammation. Two-photon polymerization may be used to fabricate microneedles with patient-specific use, including (a) use for depth-dependent transdermal delivery and (b) use for delivery of quantum dots as well as for withdrawal of blood and/or interstitial fluid. It is anticipated that microneedles fabricated by means of two photon polymerization may enable precise transport of theranostics agents into epidermal, dermal, or subdermal tissues.

References

1 F. J. Picard and M. G. Bergeron, *Drug Discovery Today*, 2002, 7, 1092–1101, DOI:

10.1016/S1359-6446(02)02497-2.

2 S. Warner, *Scientist*, 2004, 18, 38–39.

3 L. Bissonnette and M. G. Bergeron, *Expert Rev. Mol. Diagn.*, 2006, 6, 433–450, DOI:

10.1586/14737159.6.3.433.

4 P. Debbage and W. Jaschke, *Histochem. Cell Biol.*, 2008, 130, 845–875, DOI: 10.1007/s00418-008-0511-y.

5 B. Sumer and J. Gao, *Nanomedicine*, 2008, 3, 137–140, DOI: 10.2217/17435889.3.2.137.

6 D. Roland, *Pers. Med.*, 2007, 4, 439–444, DOI: 10.2217/17410541.4.4.439.

7 M. Bruchez, M. Moronne, P. Gin, S. Weiss and A. P. Alivisatos, *Science*, 1998, 281, 2013–2016.

8 C. M. Niemeyer, *Angew. Chem., Int. Ed.*, 2001, 40, 4128–4158.

9 E. Klarreich, *Nature*, 2001, 413, 450–452.

10 C. Seydel, *Science*, 2003, 300, 80–81.

11 M. E. Akerman, W. C. W. Chan, P. Laakkonen, S. N. Bhatia and E. Ruoslahti, *Proc. Natl. Acad. Sci. U. S. A.*, 2002, 99, 12617–12621, DOI: 10.1073/pnas.152463399.

12 Z. A. Peng and X. G. Peng, *J. Am. Chem. Soc.*, 2001, 123, 183–184.

- 13 X. Michalet, F. F. Pinaud, L. A. Bentolila, J. M. Tsay, S. Doose, J. J. Li, G. Sundaresan, A. M. Wu, S. S. Gambhir and S. Weiss, *Science*, 2005, 307, 538–544, DOI: 10.1126/science.1104274.
- 14 Y. Ho and K. W. Leong, *Nanoscale*, 2010, 2, 60–68, DOI: 10.1039/b9nr00178f.
- 15 H. Tada, H. Higuchi, T. M. Wanatabe and N. Ohuchi, *Cancer Res.*, 2007, 67, 1138–1144, DOI: 10.1158/0008-5472.CAN-06-1185.
- 16 A. M. Derfus, A. A. Chen, D. Min, E. Ruoslahti and S. N. Bhatia, *Bioconjugate Chem.*, 2007, 18, 1391–1396.
- 17 S. Dwarakanath, J. G. Bruno, A. Shastry, T. Phillips, A. John, A. Kumar and L. D. Stephenson, *Biochem. Biophys. Res. Commun.*, 2004, 325, 739–743.
- 18 Y. Li, Z. He, P. Zhang, J. Gao, C. Cheng and H. Zhang, *J. Nanosci. Nanotechnol.*, 2010, 10, 520–524.
- 19 V. Bagalkot, L. Zhang, E. Levy-Nissenbaum, S. Jon, P. W. Kantoff, R. Langer and O. C. Farokhzad, *Nano Lett.*, 2007, 7, 3065–3070.
- 20 W. Cai and X. Chen, *Nat. Protoc.*, 2008, 3, 89–96.

- 21 W. I. Hagens, A. G. Oomen, W. H. de Jong, F. R. Cassee and A. J. A. M. Sips, Regul. Toxicol. Pharmacol., 2007, 49, 217–229, DOI: 10.1016/j.yrtph.2007.07.006.
- 22 K. R. Vega-Villa, J. K. Takemoto, J. A. Yanez, C. M. Remsberg, M. L. Forrest and N. M. Davies, Adv. Drug Delivery Rev., 2008, 60, 929–938, DOI: 10.1016/j.addr.2007.11.007.
- 23 H. J. G. E. Gardeniers, R. Luttge, E. J. W. Berenschot, M. J. de Boer, S. Y. Yeshurun, M. Hefetz, R. van't Oever and A. vanden Berg, J. Microelectromech. Syst., 2003, 12, 855–862, DOI: 10.1109/JMEMS.2003.820293.
- 24 H. S. Gill, D. D. Denson, B. A. Burris and M. R. Prausnitz, Clin. J. Pain, 2008, 24, 585–594.
- 25 S. D. Gittard and R. J. Narayan, in Toxicology of the Skin, ed. N. A. Monteiro-Riviere, Informa Healthcare, New York, NY, 2010, pp. 301–316.
- 26 L. Nordquist, N. Roxhed, P. Griss and G. Stemme, Pharm. Res., 2007, 24, 1381–1388, DOI: 10.1007/s11095-007-9256-x.
- 27 S. D. Gittard, A. Ovsianikov, B. N. Chichkov, A. Doraiswamy and R. J. Narayan, Expert Opin. Drug Delivery, 2010, 7, 513–533, DOI: 10.1517/17425241003628171.

28 S. A. Coulman, A. Anstey, C. Gateley, A. Morrissey, P. McLoughlin, C. Allender and J. C. Birchall, *Int. J. Pharm.*, 2009, 366, 190–200, DOI: 10.1016/j.ijpharm.2008.08.040.

29 D. V. McAllister, P. M. Wang, S. P. Davis, J. H. Park, P. J. Canatella, M. G. Allen and M. R. Prausnitz, *Proc. Natl. Acad. Sci. U. S. A.*, 2003, 100, 13755–13760, DOI: 10.1073/pnas.2331316100.

30 S. Bal, A. C. Kruithof, H. Liebl, M. Tomerius, J. Bouwstra, J. Lademann and M. Meinke, *Laser Phys. Lett.*, 2010, 7, 242–246, DOI: 10.1002/lapl.200910134.

31 A. Doraiswamy, C. Jin, R. J. Narayan, P. Mageswaran, P. Mente, R. Modi, R. Auyeung, D. B. Chrisey, A. Ovsianikov and B. Chichkov, *Acta Biomater.*, 2006, 2, 267–275, DOI: 10.1016/j.actbio.2006.01.004.

32 A. Ovsianikov, B. Chichkov, P. Mente, N. A. Monteiro-Riviere, A. Doraiswamy and R. J. Narayan, *Int. J. Appl. Ceram. Technol.*, 2007, 4, 22–29.

33 S. D. Gittard, A. Ovsianikov, N. A. Monteiro-Riviere, J. Lusk, P. Morel, P. Minghetti, C. Lenardi, B. N. Chichkov and R. J. Narayan, *J. Diabetes Sci. Technol.*, 2009, 3, 304–311.

34 S. D. Gittard, R. J. Narayan, C. Jin, A. Ovsianikov, B. N. Chichkov, N. A. Monteiro-Riviere, S. Stafslie and B. Chisholm, *Biofabrication*, 2009, 1, 041001, DOI: 10.1088/1758-5082/1/4/041001.

35 S. D. Gittard, A. Ovsianikov, H. Akar, B. Chichkov, N. A. Monteiro-Riviere, S. Stafslie, B. Chisholm, C. Shin, C. Shih, S. Lin, Y. Su and R. J. Narayan, *Adv. Eng. Mater.*, 2010, 12, B77–B82, DOI: 10.1002/adem.200980012.

36 A. Doraiswamy, A. Ovsianikov, S. D. Gittard, N. A. Monteiro-Riviere, R. Crombez, E. Montalvo, W. Shen, B. N. Chichkov and R. J. Narayan, *J. Nanosci. Nanotechnol.*, 2010, 10, 6305–6312.

37 S. D. Gittard and R. J. Narayan, *Expert Rev. Med. Devices*, 2010, 7, 343–356.

38 A. Ovsianikov, B. Chichkov, O. Adunka, H. Pillsbury, A. Doraiswamy and R. J. Narayan, *Appl. Surf. Sci.*, 2007, 253, 6603–6607, DOI: 10.1016/j.apsusc.2007.01.062.

39 R. Weissleder and M. J. Pittet, *Nature*, 2008, 452, 580–589, DOI: 10.1038/nature06917.

40 P. M. Wang, M. Cornwell and M. R. Prausnitz, *Diabetes Technol. Ther.*, 2005, 7, 131–141, DOI: 10.1089/dia.2005.7.131.

41 Y. Kim, P. J. Ludovice and M. R. Prausnitz, *J. Controlled Release*, 2007, 122, 375–383, DOI: 10.1016/j.jconrel.2007.05.031.

42 S. Choi, Y. Kim, J. Park, J. Hutcheson, H. Gill, Y. Yoon, M. Prausnitz and M. Allen, *Biomed. Microdevices*, 2010, 12, 263–273.

43 P. Maffia, B. H. Zinselmeyer, A. Ialenti, S. Kennedy, A. H. Baker, I. B. McInnes, J. M. Brewer and P. Garside, *Circulation*, 2007, 115, e326–e328, DOI: 10.1161/CIRCULATIONAHA.106.658492.

44 M. Stroh, J. P. Zimmer, D. G. Duda, T. S. Levchenko, K. S. Cohen, E. B. Brown, D. T. Scadden, V. P. Torchilin, M. G. Bawendi, D. Fukumura and R. K. Jain, *Nat. Med.*, 2005, 11, 678–682, DOI: 10.1038/nm1247.

45 D. R. Larson, W. R. Zipfel, R. M. Williams, S. W. Clark, M. P. Bruchez, F. W. Wise and W. W. Webb, *Science*, 2003, 300, 1434–1436.

46 H. A. Lee, M. Imran, N. A. Monteiro-Riviere, V. L. Colvin, W. W. Yu and J. E. Riviere, *Nano Lett.*, 2007, 7, 2865–2870, DOI: 10.1021/nl071563c.

47 S. Frank, in *A New Model for European Medical Device Regulation: A Comparative Legal Analysis in the EU and the USA*, Europa Law Publishing, Groningen, 2003, pp. 15–69.

48 W. C. Oliver and G. M. Pharr, *J. Mater. Res.*, 1992, 7, 1564–1583.

49 T. Mosmann, *J. Immunol. Methods*, 1983, 65, 55–63.

50 C. G. Grant, R. Warren and E. Salter, *Burns*, 1980, 7, 57–69.

51 C. A. Khatri, J. W. Stansbury, C. R. Schultheisz and J. M. Antonucci, *Dent. Mater.*, 2003, 19, 584–588, DOI: 10.1016/S0109-5641(02)00108-2.

52 H. Park, M. G. Allen and M. R. Prausnitz, *J. Controlled Release*, 2005, 104, 51–66, DOI: 10.1016/j.jconrel.2005.02.002.

53 J. H. Park and M. R. Prausnitz, *J. Korean Phys. Soc.*, 2010, 56, 1223–1227, DOI: 10.3938/jkps.56.1223.

54 J. P. Ryman-Rasmussen, J. E. Riviere and N. A. Monteiro-Riviere, *Toxicol. Sci.*, 2006, 91, 159–165, DOI: 10.1093/toxsci/kfj122.

55 M. J. Levene, D. A. Dombeck, K. A. Kasischke, R. P. Molloy and W. W. Webb, *J. Neurophysiol.*, 2004, 91, 1908–1912, DOI: 10.1152/jn.01007.2003.

3.10 Supercapacitive transport of pharmacologic agents using nanoporous gold electrodes

*The following section is the pre-peer reviewed version of the following article: **Biotechnology Journal**, Volume 5, Gittard SD, Pierson BE, Ha CM, Wu CAM, Narayan RJ, Robinson D.B. Supercapacitive transport of pharmacologic agents using nanoporous gold electrodes, pages 192-200, Copyright 2010. Reproduced by permission of Wiley-VCH Verlag GmbH & Co. KGaA*

Technical Report

Supercapacitive transport of pharmacologic agents using nanoporous gold electrodes

Shaun D. Gittard¹, Bonnie E. Pierson¹, Cindy M. Ha², Chung-An Max Wu², Roger J. Narayan¹ and David B. Robinson²

¹Joint Department of Biomedical Engineering, University of North Carolina Chapel Hill and North Carolina State University, Raleigh, NC, USA

²Sandia National Laboratories, Livermore, CA, USA

In this study, nanoporous gold supercapacitors were produced by electrochemical dealloying of gold-silver alloy. Scanning electron microscopy and energy dispersive X-ray spectroscopy confirmed completion of the dealloying process and generation of a porous gold material with ~10 nm diameter pores. Cyclic voltammetry and chronoamperometry of the nanoporous gold electrodes indicated that these materials exhibited supercapacitor behavior. The storage capacity of the electrodes measured by chronoamperometry was ~3 mC at 200 mV. Electrochemical storage and voltage- controlled delivery of two model pharmacologic agents, benzylammonium and salicylic acid, was demonstrated. These results suggest that capacitance-based storage and delivery of pharmacologic agents may serve as an alternative to conventional drug delivery methods.

Keywords: Drug delivery · Dealloying · Nanotechnology · Supercapacitor

Correspondence:

Dr. David B. Robinson, Sandia National Laboratories, PO Box 969 Mail Stop 9291,
Livermore,

CA 94551-0969, USA

E-mail: drobins@sandia.gov

Fax: +1-925-294-3020

1 Introduction

Many protein- and nucleic acid-based pharmacologic agents cannot be administered in oral form, because they may be metabolized by the intestine, liver, or kidneys before reaching systemic circulation [1]. These pharmacologic agents are currently administered *via* intravenous injection in order to avoid diffusional barriers and enzymatic barriers; intravenous administration provides complete and instantaneous absorption of a pharmacologic agent. Protein- and nucleic acid-based pharmacologic agents may also be injected using hypodermic needles into dermal tissue (intradermal injection), muscular tissue (intramuscular injection), or subcutaneous tissue (subcutaneous injection).

Use of hypodermic needles is associated with several shortcomings, including pain to the patient, trauma at the injection site, and medical expertise to administer the injection [2–4]. For example, Gill *et al.* [5] determined that the average visual analog scale pain score for

subcutaneous insertion of hypodermic needles was 39 mm on a 100 mm scale. Discomfort may persist after hypodermic needle-based injection of a pharmacologic agent; Nir *et al.* [6] showed that 35% of patients noted persistence of mild to moderate pain 3 days after receiving injected vaccinations.

Several alternatives to hypodermic needle-based injection have been developed for directly administering pharmacologic agents through the skin [7–11]. For example, transdermal patches are a commonly used alternative to hypodermic needles for transdermal delivery of pharmacologic agents [12]. It should be noted that the outermost layer of the skin (the stratum corneum) contains corneocytes as well as intercorneocyte lipids, which serve as a microscopic “brick and mortar” diffusion barrier that limits transport of large, charged, or polar molecules; use of transdermal patches is currently limited to small molecular weight neutral pharmacologic agents [13–16]. Another method for enhancing transport of pharmacologic agents across the skin is by disrupting the ordered lipid structure of the stratum corneum with chemical penetration enhancers [17]. Unfortunately, many chemical penetration enhancers are associated with skin irritation [12]. Ultrasound may also be used to disrupt the lipid structure of the stratum corneum and improve transport of pharmacologic agents [18]. Low frequency (~20 kHz) ultrasound induces the formation of cavitation bubbles, which reversibly increase the permeability of the stratum corneum; this technique enables transport of only low molecular weight pharmacologic molecules [12, 19]. In iontophoresis, a low voltage is used to drive pharmacologic agents across the stratum corneum [20]. This method is an efficient mechanism for delivering charged molecules,

although transport of neutral molecules has also been achieved [21]. The benefit of this technique is that the drug delivery rate can be easily altered by modulating the voltage that is applied between the reservoirs. It should be noted that the use of iontophoresis for drug delivery is associated with several shortcomings. For example, current regulations require the current in iontophoresis devices to remain below 0.5 mA/cm², which places an upper limit on pharmacologic agent flux [1]. In addition, application of current to the skin can cause irritation and damage [1]. It should also be noted that ions with high mobilities in the surrounding tissue as well as counter ions in the device (*e.g.*, Na⁺ and Cl⁻) can balance the voltage difference and reduce pharmacologic agent transport [20]. It has been difficult to achieve reproducible outcomes using ultrasound- or iontophoresis- mediated delivery due to variations in skin anatomy between patients.

Microneedles are microscale lancet- or hypodermic needle-shaped devices exhibiting at least one dimension that is less than 1 mm in length [22–29]. These devices create pores in stratum corneum, which serve as conduits for transport of pharmacologic agents. Pain to the patient may be reduced or eliminated due to the fact that there are limited interactions between microneedles and Meissner's corpuscles, Pacinian corpuscles, and other nerve endings [5]. Drug delivery has been achieved using a variety of methods, including coating microneedles with pharmacologic agents [23] as well as suspending pharmacologic agents within biodegradable microneedles [24–26]. Hollow microneedles may enable diffusion- or pressure- driven transport of pharmacologic agents through the stratum corneum to be adjusted over an extended period [27–31]. Pumps used for the delivery of pharmacologic

agents through microneedles may also be used for the extraction of blood and other biological fluids. Several concerns remain regarding the use of microneedles, including skin damage, dose titration, and pharmacologic agent stability, and kinetics of pharmacologic agent movement [22].

Electrically-induced delivery from a porous electrode may also be used for the administration of pharmacologic agents. In this technique, an electrochemical double-layer supercapacitor, which consists of two electrodes in a salt solution, is used to administer anionic or cationic pharmacologic agents. A voltage is applied between the two electrodes in the double layer capacitor. An increased number of anions in the salt solution are electrostatically adsorbed onto the surface of the positively biased electrode (working electrode). Cations in the solution are adsorbed onto the opposite electrode, which is known as the counter electrode. In an ideal capacitor, the applied voltage is proportional to the amount of charge adsorbed to the surface. As a result, adsorbed ions are released from the surface when the voltage between the electrodes is reduced.

A conventional parallel-plate electrode pair does not have sufficient storage capacity in order to medically relevant amounts of pharmacologic agents. For example, the specific capacitance of a planar bare metal electrode C_{dl} charged with a typical salt (*e.g.*, sodium chloride) is $\sim 10^{-5}$ F/cm². Converted with Faraday's constant ($F = 105$ Coulombs/ mole), this is 10^{-10} moles/Vcm². Charged to 1 V, an electrode pair the size of a football field would be required to store only a few millimoles of a charged pharmacologic agent.

Relatively large surfaces can be incorporated into small volumes in nanoporous materials. We take as an example a nanoporous electrode in which each point on the electrode is within a few atoms of the surface. These electrodes can be modeled as arrays of cylindrical pores, each with capacitance:

$$C_{pore} = C_{dl} 2\pi rL \quad (1)$$

If the electrode is considered as a cube in which the pores are densely packed in a square array and are separated by one pore radius, then the number of pores is $L^2/(3r)^2$. The capacitance per unit volume can be written as:

$$C_{vol} = \frac{2\pi C_{dl}}{9r} \quad (2)$$

The molarity of stored salt in the electrode per volt can be written as:

$$\frac{molarity}{volt} = \frac{2\pi C_{dl}}{9Fr} \quad (3)$$

Table 1 shows the predicted number of moles stored per liter of electrode volume *per volt* as a function of pore radius in which $C_{dl} = 20 \mu\text{F}/\text{cm}^2$. Pores in the 1–10 nm range are achievable through various methods, including pyrolysis of template polymers to form

porous carbon electrodes [32], reduction of metals in surfactant templates [33, 34], and dealloying [35–37]. It should be noted that structures prepared using these techniques are not square arrays of uniform cylindrical pores. In addition, specific adsorption can affect the amount of the pharmacologic agent that may be delivered [38]. In any case, this model can closely capture the behavior of nanoporous materials. The charging rate of porous electrodes has been examined by several investigators, including Keiser et al., Posey, and de Levie [39–42].

Porosity-enabled supercapacitance has been investigated for a number of applications. For example, porosity-enabled supercapacitance is being considered for use in energy storage [44–46], desalination [47, 48], and other chemical separation processes [49]. A number of pharmacologic agents have been electrically delivered from conducting polymer films, including salicylate, dopamine, glutamate, and nucleic acid-based agents [50–53]. Supercapacitance-based delivery offers several advantages over hypodermic needle-based injection and other transdermal drug delivery techniques. For example, many conventional transdermal drug delivery methods require pharmacologic agents to be administered in liquid form. Injection of liquid into tissues may result in swelling, tissue damage, and pain [54, 55]. This liquid injection-related pain may be observed over a relatively large area and for a significant period of time after the hypodermic needle injection. Pain, swelling, and tissue damage associated with injection of liquids may be eliminated since no liquid medium is utilized for supercapacitance-based delivery of pharmacologic agents. The release of

pharmacologic agents from supercapacitance-based devices is voltage-dependent and may be readily altered.

In this study, fabrication of nanoporous gold supercapacitors by electrochemical dealloying for use as drug delivery devices was demonstrated. Electrochemical characterization *via* cyclic voltammetry and chronoamperometry confirmed the capacitive behavior of the nanoporous gold electrodes. Loading and delivery of a model drug was demonstrated through both electrical and spectroscopic studies.

Table 1. Theoretical storage capacity versus pore diameter for porous capacitor

Pore diameter	Storage capacity
10 μm	0.14 mM/V
1 μm	1.40 mM/V
100 nm	14.00 mM/V
10 nm	0.14 M/V
1 nm	1.40 M/V

2 Experimental procedure

All chemicals were supplied obtained from a commercial source (Sigma–Aldrich, St. Louis, MO, USA). Electrochemical etching of 1:1 weight ratio Au–Ag alloy wires (Refining Systems Inc, Las Vegas, NV, USA) was performed in order to create nanoporous Au wires. First, a 0.1 mm diameter gold wire (Alfa Aesar, Ward Hill, MA, USA) was loosely coiled

around a 2 cm segment of a 0.2 mm diameter Au–Ag alloy wire. Coiling density was approximately five turns *per* centimeter. The pure gold wires were manipulated after etching in order to ensure that a defined porous wire length was exposed to the solution [35, 36]. The braided wires were then annealed at 650°C overnight, which served to minimize wire fracture. The annealed wires were then placed in a bath of 1 M HNO₃ and 10 mM AgNO₃. The annealed alloy wires, a platinum wire, and a silver wire were then connected to the working, counter, and reference leads of a Model 273A potentiostat (Princeton Applied Research, Oak Ridge, TN, USA), respectively. A diagram of this etching setup is provided in Fig. 1a. A voltage of 1200 mV was then applied for 30 min between the working and counter electrodes in order to initiate the dealloying process. The applied voltage induced galvanic corrosion of the alloy, which resulted in transfer of silver to the counter electrode. The departure of silver resulted in the formation of nanoscale pores in the Au–Ag alloy. Field emission scanning electron microscopy (JEOL, Tokyo, Japan) was performed on electrochemically etched gold wires in order to examine surface morphology of these materials. Energy dispersive X-ray spectroscopy was carried out using an S-3200 scanning electron microscope (Hitachi, Tokyo, Japan) in order to determine the elemental composition of the nanoporous wires.

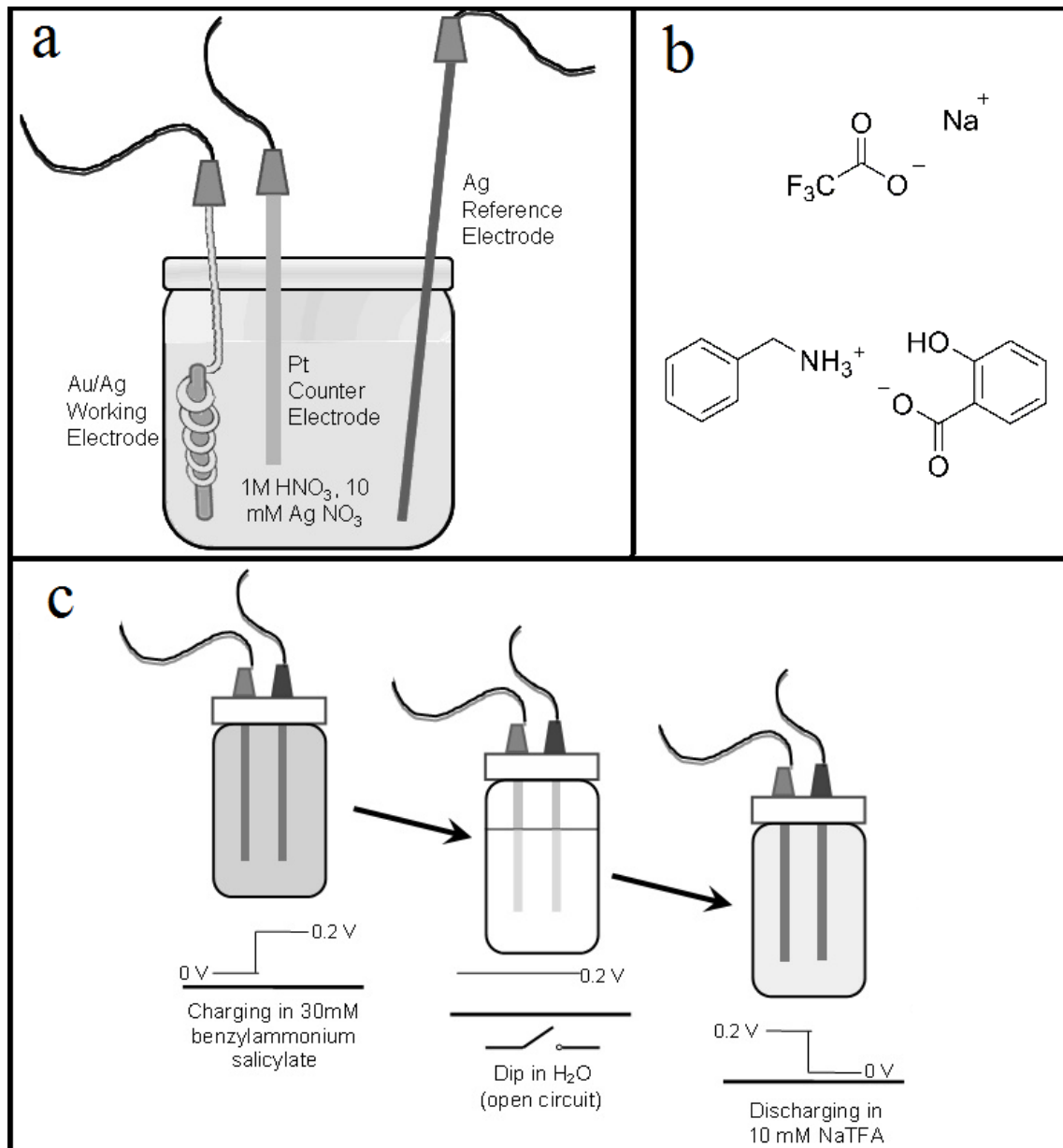


Figure 1. (a) Diagram showing electrochemical dealloying of Au–Ag alloy to produce nanoporous gold electrodes. (b) Chemical structure of sodium trifluoroacetate and benzylammonium salicylate. (c) Diagram of apparatus used for examining capacitive storage and delivery of benzylammonium salicylate.

A two-electrode electrochemical cell was created by connecting one nanoporous gold wire to the working lead and the other wire to the counter and reference leads of the potentiostat. The gold support wires were threaded through holes in the lid of a 4 mL cuvette in order to allow the wires to be handled simultaneously without coming into contact during testing. The wires were then submerged in an analyte by placing a lid on a cuvette that contained the analyte of interest. Three electrochemical characterization studies were performed using the two electrode cells in order to assess their electrochemical behavior. First, cyclic voltammetry was performed in order to determine the charging dynamics of the nanoporous electrodes. In the cyclic voltammetry study, a triangular voltage wave was applied between the electrodes and the current flow was measured. A voltage sweep was performed at 5 mV/s over a range from -200 to 200 mV. Chronoamperometry was performed by applying a voltage and obtaining current measurements over time. Voltages of 100 and 200 mV were applied to the electrodes. Both of these experiments were performed in 100 mM sodium trifluoroacetate and 50 mM benzylammonium salicylate.

Two salt solutions were used as test analytes in the electrochemical cell: sodium trifluoroacetate and benzylammonium salicylate. Sodium trifluoroacetate was selected due to the nearly identical mobilities of the two ions, a characteristic that is desirable for examining the charging dynamics of an electrochemical cell. Benzylammonium salicylate was chosen as an analyte for modeling drug delivery. Both ions in this salt solution served as model pharmacologic agents. Benzylamine is chemically similar to pharmacologic agents that are commonly used for topical treatment of dermatophyte infections, including butenafine

hydrochloride (Lotrimin Ultra™) and terbinafine hydrochloride (Lamisil™) [56]. Salicylic acid is a pharmacologic agent similar to aspirin (acetylsalicylic acid) that used as for increasing blood circulation in the skin by means of capillary dilation [57]. The chemical structures of these molecules are shown in Fig. 1b.

As presented in Fig. 1c, the wire was charged to a defined voltage in a loading solution, rinsed, and discharged in a recovery solution. Specifically, 200 mV was applied between two nanoporous gold electrodes in a 30 mM benzylammonium salicylate cell in order to electrostatically store the pharmacologic agent on the electrodes. While maintaining an open circuit between them, the electrodes were dipped into deionized H₂O to wash off any benzylammonium salicylate that was not electrostatically bound. The electrodes were subsequently moved to a 4 mL solution of 10 mM sodium trifluoroacetate. One hundred millivolts was then applied in order to release the pharmacologic agent from the electrodes. The electrodes were then washed again in deionized H₂O and placed into a new 4 mL solution. The voltage was reduced to 0 mV, or first to 100 mV and then 0 mV. Salicylate absorbs light at $\lambda = 300$ nm; in our cuvette, its absorbance scales linearly with concentration between 0.01 and 0.1 mM. A Model SQ3802 UV–Visible spectrometer (Unico, Princeton, NJ, USA) was used to determine the amount of pharmacologic agent that was released into the solutions. Additionally, the total charge passed to and from the electrodes during storage and release was measured during steps from 200 to 0 mV and 100 to 0 mV.

3 Results and discussion

Scanning electron microscopy demonstrated that the electrochemically etched wires have a sponge-like porous morphology (Fig. 2a). The pore size was shown to be 10 ± 5 nm in diameter. Energy dispersive X-ray spectroscopy (Fig. 2b) determined that 5 wt% silver remained on the 1:1 weight ratio Au–Ag alloy wires electrodes that underwent etching. Other studies have also shown that this electrochemical etching method results in nearly complete removal of silver [35]. Cyclic voltammograms of the nanoporous gold electrodes in 100 mM sodium trifluoroacetate and 50 mM benzylammonium salicylate solutions are shown in Figs. 3a and b, respectively. The cyclic voltammograms demonstrate a tilted, parallelogram shape, suggesting that charging was not complete over the timescale of the experiment. A purely capacitive circuit would have provided cyclic voltammetry data with a more rectangular shape [58, 59]. Porous electrodes are known to charge by a $I \propto 1/\sqrt{-t}$ power law, which exhibits a long, slow asymptote as the deepest parts of the wire are charged. The capacitance of benzylammonium salicylate was lower than the capacitance of sodium trifluoroacetate and the tilt of the curve was higher; these results were attributed to the fact that benzylammonium salicylate is a bulkier ion and its resistivity inside the pore is apparently higher. Interactions with pore walls are likely to influence ion mobility; bulky ions adsorbed near the surface may interfere with transport of ions farther inward.

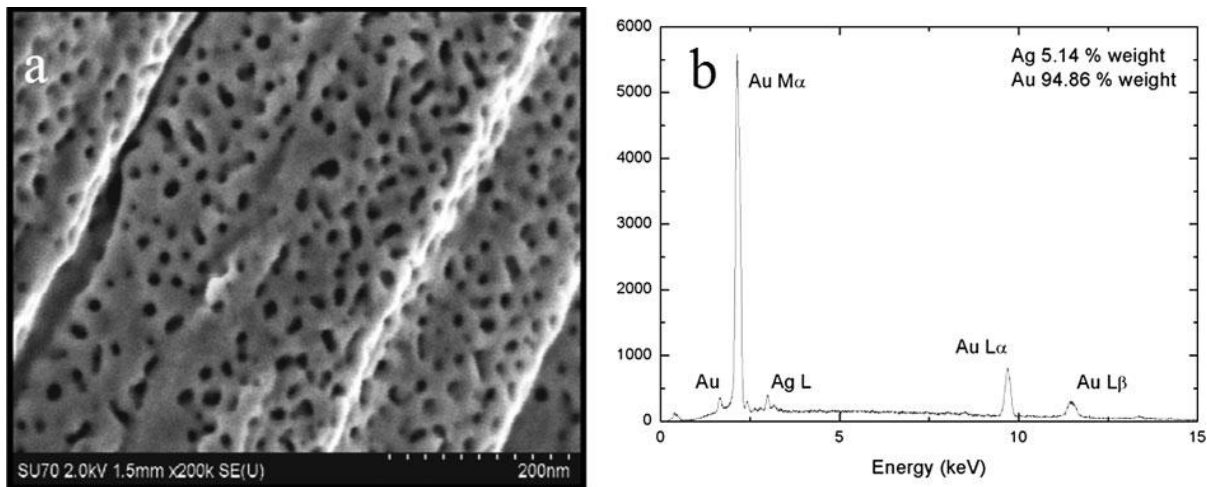


Figure 2. (a) Scanning electron micrograph of nanoporous gold electrode produced by electrochemical etching. The average pore diameter is 9.86 ± 4.92 nm. (b) Energy dispersive X-ray spectrum of etched nanoporous wire after background subtraction. The wires were shown to contain 94.86 wt% gold and 5.14 wt% silver.

We did not observe redox reactions or highly nonlinear capacitance over this range for benzylammonium salicylate and sodium trifluoroacetate. In voltammograms of other analytes, such as $\text{Fe}(\text{bipyridine})_3\text{SO}_4$ and potassium aminobenzoate, we observed large current excursions indicative of redox reactions in certain voltage ranges. Since redox reactions can alter the chemical structure and biological activity of a pharmacologic agent, it is important to maintain voltage within a range where redox of the pharmacologic agent does not occur. Studies have also indicated that electrode performance is diminished at large (> 1 V) voltages. Little variation was observed in cyclic voltammetry and chronoamperometry

data that was obtained with reused electrodes; *e.g.*, voltammograms performed in 30 mM sodium trifluoroacetate varied by about 2.5% over three scans.

The chronoamperometry responses of the electrodes in 100 mM sodium trifluoroacetate and 50 mM benzylammonium salicylate solutions are presented in Figs. 3c and d. The response with sodium trifluoroacetate is comparable to the exponential response of an ideal resistor-capacitor circuit, indicating that it becomes nearly fully charged over the timescale of the experiment.

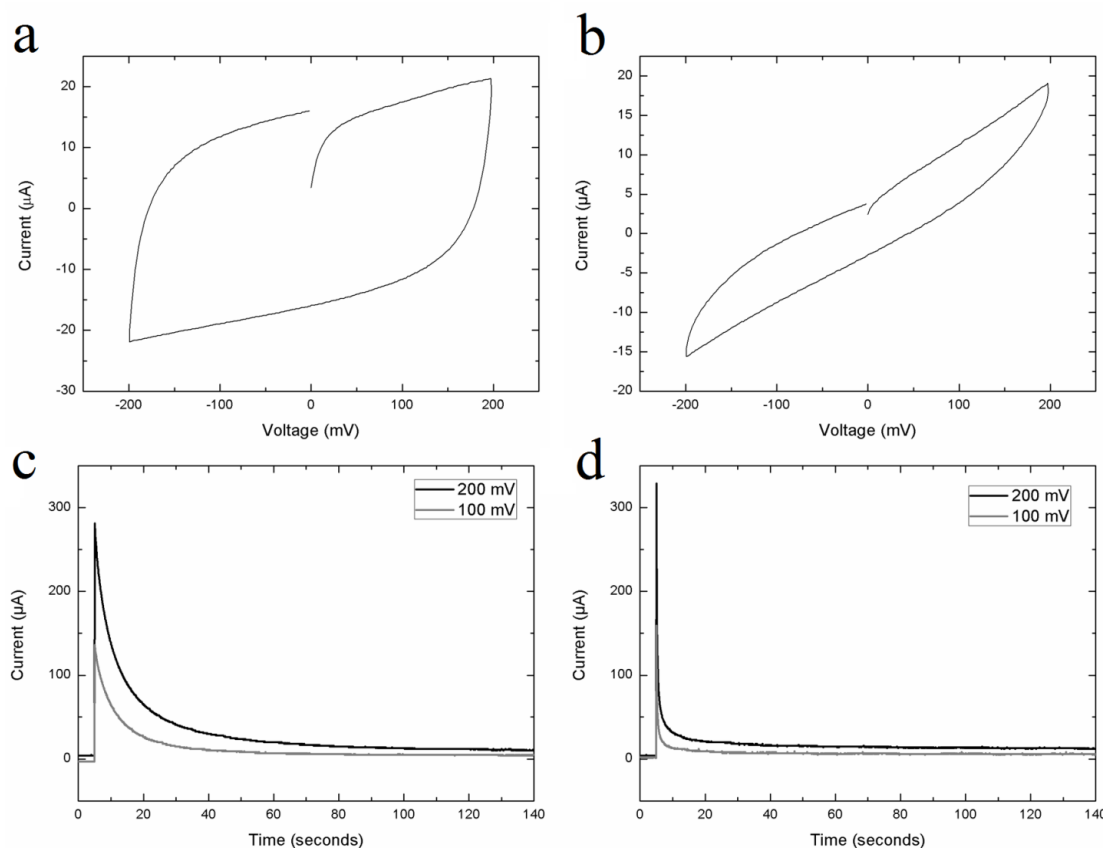


Figure 3. Electrochemical characterization of nanoporous electrodes. (a) Cyclic voltammetry of 100 mM sodium trifluoroacetate. (b) Cyclic voltammetry of 50 mM benzylammonium salicylate at a 5 mV/s scan rate. (c) Chronoamperometry of 100 mM sodium trifluoroacetate with 100 and 200 mV applied. (d) Chronoamperometry of 50 mM benzylammonium salicylate with 100 and 200 mV applied.

The total charge stored on the wire can be calculated by integrating the chronoamperometry response (Table 2). As shown in the chronoamperometry response waveforms, applying higher voltages results in greater charge storage. In addition, the storage capacity was not dependent on the analyte over the longer timescale of this experiment. Figure 4 shows the net

charge accumulated on electrodes during charging and discharging of 50 mM benzylammonium salicylate. The charging and discharging profiles are similar, indicating that the process is nearly reversible. We have also observed this phenomenon in several repeated charge-discharge cycles for sodium trifluoroacetate and sodium salicylate. The reversibility and long cycle life of porous electrodes forms the basis for use of these materials in supercapacitor and chemical separation applications [48].

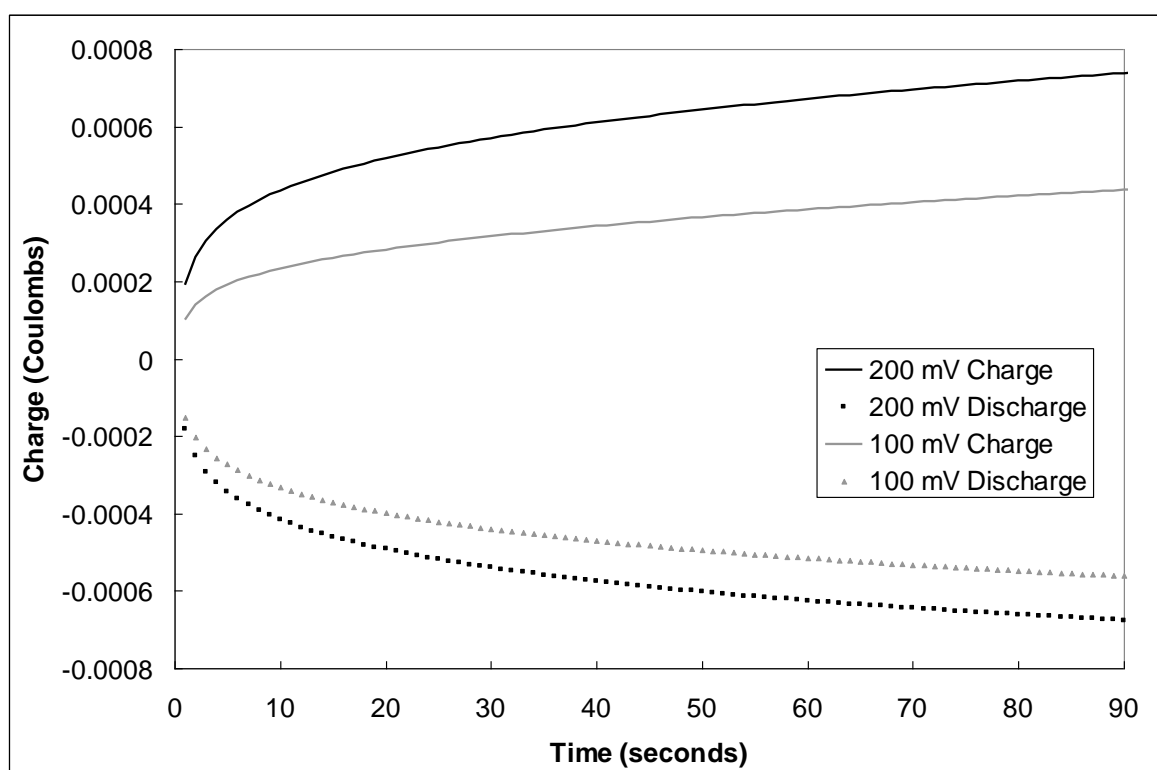


Figure 4. Net charge accumulated on electrodes during charging and discharging of 50 mM benzylammonium salicylate. Charging was performed with applied voltages of 100 and 200 mV and discharging was performed by applying 0 mV.

Table 2. Experimental charge storage of nanoporous gold wires

Analyte	Stored charge at 100 mV	Stored charge at 200 mV
100 mM sodium trifluoroacetate	1.181 mC	3.085 mC
50 mM benzylammonium salicylate	1.189 mC	3.078 mC

Table 3. Release of benzylammonium salicylate measured *via* UV spectroscopy

Voltage change	Charge released	Moles released
200–0 mV	6.33 mC	65.6 nmol
200–100 mV	3.25 mC	33.7 nmol
100–0 mV	1.77 mC	18.3 nmol

UV spectroscopy of the solutions with electrostatically delivered benzylammonium salicylate confirmed that nanoporous gold supercapacitors enabled storage and release of the model pharmacologic agent. UV absorption spectra are shown in Fig. 5; the amount of benzylammonium salicylate released by the nanoporous electrodes as computed from these is presented in Table 3. The absorption data corresponded with the trends in chronoamperometry data, which indicated that the storage capacity at 200 mV was more than double the storage capacity at 100 mV. The measured charge released *via* spectroscopy (converted from moles through Faraday's constant, 96500 Coulombs/ mole) was greater than the charge obtained from chronoamperometry, with a greater discrepancy occurring for 200 mV than for 100 mV. The measured storage capacities were 6.33 mC *versus* 3.078 mC and 1.77 mC *versus* 1.189 mC for 200 and 100 mV, respectively. One explanation for the

nonlinear storage capacity behavior is voltage dependent ion-pair adsorption. Upon a change in voltage, ion pairs can adsorb to (or desorb from) the electrode surface due to its changing chemical nature, carrying no net charge with them [59–61]. For example, this phenomenon may take place when anions coordinate to positively biased metal electrodes. Voltage dependent ion-pair adsorption would result in greater charge than what can be accounted for solely by capacitance. Chronoamperometry only measures charge storage *via* capacitance, whereas UV absorption spectroscopy measures the total charge storage; as a result, the spectroscopically derived charge storage values would be higher if voltage dependent ion-pair adsorption took place.

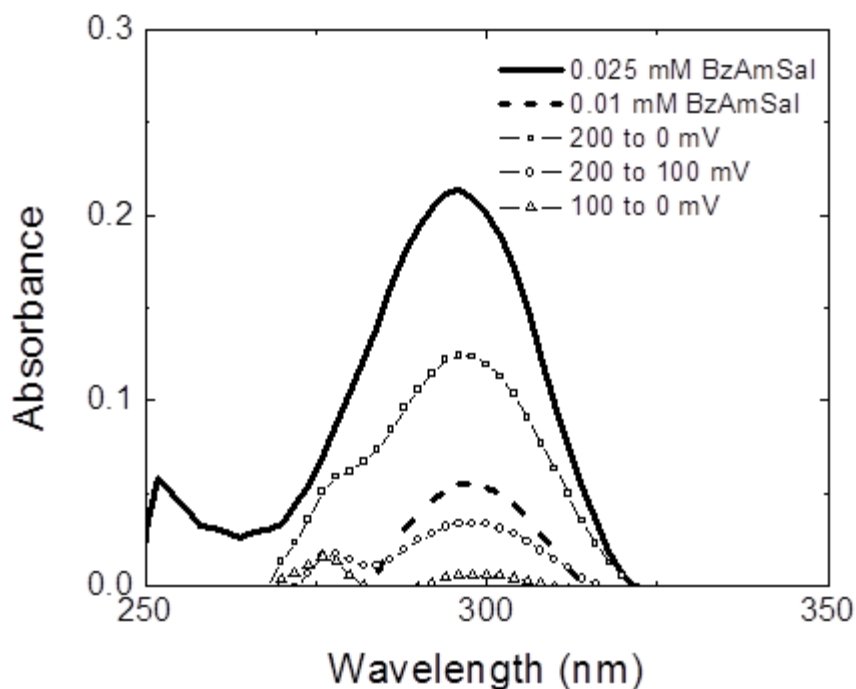


Figure 5. UV absorption spectrum of benzylammonium salicylate electrostatically stored in electrodes and delivered into 4 mL of 10 mM sodium trifluoroacetate. Quantity of drug released corresponded to voltage in a non-linear manner.

4 Conclusions

In this study, electrically controlled delivery of charged pharmacologically-relevant molecules by charging and release from supercapacitors was demonstrated. Electrochemical etching was shown to be an effective method to fabricate nanoporous electrodes out of gold–silver alloy. Ion adsorption and desorption were found to be voltage dependent but non-linear; storage capacity was shown to be augmented by voltage-dependent specific adsorption of ion pairs. This phenomenon is worthy of further study using a wider range of pharmacologic agents and electrode materials. Examination of controlled loading and release of other pharmacologically relevant molecules, particularly nucleic acids, is one promising area of future work.

Another important consideration is the nature of the liquid in which a drug is discharged. For example, when magnesium sulfate was used in the discharge solution instead of sodium trifluoroacetate, spontaneous discharge of drug was observed without altering the voltage. This behavior is expected if ion exchange is able to either decrease capacitance or introduce more favorable specific adsorbates; replacing a monovalent salt with a divalent salt is one possible mechanism for achieving this outcome. If such short-circuiting mechanisms exist, then the demonstrated voltage dependence may in fact reflect control over the rate of release and not necessarily control over the long-term absolute dose. The absolute dose may be regulated by controlling the initial amount of the pharmacologic agent that is stored in the electrodes.

At first glance, this approach appears limited to applications that require only small, targeted doses. However, integration of porous electrodes into a microneedle platform coupled to a microfluidic system may allow for repeated charging and discharging, so that overall dose is not bounded by electrode volume. *In vitro* and *in vivo* experiments are needed to examine pharmacologic agent transport in tissues after supercapacitor-based delivery. In addition, the incidence of skin trauma, inflammation, and infection following supercapacitor insertion into the skin needs to be assessed [22]. With its potential to reduce cost, minimize pain, and reduce tissue damage, supercapacitive drug delivery may provide advantages over conventional drug delivery methods.

The authors have declared no conflict of interest.

5 References

- [1] Brown, M. B., Martin, G. P., Jones, S. A., Akomeah, F. K., Dermal and transdermal drug delivery systems: Current and future prospects. *Drug Delivery* 2006, 13, 175–187.
- [2] Ovsianikov, A., Chichkov, B., Mente, P., Monteiro-Riviere, N. A. *et al.*, Two photon polymerization of polymer–ceramic hybrid materials for transdermal drug delivery. *Int. J. Appl. Ceram. Technol.* 2007, 4, 22–29.

- [3] Doraiswamy, A., Jin, C., Narayan, R. J., Mageswaran, P. *et al.*, Two photon polymerization of microneedles for drug delivery, *Acta Biomater.* 2006, 2, 267–275.
- [4] Gittard, S.D., Ovsianikov, A., Monteiro-Riviere, N. A., Lusk, J. *et al.*, Fabrication of polymer microneedles using a two-photon polymerization and micromolding process, *J. Diabetes Sci. Technol.* 2009, 3, 304–311.
- [5] Gill, H. S., Denson, D. D., Burris, B. A., Prausnitz, M. R., Effect of microneedle design on pain in human volunteers. *Clin. J. Pain* 2008, 24, 585–594.
- [6] Nir, Y., Paz, A., Sabo, E., Potasman, I., Fear of injections in young adults: Prevalence and associations. *Am. J. Trop. Med. Hyg.* 2003, 68, 341–344.
- [7] Rao, R., Nanda, S., Sonophoresis: Recent advancements and future trends. *J. Pharm. Pharmacol.* 2009, 61, 689–705.
- [8] Vandervoort, J., Ludwig, A., Microneedles for transdermal drug delivery: A minireview. *Front. Biosci.* 2008, 13, 1711– 1715.
- [9] Tanner, T., Marks, R., Delivering drugs by the transdermal route: Review and comment. *Skin Res. Technol.* 2008, 14, 249–260.

- [10] Brown, M. B., Martin, G. P., Jones, S. A., Akomeah, F. K., Dermal and transdermal drug delivery systems: Current and future prospects. *Drug Delivery* 2006, *13*, 175–187.
- [11] Lavon, A., Kost, J., Ultrasound and transdermal drug delivery. *Drug Discov.Today* 2004, *9*, 670–676.
- [12] Prausnitz, M. R., Langer, R., Transdermal drug delivery. *Nat. Biotechnol.* 2008, *26*, 1261–1268.
- [13] Elias, P. M., The stratum corneum as an organ of protection old and new concepts, in: Fritsch, P. G., Hintner, H. (Eds.), *Current Problems in Dermatology*, S. Karger Ag, Basel, Switzerland 1989, pp. 10–21.
- [14] Prausnitz, M. R., Mitragotri, S., Langer, R., Current status and future potential of transdermal drug delivery. *Nat. Rev. Drug Discov.* 2004, *3*, 115–124.
- [15] Chabri, F., Bouris, K., Jones, T., Barrow, D., *et al.*, Microfabricated silicon microneedles for nonviral cutaneous gene delivery. *Br. J. Dermatol.* 2004, *150*, 869–877.
- [16] Mukerjee, E., Collins, S. D., Isseroff, R. R., R. L., Microneedle Array for transdermal biological fluid extraction and in situ analysis. *Sens. Actuators* 2004, *114A*, 267–275.

- [17] Williams, A. C., Barry, B. W., Penetration enhancers. *Adv. Drug Delivery Rev.* 2004, 56, 603–618.
- [18] Mitragotri, S., Blankschtein, D., Langer, R., Transdermal drug delivery using low-frequency sonophoresis. *Pharm. Res.* 1996, 13, 411–420.
- [19] Paliwal, S., Menon, G. K., Mitragotri, S., Low-frequency sonophoresis: Ultrastructural basis for stratum corneum permeability assessed using quantum dots. *J. Invest. Dermatol.* 2006, 126, 1095–1101.
- [20] Kalia, Y. N., Naik, A., Garrison, J., Guy, R. H., Iontophoretic drug delivery. *Adv. Drug Delivery Rev.* 2004, 56, 619–658.
- [21] Pikal, M. J., The role of electroosmotic flow in transdermal iontophoresis. *Adv. Drug Delivery Rev.* 2001, 46, 281–301.
- [22] Birchall, J. C., Microneedle array technology: The time is right but is the science ready? *Expert Rev. Med. Devices* 2006, 3, 1–4.
- [23] Gill, H. S., Prausnitz, M. R., Coated microneedles for transdermal delivery. *J. Controlled Release* 2007, 117, 227–237.

[24] Park, J. H., Allen, M.G., Prausnitz, M. R., Polymer microneedles for controlled-release drug delivery. *Pharm. Res.* 2006, 23, 1008–1019.

[25] Miyano, T., Tobinaga, Y., Kanno, T., Matsuzaki, Y., Sugar micro needles as transdermic drug delivery system. *Biomed. Microdev.* 2005, 7, 185–188. [26] Lee, J.W., Park, J. H., Prausnitz, M. R., Dissolving microneedles for transdermal drug delivery. *Biomaterials* 2008, 29, 2113–2124.

[27] Wang, P. M., Cornwell, M., Hill, J., Prausnitz, M. R., Precise microinjection into skin using hollow microneedles. *J. Invest. Dermatol.* 2006, 126, 1080–1087.

[28] Suzuki, H., Tokuda, T., Kobayashi, K., A disposable “intelligent mosquito” with a reversible sampling mechanism using the volume-phase transition of a gel. *Sens. Actuators* 2002, 83B, 53–59.

[29] Zahn, J. D., Deshmukh, A., Pisano, A. P., Liepmann, D., Continuous on-chip micropumping for microneedle enhanced drug delivery. *Biomed. Microdev.* 2004, 6, 183–190.

[30] Davis, S. P., Martanto, W., Allen, M. G., Prausnitz, M. R., Hollow metal microneedles for insulin delivery to diabetic rats. *IEEE Trans. Biomed. Eng.* 2005, 52, 909–915.

- [31] Smart, W. H., Subramanian, K., The use of silicon microfabrication technology in painless blood glucose monitoring. *Diabetes Technol. Ther.* 2000, 2, 549–559.
- [32] Takeichi, T., Yamazaki, Y., Zuo, M., Ito, A. *et al.*, Preparation of porous carbon films by the pyrolysis of poly(urethaneimide) films and their pore characteristics. *Carbon* 2001, 39, 257–265.
- [33] Attard, G. S., Corker, J. M., Goltner, C.G., Henke, S. *et al.*, Liquid-crystal templates for nanostructured metals. *Angew. Chem., Int. Ed. Engl.* 1997, 36, 1315–1317.
- [34] Robinson, D. B., Fares, S. J., Ong, M. D., Arslan, I. *et al.*, Scalable synthesis of nanoporous palladium powders. *Int. J. Hydrogen Energy* 2009, 34, 5585–5591.
- [35] Biener, J., Hodge, A. M., Hamsa, A. V., Hsiung, L. M. *et al.*, Nanoporous Au: A high yield strength material. *J. Appl. Phys.* 2005, 97, 024301, DOI: 10.1063/1.1832742.
- [36] Biener, J., Hodge, A. M., Hamza, A. V., Microscopic failure behavior of nanoporous gold. *Appl. Phys. Lett.* 2005, 87, 121908, DOI: 10.1063/1.2051791.
- [37] Pierson, B. E., *Characterization and Evaluation of a Novel Nanoporous Gold Biosensor Substrate*, M.S. thesis, North Carolina State University 2009.

- [38] Ying, T. Y., Yang, K. L., Yiacoumi, S., Tsouris, C., Electrosorption of ions from aqueous solutions by nanostructured carbon aerogel. *J. Colloid Interface Sci.* 2002, 250, 18–27.
- [39] de Levie, R., On porous electrodes in electrolyte solutions: I. Capacitance effects. *Electrochim. Acta* 1963, 8, 751–780.
- [40] de Levie, R., On porous electrodes in electrolyte solutions – IV. *Electrochim. Acta* 1964, 9, 1231–1245.
- [41] Keiser, H., Beccu, K. D., Gutjahr M. A., Abschätzung der porenstruktur poröser elektroden aus impedanzmessungen. *Electrochim. Acta* 1976, 21, 539–543.
- [42] Posey, F. A., Methods for the calculation of polarization in porous electrodes. *J. Electrochem. Soc.* 1964, 111, 1173–1181.
- [43] Forty, A. J., Durkin, P., A morphological study of the dissolution of silver-gold alloys in nitric acid. *Philos. Mag. A* 1980, 42, 295–318.
- [44] Vix-Guterl, C., Frackowiak, E., Jurewicz, K., Friebe, M. *et al.*, Electrochemical energy storage in ordered porous carbon materials. *Carbon* 2005, 43, 1293–1302.

- [45] Terres, E., Panella, M., Hayashi, T., Kim, Y.A. *et al.*, Hydrogen storage in spherical nanoporous carbons. *Chem. Phys. Lett.* 2005, *403*, 363–366.
- [46] Simon, P., Gogotsi, Y., Materials for electrochemical capacitors. *Nat. Mater.* 2008, *7*, 845–854.
- [47] Farmer, J. C., Fix, D.V., Mack, G.V., Pekala, R.W. *et al.*, Capacitive deionization of NaCl and NaNO₃ solutions with carbon aerogel electrodes. *J. Electrochem. Soc.* 1996, *143*, 159–169.
- [48] Oren, Y., Capacitive deionization (CDI) for desalination and water treatment – past, present, and future (a review). *Desalination* 2008, *288*, 10–29.
- [49] Deinhammer, R. S., Ting, E. N., Porter, M. D., Electrochemically modulated liquid chromatography (EMLC): A new approach to gradient elution separations. *J. Electroanal. Chem.* 1993, *362*, 295–299.
- [50] Chang, A.C., Miller, L. L., Electrochemically controlled binding and release of salicylate, TCNQ and ferrocyanide from films of oligomeric 3-methoxythiophene. *J. Electroanal. Chem.* 1988, *247*, 173–184.

- [51] Miller, L. L., Zhou, Q. X., Poly(*N*-methylpyrrolylium) poly(styrenesulfonate) – a conductive, electrically switchable cation exchanger that cathodically binds and anodically releases dopamine. *Macromolecules* 1987, 20, 1594–1597.
- [52] Blankespoor, R., Miller, L. L., Polymerized 3-methoxythiopene: A processable material for the controlled release of anions. *J. Chem. Soc. Chem. Commun.* 1985, 90–92.
- [53] Wang, J., Jiang, M., Fortes, A., Mukherjee, B., New label-free DNA recognition based on doping nucleic-acid probes within conducting polymer films. *Anal. Chim. Acta* 1999, 402, 7–12.
- [54] Brazeau, G. A., Fung, H. L., An *in vitro* model to evaluate muscle damage following intramuscular injections. *Pharm. Res.* 1989, 6, 167–170.
- [55] Jorgensen, J.T., Romsing, J., Rasmussen, M., Moller-Sonnergaard, J. *et al.*, Pain assessment of subcutaneous injections. *Ann. Pharmacother.* 1996, 30, 729–732.
- [56] Kyle, A. A., Dahl, M.V., Topical therapy for fungal infections. *Am. J. Clin. Dermatol.* 2004, 5, 443–451.
- [57] Matthews, P., Derry, S., Moore, R. A., McQuay, H. J., Topical rubefacients for acute and chronic pain in adults. *Cochrane Database Syst. Rev.* 2009, 8, CD007403.

[58] Bard A. J., Faulkner, L. R. (Eds.), *Electrochemical Methods: Fundamentals and Applications*, John Wiley & Sons, 1980, New York.

[59] Pell, W. G., Conway, B. E., Voltammetry at a de Levie brush electrode as a model for electrochemical supercapacitor behaviour. *J. Electroanal. Chem.* 2001, 500, 121–133.

[60] Grahame, .C., The electrical double layer and the theory of electrocapillarity. *Chem. Rev.* 1947, 41, 441–501.

[61] Barclay, D. J., Chemical softness and specific adsorption at electrodes. *J. Electroanal. Chem.* 1968, 65, 318–321.

4. RAPID PROTOTYPING OF MICRO- AND NANOSCALE DEVICES FOR REGENERATIVE MEDICINE

4.1 Rapid prototyping of scaphoid and lunate bones

*The following section is the pre-peer reviewed version of the following article:
Biotechnology Journal, Volume 4, Gittard SD, Narayan RJ, Lusk J, Morel P, Stockmans F,
Ramsey M, Laverde C, Phillips J, Monteiro-Riviere NA, Ovsianikov A, Chichkov BN. Rapid
prototyping of scaphoid and lunate bones, pages 129-134. Copyright 2009. Reproduced by
permission of Wiley-VCH Verlag GmbH & Co. KGaA*

Short Communication

Rapid prototyping of scaphoid and lunate bones

Shaun D. Gittard¹, Roger J. Narayan¹, Jason Lusk², Pierre Morel², Filip Stockmans³, Michael Ramsey⁴, Claire Laverde⁴, Jack Phillips⁴, Nancy A. Monteiro-Riviere^{1,5}, Aleksandr Ovsianikov⁶ and Boris N. Chichkov⁶

¹Joint Department of Biomedical Engineering, University of North Carolina/North Carolina State University, Raleigh, NC, USA

²ElectroForce Systems Group, Bose Corporation, Eden Prairie, MN, USA

³Katholieke Universiteit Leuven, Heule Kortrijk, Belgium

⁴Cardinal Health, Creedmoor, NC, USA

⁵Center for Chemical Toxicology Research and Pharmacokinetics, North Carolina State University, Raleigh, NC, USA

⁶Nanotechnology Department, Laser Zentrum Hannover e.V., Hannover, Germany

In this study, a novel rapid prototyping technology was used to fabricate scaphoid and lunate bone prostheses, two carpal bones that are prone to avascular necrosis. Carpal prostheses were fabricated with an Envisiontec Perfactory® SXGA stereolithography system using Envisiontec eShell 200 photocurable polymer. Fabrication was guided using 3-D models, which were generated using Mimics software (Materialise NV, Leuven, Belgium) from patient computer tomography data. The prostheses were fabricated in a layer-by-layer

manner; ~50- μ m thick layers were observed in the prostheses. Hardness and Young's modulus values of polymerized eShell 200 material were 93.8 ± 7.25 MPa and 3050 ± 90 MPa, respectively. The minimum compressive force required for fracture was 1360 N for the scaphoid prosthesis and 1248 N for the lunate prosthesis. Polymerized Envisiontec eShell material exhibited high human neonatal epidermal keratinocyte cell viability rate in an MTT assay. The results of this study indicate that small bone prostheses fabricated by stereolithography using eShell 200 polymer may have suitable geometry, mechanical properties, and cytocompatibility properties for *in vivo* use.

Correspondence: Dr. Roger Narayan, University of North Carolina –
Biomedical Engineering, 152 Macnider Hall Campus Box 7575, Chapel
Hill, North Carolina 27599-7575, NC, USA

E-mail: roger_narayan@msn.com

Fax: +1-509-696-8481

Abbreviations: **CAD**, computer-aided design; **MT**, 3-(4,5-Dimethylthiazol-2-yl)-2,5-diphenyltetrazoliumbromide.

Keywords: Biomaterials · Prostheses · Rapid prototyping

Fracture of the carpal bones (small bones in the hand) commonly occurs as a result of motor vehicle accident or physical activity. Avascular necrosis (absence of blood supply to the

bone) can result from fracture to these bones. Nonunion of the wrist bones can in turn result in arthritis, which is associated with several problems, including pain, reduced range of motion, weakened grip strength, and joint instability [1].

The scaphoid and lunate are two carpal bones that are frequently affected by avascular necrosis [2]. These bones are located on the proximal row of the carpal bones, where they articulate with a bone in the forearm known as the radius. The multiple surfaces of these bones allow the wrist joint to exhibit wide range of motion and maintain stability. The scaphoid exhibits a boat-like shape and a length of ~25.8 mm [3]. The superior, inferior, medial, and distal convex surfaces of the scaphoid articulate with the surrounding bones. On the other hand, the dorsal, volar, and lateral surfaces serve as ligament attachment sites. The lunate has a crescent shape with wedge shapes at its lateral and dorsal ends. Its superior, inferior, lateral, and medial surfaces are sites of bone articulation and the dorsal and volar surfaces are sites of ligament attachment. The shape of both scaphoid and lunate bones can vary greatly from patient to patient [3, 4].

The vascularity of the wrist provides poor circulation to the scaphoid and lunate [2]. Consequently, fracture of these bones often results in avascular necrosis [1, 2, 5]. The scaphoid is the most commonly fractured carpal bone, accounting for 71.2% of all carpal fractures [6]. Idiopathic avascular necrosis of the lunate bone (Kienböck's disease) and less commonly the scaphoid bone (Preiser's disease) have been reported [5, 7, 8, 9]. If left untreated, collapse of the affected bones can occur [2]. Diagnosis of avascular necrosis can

be performed by radiography, magnetic resonance imaging (MRI), or computed tomography (CT). Computed tomography is particularly helpful for determining the degree of bone degradation in late-stage carpal degenerative diseases [2].

Treatments for carpal avascular necrosis include electromagnetic stimulation, immobilization, operative revascularization, and vascularized bone grafting [2]. Often a combination of these treatments is used. In cases of advanced bone degeneration, resection or excision of the carpal bones is required. Swanson introduced silastic (polydimethylsiloxane) implants for replacement of resected or excised carpal bones in 1970 [10]. Carpal bone implants fabricated using conventional silicone elastomer (CSE) and high-performance silicone elastomer (HSE) have been utilized for the treatment of Kienbock's disease and other conditions [11, 12]. However, use of these implants is now discouraged due to concerns over microparticle-induced synovitis, which is a joint inflammation process that results from abrasion or other damage to the implant [12–15]. Proximal row carpectomy, arthrodesis, interposition arthroplasty, or total wrist arthroplasty are currently the most common treatments for avascular necrosis of the small hand bones [2, 16, 17].

Our approach is to utilize rapid prototyping technology to fabricate prostheses for treating carpal bone degeneration. In rapid prototyping, computer aided design (CAD) models are used to guide layer-by-layer additive fabrication of a given part. Obtaining CAD models of carpal bones for rapid prototyping is relatively simple since computed tomography data can both be used to make CAD models and diagnose carpal degeneration [18]. Computed

tomography data have provided the basis for fabrication of craniofacial prostheses [19–21], auricular prostheses [22], knee prostheses [23], and orthopedic prostheses [24–26] using computer controlled milling, fused deposition modeling, 3-D printing, selective laser sintering, stereolithography, and other rapid prototyping techniques [22, 26, 27]. The combination of computed tomography data and rapid prototyping has also been used to make molds for prosthesis fabrication [19, 21, 22]. There are several benefits to rapid prototyping of patient-specific prostheses, including reduced processing time, reduced cost, and the ability to tailor prosthesis geometry to patient requirements [26].

In this study, a Perfactory® SXGA system (Envisiontec, Gladbeck, Germany) was used to fabricate patient-specific scaphoid and lunate prostheses. This stereolithography system uses STL files to precisely guide a light beam over a photocurable resin; exposure to light results in selective polymerization of the exposed resin. Envisiontec eShell 200, a commercially available photocurable resin, was used to fabricate the carpal bone prostheses. Scanning electron microscopy (SEM), energy-dispersive X-ray spectroscopy, nanoindentation, and compression tests were performed to assess the structural and mechanical properties of these prostheses. Finally, an MTT assay was performed to determine the cell viability of the eShell 200 material that was used to fabricate the carpal bone prostheses.

Three-dimensional models of the scaphoid and lunate bones were created by Dr. Filip Stockmans from patient CT data (Katholieke Universiteit, Leuven, Belgium). The computed tomography data were imported into Mimics software (Materialise, Leuven, Belgium). This

commercial software processes and edits computed tomography, magnetic resonance imaging, and microscopy scanning data in order to produce 3-D models. Mimics software has previously been used to design custom orthopedic implants based on computed tomography data [20, 21, 23].

Prostheses of scaphoid and lunate bones were fabricated using Envisiontec eShell 200 material (Envisiontec, Gladbeck, Germany). This material is a photocurable polymer designed by Envisiontec specifically for use on their rapid prototyping systems. Information provided by the supplier indicates that eShell 200 is comprised of 60–80% wt urethane dimethacrylate, 15–30% wt propylated (2) neopentyl glycoldiacrylate, and 0.5–1.5% wt phenylbis(2,4,6 Trimethylbenzoyl)-phosphine oxide photoinitiator. Rapid prototyping of the scaphoid and lunate bone prostheses was performed using an Envisiontec Perfactory® SXGA system (Envisiontec, Gladbeck, Germany). The Envisiontec system utilized STL format three-dimensional models of the patient scaphoid and lunate bones in order to fabricate the carpal bone prostheses. This system uses a 150-W halogen bulb as the light source for resin polymerization. Illumination in the X,Y plane within the Envisiontec system was regulated by DLP (directed light projection)

optics (Texas Instruments, Dallas, TX). The DLP SXGA guidance chip used for fabrication of carpal bone prostheses exhibits 1280×1024 -pixel resolution. The scaphoid and lunate bones were fabricated in 50- μm thick layers in the Z direction. After fabrication, the Envisiontec eShell 200 prostheses were washed in isopropanol for two 10-min intervals in an

ultrasonic tank; fresh isopropanol was used for each wash cycle. Post-building curing was performed using a post-build oven with a 400-W UVA Enhanced Metal Halide Lamp (Uvitron International, West Springfield, MA). This lamp provides light exposure over a wavelength range of 275–675 nm. The prostheses were placed on a glass plate in a reflective metal bowl and baked in an oven for 60 min; the prostheses were flipped over at 30 min.

Surface morphology of the scaphoid and lunate prostheses were examined using a S3200 scanning electron microscope (Hitachi, Tokyo, Japan) equipped with a Robinson back scattered electron detector. The chemical composition of the prostheses was determined by energy-dispersive X-ray spectroscopy. Hardness and Young's modulus values of polymerized Envisiontec eShell 200 polymer were determined using a Nano Hardness Tester system (CSM Instruments, Needham, MA). Solid Envisiontec eShell 200 chips ($0.2 \times 3 \times 1.5$ cm dimensions) were examined using a maximum force of 300 mN, loading rate of 600 mN/min, and unloading rate of 600 mN/min. In this instrument, a Berkovich triangular pyramid indenter tip was driven into the material with increasing normal load. After a maximum force was attained, the load was reduced until either partial or complete relaxation took place. Hardness and Young's modulus values were derived from the resulting load/displacement curves using the Oliver and Pharr computation method [28]. Compression tests were performed on the scaphoid ($n = 3$) and lunate ($n = 3$) prostheses using a Bose ElectroForce 3300 test system (Bose, Eden Prairie, MN). The scaphoid was oriented in the load cell so one plate moved against the dorsal side of the waist and the other plate moved against the ends of the concave volar side; the loading direction was oriented perpendicularly

to the build layers. A compressive loading rate of 10 N/sec was applied to the prostheses; testing was performed under load control.

The MTT assay was used to examine the viability of neonatal human epidermal keratinocytes on Envisiontec eShell 200 polymer. Cylindrical pellets of Envisiontec eShell 200 ($n = 3$) having a surface area of 6.08cm² were fabricated by exposing liquid Envisiontec eShell 200 polymer in polydimethylsiloxane molds to a high intensity ultraviolet curing lamp with wavelengths in the visible and ultraviolet range (Thorlabs, Newton, NJ). These pellets were sterilized using ultraviolet B radiation for 4 h; the pieces were rotated every 90 min and flipped over to ensure complete sterilization. Test materials and polystyrene culture wells were washed with 1 mL of keratinocyte growth media (KGM-2). KGM-2 media consists of serum-free keratinocyte basal media supplemented with bovine pituitary extract, epinephrine, GA-1000 (gentamicin-amphotericin), human epidermal growth factor, hydrocortisone, insulin, and transferrin. A small drop of Akwa Tears® (Akorn, Buffalo Grove, IL) was placed on the bottom of the polymers to secure them to the base of each well in order to prevent floating. Human epidermal keratinocytes (Lonza, Walkersville, MD) (285 000) were seeded in 10 mL of KGM-2 media and cultured at 37°C in a humidified environment of 5% CO₂ until 70% confluency was reached. Twenty-four hours after confluency was reached, MTT assay (3-[4,5-dimethyl-2-thiazol]- 2,5-diphenyl-2H-tetrazolium bromide) was used to assess viability of the human epidermal keratinocytes [29]. A Multiskan RC ELISA plate reader (Labsystems, Helsinki, Finland) was used to determine absorbance at $\lambda = 550$ nm, which is directly proportional to mitochondrial activity. Test materials were moved to a new

plate prior to reading in order to prevent the influence of cells that were growing on the plate. Human epidermal keratinocyte counts were adjusted for surface area and statistically compared to media control using ANOVA (SAS 9.1 for Windows) (SAS, Cary, NC).

Rapid prototyping with the Envisiontec Perfactory® SXGA system produced scaphoid and lunate bone prostheses that exhibited excellent fidelity with the imaging data. Images of CAD models (Fig. 1a) and Envisiontec eShell 200 bone prostheses (Fig. 1b) demonstrate that the small bone prostheses appropriately match the shape and contours of the CAD models. The build layers of the prostheses can be seen under high magnification using scanning electron microscopy (Fig. 2). The spacing between the build layers was 50 μm ; this is the minimum layer spacing that may be obtained with eShell 200 resin in the Perfactory SXGA system. Other rapid prototyping procedures, including fused deposition modeling (254 μm) [22] and selective laser sintering (30–100 μm) [26], demonstrate a lower degree of precision. Energy-dispersive X-ray spectroscopy indicated that the polymerized Envisiontec eShell 200 polymer contains carbon, oxygen, and titanium; these elements are considered to possess excellent biocompatibility [30, 31].

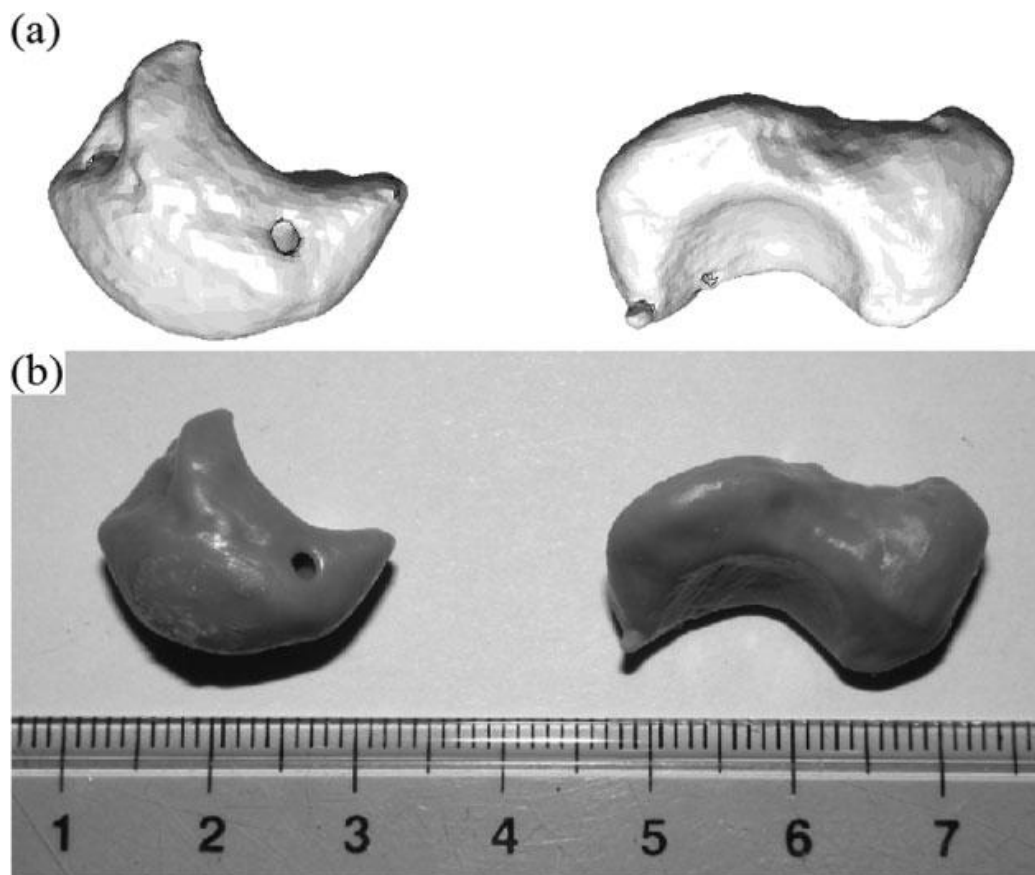


Figure 1. (a) CAD model of lunate (left) and scaphoid (right) bones based on patient computed tomography data. (b) Envisiontec eShell 200 prostheses of lunate (left) and scaphoid (right) bones.

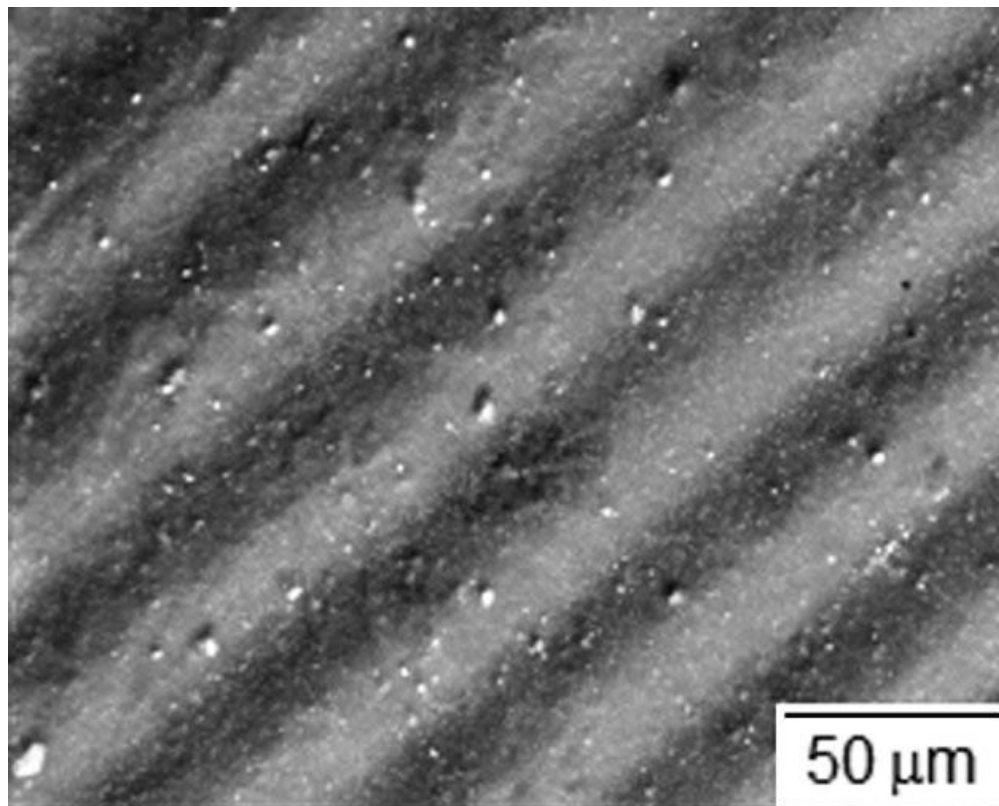


Figure 2. Scanning electron micrograph of eShell 200 material polymerized using Perfactory® SXGA system.

Nanoindentation testing determined the hardness of polymerized Envisiontec eShell 200 resin to be less than that of human bone. The hardness and Young's modulus of Envisiontec eShell 200 were 93.8 ± 7.25 MPa and 3050 ± 90 MPa, respectively; these values are lower than those of healthy human bone (hardness = 234–760 MPa) [32]. A characteristic plot of force (black line) and displacement (gray line) versus time for an eShell 200 scaphoid prosthesis is shown in Fig. 3. It was noted that prosthesis fracture occurred perpendicularly to the build layers. The minimum compressive forces required for fracture were 1360 and 1248 N for the scaphoid and lunate bone prostheses, respectively. In comparison, the fracture force

for healthy human scaphoid bones has been reported as 2410 ± 913 N [33]. The lower limit of fracture for healthy human scaphoid bones is similar to the lower limit of fracture for eShell 200 prostheses. The MTT cell viability assay indicated that Envisiontec eShell 200 does not adversely affect the cell viability of human epidermal keratinocytes (Fig. 4). The Envisiontec eShell 200 polymer demonstrated better cell viability than the polystyrene control surface. The cell viability rate of Envisiontec eShell 200 (107% viability compared to polystyrene control) is comparable to that of other photopolymers used in medical applications, including phosphate-containing hydrogel (97–113%) [34], acrylic acid-based hydrogel (95–124.6%) [35], and glass-ionomer cement (55.8–99.4%) [36].

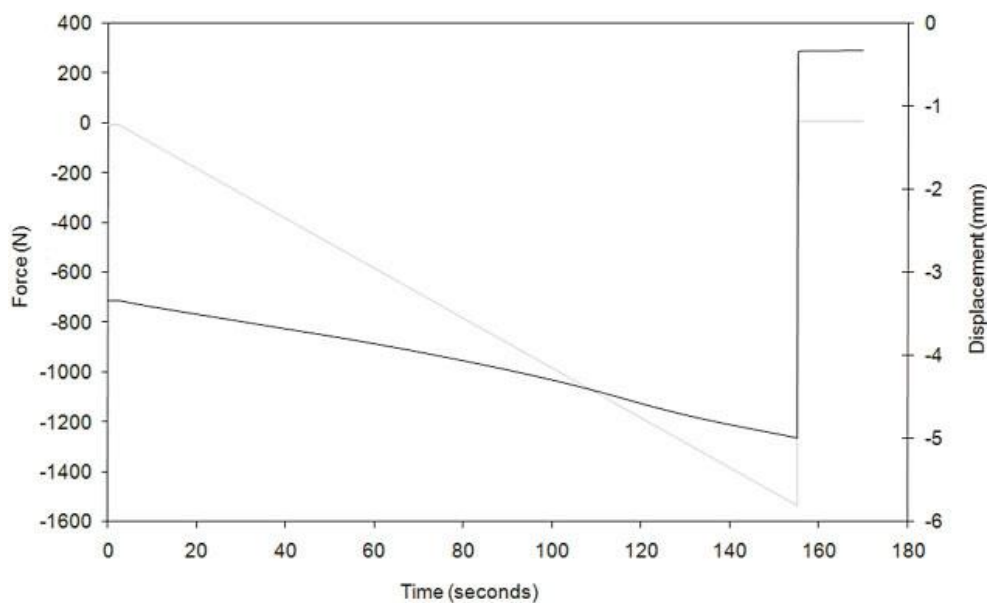


Figure 3. Characteristic plot of force (black line) and displacement (gray line) *versus* time for an eShell 200 scaphoid prosthesis.

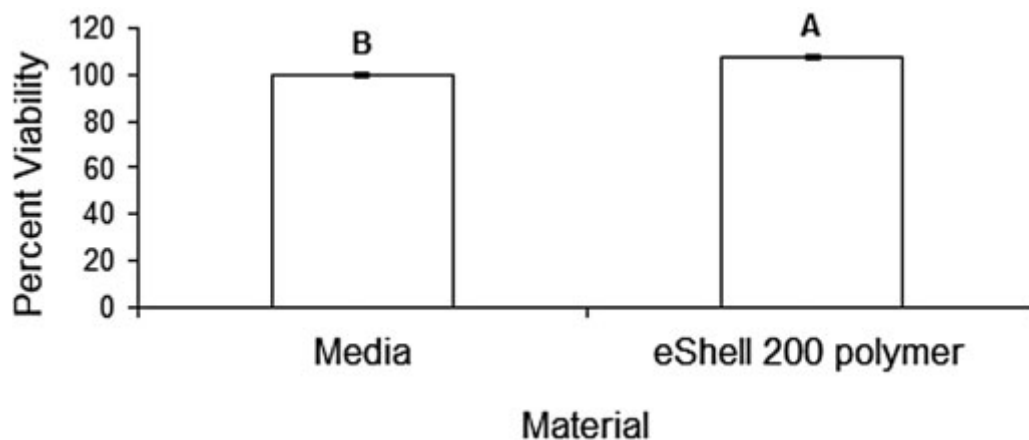


Figure 4. MTT viability of human epithelial keratinocytes on eShell 200 polymer and control substrates.

In the future, medical imaging may be employed in order to prepare patient- specific medical prostheses, which possess appropriate design features, including size, weight, and geometry, for a given condition and for a given patient. While the design of implants using three-dimensional image processing software is relatively well-established, the ability to directly write orthopedic prostheses with appropriate precision, mechanical properties, and cytocompatibility remains a challenge. Use of Envisiontec Perfactory® SXGA stereolithography system and eShell 200 polymer provides a promising step towards the development of patient-specific small bone prostheses.

The authors would like to thank K. Evaul and A. O. Inman (Center for Chemical Toxicology Research and Pharmacokinetics, North Carolina State University) for their assistance with the MTT assays.

The authors have declared no conflict of interest.

References

- [1] Lee, C. C., Syed, H., Crupi, R. S., Avascular necrosis of common bones seen in the ED. *Am. J. Emerg. Med.* 2003, 21, 336–338.
- [2] Botte, M. J., Pacelli, L. L., Gelberman, R. H., Vascularity and osteonecrosis of the wrist. *Orthop. Clin. North Am.* 2004, 35, 405–421.
- [3] Ceri, N., Korman, E., Gunal, I., Tetik, S., The morphological and morphometric features of the scaphoid. *J. Hand Surg. Eur. [Br]* 2004, 29, 393–398.
- [4] Gupta, A., Al-Moosawi, N. M., Lunate morphology. *J. Biomech.* 2002, 35, 1451–1457.
- [5] Preiser, G., Eine typische posttraumatische und zur Spontanfraktur führende Ostitis des *Naviculare carpi*. *Fortschr. Geb. Rontgenstr.* 1910, 15, 189–197.
- [6] Bunk, B., Frokjaer, J., Larsen, C. F., Johannsen, H.G. *et al.*, Diagnosis of scaphoid fractures. A prospective multicenter study of 1052 patients with 160 fractures. *Acta Orthop. Scand.* 1995, 66, 359–360.

- [7] Kienbock, R., Uber traumatische Malazie des Mondbeinesund ihre Folgezustande: Entartungsformen und Kompressionsfrakturen. *Fortschr. Geb. Roentgenstr. Nuklearmed.* 1910, *16*, 77–103.
- [8] Ferlic, D. C., Morin, P., Idiopathic avascular necrosis of the scaphoid: Preiser's disease? *J. Hand Surg. [Am]* 1989, *14*, 13–16.
- [9] Allen, P. R., Idiopathic avascular necrosis of the scaphoid: a report of two cases. *J. Bone Joint Surg. Br.* 1983, *65*, 333–335.
- [10] Swanson, A. B., Silicone rubber implants for the replacement of the carpal scaphoid and lunate bones. *Orthop. Clin. North. Am.* 1970, *1*, 299–309.
- [11] Lichtman, D. M., Alexander, A. H., Mack, G. R., Gunther, S. F., Kienbock's disease. Update on silicone replacement arthroplasty. *J. Hand Surg. [Am]* 1982, *7*, 343–347.
- [12] Khoo, C.T. K., Silicone synovitis. The current role of silicone elastomer implants in joint reconstruction. *J. Hand. Surg. [Br]* 1993, *18*, 670–686.
- [13] Alexander, A. H., Turner, M. A., Alexander, C. E., Litchman, D. M. Lunate silicone replacement arthroplasty in Kienbock's disease: a long term follow-up. *J. Hand Surg. [Am]* 1990, *15*, 401–407.

- [14] Kaarela, O. I., Raatikainen, T. K., Tornainen, P. J., Silicone replacement arthroplasty for Kienbock's disease. *J. Hand Surg. [Br]* 1998, 23, 735–740.
- [15] Eiken, O., Ekerot, L., Lindström, C., Jonsson, K., Silicone carpal implants: risk or benefit? *Scand. J. Plast. Reconstr. Surg.* 1985, 19, 295–304.
- [16] Weiss, K. E., Rodner, C. A., Osteoarthritis of the wrist. *J. Hand Surg. [Am]* 2007, 32, 725–746.
- [17] Bain, G. I., Munt, J., Turner, P. C., New advances in wrist arthroscopy. *Arthroscopy* 2008, 24, 355–367.
- [18] Ryu, J. H., Kim, H. S., Lee, K. H., Contour-based algorithms for generating 3D CAD models from medical images. *Int. J. Adv. Manuf. Technol.* 2004, 24, 112–119.
- [19] Agner, C., Dujovny, M., Evenhouse, R., Charbel, F.T., Sadler, L., Stereolithography for posterior fossa cranioplasty. *Skull Base Surg.* 1998, 8, 81–86.
- [20] Singare, S., Dichen L., Bingheng, L., Yanpu, L., Zhenyu, G., Yaxiong, L., Design and fabrication of custom mandible titanium tray based on rapid prototyping. *Med. Eng. Phys.* 2004, 26, 671–676.

[21] Singare, S., Dichen, L., Bingheng, L., Zhenyu, G., Yaxiong, L., Customized design and manufacturing of chin implant based on rapid prototyping. *Rapid Prototyping J.* 2005, *11*, 113–118.

[22] Subburaj, J., Nair, C., Rajesh, S., Meshram, S. M., Ravi, B., Rapid development of auricular prosthesis using CAD and rapid prototyping technologies. *Int. J. Oral Maxillofac. Surg.* 2007, *36*, 938–943.

[23] Harryson, O. L.A., Hosni, Y.A., Nayfel, J.F., Custom-designed orthopedic implants evaluated using finite element analysis of patient-specific computed tomography data: femoral component case study. *BMC Musculoskelet. Disord.* 2007, *8*, 91–100.

[24] Berry, E., Brown, J. M., Connell, M., Craven, C. M. *et al.*, Preliminary experience with medical applications of rapid prototyping by selective laser sintering. *Med. Eng. Phys.* 1997, *19*, 90–96.

[25] Potamianos, P., Amis, A. A., Forester, A. J., McGurk, M., Bircher, M., Rapid prototyping for orthopaedic surgery. *Proc. Instn. Mech. Engrs. Part H.* 1998, *212*, 383–393.

- [26] Hollander, D.A., Wirtz, T., von Walter, M., Linker, R. *et al.*, Development of individual three-dimensional bone substitutes using “Selective Laser Melting”. *Eur. J. Trauma* 2003, 29, 228–234.
- [27] Winder, J., Bibb, R., Medical rapid prototyping technologies: State of the art and current limitations for application in oral and maxillofacial surgery. *J. Oral Maxillofac. Surg.* 2005, 63, 1006–1015.
- [28] Oliver, W. C., Pharr, G. M., An improved technique for determining hardness and elastic modulus using load and displacement sensing indentation experiments. *J. Mater. Res.* 1992, 7, 1564–1583.
- [29] Mosmann, T., Rapid colorimetric assay for cellular growth and survival – application to proliferation and cyto-toxicity assays. *J. Immunol. Methods* 1983, 65, 55–63.
- [30] Kuhn, S.D., Sridharan, K., Hao, Z., Muir, P. *et al.*, Biocompatibility of uncoated and diamond-like carbon coated Ti-20%Hf alloy. *Mater. Sci. Technol.* 2008, 24, 575–578.
- [31] Sui, J. L., Li, M. S., Lu, Y. P., Yin, L. W., Song, Y. J., Plasma-sprayed hydroxyapatite coatings on carbon/carbon composites. *Surf. Coat. Technol.* 2004, 176, 188–192.

[32] Zysset, P. K., Guo, X. E., Hoffler, C. E., Moore, K. E., Goldstein, S. A., Elastic modulus and hardness of cortical and trabecular bone lamellae measured by nanoindentation in the human femur. *J. Biomech.* 1999, 32, 1005–1012.

[33] Spadaro, J. A., Werner, F. W., Brenner, R. A., Fortino, M. D. *et al.*, Cortical and trabecular bone contribute strength to the osteopenic distal radius. *J. Orthop. Res.* 1994, 12, 211–218.

[34] Wang, D. A., Williams, C. G., Li, Q. A., Sharma, B., Elisseff, J. H., Synthesis and characterization of a novel degradable phosphate-containing hydrogel. *Biomaterials* 2003, 24, 3969–3980.

[35] Ng, L. T., Swami, S., Copolymers of acrylic acid with N-vinylpyrrolidinone and 2-hydroxyethylmethacrylate as pH-responsive hydrogels synthesized through a photoinitiator-free photopolymerization technique. *Polymer International* 2006, 55, 535–544.

[36] Xie, D., Yang, Y., Zhao, J., Park, J. G., Zhang, J. T., A novel comonomer-free light-cured glass-ionomer cement for reduced cytotoxicity and enhanced mechanical strength. *Dent. Mater.* 2007, 23, 994–1003.

4.2 Two-photon Polymerization of Scaffolds for Tissue Engineering

Introduction

In the past decade, two-photon polymerization has developed as a power tool for tissue engineering. The flexibility in controlling geometries and fabricating scaffolds with feature sizes ranging from sub-micron to tens of hundreds of microns makes this technique particularly appealing for tissue engineering. Several factors that are limiting the use of this technology are the ability to efficiently generate large scaffolds and a lack of materials that are well suited for tissue engineering. In this study these challenges were addressed. Tissue engineering scaffolds in novel designs that allow rapid replication and assembly and direction fabrication of large scaffolds was achieved. Further, riboflavin was demonstrated as a photoinitiator that is compatible with two-photon polymerization.

Materials and Methods

Photopolymers

Tissue engineering scaffolds were produced using two different photopolymer systems. A commercially-available photosensitive polymer, e-Shell 300 (EnvisionTEC GmbH, Gladbeck, Germany) was used to produce master structures of scaffolds compatible with replication by UV soft lithography. Scaffolds designed for direct use in vascular tissue engineering were produced from polyethylene glycol diacrylate (PEGda) (SR610, Sartomer, Paris, France), which has been shown to be a nonthrombogenic material [1]. Multiple length-

scale scaffolds for replacement of vasculature were produced using SR610 with the commercial photoinitiator Irgacure 369 (BASF, Ludwigshafen, Germany).

A novel photopolymer was developed by using a composition of PEGda as the polymer, riboflavin as the photoinitiator, and triethanolamine as the coinitiator. This composition contained 0.077 mg riboflavin (Sigma Aldrich, Saint Louis, MO), 1.49 mg triethanolamine, and 5 mL 0.05 mL deionized water per mL of PEGda.

Two-photon Polymerization of Scaffolds

Scaffolds were produced using the process two-photon polymerization. This material is frequently used in two-photon polymerization of microstructures due to its favorable properties such as low shrinkage, transparency, chemical, and thermal properties. Scaffolds were produced by two-photon polymerization using an 800 nm Scientific XL femtosecond laser (Femtolaser Produktions GmbH, Vienna, Austria). Polymerization occurs at the focus of the laser and proceeds along the trace with three-dimensional movement. The unpolymerized resin was placed between two glass cover slips in a polydimethylsiloxane ring with 6 mm diameter and 1 mm height, structuring was performed by scanning with the laser inside of this resin reservoir. Lateral scanning of small-scale components (e.g. individual cylinders) was controlled by a hurrySCAN® galvano scan head (Scanlabs, Puchheim, Germany). The height of the laser focus was controlled by a C-843 linear translation stage (Physik Instrumente, Karlsruhe, Germany) and two additional stages were used to control lateral motion from one component in the structure to the next. Custom written software

(Visual Basic, Microsoft, Redmond, Washington) was used to produce the structures. Lasing was performed with a 20x epi-plan objective (Carl Zeiss AG, Jena, Germany). The remaining unpolymerized material was removed by developing in isopropanol and deionized water for e-Shell 300 and PEGda, respectively. After developing, the structures were exposed to broad spectrum light from an ELC-410 ultraviolet lamp (Electro-Lite, Bethel, CT) to ensure complete polymerization throughout the structure. Two-photon polymerization of PEGda with riboflavin was performed with a femtosecond laser emitting at 515 nm due to riboflavin having poor absorption of the 800 nm laser.

UV Soft Lithography Replication of Stackable Hexagonal Scaffolds

Replicas of tissue engineering scaffolds were produced as previously described using UV soft lithography [2]. An aluminum ring was placed on the substrate with the master structure in the center and silicone elastomer (Sylgard® 184, Dow Corning, Midland, MI) was poured over the structure. Subsequently the silicone elastomer was polymerized by heating on a hot plate with a 30 minute ramp from room temperature to 100 °C and maintaining a 100 °C for an additional 30 minutes. The polymerized mold was then separated from the master using a linear stage as previously described [3]. Replicas were produced by placing e-Shell 300 resin on the mold and vacuuming to less than 100 mbar to remove air from the mold, which can create voids in the structure. Afterwards, excess resin is scraped off of the mold. The mold is then placed onto a glass slide with the resin touching the glass and polymerizing with an ELC-410 ultraviolet curing lamp. The replica is removed from the mold using the linear

stage. The replicated structures were manually removed from the glass substrate using a razor to function as free standing scaffolds.

Results and Discussion

Stackable LegoTM-like Scaffolds

Cylinder-based scaffolds in a Lego®-like design were produced by two-photon polymerization. The children's toy Legos® served as the inspiration for this scaffold design. Like these toy blocks, scaffolds with “pegs” and “wells” where the diameter of the peg is smaller than the well, can interlock to create a larger construct. These scaffold Lego®-like blocks can then be assembled to create a large scaffold structure with a defined geometry. CAD drawings of this scaffold design are presented in Figures 1a and 1b. Large-scale (50:1 models) were produced by fused deposition modeling as a proof of concept of stacking these scaffolds. An example of 3 pieces the scale model assembled into a larger 3-D geometry. Assembling a scaffold from a series of components allows for greater control over the overall scaffold geometry. In addition, the precursor components can be seeded with cells prior to assembly of the larger construct.

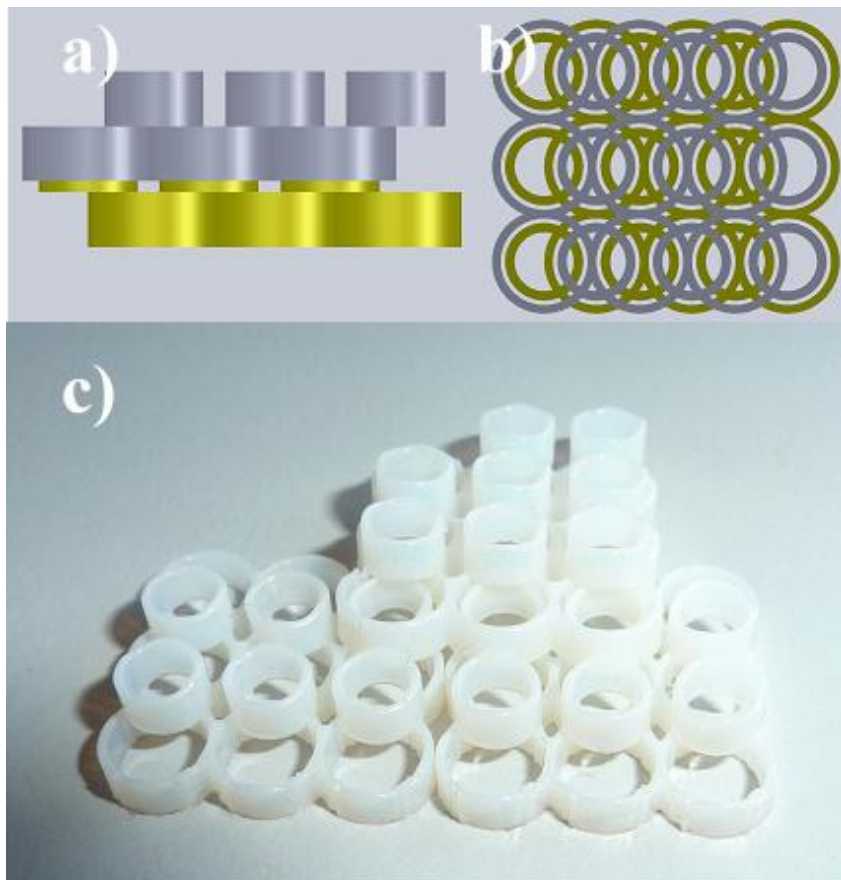


Figure 1. Stackable Lego®-like scaffolds concept: a) side view CAD drawing of two stacked scaffolds, b) top down view of two stacked scaffolds, c) 50:1 scale model of Lego®-like scaffold assembled into a 3-D shape.

Microscale Lego®-like scaffolds were produced by 2PP. These scaffolds were comprised of a lower layer of rings with a 200 μm outer diameter and 180 μm inner diameter and an upper layer of rings with an outer diameter of 140 μm and inner diameter of 60 μm . Arrays of various sizes were produced. Scanning electron microscopy images of e-Shell 300 Lego®-like scaffolds produced by 2PP.

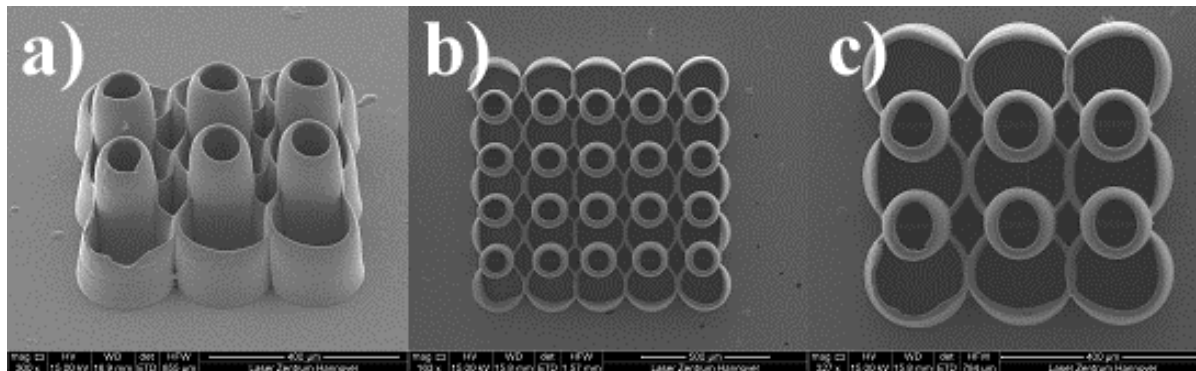


Figure 2. Scanning electron micrographs of Lego®-like scaffolds

UV Soft Lithography-Replicated Hexagon Scaffolds for Vascular Tissue Engineering

Stackable hexagonal scaffolds were made using custom written software which produces hexagonal scaffolds composed of an array of cylinders by scanning using polar coordinates. A 3-layer scaffold was produced with dimensions as described in Table 1. The inner diameter of the cylinders was 110 μm and the wall thickness was 22 μm . The first and second layers of the scaffolds were the same total size (14 cylinders per side). The hole in the first layer (11 cylinders per side) was one ring larger than the second layer (10 cylinders per side) and the third layer was a single ring that fit within the opening in the first layer (10 cylinders per side). SEM images of the master structure are provided in Figure 3. The design of this scaffold enables multiple replicas to be stacked on top of each other, resulting in a longer scaffold with a total size of 14 cylinders and hole size of 10 cylinders (Figure 4a).

Table 1: Scaffold dimensions

Layer	Total Size	Hole Size
1	14 cylinders	11 cylinders
2	14 cylinders	10 cylinders
3	11 cylinders	10 cylinders

E-shell 300 replicas of the scaffold were seeded with cells to assess their performance as a tissue engineering scaffold. After washing in ethanol for 2 hours and sterilization under UV light for approximately 30 min, the samples were placed in a 24 well plate, whose wells were each filled with 2 ml Dulbecco's Modified Eagles Medium (DMEM-F12 Ham's, Sigma Aldrich, Taufkirchen, Germany) supplemented with 10% fetal calf serum. Then, 6×10^6 cells ml⁻¹ were seeded out. After a 24 h cultivation time in a cell incubator (Thermo Electron Corporation, Bonn, Germany) at 37 °C and 5% CO₂ atmosphere, confocal microscopy was performed. The e-Shell 300 scaffolds exhibited good biocompatibility with the endothelial cells and were distributed throughout the scaffold (Figure 4b). Cells were seen to attach to and spread along the inner walls of the cylinders (Figure 4c).

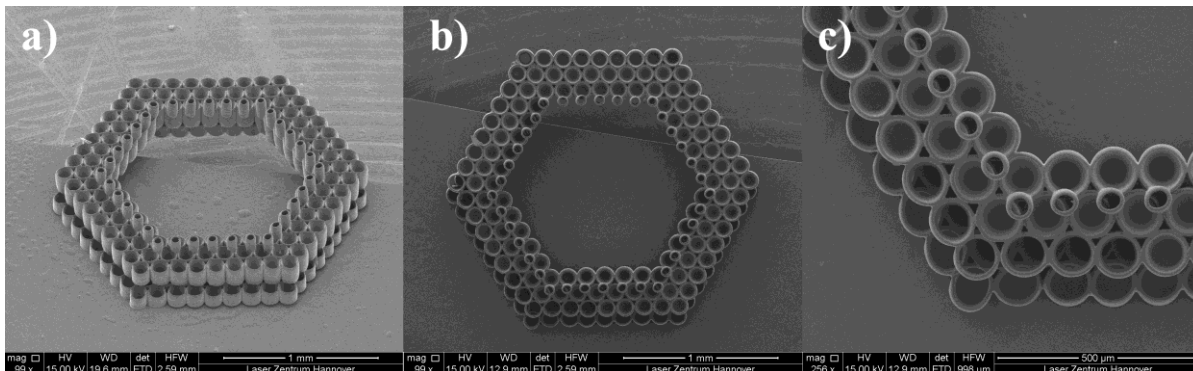


Figure 3: scanning electron microscopy images of stackable scaffolds for tissue engineering vasculature.

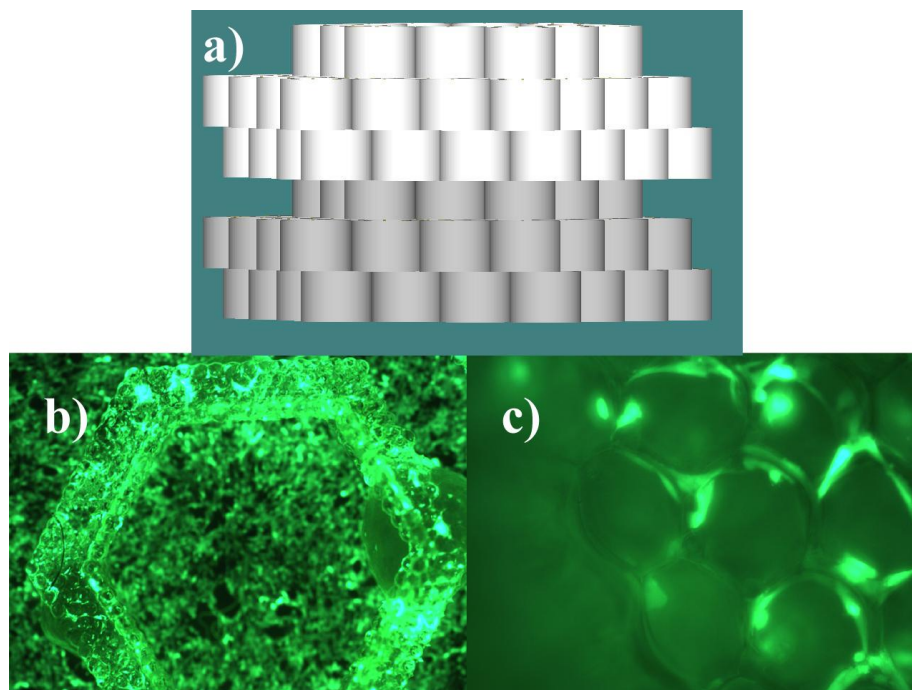


Figure 4. Hexagonal tissue engineering scaffold: a) master structure produced by 2PP, b) CAD drawing of two scaffolds stacked together, c) confocal microscopy image of e-Shell 300 replica seeded with immortal human pulmonary microvascular endothelial cells transfected with green fluorescent protein (GFP) at 5x magnification and d) 20x magnification.

Sideways Hexagonal scaffolds

Hexagonal scaffolds for tissue engineering of vasculature produced by 2PP were conventionally produced with the face in the z-direction and with pores oriented parallel to the face [2, 4]. However, there are several negative aspects of this scaffold design, particularly when used for producing large scale scaffolds. Firstly, cells are seeded and nutrients are delivered through the pores of the structure, but with the pores oriented parallel to the face of the structure, diffusion is only possible from the ends. Thus, as the scaffolds get longer nutrients and cells have to travel farther to reach their destination. Secondly, scaffolds produced in the z-direction cannot be longer than the working distance of the objective. A 20x objective generally has a working distance of approximately 7.9 mm, limiting the length of the tissue-engineered blood vessel.

To circumvent these problems, a novel scaffold design was developed where the pores are oriented perpendicular to the axis of the blood vessel and the axis of the blood vessel is oriented perpendicular to the axis of the laser. A CAD drawing of this design is provided in Figure 5. In this case the length of the scaffold is limited by the range of the stage and not the working distance of the objective. The diameter of the scaffold is now limited by the working distance of the objective, but in scaffolds for vasculature the length of the vessel is generally larger than the radius. Additionally, this design allows cells and nutrients to enter the cell along the length of the scaffold instead of from the ends, allowing easier cell seeding and nutrient transport.

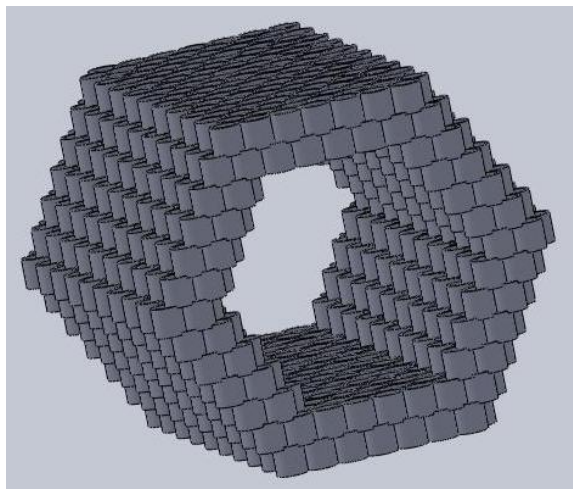


Figure 5. CAD drawing of sideways hexagon scaffold design

Perpendicular-oriented hexagonal scaffolds were produced from PEGda with 2% wt Irgacure 369. The scaffold was comprised of cylinders with an outer diameter of $80\ \mu\text{m}$ and a wall thickness of $24\ \mu\text{m}$. SEM images of a short segment (5 layers) of a perpendicular hexagonal vascular scaffold are provided in Figure 6.

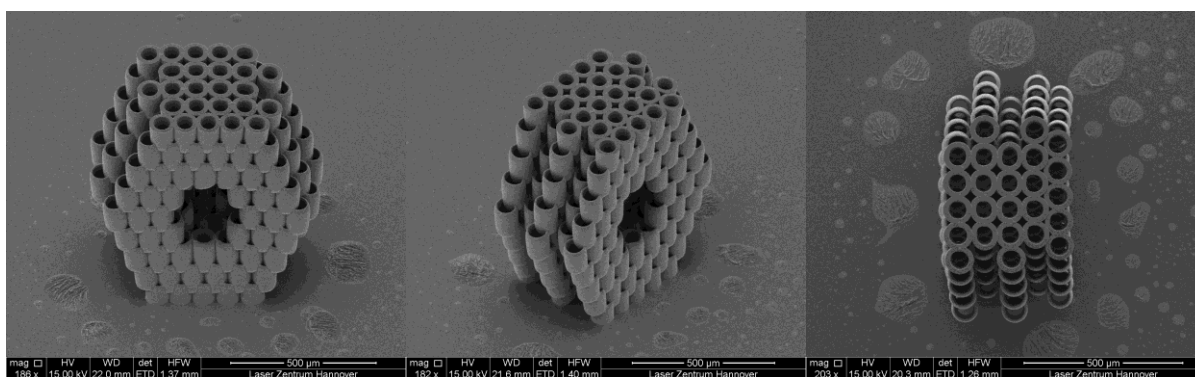


Figure 6. Scanning electron micrographs of a perpendicular hexagonal scaffold.

Larger scaffolds were produced for cell studies. Scaffolds used in cell studies were greater than 5 mm in length, had a total size of 7 cylinders per side, and a hole of 5 cylinders per side. An image of a 6 mm long scaffold is provided in Figure 7. Scaffolds were seeded with smooth murine vascular smooth muscle cells. After two days of culturing, they were stained with calcein AM for viability and Hoechst 33342 for nuclear imaging. High magnification fluorescence images of the scaffolds are provided in Figure 8. The scaffold itself is visible due to the autofluorescence of PEGda. The locations of some cells in Figure 8a are indicated by arrows. In Figure 8b cells can be seen to be attached to the walls of the cylinders. Figure 9 contains a fluorescence image of an entire scaffold. Cells can be seen to be distributed through the entire scaffold. This novel scaffold design enable 2PP-fabrication of tissue engineering scaffolds on the order of millimeters or even centimeters while still containing microscale features.

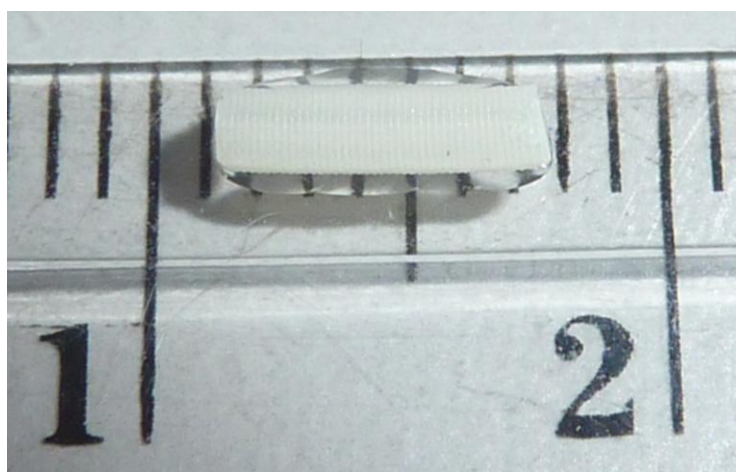


Figure 7. Six millimeter long sideways hexagon scaffold. Small lines equal 1 mm.

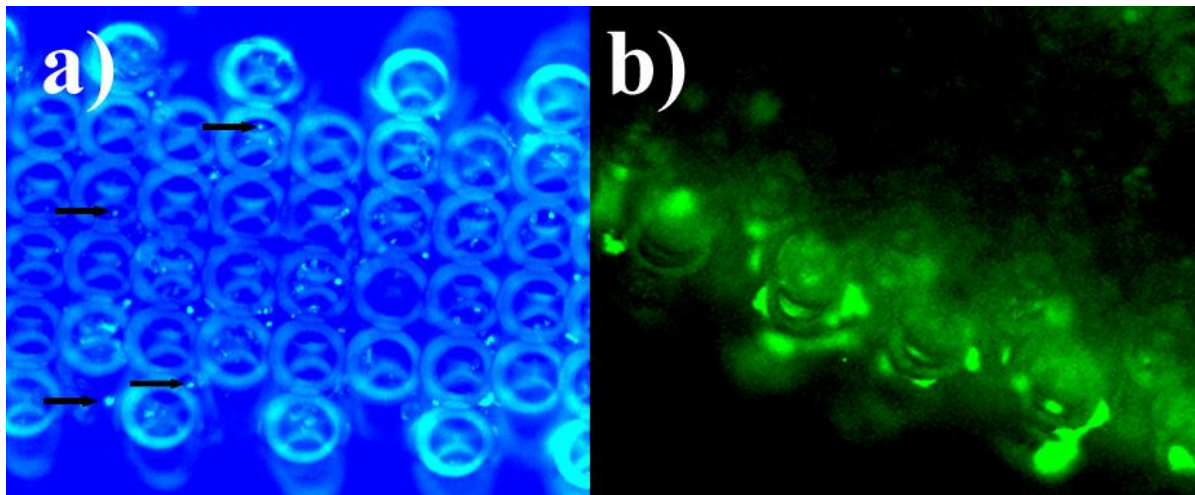


Figure 8. High magnification fluorescence images of sideways hexagon populated by vascular smooth muscle cells: a) blue fluorescence image (left) displays cell nuclei and PEGda autofluorescence; b) green fluorescence image (right) displays viable cells via calcein staining.

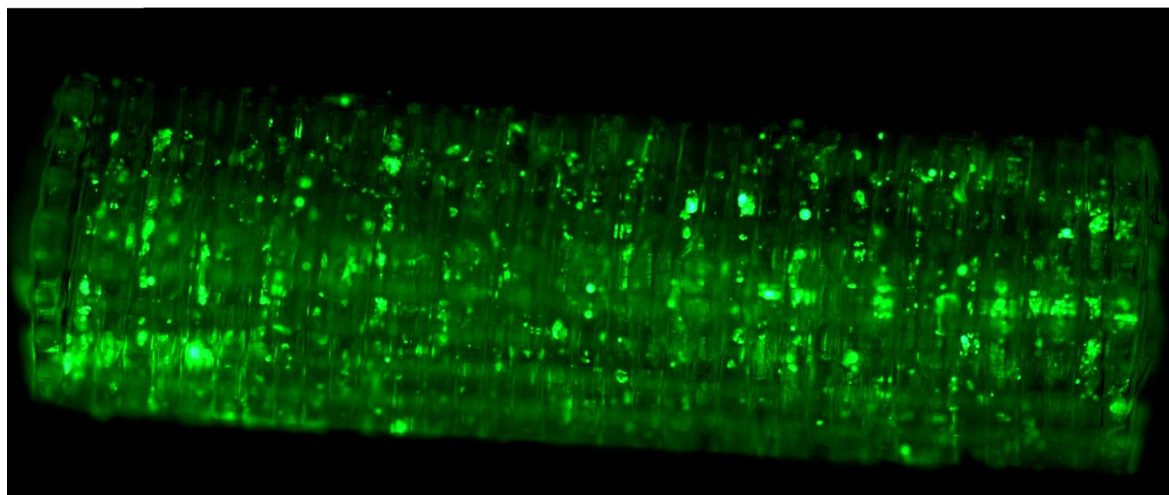
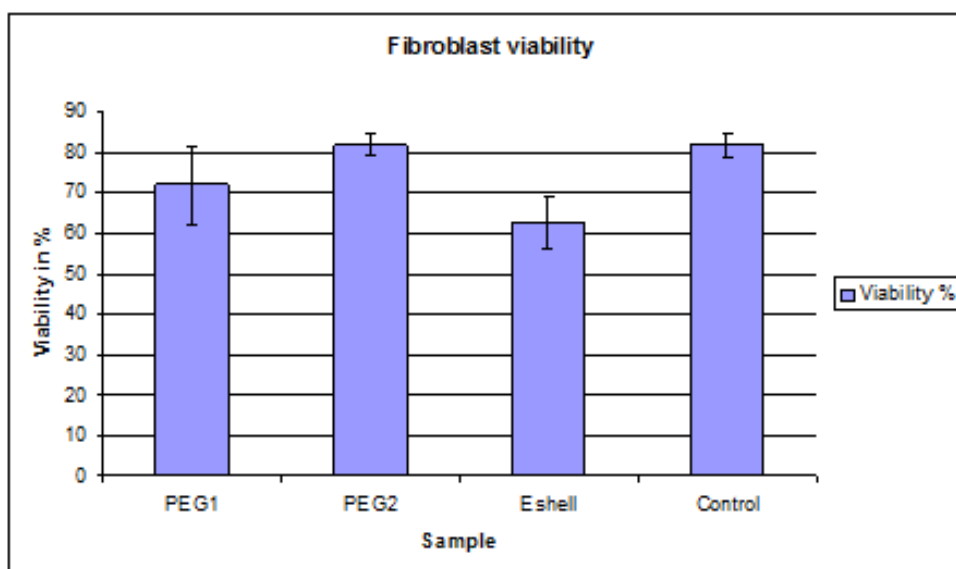


Figure 9: Entire 6mm PEGda scaffold populated with murine vascular smooth muscle cells stained for viability with calcein AM.

Polyethylene Glycol Diacrylate with Riboflavin Photoinitiator

One of the most important materials factors in tissue engineering scaffolds is biocompatibility. If the scaffold material is toxic, cells will not be able to populate the scaffold. Examples of sources of cytotoxicity in scaffolds are the material itself, unpolymerized monomer (in the case of polymer scaffolds), and photoinitiators [5]. Ovsianikov *et al.* have shown that PEGda with several commercial photoinitiators, such as Milcher's Ketone, Irgacure 369, and Irgacure 2959 are cytotoxic, though the cytotoxic components can be removed by extensive washing [5]. As a solution to this problem, the vitamin riboflavin was examined as a more biocompatible photoinitiator. Two concentrations of riboflavin in PEGda were investigated, one with 7.7 mg riboflavin per 100 mL PEGda (0.077 mg/mL) and one with 77 mg riboflavin per 100 mL PEGda (0.77 mg/mL). Both concentrations also had 1.49 mg triethanolamine, and 5 mL 0.05 mL deionized water per mL of PEGda. Six millimeter diameter and 1 mm thick wafers of these two materials were produced by polymerization with a UV curing lamp. L929 mouse fibroblasts were cultured of these two surfaces, E-shell 300, and glass as a control. Cell viability was determined using a CASY cell counter. Both of the riboflavin containing materials had high cell viabilities, with the 0.77 mg/mL concentration having similar viability to the control material (Figure 10).



PEG1: 7,7mg/100ml Riboflavin

PEG2: 77mg/100ml Riboflavin

Figure 10. Fibroblast viability measured by CASY cell counting

Polymerization of PEGda with riboflavin could not be achieved with an 800 nm femtosecond laser, which can be attributed to the poor absorption of riboflavin at 400 nm. UV-Vis spectroscopy was performed to obtain the absorption spectrum of an aqueous solution of riboflavin with triethanolamine (Figure 11). Varying the concentration of riboflavin affected the amplitude of the absorbance but produced no shift; triethanolamine concentration had no effect on absorbance.

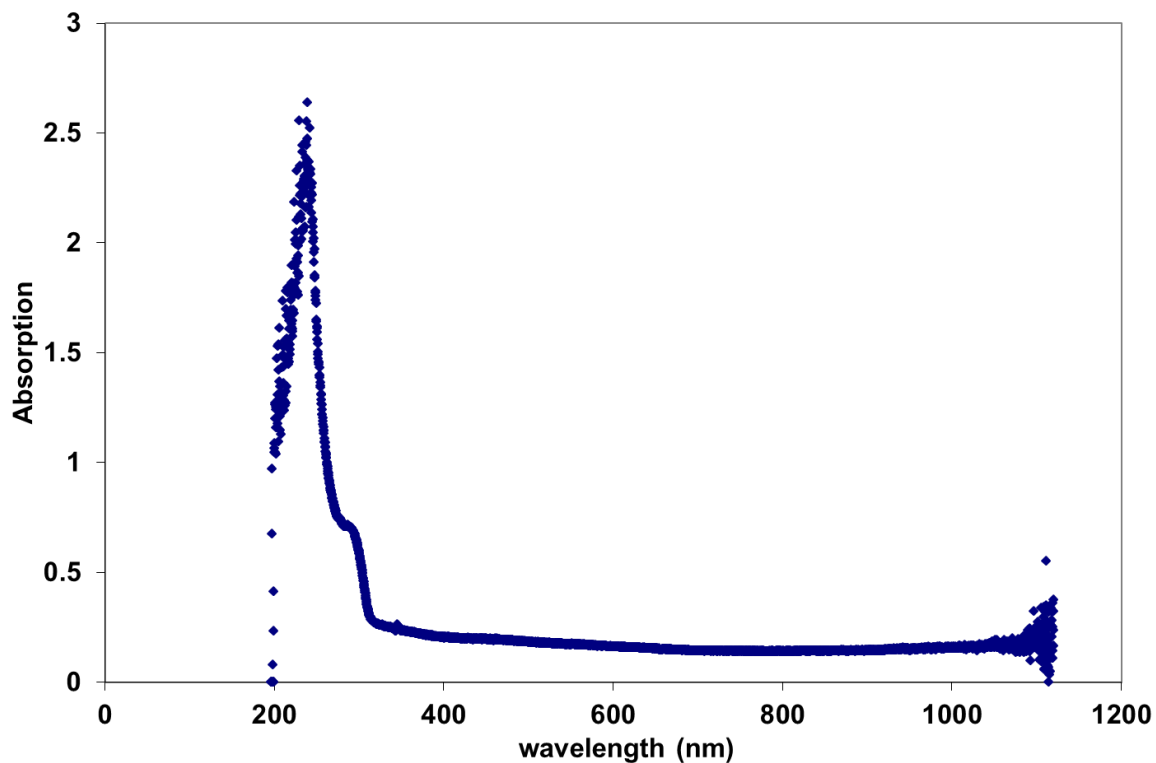


Figure 11: UV-Vis absorption spectrum of riboflavin and triethanolamine in deionized water

The material was easily polymerized with exposure to a femtosecond laser at 515 nm. Cubes of PEGda with 0.077 mg/ mL riboflavin were produced, as shown in Figure 12. Scaffolds produced using the photosensitive vitamin riboflavin as a photoinitiator may help improve the biocompatibility of tissue engineering scaffolds produced by 2PP.

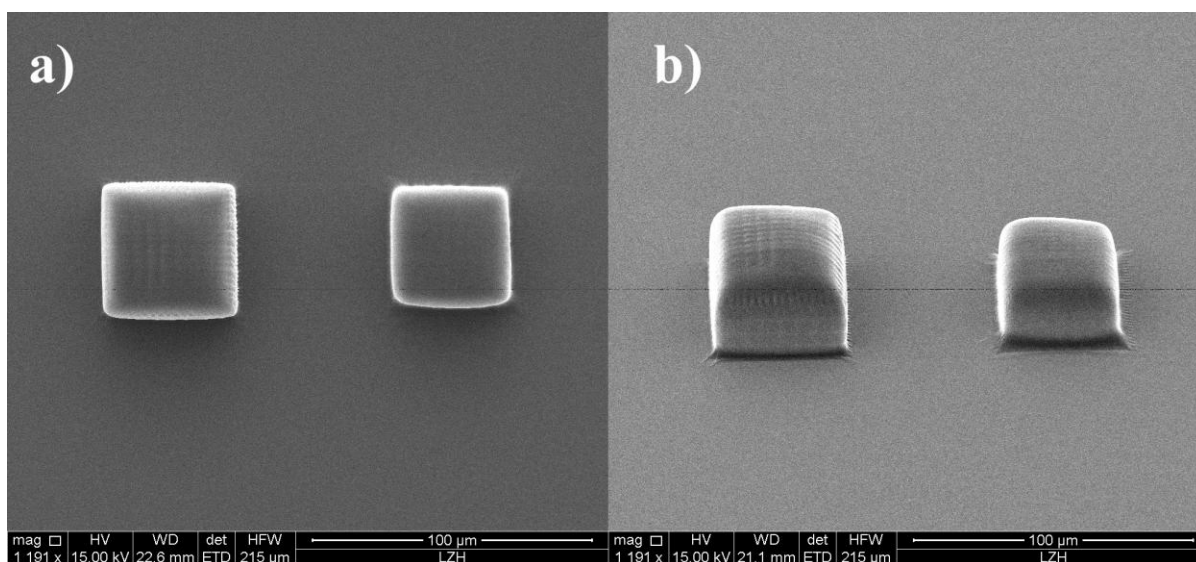


Figure 12. Microstructures of polyethylene glycol diacrylate with 0.077 mg/mL riboflavin produced by 2PP.

Conclusions

Several advances in the design, production, and materials of tissue engineering scaffolds were presented. The concept of creating scaffolds that can be reproduced by UV soft lithography and stacked to produce larger constructs was demonstrated. Further, modifying the design of hexagon scaffolds composed of cylinders enabled scaffolds on the order of several millimeters to be produced with pores oriented in a way to improve nutrient transport. Lastly, the vitamin riboflavin was shown to be a photoinitiator that is compatible with two-photon polymerization. This report is the first demonstration of using riboflavin as a photoinitiator in two-photon polymerization. These developments will help to aid the development of two-photon polymerization as a tool for tissue engineering.

Acknowledgements

Anastasia Koroleva, Andrea Diewick, Harry A Scott, Alexander Nguyen, Roger J Narayan, and Boris N Chichkov contributed to this work

References

- [1] Gittard SD, Ovsianikov A, Akar H, Chichkov B, Monteiro-Riviere NA, Stafslie S, Chisholm B, Shin C, Shih C, Lin S, Su Y, Narayan RJ. Two Photon Polymerization-Micromolding of Polyethylene Glycol-Gentamicin Sulfate Microneedles. *Advanced Engineering Materials* 2010;12(4):B77-B82.
- [2] Koroleva A, Schlie S, Fadeeva E, Gittard SD, Miller P, Ovsianikov A, Koch J, Narayan RJ. Microreplication of laser-fabricated surface and three-dimensional structures. *J Optics* 2010;12(12):124009.
- [3] Gittard SD, Ovsianikov A, Monteiro-Riviere NA, Lusk J, Morel P, Minghetti P, Lenardi C, Chichkov BN, Narayan RJ. Fabrication of Polymer Microneedles Using a Two-Photon Polymerization and Micromolding Process. *J Diabetes Sci Technol* 2009 March; 3(2):304-311.

[4] Ovsianikov A, Gruene M, Pflaum M, Koch L, Maiorana F, Wilhelmi M, Haverich A, Chichkov B. Laser printing of cells into 3D scaffolds. *Biofabrication* 2010 MAR;2(1):014104.

[5] Ovsianikov A, Malinauskas M, Schlie S, Chichkov B, Gittard S, Narayan R, Löbler M, Sternberg K, Schmitz K-, Haverich A. Three-dimensional laser micro- and nano-structuring of acrylated poly(ethylene glycol) materials and evaluation of their cytotoxicity for tissue engineering applications. *Acta Biomaterialia* 2011 3;7(3):967-974.

5. CONCLUSIONS

This work has reported on a range of advances in the fields of micro- and nanoscale drug delivery and regenerative medicine. The development of indirect rapid prototyping via two-photon polymerization and UV soft lithography has been used to produce both microneedles and scaffolds with complex overhanging geometries from a range of materials. Novel materials for two-photon polymerization and UV soft lithography were discussed, including e-Shell 200, gentamicin-doped polyethylene glycol, and polyethylene glycol with riboflavin as the photoinitiator. Studies in this work also detailed significant advances in dynamic mask stereolithography, including the first use of this technology to make patient-specific prosthetics, the first case of needles produced with this technique with antimicrobial coatings, and the first demonstrations of drug delivery through hollow microneedles produced directly by dynamic mask stereolithography. Nanoporous gold electrodes were shown to be capable of delivering ionic drugs. Numerous advances in two-photon polymerization of tissue engineering scaffolds and microneedles were described. Scaffolds several millimeters in length were produced by two-photon polymerization and novel designs allowing mass replication and assembly of scaffolds were demonstrated. Microneedle technology was extensively discussed in this work. Studies investigating the mechanical properties of microneedles, antimicrobial coatings on microneedles, and delivery of pharmacologic agents with microneedle arrays were described. The research reported throughout this work provides a comprehensive review of light-based rapid prototyping of micro- and nanoscale medical devices.